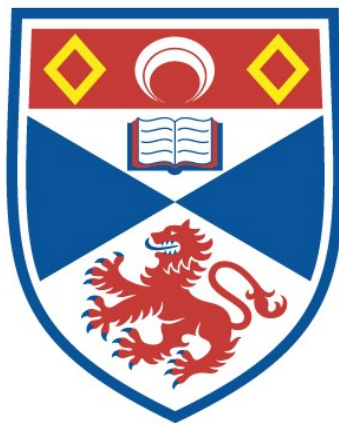


AN INVESTIGATION OF CONTACT AND NON-CONTACT BINARY SYSTEMS

Thomas M. McFarlane

**A Thesis Submitted for the Degree of PhD
at the
University of St Andrews**



1986

**Full metadata for this item is available in
St Andrews Research Repository
at:**

<http://research-repository.st-andrews.ac.uk/>

Please use this identifier to cite or link to this item:

<http://hdl.handle.net/10023/11008>

This item is protected by original copyright

AN INVESTIGATION OF CONTACT AND NEAR-CONTACT

BINARY SYSTEMS

by

THOMAS M. McFARLANE

A thesis submitted to the University of St. Andrews in application
for the degree of Doctor of Philosophy.

St. Andrews

2nd May 1986.



I acknowledge that in submitting this thesis to the University of St. Andrews I am giving permission for it to be made available for use in accordance with the regulations of the University library for the time being in force, subject to any copyright vested in the work not being affected thereby. I also understand that the title and the abstract will be published, and that a copy of the work may be made and supplied to any bona fide research worker.

Declaration

=====

The research detailed in this thesis and the composition are my own work except where reference is made to the work of others. No part of this work has been previously submitted for another degree at this or any other University. I was admitted to the Faculty of Science of the University of St. Andrews as a research student on 1st. October 1982, under Ordinance General No.12. I was accepted as a candidate for the degree of Ph.D. on the 1st. October, 1983, under Resolution of the University Court, 1967, No.1.

Thomas M. McFarlane

Certificate

=====

I certify that Thomas M. McFarlane has spent nine terms in research work at the University Observatory, St. Andrews, that he has fulfilled the conditions of the Ordinance General No.12 and the Senate Regulations under Resolution of the University Court, 1967, No.1, and that he is qualified to submit the accompanying thesis in application for the degree of Ph.D.

R. W. Hilditch.

ACKNOWLEDGEMENTS

I would like to thank the Science and Engineering Research Council for their financial support in the form of a postgraduate studentship award.

I am also indebted to my supervisor Dr.R.W.Hilditch for his patient guidance and assistance throughout this endeavour, and for many useful, and at times lively, discussions.

I would also like to express my gratitude to Prof.D.W.N.Stibbs for much valued advice on academic and other matters.

I thank Dr.Janusz Kaluzny of the Warsaw University Observatory, who suggested the method of photometric analysis employed in Chapter 7 .

I thank also the staffs of the South African Astronomical Observatory and the Instituto de Astrofisico de Andalucia for their assistance during my observing sessions, especially Peter Mack, Victor Costa, Dave Kilkenny, John Menzies and Ian Coulson.

I am also grateful to my fellow research students, past and present, who changed my attitude to scientific challenge and discovery by their example. Special thanks to Ian Skillen (for his valued comments on the finer points of statistics and Fourier analysis, and for pointing out the dangers of 'shoddy-workmanship'), to Steve Bell (for providing the graphics routines used to create many of the diagrams in this thesis, and for giving useful advice

when the computer didn't do what it was told), and to Mark Clampin (for our discussions on Fourier analysis and spectroscopic-data reduction).

Last, but certainly not least, I would like to express my thanks to my Father and Mother for their help and constant encouragement, and to my wife Margaret, who has supported me (financially and otherwise) throughout the last ten years, and without whom this work could not have been written.

FOR MAGGIE

ABSTRACT

Spectroscopic and photometric observations of six late-type contact and near-contact binaries are presented, and the results of the analyses discussed. Absolute dimensions have been deduced for three systems: YY Ceti, CX Aquarii and RV Corvi.

YY Ceti, which has an orbital period of 0.79 days, is found to be composed of a normal main-sequence star of spectral type A8 and an evolved G-type star which completely fills its Roche lobe. We argue that the system will evolve into contact within approximately 10^9 years, either by the nuclear evolution of the primary component, or by the loss of angular momentum via magnetic braking. We also propose that this may represent a route to the A-type contact binaries which does not involve a passage through the W-type phase.

The binary CX Aquarii, which has an orbital period of 0.56 days, is found to have a similar configuration to YY Ceti, except that its primary component is a main-sequence star of spectral type F5 with an evolved companion of spectral type G9. We argue that the system should achieve contact by loss of angular momentum via magnetic braking within approximately 10^8 years if the atmosphere of the primary component is convective, or within approximately 5×10^8 years if the primary possesses a radiative atmosphere.

RV Corvi is found to consist of an unevolved F2 primary component with a K-type companion which has a much larger radius and luminosity than expected for its mass. The system has an orbital period of 0.75 days. Although the binary may be semi-detached, with

the primary component completely filling its Roche lobe, it is most probably in a state of marginal contact. In order to obtain a solution to the photometric data it was necessary to treat the secondary component albedo as a free parameter, yielding a value greater than unity. This result implies that there is an abnormal distribution of luminosity on the surface of the binary, which may be interpreted either as an excess of light on the facing hemisphere of one or both of the components, or as a deficit of light on the averted hemisphere of the secondary.

The three remaining binaries, EZ Hydrae, AD Phoenicis and RS Columbae, were all identified as contact systems: EZ Hydrae as a W-type system of orbital period 0.45 days, AD Phoenicis as an A-type system of period 0.38 days, and RS Columbae as an A-type system with a period of 0.67 days. Although a value for the mass ratio of EZ Hydrae had been obtained from spectroscopic observations, no photometric solution could be found because of severe 'disturbances' in its light curve. From our sample of six systems, AD Phoenicis and RS Columbae were the only two for which there were no spectroscopic observations. Although photometric solutions were obtained for both systems, these were very insensitive to the value of mass ratio, which tended toward the physically unrealistic value of unity.

The results for YY Ceti, CX Aquarii and RV Corvi are combined with the published masses, radii and luminosities of 21 other contact and near-contact binaries. It is shown that the primary components of all contact and near-contact systems are normal main-sequence stars with radii and luminosities appropriate to their masses. The secondary components of the B-type systems and the W-type systems are all overluminous for their masses, due mostly to the radii being increased by a factor of ~ 1.7 . However, these

secondary components are segregated on the H-R diagram, where the W-type secondaries appear to the left of the main sequence band due to luminosity transfer from the primary components. The secondary components of the A-type contact systems all have radii and luminosities substantially larger than expected for their masses.

CONTENTS

CHAPTER 1 : INTRODUCTION

1.1	Introduction	1
1.2	Formation models for W Ursae Majoris binaries	3
1.2.1	The formation of W Ursae Majoris binaries from protostar fission	4
1.2.2	The formation of W Ursae Majoris binaries from detached or semi-detached binaries	14
1.3	The common convective envelope model	24
1.4	Structural models for W Ursae Majoris binaries	32
1.5	The contact discontinuity theory	33
1.6	The thermal relaxation oscillation theory	48
1.7	The angular momentum loss theory	63
1.8	A unification of the DSC and TRO theories ?	71

CHAPTER 2 : PROJECT OUTLINE

2.1	Introduction	81
2.2	Project objectives	82
2.3	Observational requirements	83
2.4	Applications for observing time	84
2.5	Binaries selected for survey	86

CHAPTER 3 : SPECTROSCOPY

3.1	Introduction	88
3.1.1	SAAO 1.9m telescope and instrumentation	88
3.1.1.1	SAAO 1.9m telescope	88
3.1.1.2	Image-Tube Spectrograph	89
3.1.1.3	Reticon Photon Counting System	90

3.1.2	Isaac Newton Telescope and instrumentation	92
3.1.2.1	Isaac Newton Telescope	92
3.1.2.2	Intermediate-Dispersion Spectrograph	92
3.1.2.3	Image Photon Counting System	93
3.2	Observations	94
3.2.1	Observations obtained with the SAAO 1.9m telescope	94
3.2.2	Observations obtained with the Isaac Newton Telescope	95
3.3	Data reduction	95
3.3.1	Initial reduction of spectra	95
3.3.2	REDUCE	96
3.3.3	Determination of stellar radial velocities	100
3.3.4	VCROSS	101
3.4	Analysis of radial-velocity data	104
Appendix 3.1	Calculation of component separation	107
Appendix 3.2	Calculation of component masses	109
 CHAPTER 4 : PHOTOMETRY		
4.1	SAAO 0.5m telescope and instrumentaion	111
4.2	Observations	112
4.2.1	Nature of observations	112
4.2.2	Selection of comparison and standard stars	113
4.2.3	Observing technique	114
4.3	Data reduction	115
4.3.1	Reduction to instrumental and standard magnitudes	115
4.3.2	Calculation of differential magnitudes	115
4.4	Data analysis	115
4.4.1	Calculation of ephemerides	115
4.4.2	Light curve analysis	116
4.4.3	WUMA3	117
4.4.3.1	Geometry of the contact-binary model	117

4.4.3.2	Light curve synthesis	119
4.4.3.3	Searching for a photometric solution	124
4.4.4	LIGHT	126
4.4.4.1	Geometry of the binary model	126
4.4.4.2	Light curve synthesis	127
4.4.4.3	Solving the light curve	128
Appendix 4.1	Calculation of transformation coefficients and zero-point constants using the SAAO photometry package	129
Appendix 4.2	Interstellar extinction	131
 CHAPTER 5 : YY CETI		
5.1	Introduction	133
5.2	BVRI _c photometry	133
5.3	Correction to ephemerides	135
5.4	Spectroscopy	136
5.5	Spectroscopic analysis	137
5.6	Photometric analysis	141
5.7	Discussion	144
Appendix 5.1	Component mass-ratio, minimum masses and separations calculated from the Lehman-Filhes orbit solution	160
Appendix 5.2	Interstellar reddening	163
Appendix 5.3	Primary-component absolute visual magnitude from the ubvy β indices	165
Appendix 5.4	Component visual and bolometric magnitudes and luminosities	166
Appendix 5.5	Expected colours of YY Cet	168
Appendix 5.6	Angular momentum of YY Cet	171
Appendix 5.7	Estimate of angular momentum loss required for contact, assuming constant mass ratio	174

Appendix 5.8	Estimate of rate of angular momentum loss by magnetic braking	178
Appendix 5.9	Estimate of timescale for YY Cet to evolve into contact via magnetic braking	181

CHAPTER 6 : CX AQUARII

6.1	Introduction	183
6.2	Observations	183
6.3	Revised ephemeris	185
6.4	Spectroscopic analysis	186
6.5	Photometric analysis	187
6.6	Discussion	189
Appendix 6.1	Component mass-ratio, minimum masses and separations calculated from the radial-velocity data	211
Appendix 6.2	Component visual and bolometric magnitudes and luminosities	212
Appendix 6.3	Expected colours of CX Aqr	214
Appendix 6.4	Angular momentum of CX Aqr	216
Appendix 6.5	Estimate of angular momentum losses required for contact, assuming constant mass ratio	217
Appendix 6.6	Estimate of rate of angular momentum loss by magnetic braking	218
Appendix 6.7	Estimate of timescale for CX Aqr to evolve into contact via magnetic braking	220

CHAPTER 7 : RV CORVI

7.1	Introduction	222
7.2	Observations	223
7.3	Revised ephemeris	225
7.4	Spectroscopic analysis	226

7.5	Photometric analysis	228
7.6	Discussion	232
Appendix 7.1	Component mass-ratio, minimum masses and separations calculated from the Lehman-Filhes orbit solution	253
Appendix 7.2	Component visual and bolometric magnitudes and luminosities	255
Appendix 7.3	Expected colours of RV Crv	257
Appendix 7.4	Angular momentum of RV Crv	259
CHAPTER 8 : EZ HYDRAE, AD PHOENICIS & RS COLUMBAE		
8.1	Introduction	260
8.2	Photometric observations	261
8.3	Revised ephemerides	263
8.4	Photometric analyses	265
8.5	Conclusions	269
CHAPTER 9 : CONCLUSIONS		
9.1	Evolution into contact	319
9.2	The B-type contact binaries	319
9.3	Contact-binary data	320
9.4	Concluding remarks	323
APPENDIX A : CALCULATION OF ERRORS		333
APPENDIX B : COMMENTS AND CORRECTIONS		334
REFERENCES		336

CHAPTER 1

INTRODUCTION

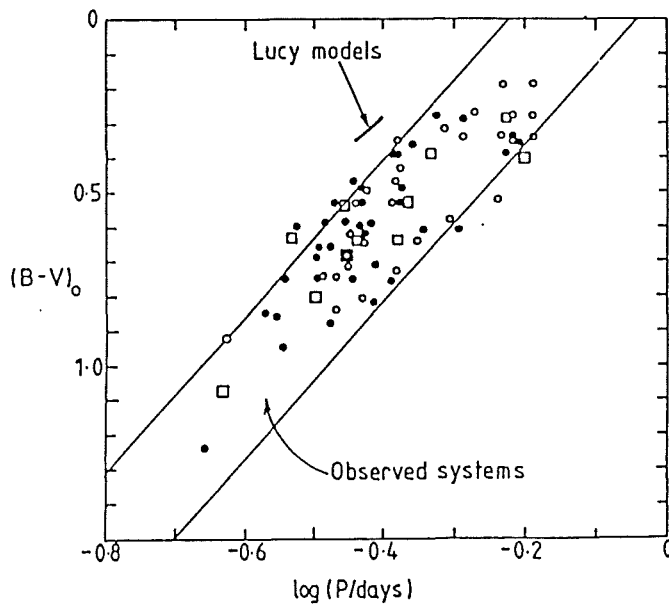
1.1. INTRODUCTION:

In recent years the evolution and structural form of W Ursae Majoris binaries has been the subject of some lively, and at times acrimonious, debate. These systems, which form a significant proportion of all late-type stars in the solar neighbourhood, are a class of contact binary composed of components of spectral-type $\sim F_0$ or later, with very short orbital periods (less than ~ 0.6 days), and observed mass ratios between about 0.08 and 0.88. Their light curves display curved maxima and nearly equal depth minima, implying that the components possess similar surface temperatures and are heavily distorted due to their close proximity to one another.

There are two recognised sub-categories of W UMa binaries, called A-type and W-type by Binnendijk (1965, 1970). The A-type systems have the more massive component covered during primary eclipse, and the binaries are found to be well over-contact, that is, their surfaces substantially exceed their Roche 'inner contact surfaces'. The W-type systems, on the other hand, have the less massive component covered during primary eclipse, and the systems are shown to be in thin or marginal contact (eg. Lucy, 1973).

While the A-type systems are believed to be evolved, and essentially in equilibrium, the W-type systems are believed to be unevolved, and show several signs of not being in equilibrium, for example, erratic period and light curve changes. The A-type systems tend to have smaller mass-ratios than the W-types, they also tend to be hotter and more massive. (A more comprehensive comparison of the A-type and W-type systems will be discussed later.)

Eggen (1961, 1967), observed that the W UMa binaries followed a fairly well defined period - colour relationship, with the shorter period systems lying towards redder colours (Figure 1.1).



The period-colour diagram for the systems listed by Mochnacki (1981) (●), with additional systems from Eggen (1967) (○) and Whyte (1984 unpublished catalogue) (□). The colours from Whyte are not corrected for reddening. The observed systems lie within a broad strip, roughly bounded by the diagonal lines (taken from Eggen 1967); the original Lucy models fall outside that strip.

Figure 1.1. Eggen's period - colour relation.

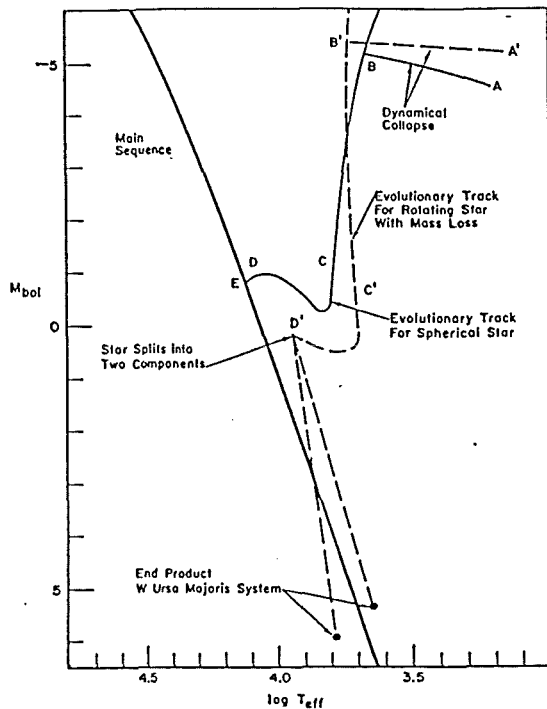
1.2. FORMATION MODELS FOR W URSAE MAJORIS BINARIES:

Two separate formation processes have been proposed for W UMa binaries. Firstly it has been argued that the binaries arise from the fission of rapidly rotating protostars during their pre-main-sequence contraction phase. Secondly, evolution from a detached or semi-detached configuration into a contact state by means of angular momentum loss via a stellar wind, has been suggested. Both these processes have been the subject of debate for some years.

In the past there have been various approaches to the problem, but recent years have seen the application of many numerical techniques involving three-dimensional gas dynamic models. However, the results of these analyses should be treated with some caution since the models are attempting to simulate the macroscopic behaviour of great quantities of stellar material with only a very small number of 'particles'. Because of this limited spatial resolution, genuine physical effects which involve short distance scales, may be suppressed. The addition of unwanted effects may also be introduced due to the non-negligible errors of difference approximations. Thus, even if a particular model is created using the correct formulae, initial conditions, and boundary conditions, a totally incorrect prediction may still result.

1.2.1. The formation of W Ursae Majoris systems from protostar fission.

Consider the situation where an interstellar gas cloud is undergoing a gravitational collapse. A non-rotating cloud will continue to collapse until the internal pressure increases to the point where it balances the inward gravitational forces. The body of gas will then oscillate about a position of hydro-static equilibrium (position B on Figure 1.2). At this stage ('the Hayashi phase') the protostar is highly luminous, with a completely convective core, and a radius approximately 50 times larger than its final zero-age main-sequence value. During this phase the star continues to contract, moving almost vertically downwards on the H-R diagram (B to C on Figure 1.2).



Pre-main-sequence evolution of non-rotating and rotating stars

Figure 1.2. Pre-main-sequence stellar evolution.

As the stellar contraction continues, the luminosity decreases, and eventually a radiative core begins to develop (position C of Figure 1.2). With further contraction the radiative core continues to grow (C to D on Figure 1.2), until most of the star reaches a state of radiative equilibrium. As the star moves towards its main-sequence position on the H-R diagram, more massive stars will develop a convective core at their centres.

However, if the initial gas cloud was rotating, then the evolutionary path of the forming star could be very different to that discussed above.

The classical theory of binary star origin dates back to Jeans (1929), and is based on figures of equilibrium of uniformly rotating, viscous, liquid stars. Through later works by others (summarised by Chandrasekhar, 1969), the type and point of occurrence of the instabilities of these stars was established. In terms of the rotational kinetic energy of the star ' W ', and its gravitational potential energy ' T ', the star is axisymmetric until the ratio ' $T/|W|$ ' reaches a value of about 0.14, after which the star will undergo a secular instability and pass into an ellipsoidal sequence. When the ratio reaches a value of about 0.16, then the star moves into a dynamically unstable 'pear-shaped' configuration. Jeans (1929), assumed that the disruption of this configuration would result in the formation of a close binary system.

However, there have been many objections to this scenario; firstly, a liquid star is a very poor approximation to a real star; secondly, in real stars the viscosity is not large enough to ensure uniform rotation of the rotating protostar; and thirdly, the objection of Lyttleton (1953), who apparently 'proved' that it was impossible for a binary to be formed from a dynamical instability. (Lyttleton argued that in the absence of dissipation, ie. the transformation of energy into inaccessible forms, then reversing the sign of time, that is, running time backwards, should send a binary

back into its original state, that being a rotating protostar. But clearly this is not so, since reversing the direction of time would merely result in a binary system which rotates in the opposite direction to that of the original.)

All of these major objections will be discussed later.

Roxburgh (1966) investigated the pre-main-sequence evolution of a rotating non-magnetic star. He argued that stars forming out of slowly rotating interstellar gas clouds would have sufficient angular momentum to balance their centripetal and gravitational forces before reaching the stable Hayashi phase (track A'B' of Figure 1.2). (Obviously, before the point of dynamical stability is reached, point B', the star must have lost some matter due to its rotation.) At the point of stability the centripetal force must balance the gravitational force at the area of fastest rotation, ie. at the stellar equator.

As in the non-rotating case, once the star reached a state of dynamical stability it had a completely convective interior and a very high luminosity. Roxburgh remarked that this convective turbulence should effectively couple the central and surface regions of the star allowing a uniform stellar rotation. As the star contracted further, more material was lost from its equatorial region, decreasing the angular momentum of the body. (The subsequent contraction was investigated by Roxburgh, 1965).

Roxburgh found that as the star continued to contract it moved vertically downwards on the H-R diagram (track B'C' on Figure 1.2), until it reached a position in which a radiative core began to develop, just as in the non-rotating case (point C'). However, unlike the non-rotating case, the development of this core had a significant effect on the evolution of the star.

Roxburgh assumed that where there was a radiative zone the 'viscosity' effect of the turbulence was no longer present. Since each element of the growing core conserved its angular momentum, this resulted in an increasing angular velocity of the radiative regions with further stellar collapse, assuming that there is no other coupling mechanism such as a magnetic field (track C'D' of Figure 1.2). Roxburgh also argued that if conservation of angular momentum is assumed on fission, then stars with mass less than $4 M_{\odot}$ should result in contact binaries, whereas for heavier stars the result should be a detached binary system.

Tassoul and Ostriker (1970), carried out an analysis of uniformly-rotating, compressible stars. They examined the question of whether or not the liquid star model is a reasonable approximation to a real star, this being of paramount importance to the classical Jeans model. The results of the analysis suggested that the occurrence and form of the stellar instabilities were remarkably independent of the compressibility. The authors concluded that, if this was in fact the case, then real stars may indeed be treated as liquid stars, as Jeans suggested.

Ostriker and Bodenheimer (1973) and Bodenheimer and Ostriker (1973), tackled the second objection to the Jeans model, that is, that the viscosity in real stars is not large enough to secure uniform rotation during the contracting protostar phase of stellar evolution. They determined the stability of equilibrium models of polytropes which had a specific angular momentum per unit mass. Their analysis suggested that the differentially-rotating models behaved in a very similar fashion to the classical uniformly-rotating axisymmetric liquid stars of Jeans in their stability properties. In particular, the models were found to have a neutrally stable mode when the $T/|W|$ ratio had a value of approximately 0.14, again in good agreement with the Jeans model. Finally, at a $T/|W|$ ratio of about 0.26, the models were found to go into an 'overstable' mode, which, Ostriker and Bodenheimer suggested, may lead to fission.

A numerical approach to the fission hypothesis was taken by Lucy (1977). He described a finite size particle scheme, and tested it on several astronomical problems in order to demonstrate its good behaviour, even at low spatial resolution.

The starting point of Lucy's calculations was a rotating, axisymmetric, optically thick protostar of homogeneous composition. He followed the protostars' evolution up to, and beyond the point of instability, to a non-axisymmetric perturbation. He omitted any energy generated in the interior of the star in order that the contraction did not halt before the onset of instability.

Lucy was forced to make several compromises when approaching the fission problem. Ideally he would have preferred to begin with a uniformly rotating, $n = 1.5$, polytrope (i.e. a fully convective Hayashi star), but this approach led to two practical difficulties for the scheme; firstly, it would have been impossible to compute the Kelvin-Helmholtz contraction of the protostar because of time step difficulties, and secondly, a high spatial resolution would have been required as the model became very centrally condensed ($n \sim 3$). However, these problems were overcome by modifying the ideal problem. The time step problem was avoided by speeding up the contraction to some extent, and the problem of insufficient spatial resolution was solved by using a model with a polytropic index, $n = 0.5$. (It was assumed that neither of these changes would affect the mathematical character of the models.)

Lucy found that the following general trends emerged from the numerous cases computed:

1. Following the appearance of departures from axial symmetry, a substantial fraction of the mass was nearly always lost as debris, presumably due to the transfer of angular momentum from the interior of the protostar to its surface by the action of gravitational torques.
2. Evolution into a bar-shaped structure was common - the losses of angular momentum to the debris rarely stopped this.
3. If fission did occur, it led to a binary of small mass ratio, typically towards the lower end of the range, 0.1 - 0.5.

Lucy concluded that it may be reasonable to expect the binary to be a contact system.

Gingold and Monaghan (1977, 1978), also took a numerical approach to the fission problem. They employed a technique called 'smoothed particle hydrodynamics', in order to study the instabilities of self-gravitating gases. The main features of the method were that the stellar fluid was replaced by a set of fluid elements or 'particles', and that the density of the other physical fields were obtained by a statistical smoothing procedure. The equations of fluid dynamics were replaced by a set of Newtonian equations for the centre of mass coordinates of the particles.

In their 1977 paper, the authors demonstrated that, starting with a non-axisymmetric distribution of approximately 80 particles in three dimensions, the smoothed particle hydrodynamic method could reproduce the structure of uniformly rotating polytropes to within a few percent when the polytrope was distorted from a state of spherical symmetry.

Gingold and Monaghan (1978), applied this numerical approach to damped differentially-rotating polytropes, similar to those of Ostriker and Bodenheimer. (The damping they used conserved the total angular momentum, and angular momentum per unit mass.) The authors calculated the forms of equilibrium and the modes of fission of the polytropes. In their treatment, Gingold and Monaghan began with a uniformly rotating spherical protostar, and then introduced a damping term in order to remove radial motion while still conserving total angular momentum. Thus, the end products of the model sequences were a generalisation of the classical viscous model sequences.

Within this context, Gingold and Monaghan demonstrated that close binary systems may form as the result of fission. Since they did not expect the initial or damping conditions to be realistic, they made no attempt to show details of the dynamic sequence leading to the equilibrium conditions. However, the authors did show some of the details of a dynamic sequence leading to fission, since it clearly exhibited a 'bone-shaped' structure (cf. Lucy, 1977).

The results of the Gingold and Monaghan models may be summarised as follows:

1. When the ratio $T/|W|$ was low, then the damped sequences led to equilibrium forms which were similar to classical Maclaurin spheroids.
2. When the ratio $T/|W| > 0.14$, then the equilibrium forms were similar to Jacobi ellipsoids.
3. When $0.17 < T/|W| < 0.22$, the objects were found to have a pear-shaped form, but were unstable, finally reverting to an ellipsoidal form by throwing off 'particles'.
4. For higher $T/|W|$ values, the damped sequences passed through a number of forms until, at $T/|W| \sim 0.4$, a bone-shaped form emerged, which then underwent fission.
5. For a polytropic index of $n = 0.5$, it was found that fission resulted in the formation of a close binary system, but for a polytropic index of $n = 1.5$, the final state of fission was not resolved.

Finally, one very interesting aspect of Gingold and Monaghans' calculations involved the final disruption of the polytrope. They found that for polytropes with a polytropic index of $n = 0.5$, the rotating bone structure broke into two objects, regardless of whether damping was maintained or not. Since the formation of the binary was independent of damping, then it may be regarded as a dynamical instability, and thus the process was in clear conflict with Lyttleton's argument (Lyttleton, 1953) that a binary could not form from a dynamical instability.

Gingold and Monaghan believed Lyttleton's argument to be incorrect for the following reason: "Dissipation is only a description of the transformation of energy to inaccessible forms. Ordinary viscosity prevents the motion being reversible because the energy is transformed to molecular motion. This is so complicated that the chance of it returning to the initial state is negligible. For a fluid system with many degrees of freedom the same phenomenon can occur on a macroscopic scale. For example, when the binary is formed, the two separate polytropes are distorted and they begin vibrating. For the polytropes to return to exactly the same initial state (the 'bone') the vibrations would have to be back in their original state in phase with each other and with the orbital motion. The chance of this happening is low, and becomes lower as non-linear effects transfer energy amongst the modes of vibration. The motion is therefore effectively irreversible even though microscopic dissipation is excluded."

Gingold and Monaghan (1979), recomputed their fission sequences. Again they used the 'smoothed particle hydrodynamic' treatment, but with a significantly larger number of particles (800). Their results confirmed the general mode of fission found earlier for polytropes with a polytropic index of $n = 0.5$. However, with the higher resolution, a three pointed 'starfish' structure was apparent before fission, and after fission, a very low mass third companion was observed as well as the two distinct main bodies of the binary.

In their 1978 paper, Gingold and Monaghan had failed to resolve the nature of the disruption of polytropes with high polytropic indexes. They had found that the models with $n = 1.5$ 'appeared' to spray out a stream of matter rather than undergo a clear fission. However, using the 800 particle model, the authors found the situation somewhat clarified. The $n = 1.5$ polytrope was indeed found to throw out a stream of matter, and Gingold and Monaghan concluded that the ultimate state in this case would probably be a star surrounded by a diffuse disc.

1.2.2. The formation and evolution of W Ursae Majoris systems from detached or semi-detached binaries.

Schatzman (1962), proposed a mechanism by which single stars may lose large amounts of angular momentum with little loss of mass. He suggested that when ionised material is ejected from the surface of a star, then it will be compelled by the stellar magnetic field (if one is present), to rotate with the star, even at very

large distances. Thus the ejected material gains large amounts of angular momentum per unit mass at the expense of the stellar angular momentum. Schatzman argued that this mechanism should lead to large angular momentum losses from stars, for only relatively small losses of mass.

Huang (1966), suggested that this may be the mechanism by which close binary stars dissipate large amounts of angular momentum to become contact systems. He argued that if the spin angular momentum of single stars may be lost by a process of magnetic braking, then it should be equally likely that orbital angular momentum may be lost from close binaries by the same mechanism. Huang proposed that the dissipation of binary orbital angular momentum could take two slightly idealised forms. He first considered the case where the magnetic fields of the binary component stars are linked. Here the orbital angular momentum may be directly transported out of the system by ejected ionised material. The next case Huang considered was when the two component stars are not magnetically linked. He suggested that here, both components may dissipate their spin angular momentum separately, as in the single star case, but since the components of the close binary system are always coupled dynamically, then this lost spin angular momentum would eventually lead to loss of orbital angular momentum via tidal effects. By making use of the empirical mass-radius relation for main-sequence stars, Huang argued that even after the two components come into contact, loss of angular momentum would continue, with mass being transferred from the less massive to the more massive star.

In order to strengthen his case further, Huang noted that his proposed mechanism for contact binary formation is ideally sound since it is based entirely on known physical principles and is supported by observational evidence concerning magnetic activity in the early phases of stellar evolution.

Mestel (1968), lent further support to the magnetic braking hypothesis. In his paper he formulated a stellar wind theory for rotating magnetic stars surrounded by an isothermal corona, with magnetic and rotational axes parallel. Although the mechanism that Mestel proposed was the same as that put forward by Schatzman, the theory was much more comprehensive, and its relevance to close binary evolution was demonstrated. Mestel proposed a similar magnetic braking process for binary systems to that by Huang. He argued that his theory of magnetic braking could successfully explain how a close binary protostar system could remain close, even after the components had contracted by factors of 20 - 50 to their main-sequence values, eventually resulting in a contact system. The binary magnetic braking hypothesis was greatly enforced by the work of Mestel, since his theory was proposed independently from that of Huang.

The formation of W UMa type binaries by the above process was considered in greater detail by Okamoto and Sato (1970), who developed the theory further. On the basis of the Roche model, they established that after binary contact has been achieved, angular momentum loss continues and mass transfer occurs from the less massive to the more massive component, thus showing Huang's

hypothesis to be correct.

Another important proposal of Okamoto and Sato was that contact systems with smaller mass ratios tend to be more stable with respect to angular momentum loss than those of larger mass ratio because of a weaker magnetic dynamo effect. (This hypothesis assumed the Lucy (1968) model for W UMa binary structure.) The authors suggested that this may be the reason why the W UMa systems appear to so abundant.

In order to investigate the magnetic braking scenario in a more quantitative manner at least two poorly known factors were needed; the angular momentum loss-rate and the initial distribution of the physical parameters of the newly-born binaries. If these factors were known then they could be combined in order to derive some of the observable quantities which describe close contact binary systems.

First let us consider the angular momentum loss rate factor:

In order to give a quantitative description of the angular momentum loss rates in close and contact binaries it was first necessary to examine the properties of single main-sequence stars. Studies have been carried out on the magnetic braking mechanisms of solar-type main-sequence stars and the effects of differing rotational speeds. Important evidence for braking in solar-type stars came from observations of rotational velocities and Ca II emission.

Wilson (1962), argued that a correlation exists between chromospheric activity and age, in main-sequence stars. He noted that observations of the average intensities of the Calcium H and K emissions were much higher for main-sequence stars of spectral-types G0 - K2 in the Hyades, Praesepe, Coma and Pleiades clusters than for similar, and presumably older, local field stars. He also found, from observations of local visual binaries, that the H - K intensities in the members of such pairs tended to be very similar when allowance was made for spectral-type differences. Wilson came to the conclusion that the most probable explanation for these facts was that the H - K intensity in main-sequence stars, and hence the general degree of chromospheric activity, bears an inverse relationship to age. Wilson and Skumanich (1964), furnished further evidence for this proposal.

After making corrections for spectral-type effects, Skumanich (1972), compared the Ca II emission luminosity of stars in the Pleiades, Ursa Major and Hyades clusters with that of the Sun, and proposed that the emission decay varies as the inverse square root of age.

Skumanich also noted another finding which bears great relevance to the magnetic braking hypothesis. He found that the rotational decay curves also appeared to vary as the inverse square root of age. Skumanich then argued that since the Ca II emission should be linearly proportional to the surface magnetic field strength, then the surface magnetic fields appear to be proportional to angular velocity (i.e. a stellar dynamo effect), and decay as

the inverse square root of age.

Further work published by Smith (1979), confirmed the Skumanich inverse square root of age 'law', and demonstrated its validity for higher rotational velocities than were previously proposed (at least down to rotational periods of about three days).

The above works provide an important argument in favour of increasing angular momentum loss rates with decreasing rotational periods.

The other important factor in the magnetic braking scenario involved the initial distribution of the physical parameters of the newly formed binaries. Let us now consider this:

An alternative to the binary formation by fission mechanism discussed earlier, follows from the work of Larson (1969, 1972a, 1972b), who proposed a mechanism known as 'fragmentation'. Larson presented a detailed treatment of the non-homogeneous initial collapse of a rotating protostar, which apparently demonstrated that there may be no true Hayashi phase where the protostar is highly luminous, completely convective, and contracting in hydrostatic equilibrium. The results of Larson suggested that when the rotating protostar is in a state of collapse, a 'ring-like' toroidal structure may form. He argued that such a ring-like structure would almost certainly be unstable and would fragment into two or more condensations in mutual orbit. Later hydrodynamic calculations by Black and Bodenheimer (1975, 1976), Norman and Wilson (1978), and Bodenheimer (1978), confirmed the results of Larson.

Bodenheimer (1978), examined the fragmentation mechanism using two and three dimensional numerical techniques, similar to those used earlier to examine the fission process. He followed the evolution of a rotating stellar cloud, starting at interstellar densities, which collapsed to form a ring-like structure. This then fragmented into two equal parts rotating uniformly, which then, through a series of intermediate fragmentation stages, finally ended with multiple stellar systems with components near the main-sequence. He demonstrated that the observed angular momentum distribution of binaries could be arrived at by this process.

Lucy and Ricco (1979), suggested that binaries of intermediate and small total mass ($10 M_{\odot} > M_{\text{tot}} > 0.5 M_{\odot}$) and short period ($P < 25$ days) are formed by a mechanism which, in its ideal form, would create binaries of equal mass. They identified this mechanism with the heirarchical fragmentation scheme of Bodenheimer (1978). (Norman and Wilson (1978), and Cook and Harlow (1978), demonstrated, using numerical techniques, that ring fragmentation can indeed yield binaries with identical components, unlike the fission process which yields binaries of smaller mass ratio.)

Kraicheva, Popova, Tutukov and Yungel'son (1979), calculated models for the distribution of spectroscopic binary stars with respect to the mass of the primary component, the mass ratio of the system, and the semi-major axis of the orbit. The models were based on stellar evolution theory, and allowed for observational selection effects. The authors found that the initial mass ratio distributions contained only one peak, which lay at $q = 1$, lending

some support to the suggestion of Lucy and Ricco. Kraicheva et al. suggested that the initial period distribution of the binary systems is probably flat, with a short period cut-off around 2 days, and a long period cut-off at around 10^6 days.

Finally, Gingold and Monaghan (1983), applied the 'smoothed particle hydrodynamic' model to study the fragmentation of differentially rotating clouds. Their results implied that the clouds fragment into four or five components, whose total mass is about 80 per cent of the initial mass of the cloud. They found that the masses of these components were usually unequal, producing binaries of higher multiplicity than Bodenheimer's model, with components which were generally closer together. However, because the fragments were described by only about 200 particles, the resolution was inadequate for detailed study of their evolution. This fragmentation was assumed to lead to a wide variety of multiple stellar systems.

Vilhu (1982), presented a study of the detached-to-contact scenario as the formation process for W UMa binaries. He argued that the classical rotation-age dependence of Skumanich for single solar-type stars with rotational periods longer than three days, (i.e. $V_{\text{rot}} \propto t^{-1/2}$, where ' V_{rot} ' is the stellar rotational velocity and ' t ' is the stellar 'age'), probably continued to even shorter periods, but perhaps with a different exponent. He supported his case by citing activity-rotation connections in the ultraviolet and X-ray regions of the spectra.

Vilhu expressed the classical rotation-age dependence, $V_{\text{rot}} \propto t^{-1/2}$, in terms of spin angular momentum and period, i.e. $dJ_{\text{spin}}/dt \propto P^{-3}$, for periods longer than three days, and as $dJ_{\text{spin}}/dt \propto P^{-\alpha}$ ($\alpha < 3$), for shorter periods. He then coupled this angular momentum loss rate with the orbital angular momentum of close binary systems, assuming synchronous rotation of the components.

Vilhu derived some important conclusions from this detached-to-contact treatment:

1. The process produced roughly the correct mean-field density of contact systems if the contact lifetime, T_{cont} , was assumed to be about 5×10^8 years. (About 0.5 - 2% of all stars of the same spectral-type are contact binaries, this being true even with large ranges of (i.e. $1 < \alpha < 3$) and with large ranges of the short-period cut-off.)

Vilhu suggested that the typical progenitors of W UMa systems may be detached binaries with periods initially (i.e. after formation), of between 1 and 4 days, and that these evolve towards contact binaries by losing angular momentum, gradually showing more and more RS CVn - type activity. He also suggested that some short period RS CVn - type systems may at present be evolving into W UMa binaries.

2. W UMa binaries may be produced by this process in old ($\sim 5 \times 10^9$ years) and in intermediate age ($\sim 5 \times 10^8$ years) clusters, but in very young ones ($< \sim 10^8$ years) only if the initial period distribution reached down to sufficiently short periods. (Vilhu remarked that different individual clusters may have different initial period distributions.)

3. A smooth period cut-off at around 2 days in the initial period distribution produced roughly equal numbers of evolved and non-evolved contact systems.

4. When the angular momentum loss rate factor, ' α ', was chosen to be about 1.5, then the corresponding angular momentum losses from the binaries were sufficient to avoid (or weaken) the thermal relaxation oscillations of the TRO theory (discussed later).

5. Vilhu found it difficult to choose the optimum values of the various parameters involved in his scenario, but however, the choices (which may not be unique),

$$\alpha = 1.5 ,$$

$$P_{\min} = 0.9 \text{ days (initial distribution minimum period),}$$

$$P_{\text{cut}} = 2.0 \text{ days (initial distribution short-period cut-off),}$$

$$T_{\text{cont}} = 5 \times 10^8 \text{ years ,}$$

were not incompatible with the statistics of observation.

6. The above parameters also produced a ratio of low-mass binaries (excluding W UMa type) with periods less than two days, to those with periods greater than two days, of about 1:60 . This figure is in agreement with Popova et al. (1982), who carried out a statistical study of such systems.

Vilhu remarked that since these results demonstrated that the values of the various parameters involved in his scenario need not be extremely peculiar for the process to work, and that the estimates suggested that the process was realistic, then the scenario probably represented the correct mechanism of W UMa binary production.

1.3. THE COMMON CONVECTIVE ENVELOPE MODEL:

Kuiper (1941), demonstrated, by simple argument, that the sizes of isolated zero-age main-sequence stars are incompatible with the requirements of the Roche geometry of zero-age contact binaries, unless the component stars are identical.

He argued that if both components filled their critical Roche lobes, then the relation between their masses and radii may be approximated to,

$$R_2/R_1 = (M_2/M_1)^a, \text{ where } a \approx 0.46.$$

However, since the mass-radius relation for isolated zero-age main-sequence stars gives the value of 'a' as about 0.88 (Patterson, 1984), then the above relationship cannot hold unless the masses and radii of the component stars are identical.

This gave rise to an apparent contradiction; W UMa binaries may indeed be composed of unevolved main sequence stars whose mass ratio is not unity, but typically 0.5. In fact, contact systems of mass ratio unity are not observed at all, even although selection effects would favour their discovery.

In order to avoid Kuiper's paradox, three possible assumptions may have been made:

1. The binaries were not in equilibrium.

(This was Kuipers' proposition, and may well be the case. The

equilibrium and non-equilibrium models will be discussed later.)

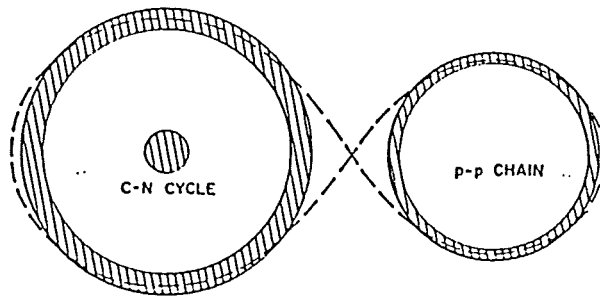
2. The contact binary components were evolved to some extent.

(Various studies have shown that although the components of many W UMa binaries are evolved, this is probably not the case for all systems. Mochnacki (1981) argues that the W-type systems are unevolved.)

3. The atmospheric structure of the W UMa component stars may be different to those of isolated stars.

(It was suggested that the the component stars of the W UMa binaries were surrounded by an optically-thick common convective envelope.)

The common convective envelope (CCE) structure of contact binaries was investigated by Lucy (1968a). Lucy argued that if the common envelope surrounding the components is convective, then the adiabatic constants of the envelope around each component must be equal. He proposed that the changes resulting from the equality of adiabatic constants allowed contact of the components. Lucy neglected any distortion of the components in his treatment (Figure 1.3.).



Model for a W UMa star at age zero. The surface of the binary for which this model is a first approximation is shown as a dashed line. Hatched areas denote convection zones. Also indicated is the dominant nuclear reaction in the interior of each component.

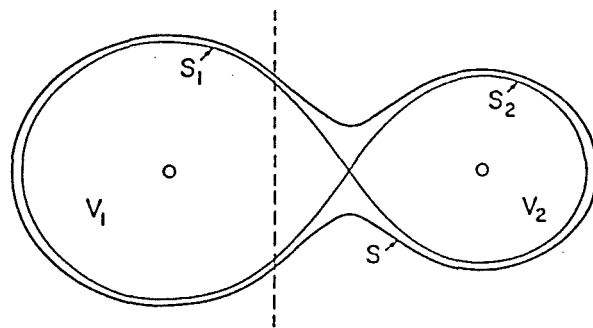
Figure 1.3. Lucy's (1968a) model for an unevolved W UMa binary.

The Lucy model however, gave rise to major theoretical problems concerning the luminosity distribution in contact binaries. Observational evidence suggested that both components of W UMa systems had almost equal surface fluxes. In Lucy's model the similar surface brightness arose from the flow of convected energy between the components via the common convective envelope, leading to a cooling of the primary and a heating of the secondary, with the CCE at an intermediate temperature. However, the mechanism which transforms the luminosities emerging from the stellar interiors to the brightness distribution characteristic of the W UMa binaries, has been a subject of great controversy for some years, and will be discussed later.

The predictions of the Lucy model were found to give some qualitative agreement with observation, but detailed agreement, especially with Eggen's period - colour relation, was not very good.

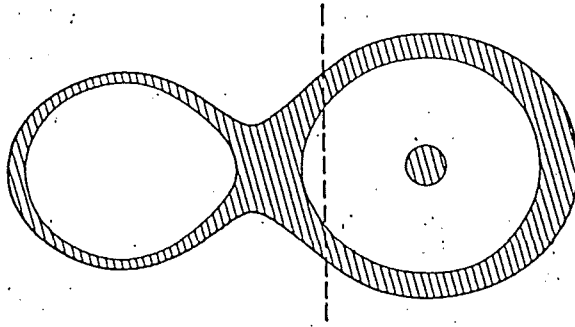
On the basis of the theoretical structure of W UMa systems given in his 1968a paper, Lucy (1968b), presented a model for calculating their light curves, thus testing the theory further.

In his previous paper Lucy had neglected any distortion of the components, but since distortions may cause light variations comparable with those of eclipses, they were therefore an essential part of light curve analysis and could not be ignored. Lucy assumed (as is now standard in the theory of light curve analysis of eclipsing binaries), that the surfaces of the contact binaries were equipotentials, and used the Roche model to calculate them. (See figures 1.4, 1.5.)



Geometry of a contact binary. The equipotential surface S is the common photosphere and the equipotential surface S_1S_2 (the inner contact surface) is the lower boundary of the common envelope. Vertical dashed line is the axis of rotation.

Figure 1.4. Contact binary geometry.



Model for a W UMa system. The hatched areas denote convection zones, and the vertical dashed line is the axis of rotation.

Figure 1.5. Lucy's (1968b) W UMa binary model.

The Lucy model provided an explanation for the anomalous luminosity ratios of the W UMa systems and correctly predicted the major characteristics of their light curves. However, it failed to explain the asymmetries found in many of the observed W UMa light curves. Furthermore, the primary minima of the theoretical light curves were due to the eclipse of the more massive components, which is not true for many observed systems.

In an attempt to explain the eclipse discrepancy, a number of theoretical studies (eg. Whelan (1972), Moss and Whelan (1973), Mochnacki and Whelan (1973), Biermann and Thomas (1972, 1973) and Vilhu (1973)) suggested that energy exchange in the superadiabatic parts of the CCE may make the secondary component slightly hotter (by a few hundred degrees centigrade) than its more massive companion, the temperature difference depending on the degree of contact between the components.

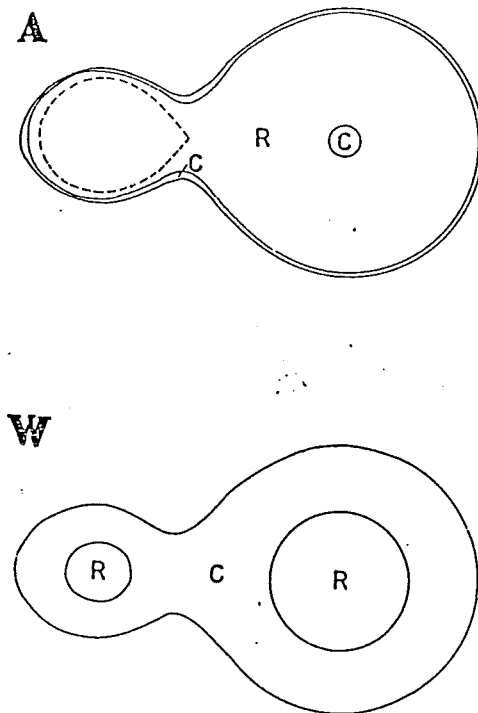
It should be noted that there is now mounting evidence to suggest that the secondary components of W-type W UMa binaries are not in fact hotter than the primaries. It has been argued that starspots on the primary components may decrease their surface brightness, giving the appearance that they are cooler than their companions. eg. Mullan (1975), Eaton, Wu and Rucinski (1980b), Eaton and Wu (1981), and Kaluzny and Pojmanski (1983). Indeed, the light curve of at least one system, TZ Boo, has been observed to alternate between A-type and W-type several times during recent years, eg. Rucinski (1985).

Lucy's CCE model, however, yielded close fits to Binnendijk's A-type W UMa systems (eg. Mochnacki and Doughty (1972a, 1972b), Rucinski (1973, 1974), and Lucy (1974)). But, further investigations of the A-type and W-type W UMa binaries gave rise to more problems concerning Lucy's CCE model. Studies by Rucinski (1973, 1974), suggested that the A-type systems had only shallow CCE's but with a greater degree of contact, while the W-type systems had deeper CCE's but with lesser degree of contact (Table 1.1 and Figure 1.6). Thus, it is the W-type W UMa binary structure which appears to resemble the Lucy model, not the A-type structure as one would have expected. This raises the question as to why this should be so; surely the cooler W-type systems with their deeper CCE's should be able to redistribute their individual stellar luminosities far better than the hotter A-type systems with their shallower CCE's ?

Comparison of the A- and W-type W UMa systems.

Property	A	W	Remarks
1. Spectral type	earlier	later	differences slightly marked
2. Luminosity	higher	lower	differences slightly marked
3. Mass	larger	smaller	differences slightly marked
4. Activity (changes of light curves, asymmetries of maxima)	moderate or absent	strong or very strong (almost every system)	
5. Period	either chan- ging or cons- tant	always changing	Kelvin-Helmholtz time- scale or slightly slower
6. Mass-ratio	small 0.08 - 0.54	larger 0.33 - 0.88	upper limit more certain
7. Degree of contact	envelopes slightly thicker than in W-type	shallow envelo- pes	
8. Photometric conformity to the contact model	good	poor (less massive comp. hotter)	
9. Energy exchange takes place in	adiabatic parts of the conv. envelo- pe	superadiabatic parts of the conv. envelope	
10. Peculiar systems	not too many; systems of very small q , early-type contact sys- tems	many: SW Lac, $q = 0.88$; AB And and ER Ori, deviation from the mass-lumino- sity relation; many other with changing light curves	

Table 1.1. Rucinski's table comparing A-type and W-type W UMa binaries.



The schematic picture of internal structure of a hotter (A-type) and a cooler (W-type) contact systems. In the former the outer convective zone (C) is too thin to affect the energy transfer; its presence does, however, influence the internal structure of both components. The broken line marks the last common equipotential delimiting parts of secondary very strongly and less strongly coupled with the structure of primary. The internal structure of the W-type system is as proposed by Lucy (1968a).

Figure 1.6. A-type and W-type W UMa binary structure.

1.4. STRUCTURAL MODELS FOR W URSAE MAJORIS BINARIES:

At present there is no single structural model able to explain all observed properties of W UMa systems. However, there are three possible theories which, with further development, may yield a full description of the W UMa binary structure. These are:

The 'contact discontinuity (DSC) theory', whose origin traces back to Biermann and Thomas (1972, 1973), Moss and Whelan (1973) and Vilhu (1973), and was later advanced by Shu, Lubow and Anderson (1976, 1979).

The 'thermal relaxation oscillation (TRO) theory', proposed by Lucy (1976), and further advanced by Flannery (1976), Rahunen and Vilhu (1977), and Robertson and Eggleton (1977).

The 'angular momentum loss (AML) theory', developed by Vilhu and Rahunen (1980, 1981), Rahunen (1981), and Vilhu (1982).

These theories are discussed in the following sections.

1.5. THE CONTACT DISCONTINUITY THEORY:

Biermann and Thomas (1972), were able to construct zero-age contact binary models by allowing the convective envelopes of the primary and secondary components to have unequal entropies. They were able to explain several important observed properties of the W UMa binaries. They found that their systems lay on the main populated region of Eggen's period - colour diagram, whereas all previous zero-age models (eg. Lucy(1968a), Moss and Whelan (1970)) had periods which were systematically too high and/or colours which were too blue. The Biermann and Thomas models also covered the main region of the observed systems in the 'mass ratio-period' diagram, unlike the models of Lucy, and of Moss and Whelan, which produced periods which were too high for a given mass ratio. However, the Biermann and Thomas models were unable to reproduce the nearly equal depth minima of the observed W UMa light curves.

Biermann and Thomas (1973), investigated the possibility that the exchange of luminosity in W UMa binaries was limited to the outer regions of the convection zones. They assumed that all exchanged luminosity was transported on equipotential (or contact) surfaces, and discovered that the nearly equal depth minima of the light curves could be reproduced if the contact surface was situated high in the convection zone.

Biermann and Thomas then investigated the evolution of their unequal-entropy W UMa binary models, and found that they evolved to lower mass ratios and longer periods on the nuclear timescale of the primary component.

From a discussion of light curves, Biermann and Thomas concluded that their contact surface moved deeper into the component convection zones during evolution, producing a situation where the two zones became more similar, thus approaching Lucy's concept of equal entropy constants for the components.

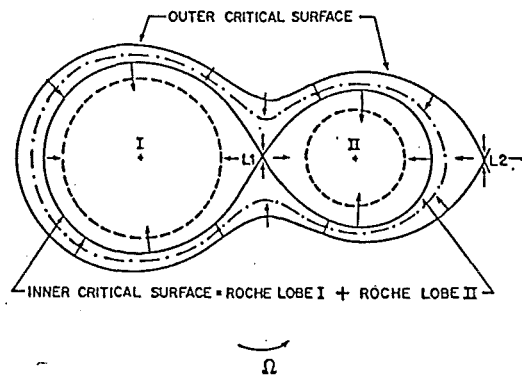
Vilhu (1973), carried out a numerical examination of the evolution of various contact binaries having a total mass of $1.8 M_{\odot}$. The initial parameters were chosen with the assumption that systems were formed during the rapid mass transfer phase of Case A evolution. Vilhu calculated the further evolution of the systems by determining mass and energy exchanges between the components. He found that the systems evolved with increasing mass ratios and with increasing luminosity transfer from the primary to secondary components, confirming the results of Biermann and Thomas (1973). By the use of some numerical experiments, Vilhu also demonstrated the importance of the outer layers of the CCE in making the secondary hotter, agreeing with the results of Whelan (1972) and Biermann and Thomas (1973).

However, like the original Biermann and Thomas models, Vilhu's evolving models together with the energy transfer picture adopted, could not alone explain the near equal depth minima of the observed W UMa light curves.

Mochnaeki and Whelan (1973) and Moss and Whelan (1973), also presented similar modified contact binaries based on the Lucy CCE model. As with the models of Biermann and Thomas (1972, 1973) and Vilhu (1973), these models were constructed with unequal entropies in the adiabatic regions of the components' convection zones, with energy exchange occurring largely through the superadiabatic parts of the CCE.

All of the various models discussed so far have been constructed with the ad hoc assumption that the CCE had no crucial influence on the internal structures of the component stars. However, Hazlehurst (1974), argued that these unequal entropy models were in fact unstable. Hazlehurst derived a condition for the secular stability of a contact binary in which the components shared a CCE. He found that, for a large class of models, this stability condition could not be satisfied if the adiabatic constants of the component convection zones differed by more than a small amount. (Although Hazlehurst's argument was later shown to be incorrect, work by Hazlehurst and Refsdal (1980), and Hazlehurst, Hoppner and Refsdal (1982), confirmed his conclusion.)

On the basis of the unequal entropy models, Shu, Lubow and Anderson (1976), proposed the 'contact discontinuity (DSC) theory'.



The inner and outer critical surfaces of the Roche model plotted in the equatorial plane. The arrows are perpendicular to the equipotentials and indicate the direction of the effective gravitational field. The effective gravity vanishes at the inner and outer Lagrangian points, L_1 and L_2 . Gravitational confinement of a gas against the expansive tendency of its internal pressure is possible only if the physical surface(s) of the system lies beneath the outer critical surface. For a detached binary, the two stellar surfaces (*dashed curves*) both lie beneath the inner critical surface; for a contact binary, the common stellar surface (*dashed-dotted curve*) lies between the inner and outer critical surfaces.

Figure 1.7. Structure of the contact-binary equipotentials.

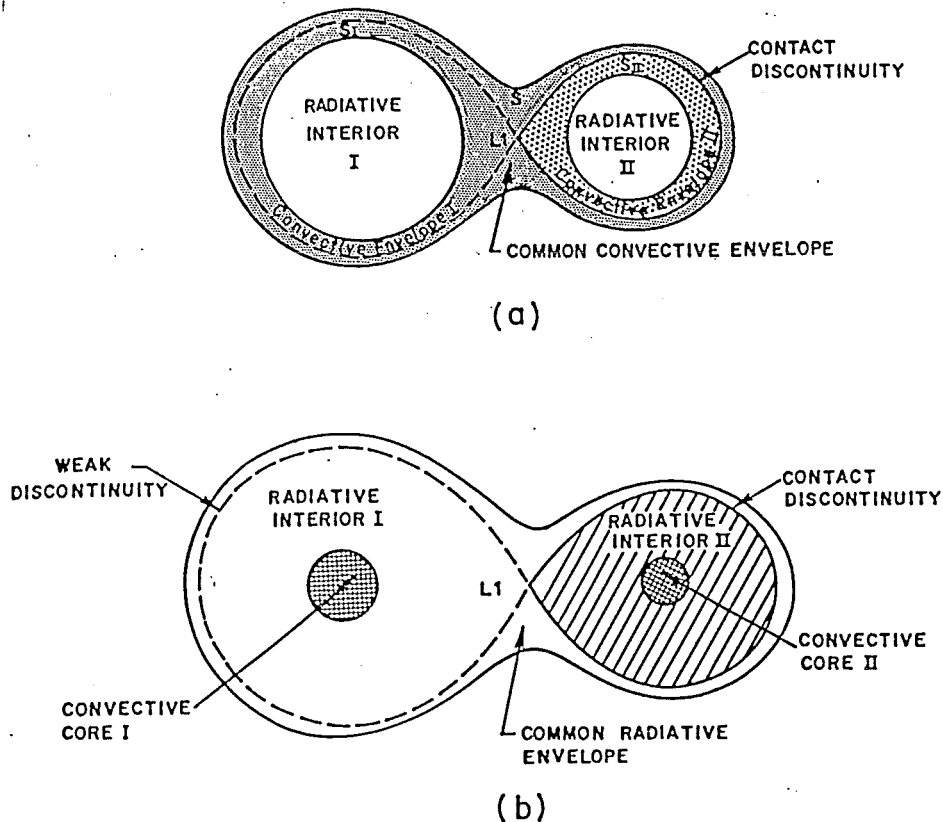
As in the earlier unequal entropy models, Shu, Lubow and Anderson assumed that the horizontal transportation of mass and heat in the CCE only takes place effectively along closed equipotential surfaces common to both stars. Within these regions, lying between the inner and outer critical Roche surfaces (Figure 1.7), it was assumed that slight horizontal pressure differences could easily move material from one star to the other. Below the inner critical surface however, the redistribution of material was not so straightforward since the only access between components, without working against gravity, was via the inner Lagrangian point. The authors argued that because the stars were almost decoupled below their Roche lobes, the possibility of nearly discontinuous behaviour across the inner critical surface had to be considered.

Shu et al. proposed that although the strong mechanical requirements of the above situation implied that the pressure had to be continuous across the inner critical surface, they allowed the temperature and density and/or their gradients to be discontinuous (i.e. they allowed the possibility of a contact and/or weak discontinuity).

The authors realised that if the CCE was at an intermediate temperature somewhere between that of the components, then on one of the stars there would be a cooler body of gas lying above the hotter stellar atmosphere. This situation would be dynamically unstable since rising elements of hot gas and descending elements of cooler gas would, on a dynamical timescale, destroy any contact discontinuity which existed. Because of this problem, only one of the components, the cooler star, was allowed to have a contact discontinuity. The hotter component was assumed to show continuous behaviour across its Roche lobe, at best only exhibiting a weak discontinuity (i.e. continuity of pressure, density and temperature, but not necessarily their derivatives).

For their model to have any credibility, the authors had to explain the maintenance of the contact discontinuity, since on a thermal time scale, this would normally disappear as a result of diffusion.

Shu, Lubow and Anderson considered the contact discontinuity maintenance mechanism for both the common convective envelope case and the common radiative envelope (CRE) case (Figure 1.8).



Schematic diagram of the structure of contact binaries. (a) A low-mass contact binary at zero age with a common convective envelope. The specific entropy s_{II} beneath the Roche lobe of star II is less than the specific entropy s_I beneath the Roche lobe of star I. For dynamical stability, the specific entropy s in the common envelope equals s_I . (b) A high-mass contact binary at zero age with a common radiative envelope. The temperature T_{II} immediately beneath the Roche lobe of star II is less than the temperature T_I immediately beneath the Roche lobe of star I. For dynamical stability, the temperature immediately above the inner critical surface equals T_I .

Figure 1.8. Structure of the contact discontinuity models.

Shu et al. first considered the situation where both the component stars had efficient convective envelopes, and assumed that radiative transport could be ignored (Figure 1.8a). Their analysis was as follows:

If the specific entropy, S_I , of star I was greater than that of star II, then star II would exhibit the contact discontinuity, and because of the resulting buoyancy deficit, convected material from star II would be unable to penetrate the Roche lobe and thus enter the CCE (where the specific entropy, S , is equal to, S_I).

A slight heating of the interior of star II under this effective constant volume condition, then gives rise to a slight increase in the stellar pressure, causing a pressure excess. This pressure excess then pushes some stellar material from star II to star I via the inner Lagrangian point, L_1 . Once there the gas, being at almost the same pressure as the ambient medium, but considerably colder and denser, drops into the interior of star I where it is heated, eventually becoming S_I material. This new material then displaces existing S_I material, causing it to rise above the Roche lobe of star I into the CCE.

Meanwhile, the gas of the CCE lying above the Roche lobe of star II would be slowly cooling, losing heat via the stellar surface and the transition layer. (The authors remarked that although this gas was not being heated from below, it nonetheless had the structure of a convection zone since it was mechanically coupled to the convection zone of star I.) The authors argued that the heat losses would be especially great in the transition layer, which constituted the actual 'contact discontinuity'.

Shu et al. proposed that diffusive effects such as convective overshoot or radiative transfer, and circulation currents, slowly convert the S_I (or S) material into S_{II} material inside the transition layer at the Roche lobe of star II. They concluded that in a steady state situation this conversion of material would exactly balance the loss of S_{II} material lost through the inner Lagrangian region. (However, the authors conceded that this was the weakest point of their argument, and that if this balance was not exact then there may be a secular shift in mass ratio.) A schematic diagram of this model is shown in Figure 1.9.

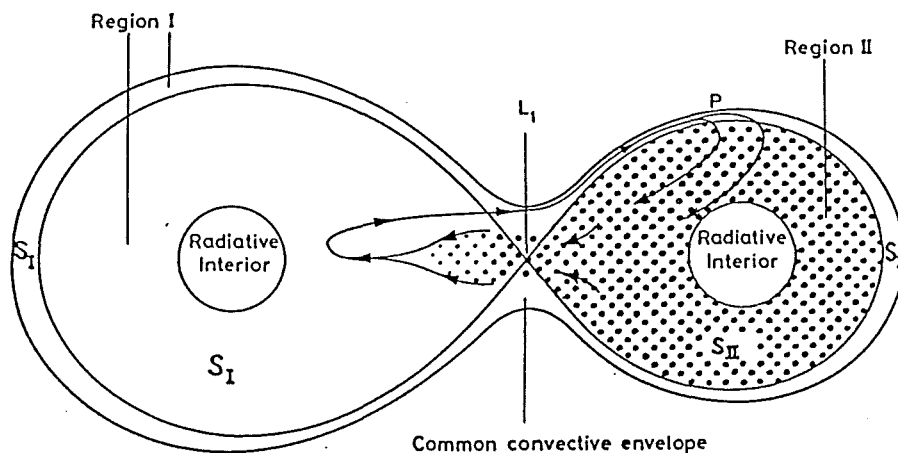


Figure 1.9. Schematic diagram of the structure of the contact binary model of Shu et al. with the mass flow pattern indicated.

Shu, Lubow and Anderson then considered the more complex case where the contact binary was surrounded by a common radiative envelope (Figure 1.8b). Their analysis was as follows:

If the temperature below the Roche lobe of star II, T_{II} , was less than the temperature below the Roche lobe of star I, T_I , and since the temperature of the CRE lies between the two, star II would exhibit the contact discontinuity. Also, the authors assumed, if the contribution to the heat transport from fluid flow could be ignored, star I would exhibit a weak discontinuity. In order to explain the mechanism by which the contact discontinuity is preserved in the CRE case, Shu et al. first considered the radiative material in the region of the inner Lagrangian point, L_1 .

The cooler material lying on star II's side of L_1 would initially be in pressure equilibrium with the hotter material lying on star I's side, and with the material around L_1 belonging to the CRE. Because of the radiative nature of the material, energy flows to the cooler gas not only from the hotter gas of star I and the CRE, but also from below, causing a slight rise in pressure. Since the effect of gravity is zero at the inner Lagrangian point, some star II material is transferred to star I. When the cooler material enters the Roche lobe of star I it is no longer buoyant in the ambient medium and falls into the interior of star I, as in the CCE case. This material is then heated, displacing star I material across the Roche lobe into the CRE.

While this process is underway, the CRE would be continually losing energy across the Roche lobe of star II. Shu, Lubow and Anderson concluded that in a steady state situation, the higher temperature material of the CRE lying on top of star II would be converted into lower temperature material over the entire transition

layer at the Roche lobe of star II, with the thickness of this layer being adjusted so that the rate of diffusion conversion exactly compensates for the rate of gas loss through L_1 .

Lubow and Shu (1977), proposed several zero-age contact binary models of roughly solar composition, using the contact discontinuity hypothesis. They found it was possible to construct contact binaries with CRE's as well as systems with CCE's. They presented two models with total masses of $1.5 M_{\odot}$ and $3.0 M_{\odot}$, and mass ratios of 0.5 (figures 1.10, 1.11).

Figure 1.12 shows the position of the $1.5 M_{\odot}$ and $3 M_{\odot}$ models on the period - effective temperature diagram for observed main-sequence contact binaries. Both models lie within the zero-age main-sequence region for systems of mass ratio 0.5 computed by the authors.

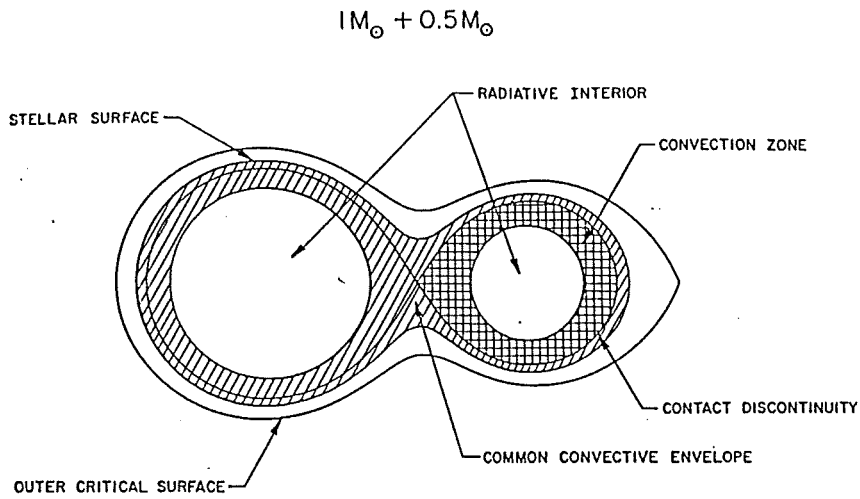


Figure 1.10. Lubow and Shu (1977) zero-age contact binary model with a common convective envelope structure.

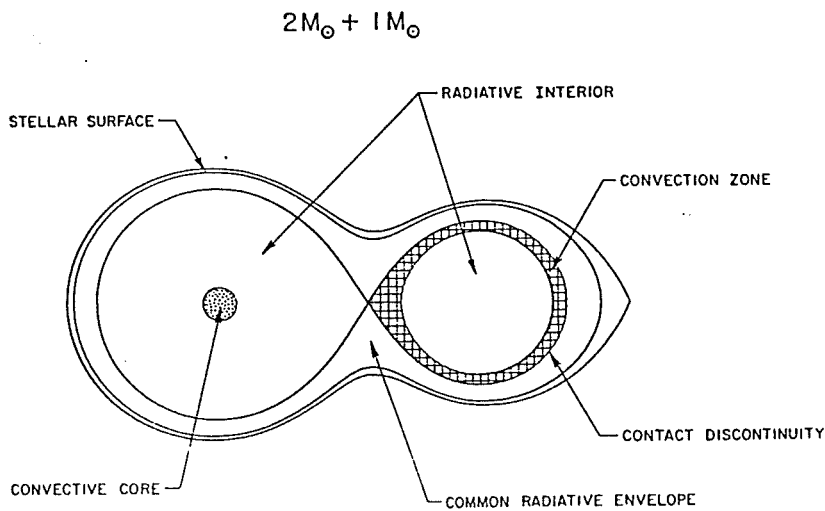


Figure 1.11. Lubow and Shu (1977) zero-age contact binary model with a common radiative envelope structure.

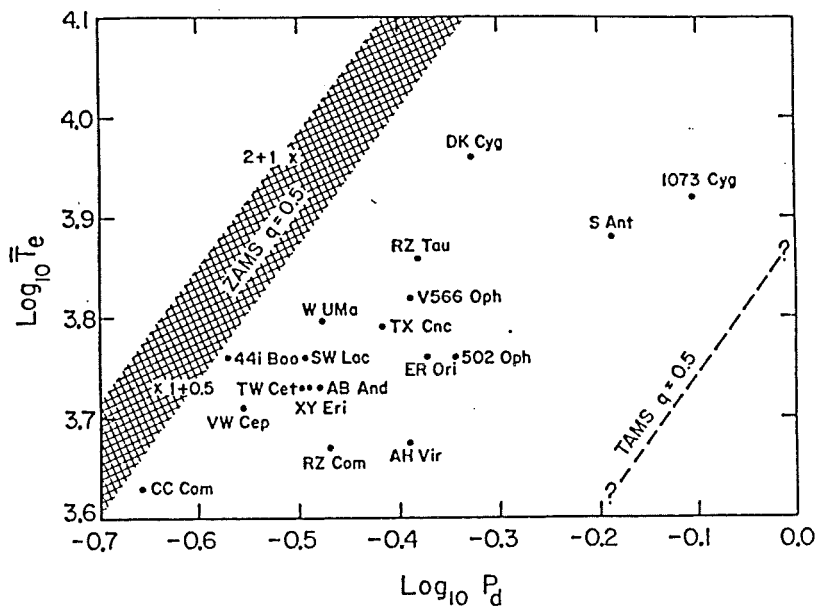


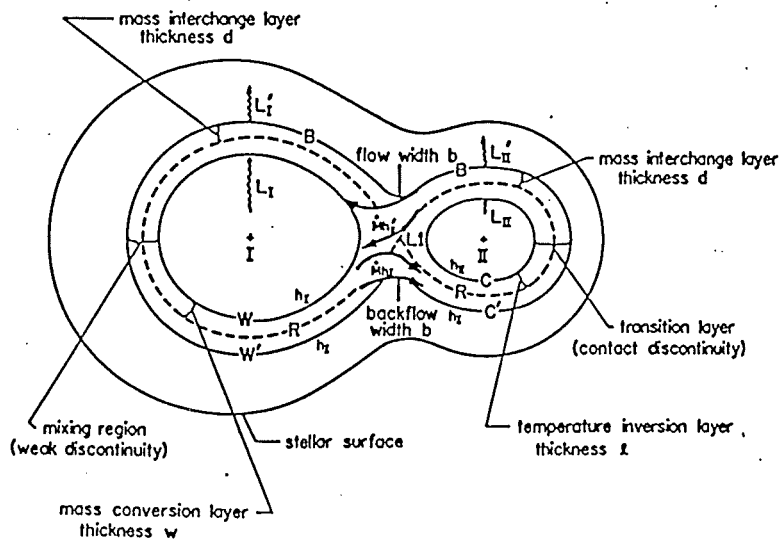
Figure 1.12. The Lubow and Shu (1977) models plotted on the 'period - effective temperature' diagram.

Lubow and Shu remarked that although their models seemed to be in good agreement with observation, it was somewhat disturbing that none of the observed systems fell within the expected ZAMS band. But on the other hand, neither the models nor the observed systems lay beyond the expected terminal-age main-sequence band.

Shu, Lubow and Anderson (1979), examined a variety of topics concerning the mass and energy flow in contact binaries, presenting a more detailed discussion of the mechanical aspects of the DSC theory. They extended some of their earlier arguments, suggesting that not only was the DSC theory sufficient to resolve Kuiper's paradox, but that the contact discontinuity was a necessary

condition for all viable models of synchronously rotating contact binaries - with or without convection zones, evolved cores or thermal equilibrium. (cf. Lucy (1976), Hazlehurst (1976) and Thomas (1977).) They concluded that this elevated the DSC model from the working hypothesis of Shu et al. (1976), to a physical requirement.

Shu, Lubow and Anderson also presented a detailed qualitative picture of the maintenance of the contact discontinuity over the Roche lobe of the cooler star. They also discussed the details of the luminosity reduction on the outside of the hotter star, i.e. the area which Shu et al. (1976) termed the 'mixing region'.



Schematic diagram of the structure and flow in the transition layer and mixing region. See text for explanations

Figure 1.13. The luminosity redistribution mechanism of the Shu et al. (1979) contact binary model.

Figure 1.13 shows schematically how Shu et al. (1979) envisaged the luminosity redistribution in contact binaries. It represented a more complicated picture than that considered previously. (Notice that the luminosity $L_I^!$ above star I is approximately equal to the luminosity $L_{II}^!$ above star II, as observed.) An explanation of the process discussed by Shu et al., and a brief description of Figure 1.13, follows:

Above the base of the common envelope defined by the equipotential B (which is divided at the neck into two parts, C' and W'), the structure was barotropic. The structure was also barotropic below the top of the interiors of the cooler and hotter stars, defined by C and W respectively. The temperature at C' was higher than that at C (i.e. the specific enthalpy $h_I > h_{II}$); hence the region CC' was the transition layer which constituted the contact discontinuity. At W and W' the temperatures were (nearly) equal but their gradients were not; hence the mixing region WW' constituted a weak discontinuity. The Roche lobes of the stars were sandwiched between the C'W' equipotential and the C and W equipotentials. Shu et al. assumed the temperature inversion layer which existed within the region CC', to be convectively stable.

While a luminosity L_{II} diffused from the interior of star II into the bottom of the transition layer C, a luminosity $L_{II}^!$ diffused from the top of C'. The authors argued that in order to effect the luminosity transformation L_{II} to $L_{II}^!$, matter must flow back and forth between the stars at a balanced rate \dot{M} (as in the Shu et al., 1979 case). This flow carried average specific enthalpy $h_{II}^!$

material from star II to star I, and specific enthalpy h_I material from star I to star II. (The authors remarked that they had naively and incorrectly assumed in their 1976 paper that $h'_{II} = h_{II}$, but after later reflection it became apparent that star II matter had to come from the top of the transition layer, making the h'_{II} material numerically closer to h_I material than to h_{II} .)

The authors concluded that from a global point of view it may be said that the net cooling of gas from specific enthalpy h_I to h'_{II} , over the Roche lobe of star II, released enough radiation to convert a small interior luminosity L_{II} into a larger one L'_{II} . Similarly, a net heating of gas from specific enthalpy h'_{II} to h_I in the mixing region of star I absorbed enough energy to convert a large interior luminosity L_I into a smaller one L'_I .

Finally, Shu (1980), argued that the existence of a contact discontinuity was sufficient to:

1. Resolve Kuiper's paradox.
2. Explain Eggen's period - colour relation for W UMa binaries.
3. Account for the existence of contact binaries with common radiative envelopes (eg. Rucinski (1973), Leung (1980)).

The DSC theory has been subject to some heavy criticism. For example, Hazlehurst and Refsdal (1978), argued that the temperature (entropy) discontinuity across the Roche lobe of the secondary disappears in a rather short time (i.e. about the thermal time scale of the secondary component), due to heating from the underlying regions. Papaloizou and Pringle (1979), reached a

similar conclusion. Lucy and Wilson (1979), criticised the model since it was not clear how evolutionary sequences could be created without introducing extra assumptions to the theory. Smith, Robertson and Smith (1980), argued that the DSC theory contained several serious inconsistencies which prove fatal to the model. Hazlehurst and Refsdal (1980), suggested that in all cases of zero-age contact binaries, instabilities occur, thus ruling out the DSC model, since it does achieve thermal equilibrium.

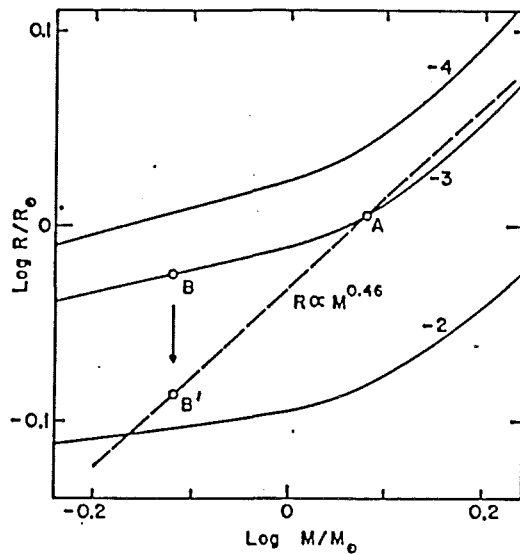
1.6. THE THERMAL RELAXATION OSCILLATION THEORY:

Studies by Rucinski (1973, 1974) and Lucy (1973), suggested that the common photospheres of W-type W UMa binaries were in close coincidence with their inner critical surfaces. Thus, it was argued, the W-type systems may be considered as having shallow common envelopes, or as being in marginal contact. In addition, by considering the instabilities exhibited by the W-type light curves, Rucinski (1973) proposed that the systems were not in a state of thermal equilibrium.

On the basis of this and similar work (eg. Mochnacki and Doughty (1972b)), Lucy (1976) presented evidence which indicated that the W-type W UMa binaries may be undergoing thermal relaxation oscillations about a state of marginal contact. Lucy produced theoretical calculations which suggested that a newly formed contact binary would evolve towards a state of marginal contact on a thermal timescale, and if this contact was then broken, would evolve back into contact, again on a thermal timescale. (Lucy's calculations

only applied to contact binaries with low enough mass to allow a CCE.)

Lucy considered the evolution of a newly formed contact binary which had settled into a state of mechanical equilibrium, but had not yet achieved thermal equilibrium. He suggested that the behaviour of the system may be anticipated and understood by considering Figure 1.14, which shows the mass-radius relation ($R \propto M^{0.46}$) corresponding to an equipotential surface (as discussed earlier), and the mass-radius relations with fixed adiabatic constant K , for the three indicated values of $\log K$.



Mass-radius relations with fixed adiabatic constant K for the three indicated values of $\log K$. Dashed line is equipotential mass-radius relation. Diagram illustrates construction of nonequilibrium contact binary by compression of component B.

Figure 1.14. Stellar mass-radius relations with fixed adiabatic constants.

Lucy argued that any zero-age contact binary in mechanical and thermal equilibrium, satisfying the equal entropy condition, had to fall at the intersection of the $R \propto M^{0.46}$ line and the relevant 'fixed adiabatic constant' line. But as Lucy pointed out, in the range of masses relevant to W UMa binaries, at all points of intersection the slopes of the mass-radius relations with fixed 'K' are everywhere less than the slopes of the equipotential mass-radius relation, thus forbidding the existence of any equilibrium solutions other than those with a mass ratio 'q' of 1. However, Lucy suggested that systems with mass ratios not equal to unity may be constructed if the thermal equilibrium constraint were lifted. He remarked that such a system may represent a newly formed binary. Lucy's analysis of the system was as follows:

Figure 1.14 shows the case where the interior of star A, the more massive component of the binary, retained thermal equilibrium; but star B, in order to obtain the appropriate equipotential surface, was compressed until it reached point B' in the diagram. (Lucy performed this task by assuming that the nuclear energy generation in the core of the star was artificially low for time $t < 0$, then, at $t > 0$, the energy generation rate was allowed its natural value.)

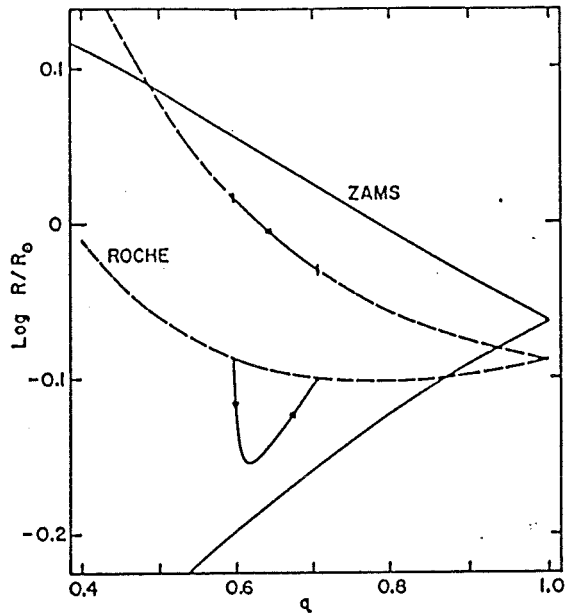
When star B was compressed, its rate of energy production exceeded the rate at which energy could flow from the radiative central zone to the surrounding convective regions. This excess then caused the expansion of star B on its thermal timescale. However, since deviations from the equipotential surface could only

be corrected for on a dynamical timescale, this expansion caused mass transfer from star B to star A, resulting in a decrease in mass ratio and, with assumed conservation of total mass and total angular momentum, an increase in separation and period.

(Lucy also considered the alternative case where, instead of compressing star B, star A was expanded. In this case mass transfer followed the same direction as before since star A's expansion resulted in a deficiency of energy production in its interior, which caused it to contract and draw mass from its companion.)

Since, as can be seen from Figure 1.14, a small mass exchange between components cannot bring about a state of thermal equilibrium, Lucy argued that evolution with decreasing mass ratio would continue until the increasing separation eventually brought the system to the point of breaking contact, that is, to a state of marginal contact. At this point the common photosphere of the binary would be coincident with the inner critical surface. Lucy assumed that when breaking finally occurred, no further energy would be exchanged between the components.

Before contact was broken, the binary system was attempting to evolve towards a (non-existent) state of thermal equilibrium. However, after contact was broken, the assumed ending of energy exchange between components implied that each star must separately try to achieve thermal equilibrium, i.e. each must evolve towards the appropriate ZAMS structure for its mass (Figure 1.15).



Secular evolution following loss of contact. Roche and ZAMS radii are plotted for each component.

Figure 1.15. Secular evolution of the binary components following the breaking of contact.

After contact was lost, the secondary component shrank towards its naturally smaller ZAMS state, after detaching from its Roche lobe. Meanwhile, the primary component expanded towards its naturally larger ZAMS state, but because it was constrained within its Roche lobe, this expansion led to a transfer of mass to the detached secondary component. Again, assuming conservation of total mass and total angular momentum, the mass transfer from the Roche-lobe filling primary component to the secondary, resulted in an increasing mass ratio and decreasing orbital separation, eventually bringing the components back into contact.

When the total mass and angular momentum are conserved, the system must undergo cycles around the state of marginal contact which is never reached. The mass transfer in the contact phase drives the system to larger separations and smaller mass-ratios until the contact is broken. The reversal branch corresponds to phases when the primary, swollen by the additional luminosity ΔL , sheds mass onto the secondary component, which is now devoid of the additional energy.

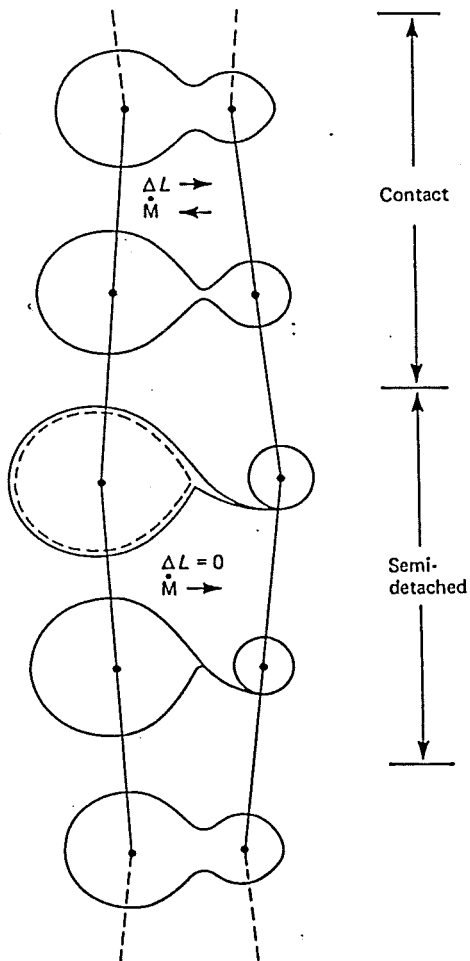


Figure 1.16. Lucy's Thermal Relaxation Oscillation scenario.

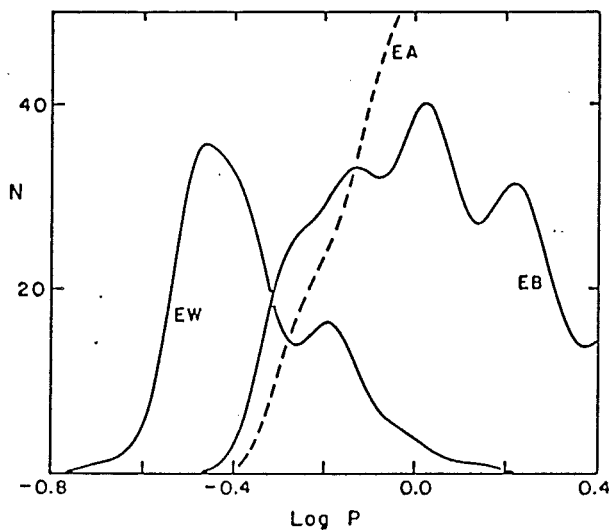
Lucy argued that the re-establishment of the CCE would be a dynamical event since both the individual stellar convective envelopes would possess different adiabatic constants.

Here Lucy ended his formal calculations but anticipated that once full contact was achieved, the direction of mass transfer would once again reverse.

The author proposed that it was impossible for such zero-age contact binaries to evolve into a state of thermal equilibrium, either with or without a contact structure. He also suggested that since such systems were shown to evolve towards breaking when in contact, and towards contact when separated, it may therefore be expected that the systems undergo thermal relaxation oscillations, with an amplitude limited by these opposing tendencies.

Lucy concluded that these ideas were probably very relevant to the W-type W UMa binaries since, as was discussed earlier, their marginal contact and observed instabilities suggest that they are probably systems for which there exists no thermal equilibrium structure. However, he conceded that it would be unlikely that real systems would undergo relaxation oscillations with as large an amplitude as his calculations suggested. Also, he remarked, during most of the semi-detached phase the model produced a difference in component effective temperatures which was too great to be consistent with observational evidence. Moreover, during the entire contact phase and most of the semi-detached phase, the results indicated timescales for the period changes which were too large, and that only during the first 2×10^4 years after breaking contact, were the period changes as rapid as those observed.

Because of the contact/non-contact behaviour, observed systems, according to the TRO model, should alternately exhibit light curves of EW-type (i.e. rounded light curves with approximately equal depth minima, as in the classical W UMa case), and EB-type (i.e. light curves which are identified with semi-detached binaries, showing continuous variation, with the secondary minimum being less deep than the primary minimum). However Lucy found, using a smoothed histogram technique (as explained by Lucy (1974)), that there was a surprising fall off of EB-type light curves at periods of around 0.45 days, and that none were observed below about 0.4 days (Figure 1.17).



Smoothed histograms showing period distributions for eclipsing binaries with $m < 12$.

Figure 1.17. Lucy's smoothed histogram plot of light-curve type against period (days).

From this evidence Lucy suggested that the barriers which limit the behaviour of the oscillations had not been correctly identified, and that the actual periods of the relaxation oscillations should be less than about 2×10^4 years.

Lucy argued that although the predictions of the TRO model were to some extent inconsistent with observational evidence, they clearly supported the interpretation of the observational data by Rucinski (1973, 1974) who conjectured that the W-type W UMa binaries were either thermally unstable or were undergoing cyclic readjustment with a thermal timescale.

Lucy also discussed the case of the A-type W UMa binaries, these being fully in contact, with stable light curves and periods. He proposed that the stability of the A-type systems lay in the fact that they had achieved thermal equilibrium. He argued that if this was the case then it must be concluded that the systems are evolved, since homogeneous contact systems with mass ratios not equal to 1 cannot be in thermal equilibrium. (cf. The DSC model of Shu, Lubow and Anderson discussed previously.)

Lucy suggested that some of the A-type systems may have evolved from oscillating W-type systems, which as a result of nuclear evolution, were able to adjust to a thermal equilibrium structure. To show that this was possible Lucy considered Figure 1.14.

Figure 1.14 indicates that the non-existence of zero-age equilibrium models may be attributed to the more massive component being undersized. Earlier the possibility of expanding the primary by lifting the thermal equilibrium constraint, was discussed. However, the same result could be achieved if the expansion of the star was due to nuclear evolution. Lucy concluded that a W-type system with a mass ratio small enough for nuclear evolution to produce a marked differential expansion of the components would, as evolution proceeds, approach a structure for which a thermal equilibrium solution existed.

Lucy also remarked that Figure 1.14 implied that for a given mass ratio, the evolutionary expansion of the more massive component required for a thermal equilibrium solution, decreases with increasing total mass. Lucy suggested that this formation mechanism for A-type systems should give rise to binaries with preferentially small mass ratios, with large total masses for their mass ratios. (This idea was in agreement with the results of Rucinski (1973, 1974), who found that the A-type systems do indeed have preferentially small mass ratios and large total masses.)

Lucy also remarked that his A-type structural model was identical to the Hazlehurst (1970) model for W UMa binaries in general. Hazlehurst however, had not considered the model's structure before the development of the evolved primary component. Lucy argued that a considerable virtue of his own model was that the evolution of the contact system in thermal equilibrium was not preceded by a non-contact system in thermal equilibrium;

consequently, there was no conflict with the W UMa binaries' virtual monopoly of the period interval 0.2 - 0.4 days.

Finally, Lucy conceded the possibility that some of the A-type W UMa systems may have evolved from short-period semi-detached binaries.

The findings of Wilson (1978) were in agreement with the evolved picture of A-type W UMa binaries. He found that for eight out of eight A-type systems, selected for having very accurately known parameters, all had larger than zero-age main-sequence radii.

Similar TRO models were proposed by Flannery (1976) and Robertson and Eggleton (1977). These differed from Lucy's treatment in that they did not use commonly accepted zeroth-order equations of stellar structure. Flannery (1976), calculated a detailed sequence of models which followed the thermal evolution of a $2 M_{\odot}$ contact binary of normal population I abundances, starting at a mass ratio close to unity. He found that an initial instability developed into a cyclic exchange of material, with the mass fraction, $M_1/(M_1 + M_2)$, oscillating between 0.56 and 0.62 with a period of about 10^7 years. Flannery argued that the mass exchange existed not just for the $2 M_{\odot}$ system studied, but for all contact binaries, and that the thermal instability associated with the rapid variations of mass, seemed likely to produce similar cycles in other cases. The author demonstrated that no particularly constraining values for the chemical composition, mass, or mass ratio were necessary for his model.

Like the cyclic model of Lucy, the Flannery model had deficiencies in that it did not satisfy observational requirements. Although when in the contact phase the predicted light curves of both models agreed closely with observation, the surface entropies and temperatures of the stars were very different during the semi-detached phase.

In an attempt to overcome this problem Robertson and Eggleton (1977), investigated the cyclic evolution in more detail, taking into account the effects of nuclear evolution and angular momentum on the system. As in the previous TRO models, Robertson and Eggleton found cyclic behaviour on a thermal timescale, with alternate contact and semi-detached phases. They also discovered that for progressively smaller values of the angular momentum of a system, the mass ratio averaged over a cycle, became progressively more extreme, at a rapid rate. As can be seen from Table 1.2, Robertson and Eggleton found that even a 7 per cent drop in angular momentum could change the mass ratio of their model from about 0.7 to about 0.5, and rapidly decrease the time spent out of contact.

Mean parameters of cycling models.

(1)	(2)	(3)	(4)	(5)	(6)	(7)	(8)	(9)	(10)	(11)	(12)
$\log_{10} H$	No. of cycles	q	P (days)	X_c	$B-V$	$\log T_e$	$\Delta L/L_1$	Lifetimes (10^6 yr)			
								contact		semi-detached	
51.705	4.5	0.70	0.25	0.70	0.64	3.773	0.51	3.2	3.8	0.6	1.6
51.700	2.75	0.65	0.26	0.70	0.62	3.778	0.52	1.5	5.5	0.6	1.6
51.675	~0.75	0.50	0.27	0.70	0.56	3.796	0.34	29:		0.9	1.3
51.705	~1	0.48	0.35	0.35	0.58	3.790	0.27	38:		0.5	0.9
51.705	-	0.42	0.40	0.15	0.55	3.798	0.30	>87		-	-

Notes:

- (i) For each system, the total mass is $1.8M_{\odot}$ and $\alpha = 10$. The zero-age composition is $X = 0.70$, $Z = 0.02$.
- (ii) The values in columns 3, 4, 6 and 7 are crude averages over the phase of good thermal contact. Columns 5 to 7 refer to the primary, but the difference in $\log T_e$ between the stars never exceeds 0.005, during this phase.
- (iii) Periods would be a little longer, and colours a little redder, if allowance were made for the effect of the rapid rotation of the components on their internal structure.
- (iv) Lifetimes are given for four stages, where these can be distinguished (see text).

Table 1.2. The mean parameters of the Robertson and Eggleton TRO models.

The authors argued that it was reasonable to assume that in reality most systems have sufficiently low angular momenta that their mass ratios are less than about 0.6, and hence, on the basis of the calculations, may spend only a few per cent of their lifetime out of contact. Robertson and Eggleton proposed that the absence of observed binaries with periods in the same range as W UMa systems, but exhibiting EB-type light curves (Figure 1.17), may not be a problem after all. (Rucinski (1978) however, suggested that light curve distortions when the binaries are in the semi-detached state, may give the appearance that the system is in contact, this possibly being due to the heating of the secondary component as a result of mass accretion from the primary.)

Robertson and Eggleton also considered the final evolutionary state of W UMa binaries. They suggested that although the long term evolution of the contact binaries may be determined by nuclear evolution, steady angular momentum loss may be a competitive, or even dominant process, in the short term. The authors also proposed that if the sensitivity of the mass ratio to angular momentum changes was really as large as their results suggested, then gravitational radiation may be an important effect, with angular momentum loss via magnetic braking being more important still. They concluded that whichever of nuclear evolution or angular momentum loss dominates, the progression towards more extreme mass ratios implies that all contact binaries finally evolve into single stars. (They suggest that if there exists a small but significant population of rapidly rotating 'K' subgiants, then this would indicate that nuclear evolution is the more important effect.)

Lucy and Wilson (1979) examined the TRO and DSC theories using a wide variety of observational tests, and concluded that the TRO theory appears to be in substantial agreement with the observational evidence. They also claimed that one of the previous difficulties of the TRO theory, namely the absence of observed systems in a state of broken contact, had to some extent been overcome by the discovery of three such possible systems: AK Her, W CrV and RW PsA. The authors labelled these binaries 'B-type' W UMa systems. (However, Mochnacki (1981) argued that these systems were in fact peculiar evolved systems, and not in broken contact.)

Lucy and Wilson also rebutted earlier objections to the TRO theories by Lubow and Shu (1977), who claimed that it was incorrect to postulate oscillations about a non-existent equilibrium configuration. Lucy and Wilson argued that this was not the case since the oscillations are not about non-existent equilibrium configurations, but are in fact about the Biermann and Thomas (1972) equilibrium configurations (i.e. unequal entropy configurations). In these configurations shallow contact was assumed to limit thermal contact (i.e. energy exchange) to the degree required to maintain the inequality of the adiabatic constants of the convective envelopes of the components. The authors explained that the secular instability of these structures accounts for the onset of the oscillations (Hazlehurst (1974)), and the existence of barriers that render the non-contact configurations inaccessible (Lucy (1976)), accounts for the continuation of the oscillations.

Lucy and Wilson (1979) also refuted the claim by Shu, Lubow and Anderson (1979) that, even if the TRO theory was basically correct, it must still be modified to incorporate a contact discontinuity during the contact phase of the relaxation oscillations. They argued that Shu et al. had considered the masses of the components as boundary conditions to be imposed on subsequent models in their evolutionary sequence, which was not the case in the TRO theory.

Finally, Shu (1980) proposed that the zero-order models of the DSC theory constituted the equilibrium states about which the TRO models oscillate, and that the two theories were in fact complementary.

1.7. THE ANGULAR MOMENTUM LOSS THEORY:

Both the DSC and TRO theories are constructed with the basic assumption that system mass and angular momentum are conserved. In actual fact, observational evidence suggests that this is probably not the case.

For example, there is a great deal of evidence to indicate that contact binaries are very magnetically active. If this is true then magnetic braking may lead to a significant loss of angular momentum (eg. van't Veer (1976, 1979), Webbink (1976), and Mochnacki (1981)). This evidence comes from observations of possible starspots on contact binary surfaces, usually on the primary component (eg. Eaton, Wu and Rucinski (1980a), Mullan (1975), Geyer (1976), Binnendijk (1977), Anderson and Shu (1977), and Hilditch (1981)), possible magnetic activity (eg. Kuhl (1964), Mullan (1975), Vilhu (1983), and Eaton (1983)), and sudden period changes (eg. Bergeat, Lunel and Sibille (1972), and Rucinski (1974)).

In addition to magnetic braking, the contact binary may lose angular momentum by mass ejection via overflow of the outer critical surface (eg. Webbink (1976), Lin (1977), and Narai (1980)), or by the effects of gravitational radiation (eg. Paczynski (1967), Webbink (1976), and Faulkner (1976)).

Rahunen (1981) proposed the 'angular momentum loss (AML) theory'. He investigated a series of evolutionary contact binary models with the assumption that angular momentum loss occurs. He chose models which were in good thermal contact, with equal entropies in their envelopes. He assumed that when the system was in deep contact the orbital angular momentum was constant, but as the depth of contact became shallow, then he treated the orbital angular momentum as a free parameter which was altered to keep the binary in marginal contact. (As discussed previously, Robertson and Eggleton (1977), had already considered this possibility and their findings suggested that such systems would evolve towards smaller mass ratios if there was steady loss of angular momentum.)

Rahunen found that it was possible to keep the model binaries in shallow contact if a hypothetical ('critical') angular momentum loss rate of, $d\ln J/dt \sim 2 \times 10^{-9} \text{ year}^{-1}$, was assumed. This, on average, corresponded to a required timescale for the losses of about 5×10^8 years. Rahunen suggested that if the angular momentum loss rate was greater than this critical value, then the binary may coalesce into a single star, but if the loss rate was less than the value, then the system would undergo a cyclic evolution alternating between detached and semi-detached phases. The author found that this cyclic behaviour was similar to that of TRO model, but with the difference that the system slowly moved towards more extreme mass ratios.

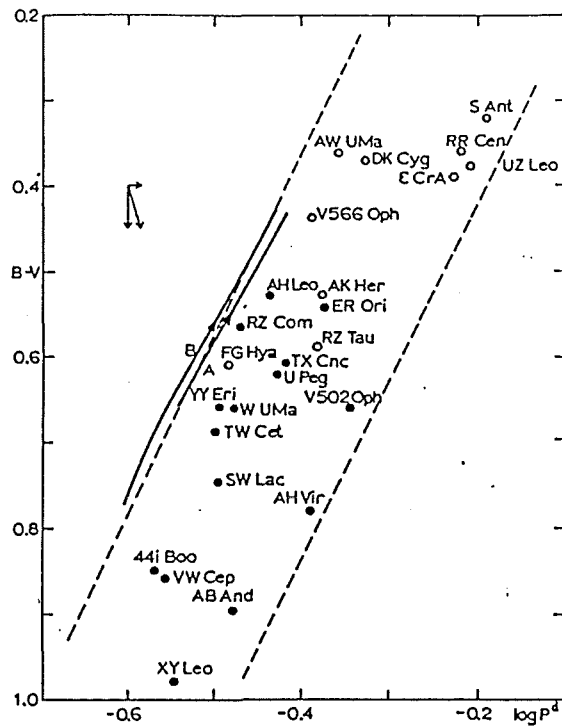
Rahunen argued that angular momentum loss via magnetic braking would be necessary for W UMa binaries since the expected angular momentum losses due to gravitational radiation were of the order of two magnitudes smaller than the hypothetical limit needed to keep the systems in contact.

To support his case Rahunen quoted van't Veer (1979), who proposed that magnetic braking may control the evolution of solar-type contact binaries, with possible contact lifetimes estimated to be in the region 5×10^7 years to 10^8 years. Rahunen remarked that there was some evidence indicating that magnetic activity in W UMa systems may be strong enough to provide sufficient angular momentum loss rates to allow the components to remain in contact (Vilhu and Rahunen (1980)). He suggested that the scenario where zero-age systems evolve towards more extreme mass ratios, was at least possible.

Rahunen argued that even a moderate angular momentum loss could have an important effect on the evolution of the W UMa binaries, provided that the timescale of the loss was less than about 5 times the nuclear timescale of the primary, i.e. about 10^{10} years for a typical W UMa system. This corresponded to a loss rate which was about 1/20 th of the critical loss rate required to keep the binary in contact.

Although this evolutionary scenario removed the greatest difficulty of the TRO models, that is, it avoided the need to break contact, it gave rise to other difficulties. For example, the resulting mass-ratio distribution calculated from Rahunen's model did not agree with the observed distribution. But on the other hand, Rahunen's constant angular momentum models confirmed the earlier results of Lucy (1976), Flannery (1976), and Robertson and Eggleton (1977), concerning cyclic evolution.

Finally, Rahunen considered the evolutionary tracks of his models on the period - colour diagram. He proposed that systems located near to the short-period boundary of the diagram were probably of zero-age, whereas systems with similar colours but longer periods were probably partially evolved. This implied that some A-type systems were nearly unevolved. The author demonstrated that angular momentum loss on a short timescale would shift his models towards bluer colours, along the short-period boundary (Figure 1.18).



The period-colour relation for the observed W UMa systems. A-type and W-type systems are indicated by open and filled circles, respectively. The solid curves denoted by A and B represent our models in good thermal contact. The dashed lines are the boundaries for the observed band taken from Eggen (1967). The vector symbol above our systems represents the correction displacement which should be applied to account for the rotation of the stars

Figure 1.18. Evolutionary tracks of the Rahunen (1981) AML models on the period - colour diagram.

Rahunen referred to the findings of Moss (1971), Biermann and Thomas (1973), and Vilhu (1973), which also suggested that nuclear evolution would shift systems towards longer periods and slightly bluer colours. He admitted that although it may be tempting to combine these two possibilities to suggest that the blue long-period A-type systems (with low mass ratios), may at one time have been red short-period W-type systems (with large mass ratios) at zero-age, there was no means of verification. (If this was the case then the

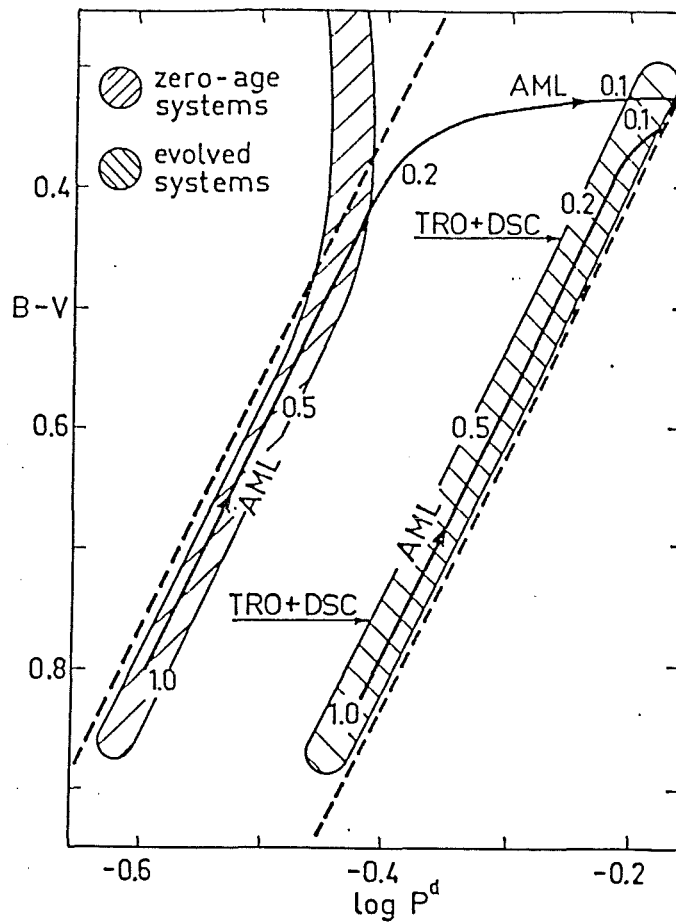
binaries must have lost a considerable amount of their original angular momentum.) However, the author conceded that it was equally likely that the A-type systems already had low mass ratios and low angular momenta when they first established contact at zero-age, or when they initially evolved into contact from a detached or semi-detached state.

Rahunen and Vilhu (1982) gave further consideration to the AML theory, comparing it to the DSC and TRO theories. The authors remarked that all constant angular momentum models (i.e. the DSC and TRO theories) required a formation mechanism which produced unequal components, and they identified this as the fission process. They also argued that whatever the mechanism was in reality, unlike the DSC or TRO theories, one AML sequence could cover all observed mass ratios.

Rahunen and Vilhu also compared the behaviour of the AML, DSC and TRO theories on the period - colour diagram (Figure 1.19). They argued that both the DSC and TRO models evolved from the short-period boundary to the long-period boundary on the nuclear timescale of the primary component, and at low mass ratios (where most of the W UMa systems are), only a relatively small range of mass ratios were reached in one evolutionary sequence. The AML models on the other hand, evolved parallel to the boundaries of the period - colour diagram with decreasing mass ratio, on the thermal timescale of the secondary.

The authors found that the horizontal distance from their AML models to the boundaries was determined by the nuclear evolutionary state of the primary at the time when contact was established, such that zero-age systems populate the short-period boundary and evolved systems populate the long-period boundary. However, when the mass ratio had decreased sufficiently, the nuclear timescale of the primary became shorter than the thermal timescale of the secondary, and when this occurred the path of the AML models turned to the right of the period - colour diagram (Figure 1.19). Using simple expressions for the timescales, Rahunen and Vilhu found they were equal when the mass ratio had achieved a value of about 0.2 . They argued that after this, further evolution was determined by the nuclear evolution of the primary, the binary eventually coalescing into a single star.

Rahunen and Vilhu conceded that in reality the angular momentum losses may not be as large as the AML models required. They suggested that if was the case, then the models may exhibit cyclic behaviour, but this being less violent than in the constant angular momentum case.



The period-colour diagram for contact binaries of W UMa type. The dashed lines show the observed boundaries. The shaded regions show the positions of thermal equilibrium models with different mass ratios (shown by the numbers 1.0 - 0.1). Evolutionary tracks of the three main theories DSC (contact discontinuity), TRO (thermal relaxation oscillations) and AML (angular momentum loss) are shown by the heavy lines.

Figure 1.19. Evolutionary tracks on the period - colour diagram for the DSC, TRO and AML models.

1.8. A UNIFICATION OF THE DSC AND TRO THEORIES ? :

As was discussed earlier, both the DSC and TRO theories depend on the thermal stability of unequal entropy models: the dependence of the TRO models being due to their oscillations around unequal entropy configurations, and that of the DSC models being due to the basic assumption that the stars have unequal entropies in their convective envelopes. Thus the question of thermal stability of unequal entropy models is of crucial importance to both theories.

Hazlehurst and Refsdal (1980), developed a method for investigating the secular stability of contact binaries using the 'stellar response functions' of Hazlehurst, Refsdal and Stobbe (1977). (The response functions described the readjustment of a star to a momentary addition of mass or energy.) They applied their method to a zero-age contact binary with component masses of $1.0 M_{\odot}$ and $0.6 M_{\odot}$, and found it to be unstable on a short timescale.

The formula which Hazlehurst and Refsdal used in their calculations coupled the energy transfer ' ΔL ', with the depth of contact ' d ', and the entropy difference ' ΔS ':

$$\text{i.e. } \Delta L = K \cdot d^m \cdot \Delta S^n ,$$

where K , m and n are constants.

The authors argued that with different choices for the parameters K , m and n , the formula may give some physical insight into the stability problem.

However, because of the linear stability analysis that Hazlehurst and Refsdal employed, they were unable to follow the evolution of the system after the instability had been established.

Refsdal and Stabell (1981), using the method of Hazlehurst and Refsdal (1980), investigated a contact binary which was near the end of its main-sequence phase. They found that the system, whose components had nearly equal temperatures, was in fact stable.

Rahunen and Vilhu (1982), and Rahunen (1982), continued the investigations of Hazlehurst and Refsdal, by examining the thermal stability and evolution of the $1.0 M_{\odot}$ and $0.6 M_{\odot}$ system using a Henyey-type stellar evolution code (Paczynski 1970a, 1970b). Since they used a non-linear approach, the authors were able to follow the further development of the instability. By examining the effect of nuclear evolution on the instability, they were able to estimate at which stage of main-sequence evolution the binary became stable.

Rahunen and Vilhu applied the same energy transfer formula as that used by Hazlehurst and Refsdal (1980), with the boundary condition,

$$R_p/R_{rp} = R_s/R_{rs} ,$$

where, R_p and R_s are the stellar radii,

and, R_{rp} and R_{rs} are the corresponding Roche 'radii'.

The authors studied the stability of the system by introducing an energy pulse from the primary to the secondary component. They assumed several different values for the transport coefficients K , m and n , and in each case studied the stability of the systems.

Properties of the two stars in the initial stationary system. L is the intrinsic luminosity of the star at the Roche lobe. The entropy difference is expressed in arbitrary units as $\Delta S = -\Delta \ln(P/T^{2.5})$

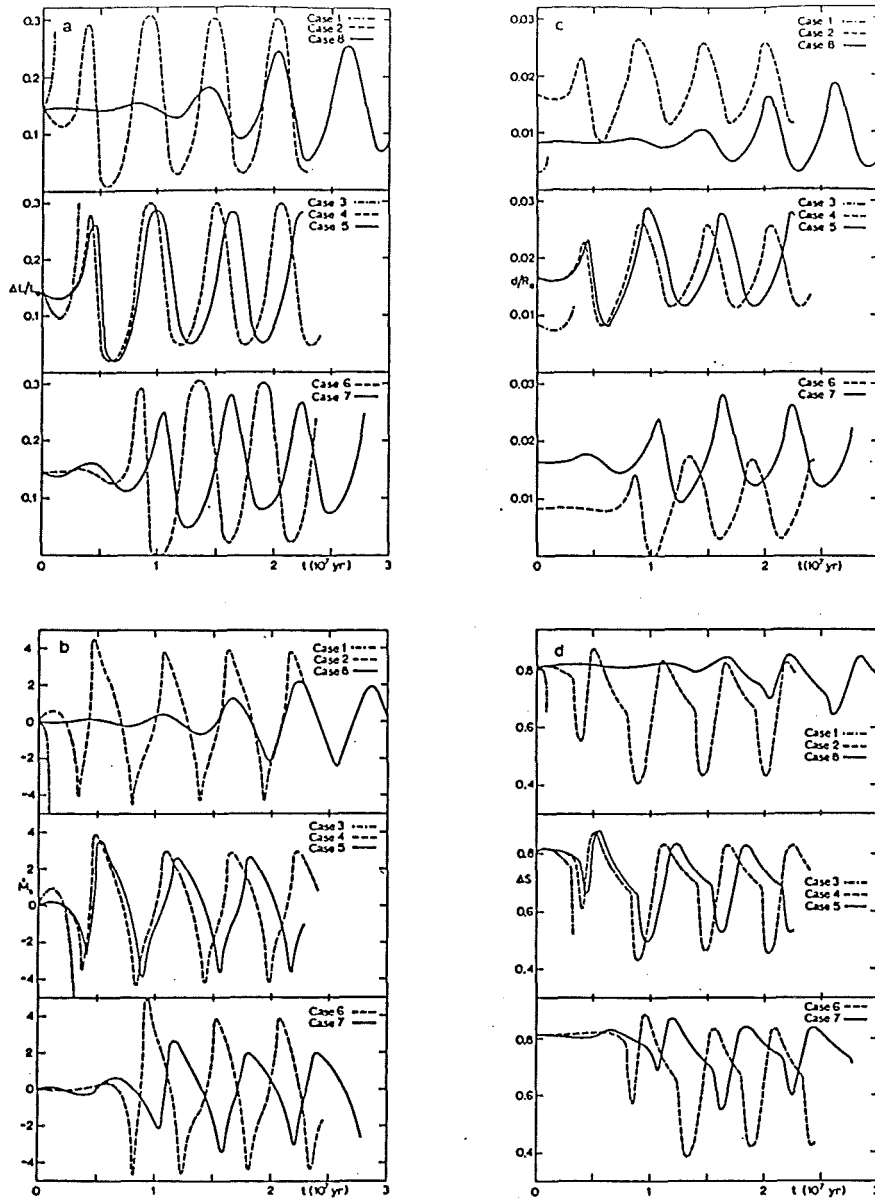
	M/M_{\odot}	R/R_{\odot}	$\log T_e$	L/L_{\odot}	$\Delta L/L_{\odot}$	ΔS	Period (days)
Primary	1.0	0.828	3.758	0.806	-0.144	0.81	0.24
Secondary	0.6	0.656	3.682	0.062	0.144		

Transport coefficients and the type of perturbation for the different cases investigated. The number of subsequent thermal cycles traced is also shown

Case	Transport coefficients			Perturbation	Cycles
	m	n	X		
1	4.5	2.0	0.004	$\Delta E = 2 L_{\odot} \text{ yr}$	-
2	4.5	2.0	0.020	-	4
3	3.0	1.0	0.010	-	-
4	3.0	1.0	0.020	-	4
5	3.0	2.0	0.020	-	4
6	2.0	1.0	0.010	-	4
7	2.0	1.0	0.020	-	5
8	1.0	1.0	0.010	$\Delta E = 1 L_{\odot} \text{ yr}$	10

Table 1.3. Parameters used by Rahunen and Vilhu (1982) in their contact binary stability investigations.

Table 1.3 shows the various values of transport coefficients for the various models investigated. (Note that instead of specifying K , Rahunen and Vilhu specified the initial dimensionless depth of contact X , in order to keep with an earlier convention of the Hazlehurst and Refsdal paper.) The results obtained by Rahunen and Vilhu are shown in Figure 1.20.



Changes of various quantities as functions of time for Cases 1-8. \dot{M}_1 is given in units of $10^{-8} M_{\odot} \text{yr}^{-1}$ and the entropy difference is expressed as $\Delta S = -\Delta \ln(P/T^{3/2})$

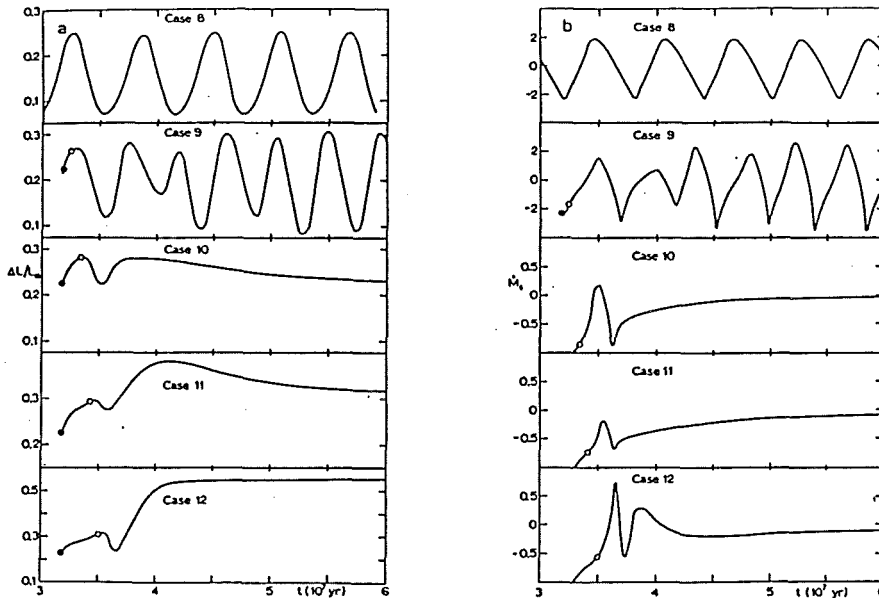
Figure 1.20. The behaviour of the Rahunen and Vilhu ZAMS binary models.

The authors remarked that although their ZAMS cycling models with unequal entropy could not explain the nearly equal surface luminosities of the components of the W UMa binaries, they could however help in their understanding.

Case 4, (cf. Figure 1.20) for example, demonstrated that the system was thermally unstable and behaved much like the TRO models. Steady cycles of period 6×10^6 years seemed to be established about 10^7 years after the introduction of the initial perturbation. However, one very important difference between the cycles of the TRO models, and those of Rahunen and Vilhu, is that the latter never break contact, this being a consequence of the energy transfer formula used.

The authors found the entropy difference between the components of their models to be fairly large (Figure 1.20), for instance, case 4 had a minimum entropy difference of about 0.45. However, they noted that these minima were sensitive to the choice of transport coefficients.

In order to examine the effects of nuclear evolution, Rahunen and Vilhu constructed similar unequal entropy models, but with various proportions of central hydrogen for the primary component (Figure 1.21). They found that the most notable effect of the initial nuclear evolution was a shortening of the periods of the various cycles, along with a slight increase in their amplitudes. However, at later stages of nuclear evolution, the authors found that stability was attained after an initial thermal relaxation phase (cases 10-12). The onset of this stability occurred at a rather early main-sequence stage when the primary had burnt 10-25 per cent of its central hydrogen, that is, when the system was between 7×10^8 to 1.5×10^9 years (i.e. after about 150-300 thermal oscillations).



The evolution of the system at different stages of nuclear evolution. The transport coefficients are the same as in Case 8 (zero-age system); which is also shown for comparison. The initial and final models of the simulated evolution (see text) are indicated by filled and open circles, respectively. \dot{M} is given in units of $10^{-8} M_{\odot} \text{yr}^{-1}$. Note that the vertical scales are different in different parts of the figure

Characteristics of evolved models. t' is the estimated age of the system (see text). For the stable models the values are taken after the relaxation of the system (after $\sim 10^9$ yr). The entropy difference is expressed as $\Delta S = -\Delta \ln(P/T^{3.5})$

Case	X_{cp}	t' (10^9 yr)	Cycle period (10^6 yr)	q		$\Delta L/L_{\odot}$		d/R_{\odot}		ΔS		$\Delta \log T_e$	
				min	max	min	max	min	max	min	max	min	max
8	0.70	0	6.0	0.58	0.63	0.07	0.25	0.004	0.017	0.66	0.84	0.059	0.080
9	0.63	0.7	4.6	0.54	0.58	0.09	0.30	0.005	0.022	0.50	0.74	0.053	0.087
10	0.53	1.5	stable	0.50		0.23		0.010		1.05		0.080	
11	0.41	2.5	stable	0.47		0.31		0.014		1.00		0.070	
12	0.19	3.5	stable	0.45		0.55		0.083		0.30		0.018	

Figure 1.21. Behaviour of the Rahunen and Vilhu evolved binary models.

The results of Rahunen and Vilhu suggested that the unevolved, unequal entropy models were unstable, and that their subsequent evolution closely resembled that of the TRO models. Rahunen and Vilhu proposed that their models, with a slightly modified energy transfer formula, may produce cycles which are consistent with those

of the TRO theory. They also remarked that the TRO models, in a similar manner, may be constructed so that their components remain in contact.

The authors also proposed that if the thermal equilibrium constraint were removed from the DSC model, and the concept taken more generally, then their unequal entropy models may be made much closer to the DSC models, assuming that the contact discontinuity could be preserved over the short timescale of one cycle (i.e. $\sim 6 \times 10^6$ years). They noted that their models had shown a tendency to develop a temperature inversion (i.e. a contact discontinuity) at a certain stage of their cycle.

Rahunen and Vilhu concluded that their results may be applied to improve both the DSC and TRO theories. They argued that the theories which at first sight look quite different, were in fact complementary, and that it may be possible to unite both the DSC and TRO models with the aid of a more refined energy transfer formula. Finally they suggested that the most probable contact binary theory may be one which combines the DSC, TRO and AML theories.

Key to illustrations:

- Figure 1.1. Smith, R. C. (1984)
Q.J.R.astr.Soc, 25, 405
figure 2.
- Figure 1.2. Roxburgh, I.W. (1966)
Astrophys.J., 143, 111
figure 1.
- Figure 1.3. Lucy, L.B. (1968a)
Astrophys.J., 151, 1123
figure 3.
- Figure 1.4. Lucy, L.B. (1968a)
Astrophys.J., 151, 1123
figure 1.
- Figure 1.5. Lucy, L.B. (1968b)
Astrophys.J., 153, 877
figure 1.
- Figure 1.6. Rucinski, S.M. (1974)
Acta Astronomica, 24, 119
figure 13.
- Figure 1.7. Shu, F.H.; Lubow, L.H. & Anderson, L. (1976)
Astrophys.J., 209, 536
figure 1.
- Figure 1.8. Shu, F.H.; Lubow, L.H. & Anderson, L. (1976)
Astrophys.J., 209, 536
figure 2.

- Figure 1.9. Hazlehurst, J. & Refsdal, S. (1978)
Astron. Astrophys., 62, L9
figure 1.
- Figure 1.10. Lubow, L.H. & Shu, F.H. (1977)
Astrophys. J., 216, 517
figure 2.
- Figure 1.11. Lubow, L.H. & Shu, F.H. (1977)
Astrophys. J., 216, 517
figure 3.
- Figure 1.12. Lubow, L.H. & Shu, F.H. (1977)
Astrophys. J., 216, 517
figure 4.
- Figure 1.13. Shu, F.H.; Lubow, L.H. & Anderson, L. (1979)
Astrophys. J., 229, 223
figure 2.
- Figure 1.14. Lucy, L.B. (1976)
Astrophys. J., 205, 208
figure 1.
- Figure 1.15. Lucy, L.B. (1976)
Astrophys. J., 205, 208
figure 3.
- Figure 1.16. Rucinski, S.M. (1985)
Interacting Binary Stars, Cambridge Univ. press.
eds. Pringle, J.E. & Wade, R.A.
page 120, figure 3.2.3. .
- Figure 1.17. Lucy, L.B. (1976)
Astrophys. J., 205, 208
figure 4.

- Figure 1.18. Rahunen, T. (1981)
Astron. Astrophys., 102, 81
figure 5.
- Figure 1.19. Rahunen, T. & Vilhu, O. (1982)
I.A.U. Coll. 69, 289
figure 1.
- Figure 1.20. Rahunen, T. (1982)
Astron. Astrophys., 109, 66
figure 2.
- Figure 1.21. Rahunen, T. (1982)
Astron. Astrophys., 109, 66
figure 5 & table 4.
- Table 1.1. Rucinski, S.M. (1973)
Acta Astronomica, 23, 79
table 7.
- Table 1.2. Robertson, J.A. & Eggleton, P.P. (1977)
Mon. Not. R. astr. Soc., 179, 359
table 1.
- Table 1.3. Rahunen, T. (1982)
Astron. Astrophys., 109, 66
tables 1 & 2.

CHAPTER 2

PROJECT OUTLINE

2.1. INTRODUCTION:

In Chapter 1 the controversy surrounding the possible formation mechanisms which may produce W Ursae Majoris binaries was discussed. It appears that the binaries must arise either from some initial pre-main-sequence contact stage, or must evolve into contact from a detached or semi-detached configuration. The discovery of contact or near-contact pre-main-sequence binaries would serve as evidence in favour of the former process, (at present only one near-contact pre-main-sequence binary is known: BM Ori in the Trapezium). Evidence for the latter scenario would result from the discovery of near-contact detached or semi-detached late-type binaries which were losing angular momentum via magnetic braking.

Several problems concerning the proposed structural models of W UMa systems were raised in Chapter 1. Perhaps the most serious of these involved the absence of observational evidence confirming the existence of W UMa binaries in the broken contact phase predicted by the TRO models. The discovery of such systems would remove many of the uncertainties surrounding the TRO theory, and would serve as a major constraint in the development of future structural models.

Another area of controversy discussed in the previous chapter involved the subsequent evolution of the newly formed W UMa binaries. The status of the A-type systems is of particular interest, i.e. whether they form directly, or whether they arise through the nuclear evolution of W-type systems. Again, the discovery of near-contact detached or semi-detached late-type binaries may go some way in clarifying the problem, especially if both components were found to be evolved.

The final problem involves the eventual fate of the contact binaries. Are they continuously evolving towards more extreme mass ratios, eventually coalescing into single stars ?

2.2. PROJECT OBJECTIVES:

The development of theoretical models describing the evolution and structure of W UMa systems has been seriously impeded by a crucial shortage of detailed information relating to short-period binaries displaying either EA or EB-type light curves. The TRO theory in particular, has suffered from an apparent lack of observed systems whose components are either in a state of broken contact, or are in physical contact, but possess widely differing temperatures.

The results of Lucy (1976) implied that, within the orbital period range 0.4 to 0.8 days, there should be roughly equal numbers of binaries exhibiting light curves of EW-type and EB/EA-type. Thus in 1979 Dr. R.W. Hilditch decided to undertake a survey of late-type eclipsing binaries whose periods lay within these limits. It was

hoped that if precise parameters were obtained for a reasonable sample of systems, then the results may resolve some of the controversy surrounding the various evolutionary and structural models, as well as improving our overall understanding of the W UMa binaries.

The main objective of this thesis is the acquisition, reduction, analysis and interpretation of data, as part of this survey of late-type binaries being conducted by Hilditch & King (cf. Hilditch et al. (1984)).

2.3. OBSERVATIONAL REQUIREMENTS:

In order to gather details of the various parameters describing the late-type binaries, high quality spectroscopic and photometric data must first be obtained. The spectroscopic data should yield radial-velocity curves from which minimum masses, minimum separations, and spectroscopic mass ratios, may be deduced, whilst relative radii, temperatures and luminosities of the components, and mass ratios, may be found from an analysis of the light curves and colour indices.

There are three major requirements which the spectroscopic observations must fulfil. Firstly they must be taken at a sufficiently high resolution to produce well-separated peaks in the cross-correlation functions, thus minimising systematic errors in the radial velocity data. Secondly, the spectra must be acquired with a reasonable signal-to-noise ratio so that spectral features should be clearly visible and the CCF peaks should be well defined.

Finally, each spectrogram must be collected in a time interval which is no greater than about 0.02 of the orbital period, in order that the effects of spectral-line 'smearing' be kept to a minimum. Clearly, if these conditions are to be satisfied, then the observations must be carried out using a large-aperture telescope.

The photometric observations on the other hand, should meet two important requirements: the data should be collected at a good signal-to-noise ratio, so as to minimise scatter in the differential magnitude data, and each integration should be as short as possible, so that rapid changes in light level may be recorded accurately. If well-resolved light curves of the eclipsing binaries are to be obtained, then the nature of the differential photometry demands that the observations be carried out using a telescope which may be manoeuvred with speed and ease. This limits the choice of telescopes to those which possess fairly small apertures (i.e. $< \sim 1.0\text{m}$).

2.4. APPLICATIONS FOR OBSERVING TIME:

A long-term allocation of observing time was essential if the proposed survey of the late-type binaries was to be completed successfully. This in effect limited the choice of possible telescopes to those funded by the United Kingdom Science and Engineering Research Council (SERC).

Although in recent years competition for observing time has been particularly fierce, a survey of this nature has two main advantages: firstly, the spectroscopic data may be obtained during 'bright' time, when applications for observing allocations are normally at a minimum, and secondly, the photometric observations may be acquired using small telescopes, which tend not to be oversubscribed to any great extent.

The South African Astronomical Observatory (SAAO), offered facilities which appeared to fulfil our requirements. The 1.9m telescope with its RPCS/ITS spectrograph and reticon detector system, seemed ideally suited for the acquisition of the spectroscopic data. Digitised spectrograms could be obtained at a dispersion of 30\AA mm^{-1} , which is quite adequate for cross-correlation analyses. On the other hand, high quality photometric data could be collected using the SAAO 0.5m telescope with its computer controlled two-channel photometer.

In 1981 a request for a long-term allocation of observing time was submitted to the SERC Panel for Allocations of Telescope Time (PATT), who awarded a total of four bright weeks on the SAAO 1.9m telescope and eight dark weeks on the SAAO 0.5m telescope, over the two year period 1982-83. An additional two bright weeks on the SAAO 1.9m telescope, four dark weeks on the SAAO 0.5m telescope, and three weeks on the 0.75m Steavenson telescope in Southern Spain, were subsequently awarded over the period 1984-85, since poorer than average weather conditions adversely affected the total time available for observing.

2.5. BINARIES SELECTED FOR SURVEY:

An original sample of sixteen binaries of spectral type F0 or later, with orbital periods in the range 0.4 - 0.8 day, and light curves of EW or EB-type, were selected by Hilditch and King from the 'Finding List for Observers of Interacting Binary Stars' (Wood, Oliver, Florkowski and Koch, 1980), as the basis of the survey. An additional system, AD Phoenicis, was included by the author at a later date. Details of these binaries are given in Table 2.1, together with notes on previous data available for the systems by 1981, obtained from the finding list.

Star	Spectral Type	Period (days)	V-magnitude			Previous photometry	Previous spectroscopy
			Max	Pri	Sec		
AQ Tuc	F2	0.595	10.5	11.0	11.0	Fairly good UBV light curves.	None known.
RT Scl	F0 F0	0.512	10.2	11.0	10.5	Very good UBV and uvby light curves.	Known spec. binary.
YY Cat		0.790	10.0	10.4	10.2	Unpublished UBV light curves.	None known.
CJ Eri	G5	0.634	8.0	8.6	8.6	No known light curves. May be C-type RR Lyrae star.	None known.
RS Col	F8 F8	0.672	9.0	9.4		Poor UBV coverage.	Known double-lined spec. binary.
EZ Hya	F9	0.450	11.0	11.5	11.5	No known light curves.	None known.
TV Mus	F2	0.446	11.0	11.3	11.3	Poor photographic light curve.	None known.
RV Crv	F0 G0	0.747	9.0	9.6	9.3	Sparse UBV light curve.	Single-lined RV-curve.
CX Vir	F5	0.746	9.2	9.7		No known light curves.	Known double-lined spec. binary.
RR Cen	F2	0.606	7.6	8.0	7.9	Good BV light curves.	None known.
FT Lup	F5	0.470	9.7	10.5		Good V light curve.	None known.
V502 Oph	F9 G2	0.453	8.9	9.4	9.4	Very good BV light curves.	Double-lined RV-curves.
RS Set	F5	0.664	10.5	11.3		V light curve and BVRI colours.	None known.
RS Ind	F4	0.624	9.9	10.3	10.0	Unpublished UBV data.	None published.
EE Aqr	F0	0.509	8.3	9.0	8.5	Good UBV light curves.	None known.
CX Aqr	F2	0.556	10.6	11.7	10.8	Photographic and unpublished UBV light curves.	None known.
AD Phe		0.613	10.0	10.5		None known.	None known.

Table 2.1. Details of binary systems selected for survey.

CHAPTER 3

SPECTROSCOPY

3.1. INSTRUMENTATION:

3.1.1. SAAO 1.9m Telescope and Instrumentation.

3.1.1.1. SAAO 1.9m Telescope.

The majority of the spectroscopic observations for the survey were carried out using the 1.9m reflecting telescope at SAAO, equipped with the Image-Tube Spectrograph (ITS) and Reticon Photon Counting System (RPCS). The instrument has a 2-pier asymmetrical mounting, and offers a choice of either Newtonian ($f/4.85$, $22.49'' \text{ mm}^{-1}$), Cassegrain ($f/18$, $6'' \text{ mm}^{-1}$), or Coude ($f/29.5$) foci. A schematic diagram of the optical layout of the telescope is shown in Figure 3.1 .

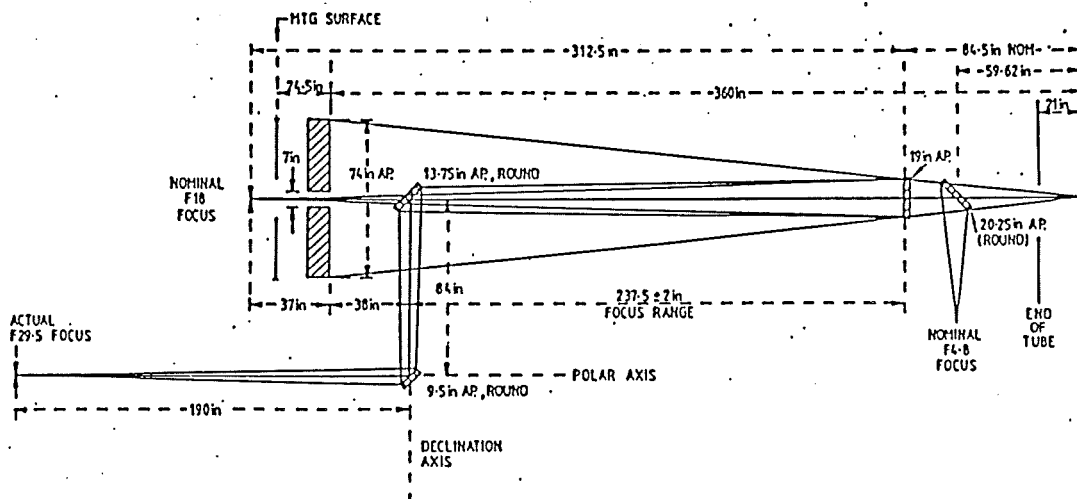


Figure 3.1. Optical diagram of the SAAO 1.9m telescope.

3.1.1.2. Image-Tube Spectrograph.

The ITS is a medium-dispersion spectrograph located at the f/18 Cassegrain focus of the 1.9m telescope. It employs a Cassegrain-type collimator producing a beam 10cm in diameter, which is brought to a focus using an f/1.4 Cassegrain-Maksutov camera (Figure 3.2). A slit width of $300\mu\text{m}$ (1.8") is normally used, with field and slit area viewed via a video-camera system. Various filters were available, together with a choice of six diffraction gratings, details of which are given in Table 3.1 .

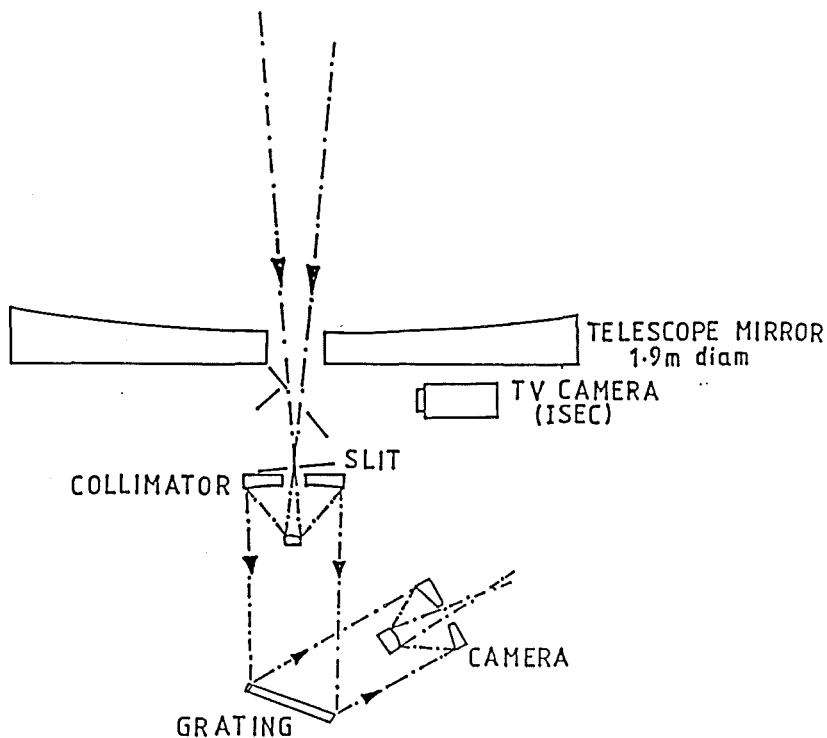


Figure 3.2. Optical diagram of the Image-Tube Spectrograph.

Although the majority of the spectrograph controls could be operated remotely, grating rotation, slit-width adjustment, and spectrograph focus, had to be carried out manually. A Cu/Ar lamp is normally used to provide the comparison spectra, while the calibration source, used for the flat-field exposures, is supplied by a Quartz-Iodine lamp.

GRATING SPECIFICATIONS

No.	Groove Density per mm	Effective Blaze λ (A)	Dispersion A/mm		Resolution (A)		Range*(A)	
			1st Order	2nd Order	1st Order	2nd Order	1st Order	2nd Order
1	300	4600	210	-	8	-	3300	-
2	400	7800,3900	150	75	6	3	2400	1200
3	830	7800,3900	65	30	2.4	1.2	1000	500
4	1200	4600	50	-	2	-	800	-
5	1200	6800,3400	50	23	2	1.0	800	400
6	600	4600	100	-	4	-	1600	-

* The useful range is about 18mm at the detector (RPCS)

Table 3.1. Specifications of the ITS gratings.

3.1.1.3. Reticon Photon Counting System.

Digitised spectrograms are obtained from the Image-Tube Spectrograph by means of the RPCS. Incident photon events are detected and amplified by an EMI 3-stage image intensifier, which in turn is optically coupled, via a lens, to a series of three VARO intensifiers which further enhance the image. Fibre-optic cable links the output of the VARO intensifiers to a Reticon diode array consisting of two rows of 936 elements, allowing simultaneous monitoring of star and sky. Scanning electronics read the contents

of the Reticon every 3ms, and any recorded events are added to memory.

A NOVA 3/12 minicomputer with 64K of core memory, controls the RPCS via a CAMAC interface, using software written at SAAO. The NOVA also stores the observations, writing the data to magnetic cartridge and disk. A schematic view of the system is shown in Figure 3.3 .

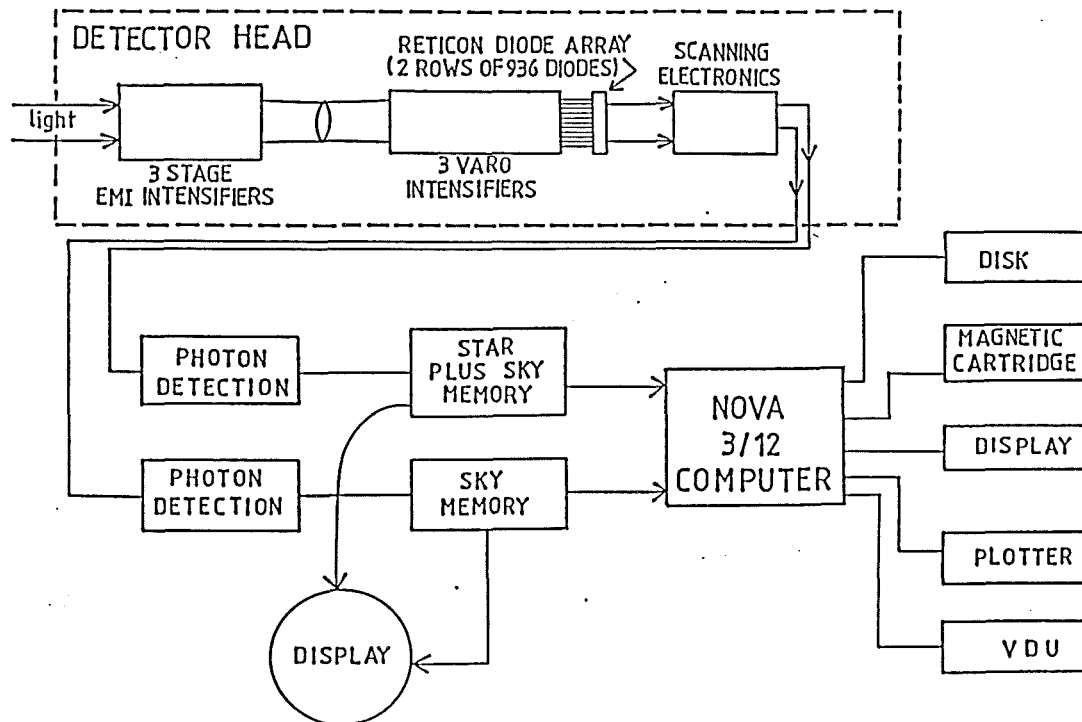


Figure 3.3. Schematic diagram of the RPCS.

3.1.2. Isaac Newton Telescope and Instrumentation.

3.1.2.1. Isaac Newton Telescope.

A few spectroscopic observations of the semi-detached binary CX Aquarii were obtained using the SERC Isaac Newton Telescope (INT) sited at the Observatorio del Roque de los Muchachos, on La Palma. The INT is a 2.5m reflecting telescope set on a polar disk/fork equatorial mount, which offers a choice of Cassegrain (f/15) or Coude (f/50) foci. For our observations the telescope was equipped with the Intermediate-Dispersion Spectrograph (IDS) and the Image Photon Counting System (IPCS).

3.1.2.2. Intermediate-Dispersion Spectrograph.

The IDS is a medium-dispersion spectrograph which is situated at the Cassegrain focus of the INT. The spectrograph offers a choice of two cameras of folded short-Schmidt-type, with focal lengths of 0.235m (Camera 1) and 0.500m (Camera 2), to focus the 8.5cm-diameter beam produced by the collimator. Slit widths ranging from $40\mu\text{m}$ (0.2") to 2mm (10.8"), may be set in steps of $5\mu\text{m}$, and like the ITS, field and slit area are viewed via a video-camera arrangement. The IDS offers a wide choice of filters and gratings. (Details of the gratings are given in Table 3.2.) Various discharge lamps are provided for comparison spectra, and a Tungsten lamp is used as the calibration source. All routine spectrograph functions are under computer control.

PRINCIPAL CHARACTERISTICS OF GRATINGS AVAILABLE ON INTERMEDIATE DISPERSION SPECTROGRAPH

Origin ⁽¹⁾	Ruling (gr mm ⁻¹)	Efficiency ⁽²⁾ (%)	CAMERA 1 (235 mm)			CAMERA 2 (500 mm)			Comments	
			at λ_{MAX} (Å)	Dispersion - at λ_c (Å mm ⁻¹)	Entrance slit for 30 μ m at detector (arcsec)	Dispersion - at λ_c (Å mm ⁻¹)	Entrance slit for 30 μ m at detector (arcsec)			
NPL	300	72	5460	138.5	5500	1.05	66.1	5500	0.52	
B+L	400	72	5100	104.5	5500	1.08	49.7	5500	0.52	
NPL	632	72	5460	66.8	5500	1.11	31.6	5000	0.54	
J-Y	1200	76	4000	35.3	3500	1.15	16.7	3500	0.55	
B+L	1200	68	6000	35.2	6500	1.33	16.4	6500	0.61	
PTX/NPL	1800	64	5300	23.2	8000 ⁽⁴⁾	1.40	10.5	5500	0.65	Holographic grating, optimized for 5000-7000 Å
							9.8	7000	0.73	
J-Y	2400	60	4000	17.6	3500 ⁽⁴⁾	1.37	8.1	3500	0.62	Holographic grating, optimized for 3500-5500 Å
							6.8	6000 ⁽⁴⁾	0.82	
Additional gratings ⁽⁵⁾ :										
B+L	150	66	5250	271.3	5500	1.03	131.2	5500	0.61	
B+L	400	59	7250	104.4	8000	1.11	49.9	8000	0.54	
B+L	831	65	7500	50.7	8000	1.27	23.9	8000	0.59	
B+L	1200	66	8000	34.8	7000 ⁽⁴⁾	1.37	15.5	8000	0.63	

Notes:

1. Keys: NPL = National Physical Laboratory; B+L = Bausch and Lomb; J-Y = Jobin-Yvon; PTX/NPL = PTX replica from NPL master.
2. Absolute efficiency values measured at RCO.
3. At low and intermediate dispersions the dispersion changes little with central wavelength.
4. Near maximum useful angle of incidence (refer to section 3.1.7).
5. These are gratings previously used on other RCO spectrographs which have been adapted for use on the IDS as an interim measure (see section 3.1.5 for further details).
6. Figures in italics show possible, but not primary, uses of some of the gratings.

Table 3.2. Specifications of the IDS gratings.

3.1.2.3. Image Photon Counting System.

The IPCS was used as the detector for the IDS, producing digitised spectrograms. The IPCS may be regarded as the two-dimensional equivalent of the RPCS. The instrument consists of a four-stage, high-gain, magnetically focussed EMI intensifier, which is optically coupled by a lens to a continuously scanning, lead oxide vidicon camera. Once individual photon events have been detected by the scanning electronics, and their position calculated, the result is added to computer memory and displayed graphically. When the integration is completed, the spectrogram is stored on magnetic disk. Since the IPCS is a two-dimensional device, stellar and sky exposures may be obtained simultaneously, so that the sky

background may be subtracted from the stellar observations immediately.

Detailed descriptions of the telescopes and instrumentation used, are given in the relevant user guides.

3.2. OBSERVATIONS:

3.2.1. Observations obtained with the SAAO 1.9m Telescope.

The spectroscopic observations were obtained using the second-order spectrum of Grating 3 of the ITS, together with a slit width of $200\mu\text{m}$. This configuration provided spectra at a dispersion of 30\AA mm^{-1} , centred at 4200\AA , and with a useful range of approximately 500\AA . (Further details of the grating are given in Table 3.1 .)

Flat-field exposures, with integration times of typically 10000 seconds, were carried out at the beginning and at the end of each night's observing run, in order that corrections for the non-uniform response of the detector may be applied in later analysis.

Where possible, spectroscopic observations of the programme stars were acquired over a wide range of phase, with data near the quadratures being of particular importance. As well as the observations of the binary stars, observations of radial-velocity standard stars were obtained at regular intervals throughout each night. Finally, all the stellar integrations were alternated with comparison-source exposures from the Cu/Ar lamp.

3.2.2. Observations obtained with the Isaac Newton Telescope.

The spectroscopic observations of CX Aquarii were obtained using the the Jobin-Yvon 1200 grating, with a slit width of $100\mu\text{m}$, and utilising Camera 2 of the IDS, providing spectra at a dispersion of 16.7\AA mm^{-1} . Spectra centred at 4040\AA and 4400\AA , with a useful range of approximately 480\AA , were obtained.

Several observations of radial-velocity standard stars were obtained each night in addition to the binary star observations. All stellar observations were alternated with comparison spectra exposures provided by a Cu/Ar lamp. Flat-field exposures from a Tungsten lamp source, were carried out at the beginning and/or end of each night's observing run.

3.3. DATA REDUCTION:

3.3.1. Initial reduction of spectra.

The spectra originally stored on disk or cartridge at the telescope, were later written to magnetic tape in standard FITS format (Wells, Greisen and Harten, 1981), to allow easy access to the data in later analysis. The SERC STARLINK software package SPICA was then used to flat-field the spectra, applying corrections for the non-uniform response of the detector. The data were then converted to the non-standard FITS format required for the spectroscopic image-processing package REDUCE (Hill, Fisher and Poeckert, 1982b).

3.3.2. REDUCE.

REDUCE is a versatile interactive graphics program designed to process spectrophotometric data obtained from PDS scans of photographic plates, or from Reticon or IPCS-type observations. The program, which runs on a DEC VAX computer, is written in a modular form to allow the data reduction to proceed in a series of logical operations selected from a main menu of operational functions. Two main subroutines form the basis of REDUCE: VELMEAS, which measures line positions and calculates radial velocities, and VLINE, which allows measurements of spectral-line equivalent widths, positions and, like VELMEAS, calculations of radial-velocities. Both subroutines were originally published as interactive reduction programs in their own right, by Hill, Ramsden, Fisher and Morris (1982), and by Hill, Fisher and Poeckert (1982a). However, since the spectrograms obtained from the RPCS and IPCS were not of a sufficiently high resolution, or signal-to-noise ratio, to allow a detailed analysis of the individual spectral features of the contact/near-contact binaries, the subroutine VLINE was not utilised in the reduction of the spectroscopic observations. A detailed description of REDUCE is given by Hill, Fisher and Poeckert (1982b).

The subroutine VELMEAS is designed to identify automatically and measure the positions of lines in arc or stellar spectra. The program was developed around the 'standard-plate' technique of Aitken (1935), where the positions of spectral lines are mapped according to their wavelength, by either a grating-equation,

Hartmann constants, or by polynomial coefficients. For the RPCS and IPCS observations, standard plates were created by first measuring the positions of lines of known wavelength from sample comparison-source spectra, and then calculating the appropriate polynomial coefficients, by iterative methods.

Once a standard plate has been calculated, a suitable line list selected, and the position of a reference wavelength specified (preferably located near the mid-point of the wavelength range), VELMEAS can automatically predict, identify, and measure the positions of the required spectral lines. The program initiates its search for the lines given in the line list at the position given for the reference wavelength, and requires the user to positively identify, and measure the spectral line in question. The position of the next line, relative to the first, is then predicted by means of the standard plate. All further line predictions are then calculated relative to previous line measurements. After the first few lines have been measured, and the user is satisfied that the predictor is working correctly, the program may be run in automatic mode.

The positions of the spectral lines are calculated by fitting a parabola to the peak of each line profile. When the relevant portion of the spectrum is displayed on the graphics terminal, the user measures the position of the line by two cursor placements: the first placement identifies the centre of the line, and the second selects the line wing. The program then reflects the position of the second placement across that of the first to define the outer limits for the data which is to be included in the parabolic fit.

Once VELMEAS is running, if only the centre of a line is identified, then the width of the data to be used in the fit is taken to be that specified in the previous measurement.

Each stellar spectrum is accompanied by a comparison spectrum, exposed either just before or just after the stellar observation. The comparison spectra are examined first, using VELMEAS. The measured positions of the comparison lines specified in the line list are compared with the positions predicted by the standard plate. The differences in line position, in the sense $X(\text{measured})$ minus $X(\text{predicted})$, are then calculated, and plotted against $X(\text{predicted})$, for each measurement. These data are then displayed on the graphics terminal, allowing the user to discard possible line misidentifications. After any 'erroneous' measurements have been eliminated, a polynomial is fitted to the data, to serve as a correction to the standard plate. Once this correction is known, any measured position 'X', can be converted to a wavelength ' λ '. This procedure is repeated for each comparison spectrum, with the resultant polynomials (or 'arc coefficients') being stored in memory, to be applied later to the relevant stellar spectra measurements. When the arc coefficients for the individual comparison spectra are known, it is a simple matter for REDUCE to linearise each stellar spectrum (in λ). This is essential if the stellar spectra are to be manipulated in any way.

At this stage of the data reduction, it is possible, if desired, to filter the stellar spectra, using standard Fourier techniques to reduce inherent noise. Before the data can be filtered, a 'filter' function must first be defined. REDUCE does

this by first displaying the observed power spectrum of the star (i.e. the square of the Fourier transform of the stellar spectrum), in terms of the Nyquist frequency, and then allowing the user to define a high frequency cut-off for the filter. The inverse Fourier transform of this 'box' function is then tapered using one of six possible taper functions (a Gaussian is normally used), and the resultant filter function is stored in real space. To filter a stellar spectrum, the Fourier transforms of the spectrum and of the filter function are calculated, and multiplied together. The filtered spectrum is obtained from the inverse Fourier transform of this product.

The next step in the reduction process is the rectification of the stellar spectra. Before a spectrum can be rectified, a fit must be made to the stellar continuum. To do this REDUCE first displays the spectrum and requires the user to select a number of small wavelength ranges, from which averages of the local stellar continuum are calculated. (This, in theory, should reduce any bias in an individual user's measurements to a minimum.) A fit is then made to these selected points, using the interpolation program INTEP (Hill, 1982c), which is able to draw smooth, stable curves through the points, rather than the usual oscillating curves of the typical polynomial fit. The stellar spectrum is then rectified by subtracting (in density, or $\log(\text{intensity})$), the measured continuum from the spectrum. REDUCE may be run in automatic mode when measuring the continuum, if the positions of the cursor placements have been given in advance. Once the data have been rectified, REDUCE will further linearise the spectra (in $\ln \lambda$), ready for cross-correlation analysis.

3.3.3. Determination of stellar radial velocities.

The determination of radial velocities from the spectra of isolated single stars is a relatively straight forward procedure; once the stellar spectra have been compared to a comparison spectrum from a discharge lamp, and the Doppler shifts of their spectral features have been estimated, the required radial velocities may be calculated. As discussed in the previous section, the spectrophotometric data reduction program REDUCE is capable of carrying out the necessary measurements and calculations. However, the determination of the radial velocities of the components of late-type contact and near-contact binaries is a far more difficult problem, since the observed spectra of the systems are composed of light from both stars. The identification of the individual spectral lines of each component, essential if REDUCE is to operate successfully, is almost impossible; the Doppler shifts in the binary component spectra due to the orbital motion, which are in opposite sense, create a very confused blending of the lines, while the rapid rotation of the components give rise to a broadening of the line profiles. Another problem arises from the magnitude difference in the blue-region of the spectrum, between the components of the contact and near-contact binaries, which is often as great as 2-3 magnitudes. This suggests that the contribution of the secondary component to the observed spectra of the binaries is very small, and that if measurements of individual absorption lines are to be carried out, then spectra of much higher resolution and much better signal-to-noise than those obtained for this project, would have to be acquired. However, we can determine the required radial

velocities from the spectra by cross-correlation analysis, since this technique does not involve the identification or measurement of individual line profiles.

3.3.4. VCROSS.

VCROSS is a program employing cross-correlation techniques to obtain relative radial velocities from log-linearised stellar spectra. Details of the program were published by Hill (1982b).

The determination of the radial velocities involves the cross correlation of one spectrum with another. VCROSS does this by first calculating the Fourier transform of a comparison star spectrum, which it then multiplies with the conjugate Fourier transform of a programme star spectrum. The inverse Fourier transform of this product, suitably normalised, yields the desired cross-correlation function (CCF). The position of the peak of this function corresponds to the relative observed radial velocity between the comparison and programme stars. When choosing comparison and programme stars, it is important that both stars be of similar spectral-type, in order to reduce the possibility of systematic errors being introduced, and to ensure that the peaks of the CCFs are as sharp as possible.

Because the spectra obtained from REDUCE are in a digitised format, where the discrete data points are evenly spaced apart, Fast Fourier Transform (FFT) techniques (Cooley and Tukey, 1965) may be applied, greatly increasing the speed with which the required Fourier transforms can be calculated. VCROSS employs the subroutine

FOURT of Brenner (1970) to obtain the necessary FFTs.

Before any cross correlations are carried out, the user must define the regions of the spectra which are to be used in the cross-correlation analysis. 'Gross' spectral features such as the H_γ or Ca II lines, are normally 'removed' at this stage, since they would dominate the resultant CCFs, producing very wide central peaks.

As stated previously, the cross-correlation techniques yield a measurement of the relative observed radial velocities between one star and another. However, the Doppler shifts in the observed spectra are due not to the motion of the stars with respect to the Sun, but to the motion of the stars with respect to the observer at the particular time when the spectra were acquired. Thus corrections must be calculated for each stellar observation, in order that heliocentric radial velocities may be quoted. Although no allowance for the radial-velocity corrections can be made within VCROSS, the corrections may be included at the initial reduction stage of REDUCE, when the comparison spectra are being measured. If the data have been reduced in this way, VCROSS will output the measurement of the 'true' radial velocity of one star relative to the other.

The radial-velocity measurements of VCROSS have been tested against those obtained from VELMEAS, for single stars, and found to be consistent. All stellar radial-velocity determinations in this thesis were carried out using VCROSS, since the program provided quick and reliable measurements from the spectra.

When attempting to obtain radial-velocity determinations for the components of binary stars, the spectrum of a reliable radial-velocity standard star, of similar spectral-type (i.e. \sim_{-5}^{+5} subclasses), to the primary component of the binary, was always used as a comparison. The resultant CCFs take one of two forms. If the contribution of the secondary component to the spectrum of the binary is weak, either because there is a large magnitude difference between the components, or because the Doppler shift in the lines of the secondary is not large enough to be noticeable, then only a single peak, due to the primary component, will be apparent in the CCF. If, on the other hand, the secondary contribution to the observed spectrum is noticeable, then a double peak should be evident in the CCF, resulting from the Doppler shifts, in opposite senses, between the primary and secondary component spectra.

When beginning a sequence of measurements, VCROSS allows the user to provide a value for the radial velocity of the comparison star. This permits the heliocentric radial velocities of the programme stars to be measured directly, provided that the necessary radial-velocity corrections have been incorporated earlier in the reduction process.

After the CCF has been calculated, the function is displayed on the graphics terminal, within limits (in km/s) specified by the user. The position of the peak(s) of the CCF are then measured by fitting Gaussian profiles, guided by appropriate cursor placements. If only a single peak is visible, then a single-Gaussian profile is fitted, but where twin peaks are apparent, a double-Gaussian profile

is applied.

3.4. ANALYSIS OF RADIAL-VELOCITY DATA:

Once values for the stellar radial velocities have been estimated using VCROSS, the data are plotted against their relevant phase, calculated according to recent reliable and accurate ephemerides, to yield the radial-velocity curves. Since all radial-velocity curves included in this thesis were calculated using ephemerides obtained from data incorporating the author's photometry, the orbital phases of the observations could be calculated with negligible error.

Generally, the component stars in binary systems will be found to orbit their centre of mass in elliptical orbits, giving rise to radial-velocity curves which will probably be asymmetric in shape. The eccentricities and orientations of these orbits relative to the observer, must be treated as free parameters when attempting to derive the orbital elements of the binaries from their observed radial-velocity curves (eg. Smart, 1977). However, the orbits of the late-type contact and near-contact binaries are found to be circular (to within errors of observation), since very strong tidal forces act to dampen quickly any orbital eccentricity.

Circular orbits were assumed for all systems analysed in this thesis. An examination of both the spectroscopic and photometric data lent weight to this assumption: firstly, reasonable fits to the radial-velocity data could be obtained using sine waves, and secondly, the secondary minima of the light curves occurred at an

orbital phase of 0.5 . The assumption of circular orbits, together with the accurately known orbital phases and periods, greatly simplified the analysis of the radial-velocity curves, since the search for solutions only involved fitting appropriate sine waves to the data. (Details of the analysis of individual systems are given in the relevant chapters.)

Two separate techniques were employed in the analysis of the radial-velocity curves. If the curves consisted of pairs of primary and secondary component data, then a program written by Dr. R.W. Hilditch, based on the method of Irwin (1973), was used to derive the required orbital elements. The technique employs a least-squares analysis to obtain values for the mass ratios, systemic velocities, and sums of radial-velocity semi-amplitudes, from double-lined radial-velocity curves, independently of other orbital parameters, and allows weights to be assigned to the primary and secondary component data. Irwin's method is particularly useful for finding solutions when the orbits are circular, but depends on the data being accurately phased. However, for the late-type contact and near-contact binaries, where the primary component radial velocities can be measured with greater accuracy than those of the secondary, Irwin's technique tends to overestimate the error on the semi-amplitude of the primary radial-velocity curve, since this must be derived from the sum of the semi-amplitudes of both curves, retaining the corresponding error. Alternatively, if orbital elements were required from single radial-velocity curves, a program written by Dr. W.J. Skillen, based on the method of Lehmann-Filhes (eg. Smart, 1977), was used to derive solutions to the data. The Lehmann-Filhes method is more comprehensive than that

of Irwin, allowing values to be obtained for most of the elements describing the binary orbit.

When values for the systemic velocities and radial-velocity semi-amplitudes have been obtained for the binary orbits, component minimum masses and separations can be estimated. Details of these calculations are given in Appendices 3.1 and 3.2 .

Key to illustrations:

Figure 3.1. SAAO Facilities Manual, page 2-1-4., 1982.

Figure 3.2. SAAO ITS Manual by T.Lloyd Evans, page 1b, 1983.

Figure 3.3. SAAO ITS Manual by T.Lloyd Evans, page 1a, 1983.

Table 3.1. SAAO ITS Manual by T.Lloyd Evans, page 22, 1983.

Table 3.2. UK Optical Telescopes Observer's Guide: La Palma, page 2-11, 1983.

Appendix 3.1. Calculation of component separations.

From elementary theory, we have the relationship,

$$a_{pr, sec} \cdot \sin i = 1.3751 \times 10^4 \cdot (1-e^2)^{1/2} \cdot K_{pr, sec} \cdot P \text{ km} ,$$

(equation 3.1)

where,

- 'a' is the semi-major axis of the orbit (km),
- 'i' is the orbital inclination,
- 'e' is the orbital eccentricity,
- 'K' is the semi-amplitude of the radial-velocity curve (km/s),
- 'P' is the orbital period (days).

If circular orbits are assumed then the above equation becomes,

$$a_{pr, sec} \cdot \sin i = 1.3751 \times 10^4 \cdot K_{pr, sec} \cdot P \text{ km} ,$$

(equation 3.2)

The error on equation 3.2. is given by,

$$\Delta(a_{pr, sec} \cdot \sin i) = [\Delta(K_{pr, sec})^2 + (\Delta P)^2]^{1/2} ,$$

(equation 3.3)

Since, for the systems analysed in this thesis, ' ΔP ' is negligible, equation 3.3. may be further simplified to,

$$\Delta(a_{pr, sec} \cdot \sin i) = (\Delta K_{pr, sec}) ,$$

(equation 3.4)

The component separation, 'a', is given by,

$$a \cdot \sin i = (a_{pr} + a_{sec}) \cdot \sin i$$

(equation 3.5)

The error on this being,

$$\sigma(a \cdot \sin i) = [(\sigma(a_{pr} \cdot \sin i))^2 + (\sigma(a_{sec} \cdot \sin i))^2]^{1/2}$$

(equation 3.6)

(The treatment of errors is discussed in Appendix A.)

Appendix 3.2. Calculation of component masses.

From elementary theory, we have,

$$m_{pr,sec} \cdot \sin^3 i = 1.0385 \times 10^{-7} \cdot (1-e^2)^{3/2} \times (K_{pr} + K_{sec})^2 \cdot K_{sec,pr} \cdot P \cdot M_{\odot},$$

(equation 3.8)

where,

'm' is the stellar mass (M_{\odot}).

'i' is the inclination of the orbit,

'e' is the orbital eccentricity,

'K' is the semi-amplitude of the radial-velocity curve (km/s),

'P' is the orbital period (days).

Now, assuming that the orbits are circular, equation 3.8 becomes,

$$m_{pr,sec} \cdot \sin^3 i = 1.0385 \times 10^{-7} \times (K_{pr} + K_{sec})^2 \cdot K_{sec,pr} \cdot P \cdot M_{\odot},$$

(equation 3.9)

Since ' ΔP ' is negligible, the error on the equation is given by,

$$\Delta(m_{pr,sec} \cdot \sin^3 i) = [2^2 \cdot (\Delta(K_{pr} + K_{sec}))^2 + (\Delta K_{sec,pr})^2]^{1/2},$$

(equation 3.10)

where,

$$\sigma(K_{pr} + K_{sec}) = [(\sigma K_{pr})^2 + (\sigma K_{sec})^2]^{1/2},$$

(equation 3.11)

If a value for the inclination is obtained from a solution to the light curve, then the errors on the calculated component masses are given by,

$$\Delta m_{pr, sec} = [2^2 \cdot (\Delta(K_{pr} + K_{sec}))^2 + (\Delta K_{sec, pr})^2 + 3^2 \cdot (\Delta \sin i)^2]^{1/2},$$

(equation 3.12)

Finally, the spectroscopic mass ratio, ' q_{spec} ', is given by,

$$q_{spec} = K_{pr}/K_{sec} = a_{pr}/a_{sec} = m_{sec}/m_{pr}$$

(equation 3.13)

CHAPTER 4

PHOTOMETRY

4.1. SAAO 0.5m TELESCOPE AND INSTRUMENTATION:

All photometric observations for the survey were obtained using the 0.5m Cassegrain (f/18, $22.6'' \text{ mm}^{-1}$) telescope at SAAO, equipped with a Peoples Photometer. The two-channel photometer employed a blue-sensitive EMI6256 tube with an S13 photocathode, and a red-sensitive EMI9659 tube with an extended S20 photocathode, both housed in their own cold boxes and cooled to -10°C and -20°C , respectively.

A NOVA 1220 minicomputer with 16K of core memory, controlled the filter-change mechanism, timing of integrations, and the acquisition of data, using software written at SAAO. All data were stored on magnetic disk and cartridge. Further details of the 0.5m telescope and instrumentation are given in the relevant SAAO handbooks.

4.2. OBSERVATIONS:

4.2.1. Nature of observations.

Since it was essential to obtain well-resolved light curves of the programme stars, some of which are fainter than 11th magnitude, it was decided to employ a wide-band photometric system for the observations. Because the Cape-Kron system was already implemented at SAAO, and the SAAO photometry-reduction programs designed around it, this was chosen for the observations.

The Cape-Kron photometric system is similar to the Johnson UBVRI system, except that the effective wavelengths of the Cape-Kron R and I filters lie at approximately 6700\AA and 8100\AA , respectively, compared to 7000\AA and 9000\AA for the Johnson R and I filters. Details of the Cape-Kron system are given by Cousins (1980).

It was decided to observe the binaries using only the BVRI_c filters, since the observations could then be carried out using only the red channel of the Peoples Photometer, thus improving the time resolution of the light curves. Besides, little additional information would be obtained if the U filter were employed, since the binaries are of late spectral type.

4.2.2. Selection of comparison and standard stars.

A comparison star and at least one check star were selected for each variable. The stars chosen as comparisons were always of similar colour to the variables, and lay in close proximity to them in the sky. This virtually eliminates any extinction or second-order colour effects in the calculation of the differential V-magnitudes, allowing the light curves to be analysed on the instrumental system (see e.g. Henden and Kaitchuck, 1982). Literature searches were carried out to check whether the proposed comparison stars had ever been noted as variable. Once observations were underway, if any comparison star appeared to vary, then it would be replaced by the check star.

Sets of E- and F-region standards (Menzies, Banfield and Laing, 1980), of various spectral types, were observed at the beginning and end of each night (if weather permitted), and red and blue standards were observed throughout the night at intervals of approximately two hours. In addition to these, a local standard, of similar spectral type to the binary, was observed hourly to check for zero-point drifts and to serve as an additional check star.

4.2.3. Observing Technique.

Because of the rapid magnitude variations of the late-type contact and near-contact binaries, and the need to obtain well-resolved light curves over relatively short periods of time, the variable and comparison stars were monitored through the V filter only. However, in order to note any changes in the colour of the systems, the variable stars were observed through all four filters at regular intervals of approximately 25 minutes. ($\sim 2-3\%$ of the orbital periods).

In order to obtain reasonable signal-to-noise ratios during monitoring, the stellar integrations were normally carried out in units of 30 seconds, usually two consecutive integrations for the comparison star observations, alternating with four consecutive units for the variable.

When carrying out the four-colour observation sets, the binaries or standard stars were observed through the filters in the order: BVRIIRVB. These observations were then averaged to minimise errors. Integrations for the local sky background were also carried out at this stage.

4.3. DATA REDUCTION:

4.3.1. Reduction to Instrumental and Standard magnitudes.

All data were first reduced to instrumental magnitudes using the comprehensive SAAO photometry reduction package. Values for the transformation coefficients and zero-point constants were estimated from appropriate diagnostic plots (see Appendix 4.1). All four-colour observation groups were then transformed to the Cape-Kron standard system.

4.3.2. Calculation of differential magnitudes.

A computer program written by the author, employing the cubic-spline function subroutine L2FRES, of Powell (1967), was used to create the differential magnitudes. Spline functions were first fitted to the comparison star data for the observations on each night, and then the differential magnitudes were obtained by subtracting the relevant values of the function from the variable star data.

4.4. DATA ANALYSIS:

4.4.1. Calculation of ephemerides.

All orbital phases used in the spectroscopic and photometric analyses in this thesis were obtained using revised ephemerides calculated from data incorporating the author's photometric observations. Times of minima were calculated from the light curves using the method of Kwee and van Woerden (1956). These minima,

together with any previous published times of minima, were then used to obtain revised estimates of the orbital periods. Further details for individual systems are given in the relevant chapters.

4.4.2. Light curve analysis.

An analysis of the light curves of eclipsing binaries can yield information on the geometry of the system, the mass ratio, the components' temperatures and the distribution of surface brightness over the two stars. All modern techniques of light curve analysis assume Roche geometry and rely upon the creation of theoretical light curves generated from computer models of binary stars. When searching for a 'solution' to the observed light curve, an initial configuration is assumed. Several, or all, of the parameters describing the model are then allowed to vary within limits specified by the user. The computer then generates further theoretical light curves, altering each of the original parameters, in an attempt to obtain a closer match to the observed data. It will almost certainly be necessary to run such computer codes many times before a final solution can be adopted, and sometimes a close fit to the data can never be obtained.

Two separate light-curve synthesis codes were used to analyse the photometric data obtained for this thesis: if the components of the binary components appeared to be in contact, then the WUMA3 code of Rucinski (1973) was employed; if, however, the system appeared to be semi-detached or in marginal contact, then the code LIGHT of Hill (1979) was applied. Light uses the atmospheres of Kurucz et al. (1974) to calculate stellar fluxes, and the tables of

Carbon and Gingerich (1969) to calculate the limb darkening coefficients. WUMA3 on the other hand, allows the user to define the atmospheres to be used in the light curve synthesis. For the systems analysed in this thesis, the atmospheres from Table 5b of Kurucz (1979) were employed.

4.4.3. WUMA3

4.4.3.1. Geometry of the contact-binary model.

The geometrical configuration of contact binaries can be defined by a relatively small number of parameters, since the surface of the common envelope may be assumed to follow an equipotential surface lying somewhere between the inner and outer critical surfaces (see Figure 1.7). Thus, if S_i and S_o denote the potentials at the inner and outer critical surfaces, respectively, and S corresponds to the potential at the surface of the contact-binary common envelope, then $S_o > S > S_i$. Using this relationship it is possible to define a parameter, f , which measures the degree of contact of the binary components. There is more than one definition of the 'fill-out' factor f , but the most common, used by Rucinski (1973), is:

$$f = (S - S_o) / (S_i - S_o)$$

(equation 4.1)

$$\Rightarrow 0 < f < 1,$$

where, $f = 1$, if the surface of the contact binary is coincident with the inner critical surface, or $f = 0$, if the binary surface lies at the outer critical surface.

The value of the potential V at point P depends only on the distance to both masses r_1 and r_2 and on the distance from the axis of rotation $\tilde{\omega}$. O is the mass centre of the binary system.

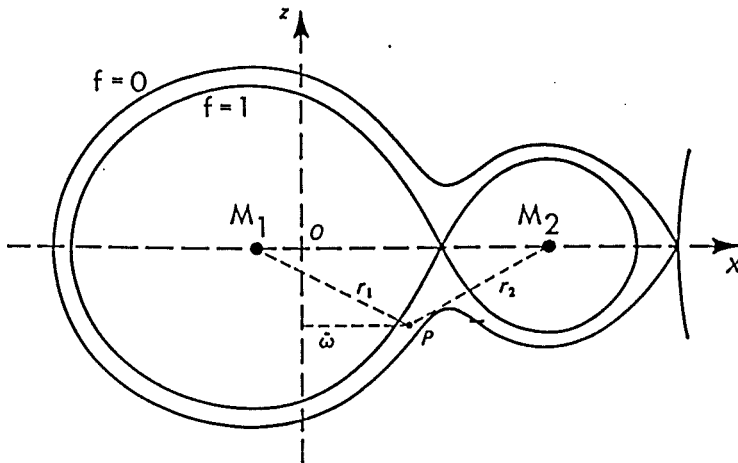


Figure 4.1. Geometry of the contact-binary model.

The values of the critical potentials, S_i and S_o , depend only upon the mass ratio of the binary, q . The potential, S , at some point, P , between the critical surfaces (see Figure 4.1), is given by,

$$S = \frac{G(M_1 + M_2)}{2a} \cdot V ,$$

(equation 4.2)

where,

$$V = \frac{2}{1+q} \cdot \frac{1}{r_1} + \frac{2q}{1+q} \cdot \frac{1}{r_2} + \tilde{\omega}^2 ,$$

(equation 4.3)

using a corotating system of coordinates, where,

G is the gravitational constant,

M_1 and M_2 are the component masses,

V is the 'unscaled' potential at the point P ,

a is the separation between the centres of mass of the two components,

r_1 and r_2 are the distances from the point P to M_1 and M_2 , respectively,

$\tilde{\omega}$ is the distance of the point P from the orbital axis.

Since the absolute dimensions of the components have no relevance to the contact binary model, the equations are simplified by defining the separation between the component centres of mass as unit length. Thus, the surface of the contact binary may be defined by only two parameters, namely f and q. Now, defining the X-axis to lie along the line joining the component centres of mass, and the Z-axis as the axis of rotation (Figure 4.1), then,

$$r_i = [(x - x_i)^2 + (y - y_i)^2 + (z - z_i)^2]^{1/2}, \quad i = 1, 2$$

$$\tilde{\omega}^2 = x^2 + y^2,$$

$$x_1 = -q \cdot (1 + q)^{-1},$$

$$x_2 = (1 + q)^{-1},$$

$$y_i = z_i = 0, \quad i = 1, 2$$

(equations 4.4)

4.4.3.2. Light curve synthesis.

The observed brightness of a contact binary defined by the parameters f and q, depends upon the orientation of the system relative to the observer. This in turn depends on the inclination of the orbital plane relative to the observer, i , and the orbital phase of the binary, ϕ . Using these four parameters it is possible to generate a theoretical light curve for the binary, by calculating the change of total light seen by the observer as the binary rotates

in its orbit. The simplest way to do this is to set up a second coordinate system, $X'Y'Z'$, which, unlike the first coordinate system, XYZ , remains stationary in the observers' frame of reference as the binary rotates (Figure 4.1). The X' -axis of the new coordinate system is directed towards the observer, while the Y' - and Z' -axes are orientated in such a way that when the X' - and X -axes are coincident, then the Y' - and Y -axes, and Z' - and Z -axes are also. Any point (x',y',z') in the primed coordinate system may be transformed to the corresponding point (x,y,z) in the corotating system, by the transformation:

$$\begin{bmatrix} x \\ y \\ z \end{bmatrix} = \begin{bmatrix} \sin i \cdot \cos \phi & \sin \phi & \cos i \cdot \cos \phi \\ -\sin i \cdot \sin \phi & \cos \phi & -\cos i \cdot \sin \phi \\ -\cos i & 0 & \sin i \end{bmatrix} \begin{bmatrix} x' \\ y' \\ z' \end{bmatrix}$$

(equation 4.5)

Rucinski calculates the total light emitted in the direction of the X' axis, i.e. towards the observer, by considering a grid of rectangles (typically 100 x 100), of size $\Delta y'$ by $\Delta z'$ positioned at (y'_i, z'_j) , covering the $Y'Z'$ -plane in the region of the model binary. By stepping down from large values of x' for given values of (y'_i, z'_j) , or by methods of iteration, the intersections of the observers' line of sight with the binary surface can be calculated by considering the transformation of the binary surface from XYZ to $X'Y'Z'$ coordinates. For each surface element intercepted on the surface of the binary, the local intensity, I_{ij} , emitted in the direction of the observer, (called the 'emergent intensity'), is calculated. The addition of the intensity contributions from all surface elements then yields the total observed intensity for that particular orientation of the binary. Thus, by rotating the XYZ

coordinate system around the orbital axis, and by repeating the above process for other orientations of the binary, theoretical light curves can be generated. The total observed intensity for any given orientation for the model binary, can be expressed,

$$L_{th}(\phi, f, q, i) = \Delta y' \cdot \Delta z' \sum_{i,j} I_{ij} ,$$

(equation 4.6)

where, for any specific generated light curve, f, q and i are fixed.

In order to generate accurate theoretical light curves, realistic estimates for the values of the emergent intensities, I_{ij} , must be calculated. If the surface of the common envelope radiated as a black body, then the problem would be rather straightforward, since the relative value of any particular I_{ij} would depend purely on the size of the projected surface, as seen by the observer. However, in reality, the situation is somewhat more complex: firstly, the common envelope surrounding the binary will not be of uniform brightness over all of its surface, either because of gravity darkening effects, differences in component temperatures, reflection effects, or anomalous distribution of luminosity (i.e. starspots or hotspots); and secondly, the intensity of a given surface element may depend on the angle from which it is observed, because of the limb darkening effect.

The effect of gravity darkening on the local effective temperature, T_e , is given by the relationship,

$$T_e = T_{e0} \cdot (g/g_0)^\beta ,$$

(equation 4.7)

where, β is the gravity darkening exponent,

g is the local gravity,

g_0 and T_{e0} are the local gravity and effective temperature at some arbitrary reference point.

The values for β range from 0.25 for stars with radiative atmospheres, to about 0.08 for stars with convective atmospheres. Values for β as low as zero have been proposed for the common envelopes of contact binaries.

The local gravity (in cgs units) at any point on the surface of the contact binary is given by,

$$\log g = \log |\nabla V| + (1/3) \cdot \log(M_1 + M_2) - (4/3) \cdot \log P + 2.89$$

(equation 4.8)

where, P is the orbital period in days,

and, g , V , M_1 , M_2 are as before.

Limb darkening occurs because stellar atmospheres are transparent to some extent, allowing the observer to see beyond the surface of the star, into deeper and hotter regions. This makes the outer limb of the star appear cooler and darker than the more centralised areas of the stellar disk. The extent of the limb darkening is dependant on wavelength.

The angle from which an observer views the stellar atmosphere is defined as,

$$\mu = \cos \theta,$$

(equation 4.9)

where, θ is the angle between the observers line of sight and the local normal to the stellar surface.

If $I_\lambda(\mu)$ is the emergent intensity at some value of μ , then, for a blackbody,

$$I_{\lambda}(\mu) = I_{\lambda}(1) = \text{constant} ,$$

(equation 4.10)

Expanding equation 4.10 to take into account the effects of limb darkening, we obtain,

$$I_{\lambda}(\mu) = I_{\lambda}(1) - u_{\lambda} \cdot I_{\lambda}(1) \cdot (1-\mu) ,$$

(equation 4.11)

where, u_{λ} is the linear limb darkening coefficient.

Although, in practice, the above expression will give an adequate approximation to the effects of limb darkening, equation 4.11 may be expanded further:

$$I_{\lambda}(\mu) = I_{\lambda}(1) - u_{\lambda} \cdot I_{\lambda}(1) \cdot (1-\mu) \\ - b_{\lambda} \cdot I_{\lambda}(1) \cdot (1-\mu)^2 - c_{\lambda} \cdot I_{\lambda}(1) \cdot (1-\mu)^3 ,$$

(equation 4.12)

where, b_{λ} and c_{λ} are additional limb darkening coefficients.

Values for u_{λ} , b_{λ} and c_{λ} may be calculated from limb-darkening tables, such as those published by Carbon and Gingerich (1969).

The reflection effect is of relatively minor importance in the synthesis of the contact binary light curves, since the components are usually of similar temperature, and the relevant angles of incidence tend to be very oblique. The unequal temperatures of the components may also be treated as a free parameter in Rucinski's code. This temperature difference is expressed in the factor, X , where,

$$X = (T_1 - T_2) \cdot (T_1 + T_2)^{-1} ,$$

(equation 4.12a)

where, T_1 and T_2 are the component temperatures.

Finally, it is not possible to include any anomalous distributions of luminosity on the binary surface, such as hotspots or starspots, as free parameters, since this is well outside the scope of the present model.

4.4.3.3. Searching for a photometric solution.

So far, only the process of generating theoretical light curves has been discussed, however, the prime objective of the synthesis techniques is to yield photometric solutions to observed light curves. Such solutions are obtained by finding the theoretical curve which provides the closest match to the observed data.

The first stage in the process of searching for a photometric solution involves generating light curves until a reasonable match to the observed light curve is obtained. A number of additional light curves are then generated around the original, by adding and subtracting constants to each of the (chosen) parameters in turn. Once this has been done, the effects of these changes on the original theoretical light curve can be estimated, and corrections, which would improve the 'fit', calculated.

The differences between the theoretical light curve, L_{th} , and the observed light curve, L_{obs} , at phase ϕ , is given by,

$$L_{obs}(\phi) - L_{th}(\phi) = \sum_k (\delta L_{th} / \delta e_k) \cdot \Delta e_k ,$$

(equation 4.13)

where, e_k is any parameter describing the theoretical light curve,

$\delta L_{th} / \delta e_e$ is the partial differential expressing the effect

on the theoretical light curve of any change in the parameter e_k (at phase ϕ), Δe_k is the correction to the original value of e_k (at phase ϕ).

The above expression is calculated for each of the chosen parameters, e_k , and at other phases, ϕ . (Normally a spline function is fitted to the observed data, which is then used to calculate values of $L_{\text{obs}}(\phi)$, at regular phase intervals of 0.01 .) Once the calculations have been completed for all given values of ϕ , and the final values for Δe_k obtained, the corrections are then applied to the original theoretical data, and the procedure is repeated. Thus, by iterative methods, we hope to obtain the theoretical light curve which best describes the observed data.

The search for a photometric solution will probably not be as straightforward as the above procedure suggests. The majority of contact binary light curves are 'distorted' by anomalous distributions of luminosity on the surface of the systems, caused either by hotspots or starspot activity. So, in practice, each half of the light curve (i.e. phase 0.0 to 0.5, and, phase 0.5 to 1.0), has to be analysed separately, otherwise a close fit to the data may never be found. It may also be necessary to shift the observed data by 0.5 in phase, if the contact binary is a W-type system, since Rucinski's code always assumes that the larger component is eclipsed at primary minimum. Another problem arises because the partial differentials may be interdependent, possibly preventing solutions of all the desired parameters simultaneously. Finally, there is no guarantee that any final photometric solution is unique. Thus it is important to restrain as many of the parameters as possible, for, by

example, assuming a value for the gravity-darkening exponent, or by determining a value for the mass ratio from spectroscopic observations. It is this latter constraint which is particularly important.

4.4.4. LIGHT.

4.4.4.1. Geometry of the binary model.

The geometry of the binary model used in LIGHT is rather more complex than that used in WUMA3, since the program must cope with binaries which may not be in contact, and which may have eccentric orbits. Although LIGHT uses Roche geometry to calculate the binary component surfaces, the potentials may be modified if the components are not rotating synchronously.

For the case where the binary components are rotating synchronously, the shape of the stars may be defined again only by the mass ratio of the system and the relative radii of the components, that is, the stellar radii measured relative to the separation of their centres of mass; which remains constant where the orbits are circular. (Further details of LIGHT are given by Hill, 1979.)

4.4.4.2. Light curve synthesis.

The coordinate scheme used in LIGHT is similar to that used in WUMA3, where two sets of coordinates are defined: one fixed relative to the binary, with the other fixed relative to the observer (see Section 4.4.3.2.).

LIGHT calculates light curves by first determining the flux from each star, whether or not one of the stars is being eclipsed. Obviously, at this stage the projected shapes of the stars on the Y'Z'-plane (retaining the nomenclature of Section 4.4.3.2.), must be calculated. The program then tests if an eclipse is present, and adjusts the integrations accordingly. LIGHT uses atmospheres of Kurucz et al. (1974), to calculate relative-flux ratios for the stars at the specified wavelength(s), (i.e. 5500 \AA for the systems analysed in this thesis), in order to keep the model as physically realistic as possible. (Ideally, one would like to convert the tabulated atmospheres into broad-band colours as the data is being read by the program, but the increase in computing time required for these calculations make this approach impractical.) The program employs interpolation formulae, similar to equation 4.12, to estimate $I_{\lambda}(\mu)$, for any given values of T_{eff} , $\log g$, or λ , from the tables of Carbon and Gingerich (1969).

Finally, LIGHT is somewhat more sophisticated than WUMA3, being able to treat heating and reflection effects, as well as the presence of a third body, as independent parameters.

4.4.4.3. Solving the light curve.

LIGHT uses the program CURFIT (Bevington, 1969), which employs a differential correcting procedure, to search for photometric solutions. The physical parameters which may be input to CURFIT are: mass ratio, relative polar radii, polar temperatures, linear limb darkening coefficients, gravity darkening exponents, heating and reflection efficiencies, inclination, eccentricity and orientation of orbit, and third-body radius and temperature.

Since we are dealing with contact and near-contact binaries, circular orbits may be assumed (see Chapter 3). Once temperatures for the primary and secondary components have been estimated from the observed colour indices, the primary component temperature is fixed, and values for the gravity darkening exponents, and heating and reflection efficiencies, are also assumed. LIGHT is normally set to calculate automatically the required limb darkening coefficients. Finally, the search for a photometric solution is greatly simplified if a value for the mass ratio has been established from spectroscopic observations.

Figure 4.1 : Adapted from Figure 3.1.6 of Rucinski (1985).

Appendix 4.1 Calculation of transformation coefficients and zero-point constants using the SAAO photometry package.

Values for the first-order and second-order extinction coefficients, determined from previous analyses, were assumed throughout the photometry-reduction process. Initially, all data were converted to magnitudes and colours on the natural system of the detector, yielding values for v_o , $(b-v)_o$, $(v-r)_{kc o}$ and $(v-i)_{kc o}$. Values for the transformation coefficients were obtained as follows:

We have the fundamental relationships,

$$V-v_o = T_v \cdot (V-I) + Z_v ,$$

$$(B-V) - (b-v)_o = (1-T_{bv}^{-1}) \cdot (B-V) + Z_{bv}/T_{bv} ,$$

$$(V-R)_{kc} - (v-r)_{kc o} = (1-T_{vr}^{-1}) \cdot (V-R)_{kc} + Z_{vr}/T_{vr} ,$$

$$(V-I)_{kc} - (v-i)_{kc o} = (1-T_{vi}^{-1}) \cdot (V-I)_{kc} + Z_{vi}/T_{vi} ,$$

where, V , $(B-V)$, $(V-R)$ and $(V-I)$ denote the accepted V magnitudes and colour indices of the standard stars,

T_v , T_{bv} , T_{vr} and T_{vi} are the transformation coefficients,

Z_v , Z_{bv} , Z_{vr} and Z_{vi} are the zero-point constants.

Values for the transformation coefficients and zero-point constants were determined for each night from the relevant standard star observations, by plotting,

$V-v_o$ against $(V-I)$ to yield T_v ,

$(B-V) - (b-v)_o$ against $(B-V)$ to yield T_{bv} ,

$(V-R)_{kc} - (v-r)_{kc o}$ against $(V-R)_{kc}$ to yield T_{vr} ,

$(V-I)_{kc} - (v-i)_{kc o}$ against $(V-I)_{kc}$ to yield T_{vi} .

Once the transformation coefficients have been obtained, the zero-point constants are calculated by subtracting the transformed extra-atmospheric magnitudes and colours of the observed standards, from their accepted (standard) values.

Appendix 4.2 Interstellar extinction.

The colour excess in magnitudes, for a given colour index '(L-V)', where 'L' is some arbitrary wavelength, and 'V' is the visual wavelength of the UBV system, i.e. 5500\AA , is given by,

$$E(L-V) = C.[(A_L/A_V)-1].E(B-V)$$

(equation 4.14)

where,

A_L is the interstellar extinction in magnitudes at wavelength L,

A_V is the interstellar extinction in magnitudes at wavelength V,

$E(L-V)$ is the colour excess in magnitudes for the colour index (L-V),

$E(B-V)$ is the colour excess in magnitudes for the colour index (B-V) of the UBV standard system,

C is the ratio $A_V/E(B-V)$, which is thought to be fairly constant with a value of about 3.2 ± 0.1 .

Now, for the Johnson and Cape-Kron standard systems, the effective wavelengths of the various filters are:

Filter	Effective wavelength
B	4400\AA
V	5500\AA
R	7000\AA
I	9000\AA
R_{kc}	6700\AA
I_{kc}	8100\AA

Now, Scheffler (1982), gives,

$$A_R/A_V \simeq 0.73 ,$$

$$A_I/A_V \simeq 0.52 ,$$

$$A_{R(kc)}/A_V \simeq 0.78 ,$$

$$A_{I(kc)}/A_V \simeq 0.62$$

Substituting these values into equation 4.14, assuming a value of 3.2 ± 0.1 for C, yields,

$$E(V-R) \simeq (0.86 \pm 0.03).E(B-V) ,$$

$$E(V-I) \simeq (1.54 \pm 0.05).E(B-V) ,$$

$$E(V-R)_{kc} \simeq (0.70 \pm 0.02).E(B-V) ,$$

$$E(V-I)_{kc} \simeq (1.22 \pm 0.04).E(B-V)$$

CHAPTER 5

YY CETI

5.1. INTRODUCTION:

Within our original sample of 16 systems with orbital periods in the range 0.4-0.8 day, light curves of EW or EB/EA type, and spectral types of F or later, YY Cet was just included with a period of 0.79 day. Prior to this investigation, no spectroscopic work had been reported and only a limited amount of photometry had been published.

An ephemeris for the system was published by Strohmeier and Knigge (1969) using a period found by Markworth. A list of times of minima were given by Strohmeier (1967), and Williamon (1977, 1978) reported a complete photoelectric light curve. Wolf and Kern (1983) published $uvby\beta$ indices of YY Cet in their survey of southern-hemisphere eclipsing binaries.

5.2. BVRI_c PHOTOMETRY:

The photoelectric observations were obtained at Sutherland, SAAO, by Dr.D.J.King during October 1982, by Dr.D.Kilkenny during January 1983, and by the author during November 1983, using the 0.5m telescope equipped with a Peoples photometer. The two-channel photometer employed a blue-sensitive EMI6256 tube with an S13

photocathode, and a red-sensitive EMI9659 tube with an extended S20 photocathode, both housed in their own cold boxes. The filter change mechanism could be operated manually or be controlled via a NOVA minicomputer. For our purposes, only the red sensitive tube was used together with a set of BVRI_c filters (Cousins, 1980). The data were acquired automatically via the NOVA controlled system, and written to disk, tape and printer.

Because of the rapid magnitude variations of the late-type contact and near-contact binaries and the need to obtain a well-resolved light curve in the short time available, the variable and comparison stars were monitored through the V filter only. Observations of the variable through all four filters were taken at regular intervals of approximately 25 minutes (~ 0.02 period) to note any colour changes.

In order to obtain reasonable signal-to-noise ratios during monitoring, integrations were carried out in units of 30 seconds, two consecutive units for comparison star observations alternating with four consecutive units for the variable. The comparison star, HD12383 (V=8.9), and check star, SA0148152 (V=9.1), were chosen since they were both of similar colour to the variable and lay in close proximity to it in the sky, thus virtually eliminating any extinction or second-order colour effects in the calculation of the differential magnitudes. Both stars were found to be constant in brightness to better than 0.01 mag. .

Sets of E and F region standards (Menzies, Banfield and Laing, 1980) were observed at the beginning and end of each night, with red and blue standards being regularly observed throughout the night. In addition to these a local standard, HD10167 (E142, V=6.7), was observed hourly as a check for zero-point drifts and to serve as an additional check star.

All data were reduced via the SAAO photometry reduction package to the instrumental system, the consecutive integrations being averaged to single values. All four-colour observation groups were then transformed to the Cape-Kron standard system (Cousins, 1980).

A computer program, written by the author, and employing the cubic spline function subroutine of Powell (1967), was used to create the differential V-magnitudes by first fitting a spline through the comparison star data for each nights' observations, and then subtracting the relevant values of the fit from the variable star data.

5.3. CORRECTION TO EPHEMERIS:

A new epoch of primary minimum was established from the observations obtained on 17 October 1982 using the method of Kwee and van Woerden (1956). A linear least-squares solution for the orbital period using all published times of minima (Strohmeier, 1967), shown in Table 5.2, then yielded a revised ephemeris of

$$\text{MJD } 45259.0560^{+0.0006} + 0.7904596^{+0.0000009} E \quad (\text{s.e.})$$

This new determination of the orbital period is slightly longer than the previous published value of 0.790453 days. The (O-C) residuals, calculated using the new ephemeris, indicate that the orbital period has remained constant for the past 50 years. All orbital phases quoted hereafter, are calculated using this revised ephemeris.

The differential V-magnitudes, modified Julian dates and orbital phases are shown in Table 5.1 and in Figure 5.1, while the BVRI_c data are given in Table 5.3 and Figure 5.3. Errors of observation are typically 0.005 mag. for the differential V-magnitudes and 0.01 mag. for the colour indices.

5.4. SPECTROSCOPY:

The spectroscopic observations of YY Cet were obtained by Dr.D.J.King during the period 15-22 November 1983 at Sutherland, SAAO, with the RPCS/ITS spectrograph and reticon detector system at the f/18 Cassegrain focus of the 1.9m telescope. Grating 3 was used, providing 30Å per mm in the blue region of the second-order spectrum. Spectra centred at about 4200Å with a useful range of approximately 500Å were obtained, using integration times of typically 1000s (~1.5% of orbital period) and a slit width of 200μm. Integrations on the star were alternated with 100s comparison-source exposures (a Cu-Ar lamp). On most nights, four radial-velocity standard stars were observed, covering a spectral range F2V to M1.5V.

The spectra were initially stored on cartridges by the NOVA 3/12 minicomputer controlling the RPCS and then written to magnetic tape in FITS format (Wells, Greisen and Harten, 1981) at Cape Town. The data were later processed on a VAX 11/750 at the University of Durham, using the SPICA package to flat field the spectra, and convert them to a form suitable for the spectroscopic image-processing package, REDUCE (Hill, Fisher and Poeckert, 1982b), which was run on a VAX 11/780 at the University of St. Andrews.

5.5. SPECTROSCOPIC ANALYSIS:

In addition to the 37 spectrograms of YY Cet, a total of 19 spectrograms of 11 radial-velocity standard stars, selected from the lists of Evans et al. (1957, 1959, 1964), were obtained. The comprehensive REDUCE package was used to measure the comparison spectra, and rectify and linearise (in $\ln \lambda$) the stellar spectra.

The standard star spectra were then measured using the cross-correlation program VCROSS (Hill, 1982b). The spectra were cross-correlated against several comparison stars of various spectral types, the best results being obtained with a G0V standard, HD283, using a single Gaussian profile. The mean residual, in the sense standard minus observed, was $-1.6 \pm 6.8(\text{sd})$ km/sec. The results indicated no hour angle dependence or other peculiarities.

The variable star data were cross-correlated against the F2V standard star HD29875, since this was found to produce the most well-defined peaks in the cross-correlation functions. Gaussian profiles were fitted by least squares to the resultant cross-correlation functions, a double Gaussian fit being adopted for the double-lined phases. The resultant velocities for the primary and secondary components, together with times of observations, are presented in Table 5.4 and Figure 5.4 .

It should be noted that it is only by careful use of the cross-correlation technique that we have been able to detect the secondary spectrum at all. With a magnitude difference in the blue region of ~ 2.7 mag. it is not possible to consider individual absorption line measurements without spectra obtained at much higher resolution and much higher S/N ratio.

The greater scatter of the radial velocities of the secondary component around second quadrature results from the fact that the peaks of the cross-correlation functions due to the secondary component were much less well-defined here than at first quadrature. The reason for this effect is unclear. (Perhaps it may be the result of atmospheric disturbance on one side of the secondary component.) The effects of rotational distortion can be seen to either side of the primary eclipse of the radial-velocity curve.

Since the secondary minimum of the differential V-magnitude curve occurs at exactly phase 0.5, and the radial-velocity curve of the primary component appears to be fairly sinusoidal in form (allowing for the rotational distortion effects), it is reasonable to assume a circular orbit.

Initial attempts at finding the orbital elements from the primary and secondary radial-velocity curves using the method of Irwin (1973) were unsatisfactory since the results were found to be very sensitive to the selection of the secondary component data points. This problem probably arises from the large scatter of the radial velocity data for the secondary component around second quadrature. To overcome this difficulty, the Lehman-Filhes method was applied to the radial-velocity curve of the primary component, assuming a circular orbit, to derive values for the systemic velocity, V_o , and the semi-amplitude, K_{pr} . (See Figure 5.4). Using these values, together with the measured radial velocities for the secondary component around first quadrature (i.e. between phase 0.17 and 0.27), the spectroscopic mass ratio was obtained. Since good agreement exists between the spectroscopic and photometric mass ratios, values of the velocity semi-amplitude K_{sec} of the secondary component, and the minimum masses and separations, were calculated using an average of the ratios, in order to minimise errors. These results are given in Table 5.5. (Also, see Appendix 5.1.)

The rms scatter of the radial velocities of the primary component about the adopted radial velocity curve provides a realistic estimate of the external error of these measurements, for the secondary component, the external error is worse by a factor of $\sqrt{3}$ (cf. Table 5.5).

No attempt has been made in this analysis to correct for the effects on the radial velocity curve of the mutual irradiation and distortion of the components. According to Hutchings (1973), velocity semi-amplitudes are systematically overestimated by up to 15 per cent for very distorted systems. Effects of spectral line blending act in the opposite sense (eg. Hilditch 1973). It would appear that the net result of the systematic errors involved in determining semi-amplitudes of velocity curves from these spectra lies within the rms errors of determining individual radial velocities.

A computer program written by Dr. R.W. Hilditch, based on the binary model of Napier (1981), was used to estimate the expected rotational distortion through the primary eclipse of the radial-velocity curve. The calculations involved the various stellar parameters found in the analysis, and assumed a circular orbit, and a synchronously rotating primary component. (See Figure 5.4.)

5.6. PHOTOMETRIC ANALYSIS:

The differential V-magnitude light curve of YY Cet, shown in Figure 5.1, exhibits rounded maxima and widely differing depths of minima, implying a significant temperature difference between the components. An examination of the radial-velocity curves and the various colour indices demonstrates that primary eclipse is due to the transit of the cooler, less massive secondary component across the face of the hotter primary. In turn, the flat secondary minimum of the light curve suggests that the smaller secondary undergoes a total eclipse by the larger primary component.

It was noted that during the observation of secondary eclipse the sensitivity of the photometer increased at a very considerable rate, probably due to the dissipation of moisture on the photocathode tube. However, the fact that this drift has little effect on the differential magnitudes is evident from the flat secondary minimum. The local standard HD10167 was observed during the eclipse, and there was no difficulty in transforming to the standard system. Although the colour indices are unaffected by the increasing photometer response, the standard V-magnitudes, as shown in Table 5.3, are clearly in error.

The temperature of the primary component was estimated by examining the Cape-Kron colour indices observed during secondary eclipse, since it may be assumed that these are due to the primary-component light alone. These indices were then transformed to the Johnson (1966) BVRI system using the conversion formulae of

Cousins (1980). The $uvby\beta$ indices of Wolf and Kern (1983), together with the empirical calibrations of Crawford (1979), allowed an estimate of the interstellar reddening, (see Appendix 5.2). The de-reddened BVRI colours suggested a temperature of about 7500K, i.e. a spectral type of about A8, for the averted hemisphere of the primary component.

Since the comparison star was chosen so that any extinction or second-order colour effects could be ignored, the light curve could be analysed on the instrumental system without the need for transformation to the standard system. The differential V-magnitude light curve was analysed using the light curve analysis program LIGHT (Hill, 1979).

All attempts at finding a solution to the light curve were sought with the primary-component temperature fixed at 7500K. Initial attempts, solving for primary and secondary radii, secondary temperature, inclination and mass ratio, indicated that the secondary component was oversized for its main-sequence radius. A solution was finally obtained with the secondary-component radius at its Roche limit value, the corresponding mass ratio being close to the spectroscopic value. The results of the light-curve analysis are shown in Table 5.6, and demonstrate that the primary component lies well within its Roche lobe. (The V-magnitude residuals of the fit are shown in Figure 5.2.)

With the luminosity ratio from the LIGHT solution, values of the absolute visual magnitudes and luminosities of the primary and secondary components were estimated using the Wolf and Kern $uvby\beta$ indices and the calibrations of Crawford (1979), (see Appendices 5.3,5.4). These were in good agreement with an independent estimate of the absolute visual magnitudes from the de-reddened BVRI indices. The final values for the masses, radii, luminosities, magnitudes and reddening for the components of YY Cet are given in Table 5.7. A comparison of these data with the mass-radius and mass-luminosity data for main-sequence detached binaries (Popper, 1980) clearly demonstrates that while the primary component lies within the main-sequence band, the secondary component lies above it, being oversized and overluminous (~ 1.0 bol.mag.) for its mass, (see Figures 5.5,5.6).

The system is therefore composed of a normal main-sequence primary component which lies well within its limiting Roche surface, and an evolved secondary component which, within errors of observation, fills its Roche lobe completely. This semi-detached, Algol-type system has a rather high mass ratio in comparison with the classical Algol types ($q \sim 0.22$), but in other respects is very similar.

5.7. DISCUSSION:

The evolved secondary component strongly suggests that at some time in the past the binary has undergone a phase of mass reversal, the present secondary being the remnant of the former primary component.

The total angular momentum of YY Cet, (orbit + spin), is estimated to be of the order of $(1.8_{-0.3}^{+0.3}) \times 10^{45} \text{ kg m}^2 \text{ s}^{-1}$, (Appendix 5.6). A rough estimate of the angular momentum losses required for the system to come into contact, assuming that the mass ratio remains constant, is shown in Appendix 5.7. (The assumption of constant mass ratio seems perfectly reasonable, because, if the separation between the components were to decrease so that contact were achieved, very little of the total mass of the secondary component would be transferred across the inner Lagrangian point.) As explained in Appendix 5.7, the assumption of constant mass ratio also allows the errors on the angular momentum loss required for contact to be kept to a minimum, since the stellar masses remain constant.

Any angular momentum loss from the binary by magnetic braking must originate from the magnetic field of the secondary component since the primary has a radiative atmosphere, and should thus possess no magnetic field of any significance. Rough estimates of the rate of this angular momentum loss, on the basis of the equations of Vilhu (1982), are shown in Appendix 5.8. These vary between about $-2 \times 10^{35} \text{ kg m}^2 \text{ s}^{-1} \text{ yr}^{-1}$ with an α exponent of 1, to,

$-3 \times 10^{36} \text{ kg m}^2 \text{ s}^{-1} \text{ yr}^{-1}$ with an α of 3, and, with perhaps the most likely value of $\alpha=1.5$, the resultant angular momentum loss is $-(3.7_{-0.6}^{+0.6}) \times 10^{35} \text{ kg m}^2 \text{ s}^{-1} \text{ yr}^{-1}$. The corresponding estimates for the expected timescales for the binary to evolve into contact by this process are calculated in Appendix 5.9. These range from 1×10^9 years, with $\alpha=1$, 5×10^8 years, with $\alpha=1.5$, to 7×10^7 years, when $\alpha=3$. However, the primary component, with a mass of $(1.84_{-0.26}^{+0.26}) M_{\odot}$, is expected to evolve from the main-sequence within 0.6×10^9 to 1.4×10^9 years, Iben (1967).

If contact is achieved before the primary component evolves from the main-sequence, then the result would appear to be a W-type W UMa binary with an unevolved primary component. If, on the other hand, contact is achieved by the nuclear evolution of the primary rather than by magnetic braking alone, then the formation of an evolved A-type W UMa system should result. Indeed, such a scenario has already been proposed by Tapia and Whelan (1975) as a possible formation mechanism for the A-type W UMa star ϵ CrA. If this scenario is correct, then we have an alternative evolutionary path to the A-type W UMa binaries which does not involve a passage through the unevolved W-type phase. Unfortunately, no firm prediction can be made as to which evolutionary path the binary will follow. The error on the primary-component mass gives rise to a wide range of possible main-sequence lifetimes, while the parameter α , which determines the rate of angular-momentum loss by magnetic braking, is not known with any great certainty. In addition to this, we must bear in mind the alteration to Vilhu's expression for the rate of angular momentum loss by magnetic braking, which we assumed in Appendix 5.8, and the simplistic manner in which the

angular momentum loss requirements, in Appendix 5.7, have been estimated.

A binary, very similar to YY Cet, has been analysed by Kaluzny and Semeniuk (1984). They found the system, EG Cep, to be semi-detached, with a mass-ratio between 0.45 and 0.50 . EG Cep is apparently composed of an unevolved primary component of mass $1.8 M_{\odot}$, and an evolved secondary component, which completely fills its Roche lobe. The stars appear to be closer together than those of YY Cet, with mass transfer taking place from the secondary to the primary component. EG Cep is expected to evolve into contact in the near future.

Table 5.1. Differential V-magnitudes of YY Cet.

MJD	PHASE	Diff. Mag. (v-c)	MJD	PHASE	Diff. Mag. (v-c)
45000.0+			45000.0+		
257.92343	0.5672	1.228	260.01782	0.2168	1.025
257.94864	0.5991	1.157	260.02139	0.2213	1.008
257.97037	0.6266	1.095	260.02625	0.2274	1.013
257.97821	0.6365	1.087	260.03308	0.2361	1.020
257.98239	0.6418	1.075	260.03662	0.2406	1.003
257.98666	0.6472	1.078	260.04037	0.2453	1.011
257.99237	0.6544	1.072	260.05804	0.2677	1.011
258.00009	0.6642	1.075	260.06372	0.2749	1.029
258.00400	0.6691	1.064	260.06702	0.2790	1.019
258.00781	0.6740	1.051	260.07040	0.2833	1.033
258.02094	0.6906	1.038	260.07581	0.2901	1.024
258.02640	0.6975	1.025	260.08102	0.2967	1.029
258.03006	0.7021	1.025	260.08420	0.3008	1.030
258.03354	0.7065	1.022	260.08749	0.3049	1.033
258.04645	0.7228	1.003	260.09885	0.3193	1.053
258.05286	0.7309	1.013	260.10367	0.3254	1.048
258.05682	0.7360	1.014	260.10696	0.3296	1.073
258.06064	0.7408	1.003	261.92505	0.6296	1.089
258.93140	0.8424	1.058	261.93130	0.6375	1.082
258.95651	0.8741	1.115	261.93582	0.6432	1.075
258.96280	0.8821	1.136	261.94009	0.6486	1.078
258.96725	0.8877	1.160	261.94641	0.6566	1.068
258.97116	0.8927	1.166	261.95038	0.6616	1.063
258.97916	0.9028	1.203	261.95496	0.6674	1.058
258.98532	0.9106	1.251	262.94827	0.9241	1.334
258.98907	0.9153	1.274	262.95410	0.9314	1.381
258.99295	0.9202	1.308	262.95767	0.9360	1.413
259.00833	0.9397	1.463	262.96109	0.9403	1.447
259.01428	0.9472	1.531	262.96609	0.9466	1.504
259.01794	0.9519	1.581	262.97137	0.9533	1.572
259.02219	0.9572	1.633	262.97510	0.9580	1.627
259.02841	0.9651	1.733	262.98022	0.9645	1.747
259.03467	0.9730	1.823	263.05450	0.0585	1.464
259.03864	0.9780	1.892	263.05838	0.0634	1.421
259.04260	0.9831	1.959	263.06241	0.0685	1.377
259.06296	0.0088	2.029	263.07346	0.0824	1.280
259.06900	0.0164	1.973	263.07880	0.0892	1.235
259.07346	0.0221	1.889	263.08270	0.0941	1.228
259.07800	0.0278	1.816	263.08612	0.0985	1.203
259.08301	0.0342	1.733	263.09088	0.1045	1.167
259.08932	0.0422	1.623	265.92920	0.6952	1.046
259.09293	0.0467	1.584	265.95065	0.7223	1.008
259.09650	0.0512	1.533	265.95462	0.7274	1.012
259.96701	0.1525	1.064	265.95929	0.7333	0.997
259.98843	0.1796	1.066	265.96411	0.7394	1.000
259.99231	0.1845	1.040	265.96899	0.7455	1.003
259.99582	0.1890	1.028	265.97250	0.7500	0.998
260.00876	0.2053	1.044	265.97614	0.7546	0.998
260.01437	0.2124	1.026	265.98721	0.7686	1.017

(continued).

Table 5.1. Differential V-magnitudes of YY Cet (continued).

MJD	PHASE	Diff. Mag. (v-c)	MJD	PHASE	Diff. Mag. (v-c)
45000.0+			45000.0+		
265.99222	0.7749	1.014	667.94165	0.2758	1.013
265.99570	0.7793	1.008	667.94574	0.2810	1.017
265.99982	0.7845	1.027	667.95142	0.2882	1.026
266.00391	0.7897	1.015	667.95966	0.2986	1.032
266.01129	0.7991	1.011	667.96417	0.3043	1.046
266.01453	0.8031	1.008	667.96863	0.3099	1.043
266.01813	0.8077	1.039	667.98047	0.3249	1.060
266.03653	0.8310	1.051	667.98785	0.3342	1.058
266.04279	0.8389	1.043	668.81519	0.3809	1.115
266.04651	0.8436	1.056	668.82220	0.3898	1.131
266.05118	0.8495	1.058	668.82648	0.3952	1.138
266.05624	0.8559	1.068	668.83228	0.4025	1.162
266.06332	0.8649	1.098	668.84436	0.4178	1.197
266.06720	0.8698	1.082	668.84894	0.4236	1.218
266.07101	0.8746	1.108	668.85315	0.4289	1.229
266.07611	0.8811	1.139	668.87598	0.4578	1.258
266.95755	0.9962	2.039	668.88025	0.4632	1.260
266.96252	0.0024	2.045	668.88501	0.4692	1.281
266.96786	0.0092	2.050	668.89532	0.4823	1.318
266.97159	0.0139	2.008	668.89966	0.4878	1.319
266.97549	0.0189	1.970	668.90350	0.4926	1.320
266.98172	0.0267	1.857	668.90717	0.4973	1.319
267.04367	0.1051	1.190	668.91101	0.5021	1.316
267.04916	0.1121	1.160	668.91461	0.5067	1.314
267.05289	0.1168	1.129	668.91882	0.5120	1.326
267.05765	0.1228	1.124	668.92261	0.5168	1.319
267.06281	0.1293	1.101	668.92706	0.5224	1.310
267.06866	0.1367	1.093	668.93225	0.5290	1.304
267.07272	0.1419	1.086	668.93677	0.5347	1.293
267.07672	0.1469	1.076	668.94043	0.5393	1.274
347.82950	0.3061	1.027	668.95050	0.5521	1.232
347.83691	0.3155	1.046	668.95526	0.5581	1.246
347.86029	0.3451	1.063	668.95911	0.5630	1.234
348.80240	0.5369	1.288	668.96362	0.5687	1.220
348.81000	0.5466	1.266	668.96912	0.5756	1.207
348.83551	0.5788	1.192	668.97314	0.5807	1.180
348.84341	0.5888	1.174			
351.80920	0.3408	1.072			
351.81580	0.3492	1.084			
667.87878	0.1963	1.042			
667.88623	0.2057	1.028			
667.89038	0.2109	1.033			
667.89636	0.2185	1.015			
667.90430	0.2285	1.015			
667.90894	0.2344	1.004			
667.91473	0.2417	1.021			
667.92303	0.2522	1.014			
667.92743	0.2578	1.019			
667.93323	0.2651	1.008			

Table 5.2. Times of minima of YY Cet and their residuals.

Ephemeris: $MJD = 45259.0560_{-0.0006}^{+0.0006} + 0.7904596_{-0.0000009}^{+0.0000009} E$

Time of minimum (MJD)	ΔMJD	$\Delta MJD/\text{period}$	Cycle No.	Residual (cycles)	
27333.034	17926.022	22677.973	-22678.0	-0.021	
27343.006	17916.050	22665.358	*
27397.808	17861.248	22596.028	-22596.0	+0.022	
27416.810	17842.246	22571.989	-22572.0	-0.009	
27416.854	17842.202	22571.934	-22572.0	-0.052	**
27420.763	17838.293	22566.988	-22567.0	-0.009	
36484.983	8774.073	11099.963	-11100.0	-0.029	
36485.019	8774.037	11099.918	-11100.0	-0.065	**
38001.913	7257.143	9180.916	-9181.0	-0.066	
38521.996	6737.060	8522.966	-8523.0	-0.027	
38710.851	6548.205	8284.048	-8284.0	+0.038	
38728.811	6530.245	8261.327	*
38737.779	6521.277	8249.981	-8250.0	-0.015	
39053.931	6205.125	7850.022	-7850.0	+0.017	
39378.051	5881.005	7439.982	-7440.0	-0.014	
39442.860	5816.196	7357.993	-7358.0	-0.006	
45259.056	0.000	0.000	0.0	0.000	
45668.910	-409.854	-518.501	518.5	+0.001	

* Data not used in calculation of period since cycle number uncertain.

** Data not used in calculation of period since minimum is covered twice.

Table 5.3. Standard Cape-Kron colour indices of YY Cet.

MJD	PHASE	V	(B-V)	(V-R) _{kc}	(V-I) _{kc}	
45000+						
257.92323	0.5672	10.702	0.290	0.192	0.374	
257.94864	0.5991	10.635	0.291	0.190	0.399	
257.97037	0.6266	10.579	0.300	0.180	0.367	
257.99236	0.6544	10.547	0.301	0.176	0.372	
258.02094	0.6906	10.532	0.294	0.178	0.371	
258.04646	0.7228	10.500	0.284	0.177	0.363	
258.93139	0.8424	10.543	0.300	0.169	0.343	
258.95650	0.8741	10.599	0.301	0.182	0.376	
258.97917	0.9028	10.688	0.313	0.173	0.373	
259.00832	0.9397	10.952	0.310	0.191	0.411	
259.02841	0.9651	11.228	0.322	0.210	0.437	
259.06295	0.0088	11.526	0.375	0.239	0.493	
259.08300	0.0342	11.218	0.328	0.216	0.434	
259.96701	0.1525	10.548	0.294	0.171	0.368	
260.00875	0.2053	10.526	0.292	0.176	0.359	
260.02624	0.2274	10.498	0.279	0.167	0.367	
260.05805	0.2677	10.487	0.286	0.168	0.345	
260.07580	0.2901	10.494	0.278	0.167	0.340	
260.09886	0.3193	10.514	0.271	0.168	0.339	
261.92506	0.6296	10.572	0.296	0.194	0.389	
261.95497	0.6675	10.537	0.296	0.183	0.370	
262.94826	0.9240	10.824	0.308	0.190	0.375	
262.96610	0.9466	11.006	0.319	0.197	0.398	
263.07346	0.0824	10.757	0.302	0.179	0.362	
263.09087	0.1045	10.632	0.280	0.179	0.368	
265.92920	0.6952	10.524	0.301	0.182	0.374	
265.96412	0.7394	10.494	0.290	0.172	0.354	
265.98721	0.7686	10.512	0.279	0.185	0.368	
266.00392	0.7897	10.511	0.278	0.170	0.337	
266.03652	0.8310	10.547	0.289	0.164	0.359	
266.05624	0.8559	10.568	0.289	0.169	0.304	
266.07610	0.8810	10.618	0.286	0.173	0.353	
266.96251	0.0024	11.521	0.366	0.248	0.502	
266.98173	0.0267	11.332	0.342	0.214	0.454	
267.04366	0.1051	10.667	0.292	0.181	0.380	
267.06282	0.1293	10.568	0.280	0.166	0.346	
667.87876	0.1962	10.523	0.287	0.177	0.342	
667.89637	0.2185	10.497	0.289	0.175	0.364	
667.91473	0.2417	10.511	0.283	0.172	0.331	
667.93325	0.2652	10.494	0.291	0.172	0.361	
667.95144	0.2882	10.508	0.298	0.167	0.337	
667.98048	0.3249	10.555	0.306	0.172	0.354	
668.81518	0.3809	11.060	0.301	0.174	0.360	*
668.83227	0.4025	11.079	0.313	0.169	0.338	*
668.89535	0.4823	10.916	0.256	0.140	0.307	*
668.91462	0.5067	10.833	0.268	0.145	0.280	*
668.92705	0.5224	10.776	0.251	0.145	0.289	*
668.95053	0.5521	10.571	0.283	0.158	0.334	*
668.96363	0.5687	10.516	0.297	0.176	0.334	*

* Substantial drift in photometer sensitivity due to moisture on detector. This only affects the standard V-magnitudes, not the colour indices.

Table 5.4. Radial velocities of YY Cet.

Spectrum No.	MJD	Phase	V _{pr} (km s ⁻¹)	V _{sec} (km s ⁻¹)
	45000+			
243/006	653.88618	0.495	-3	
243/008	653.90076	0.513	9	
243/010	653.91880	0.536	21	
243/012	653.93270	0.554	30	
243/015	653.95977	0.588	71	
243/017	653.97645	0.609	90	
243/019	653.99449	0.632	85	-262
243/021	654.01048	0.652	91	-287
243/023	654.02297	0.668	71	-312
243/025	654.04240	0.692	100	-238
243/027	654.05700	0.711	83	-211
243/062	654.45139	0.842 *
243/064	654.96946	0.865	110	-185
243/066	654.99375	0.896	85	
243/080	655.81178	0.931	80	
243/082	655.82704	0.950	67	
243/101	656.79504	0.175	-88	216
243/103	656.80825	0.191	-96	227
243/105	656.82213	0.209	-85	215
243/147	658.90189	0.846	121	-195
243/149	658.91785	0.860	98	-173
243/151	658.93383	0.878	73	
243/153	658.94910	0.900	73	-181
243/168	659.81642	0.997	37	
243/170	659.83169	0.016	-51	
243/172	659.84767	0.037	-60	
243/174	659.86364	0.057	-69	
243/176	659.87893	0.076	-71	207
243/178	659.89489	0.096	-70	198
243/180	659.91016	0.116	-75	201
243/186	659.95390	0.171	-108	184
243/188	659.96920	0.190	-100	218
243/190	659.98516	0.210	-100	215
243/192	660.00043	0.230	-107	222
243/194	660.01641	0.250	-109	192
243/196	660.03237	0.270	-104	244
243/198	660.04697	0.289	-104	244

Spectrum No. indicates RPCS tape/run number.

* Very poor cross-correlation peak. Not used for radial velocity determination.

Table 5.5. Orbital solution for YY Cet.

V_o	$= 3.5 \pm 2.6 \text{ km s}^{-1}$
q	$= 0.49 \pm 0.07$
K_{pr}	$= 109.2 \pm 3.2 \text{ km s}^{-1}$
K_{sec}	$= 214 \pm 18 \text{ km s}^{-1}$
$a_{pr} \sin i$	$= 1.71 \pm 0.05 R_\odot$
$a_{sec} \sin i$	$= 3.34 \pm 0.28 R_\odot$
$M_{pr} \sin^3 i$	$= 1.84 \pm 0.26 M_\odot$
$M_{sec} \sin^3 i$	$= 0.94 \pm 0.11 M_\odot$
$rms(pr)$	$= 13 \text{ km s}^{-1}$

Table 5.6. Light curve solution of YY Cet.

	Primary component	Secondary component
Inclination (deg)		87 ± 1
Mass Ratio		0.52 ± 0.03
Luminosity Ratio *		7.477
Temperature (K)	7500	5314 ± 55
Radius (mean) **	0.413 ± 0.003	0.322 ± 0.003
Radius (polar) **	0.392 ± 0.003	0.302 ± 0.003
Roche lobe radii **	0.437	0.324
β ***	0.25	0.03

* V filter luminosity ratio from the LIGHT solution.

** Unit is semi-major axis of the relative orbit.

*** Prescribed gravity-darkening exponents.

(The solution was not sensitive to the choice of the secondary component gravity-darkening exponent in the range 0.03-0.08 .)

Table 5.7. Astrophysical data for YY Cet.

	Primary component		Secondary component	
Mass (M_{\odot})	$1.84 \begin{smallmatrix} + \\ - \end{smallmatrix} 0.26$		$0.94 \begin{smallmatrix} + \\ - \end{smallmatrix} 0.11$	
Radius (R_{\odot})	$2.09 \begin{smallmatrix} + \\ - \end{smallmatrix} 0.12$		$1.63 \begin{smallmatrix} + \\ - \end{smallmatrix} 0.09$	
Absolute vis.mag.	$1.93 \begin{smallmatrix} + \\ - \end{smallmatrix} 0.12$	*	$4.12 \begin{smallmatrix} + \\ - \end{smallmatrix} 0.12$	**
Absolute bol.mag.	$1.92 \begin{smallmatrix} + \\ - \end{smallmatrix} 0.12$		$3.95 \begin{smallmatrix} + \\ - \end{smallmatrix} 0.12$	***
Luminosity (L_{\odot})	$12.7 \begin{smallmatrix} + \\ - \end{smallmatrix} 1.4$		$2.0 \begin{smallmatrix} + \\ - \end{smallmatrix} 0.2$	
Reddening	$E(B-V) = 0.029 \begin{smallmatrix} + \\ - \end{smallmatrix} 0.002$ (sd)			

* Calculated from equation 2 of Popper (1980) using the primary radius from the LIGHT solution, and the separation from the orbital solution.

** Calculated using the luminosity ratio from the LIGHT solution.

*** Bolometric corrections from Popper (1980).

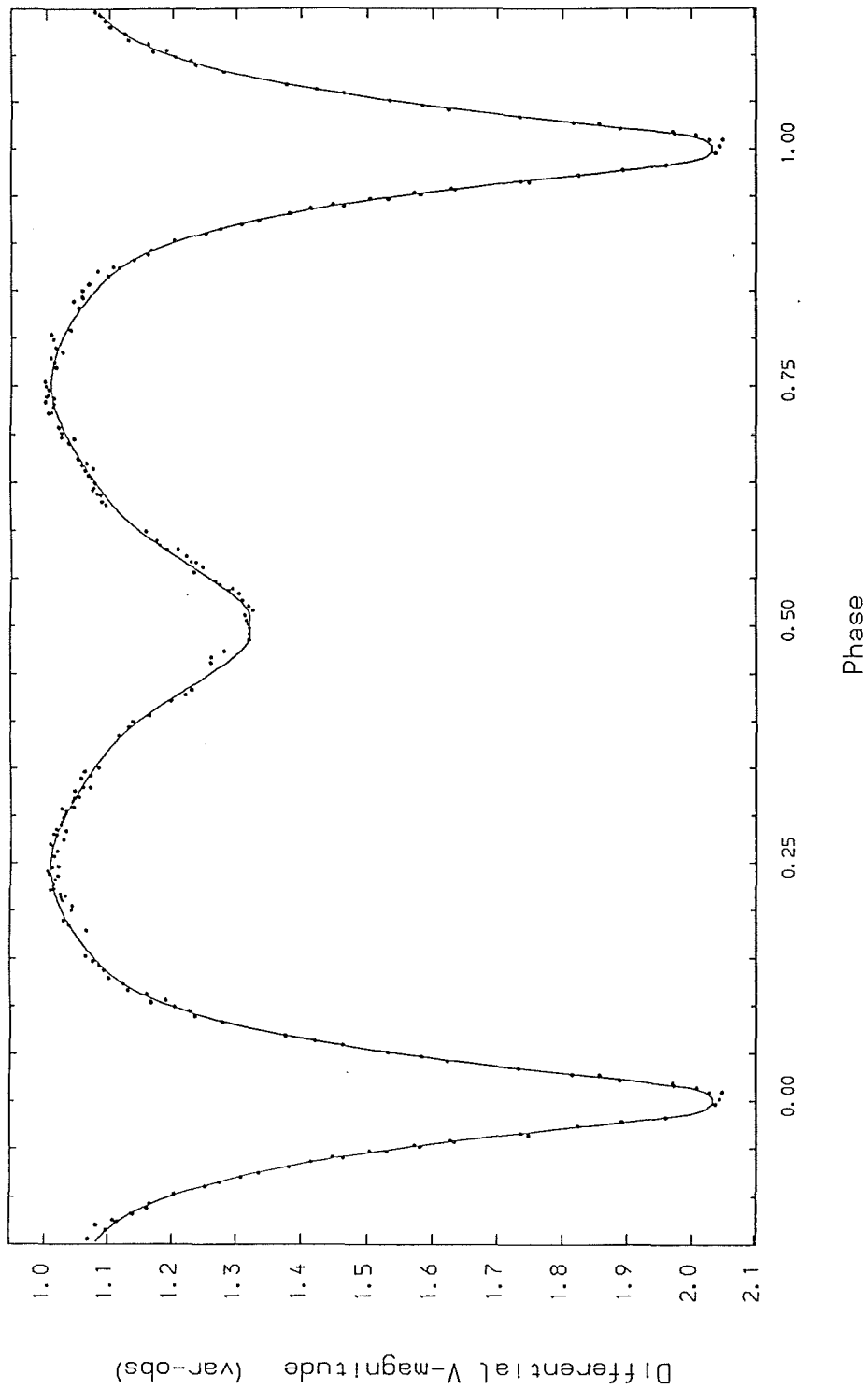


Figure 5.1.
V-light curve of YY Cet showing the individual observations from Table 5.1 and the theoretical light curve from the final model given in Table 5.6.

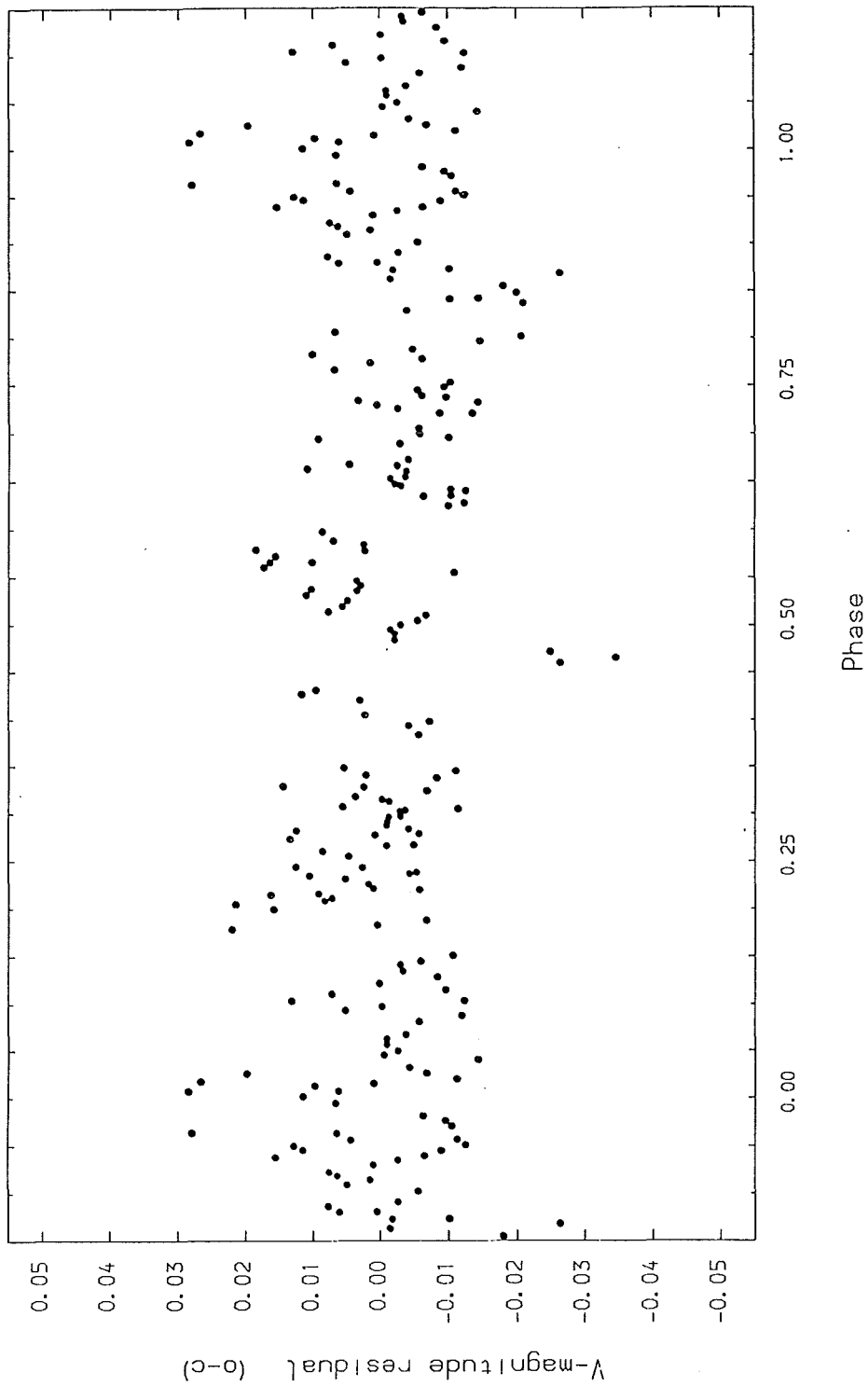


Figure 5.2.
V-magnitude residuals of the model fit shown in Figure 5.1.
Mean Residual = -0.0004, RMS = 0.0103

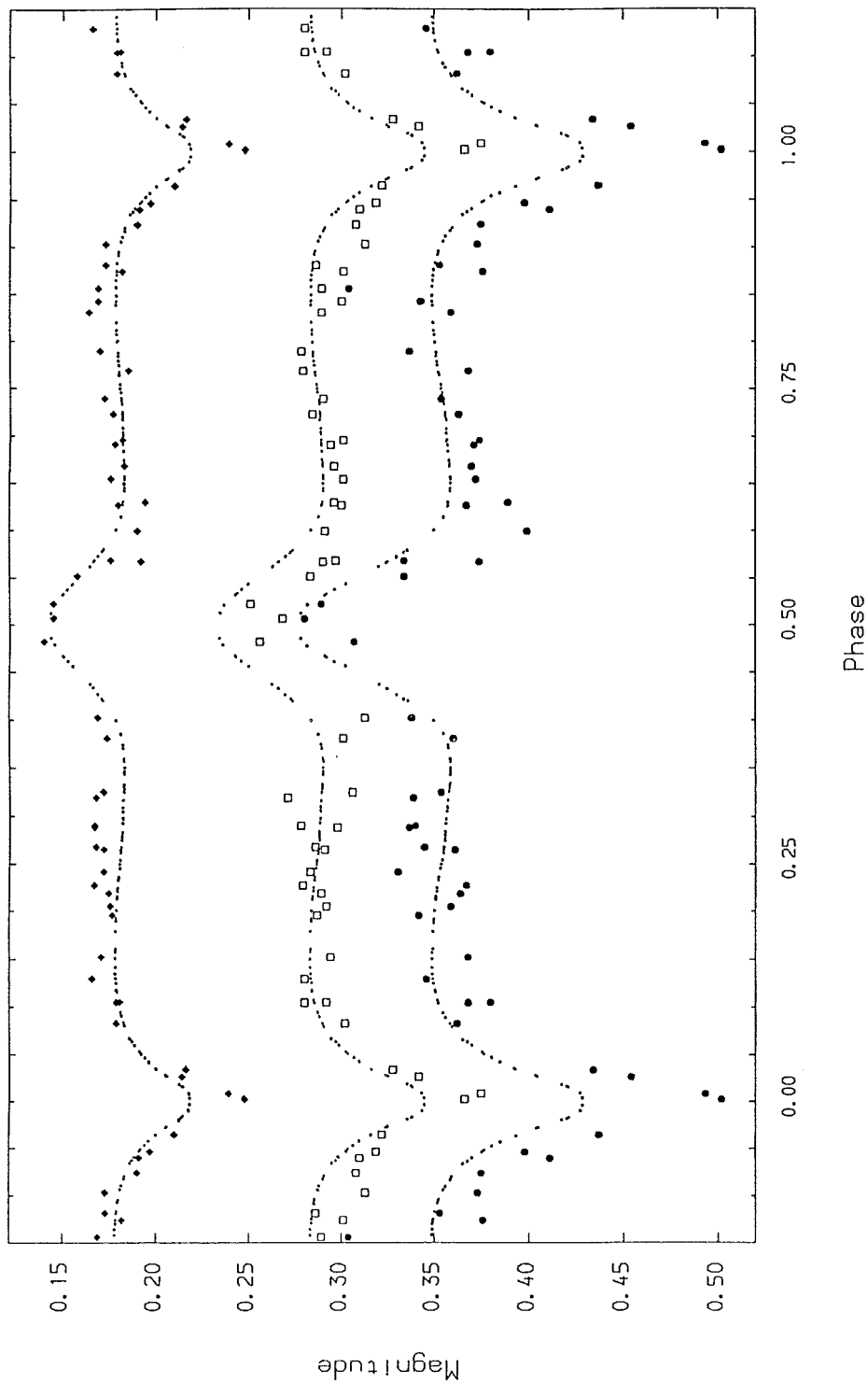


Figure 5.3.
Cape-Kron colour indices of YY Cet plotted against phase. The $(B-V)$, $(V-R)_{kc}$ and $(V-I)_{kc}$ data are open-squares, diamonds and circles, respectively. The expected colour indices, calculated from the LIGHT solution, are shown by the dots (Appendix 5.5).

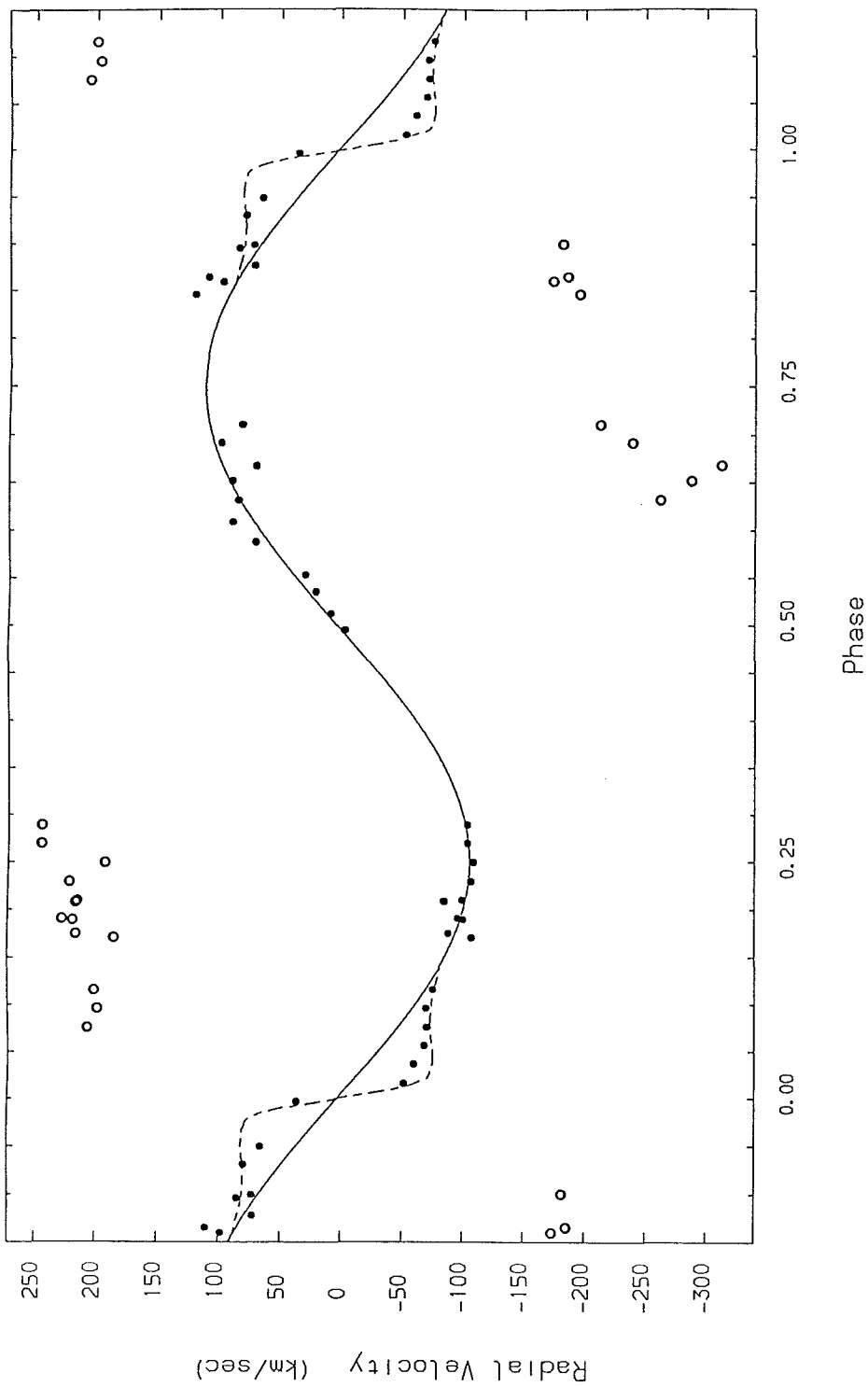


Figure 5.4.

Radial velocities of the primary and secondary components of YY Cet plotted against photometric phase, and the orbital solution for the primary component assuming a circular orbit. The broken line is the expected rotational distortion through primary eclipse of the velocity curve of the primary component, calculated from the final parameters of the system, assuming a synchronously rotating primary.

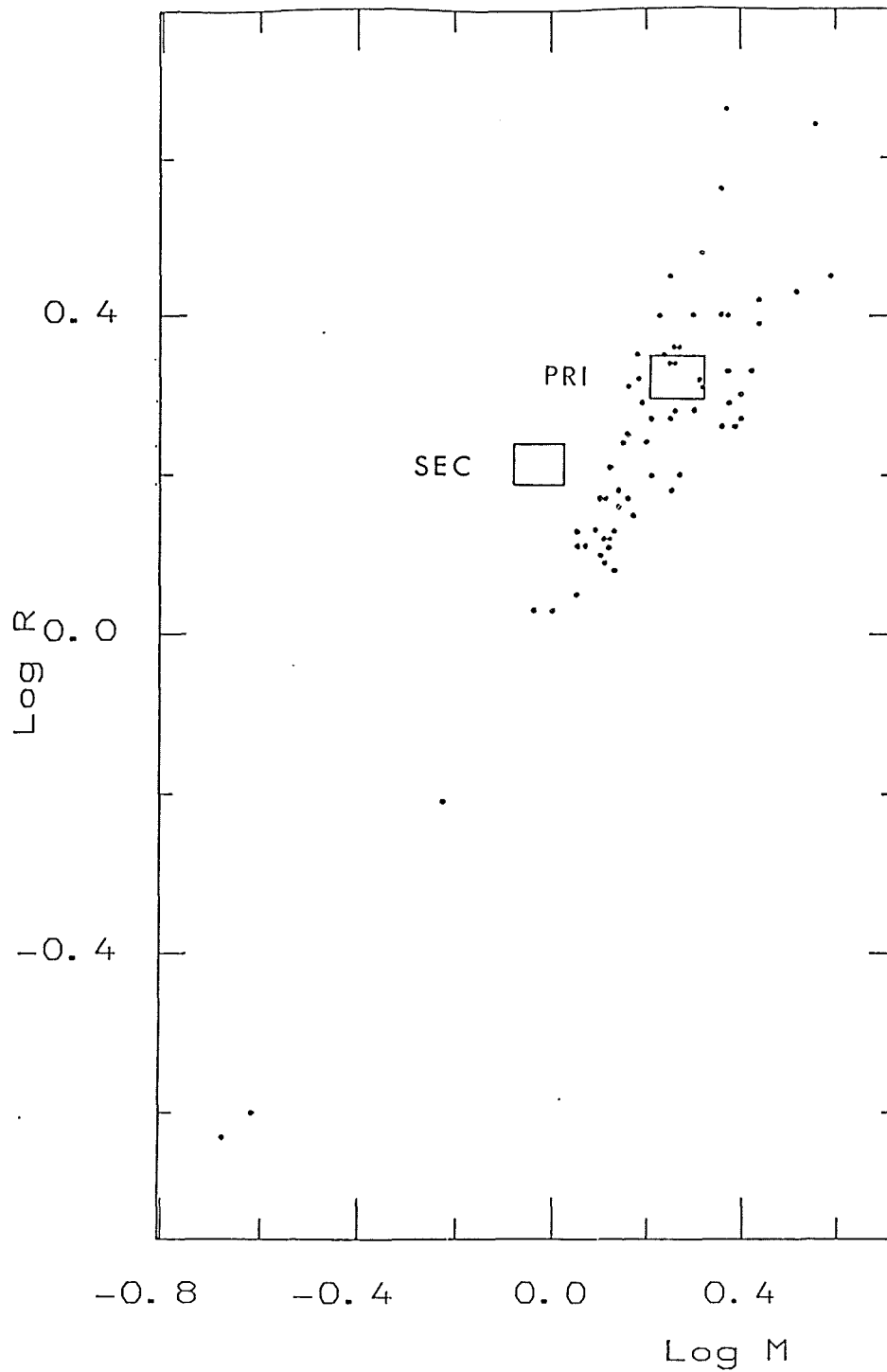


Figure 5.5.

Mass-radii data for the primary and secondary components of YY Cet plotted together with the mass-radii data for main-sequence detached binaries from Popper(1980). While the primary component lies within the main-sequence band, the secondary component lies above it, suggesting that the star is evolved. (See also Figure 5.6.)

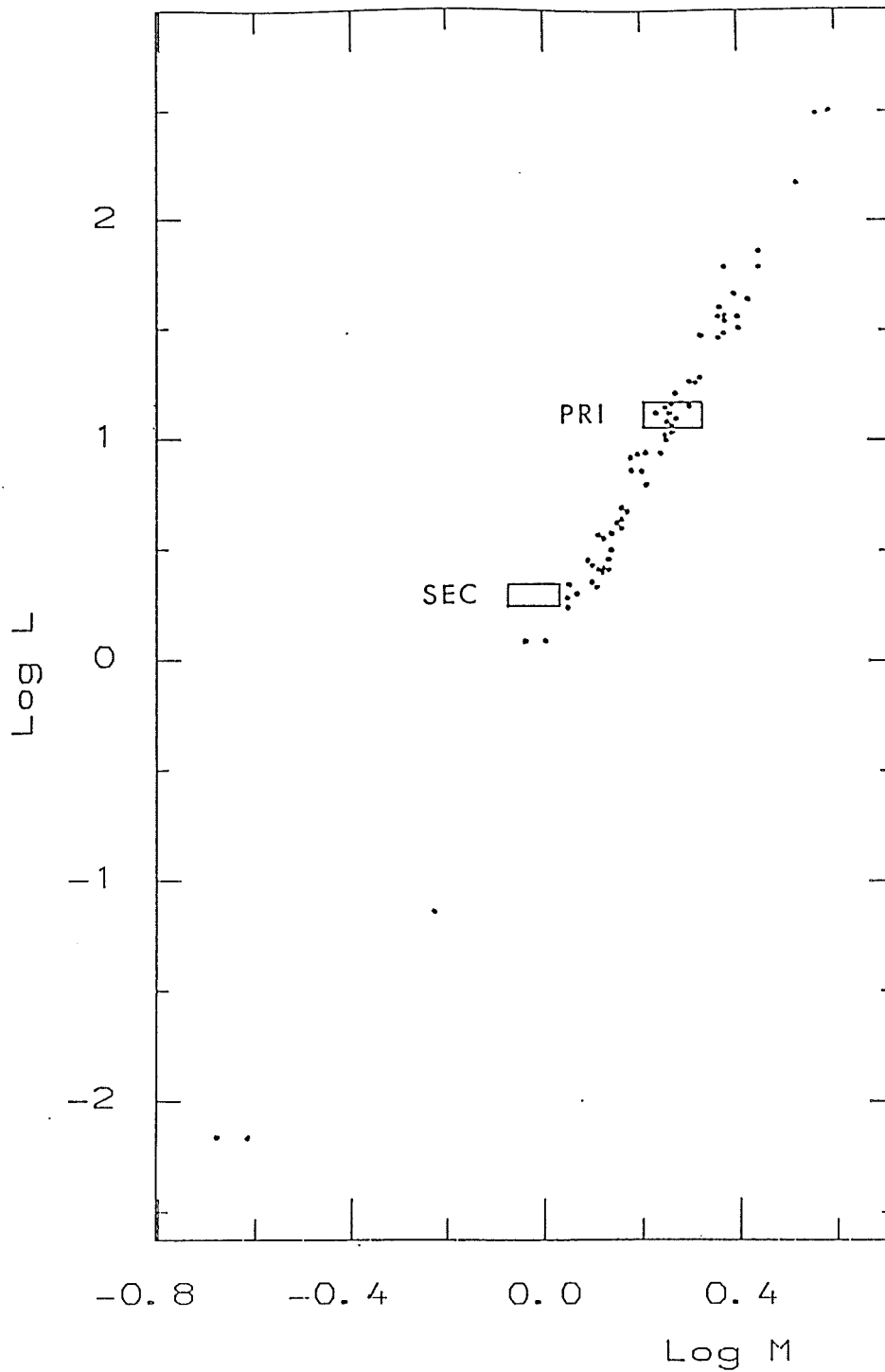


Figure 5.6.
Mass-luminosity data for the primary and secondary components of YY Cet plotted together with the mass-luminosity data for main-sequence detached binaries from Popper(1980). While the primary component lies within the main-sequence band, the secondary component lies above it, indicating that the star is evolved. (See also Figure 5.5.)

Appendix 5.1 Component mass-ratio, minimum masses and separations
calculated from the Lehman-Filhes orbit solution.

From the Lehman-Filhes analysis of the primary component
radial-velocity curve, adopting a circular orbit, we obtained:

Systemic velocity,

$$V_o = (3.5 \pm 2.6) \text{ km s}^{-1}$$

Semi-amplitude of primary component radial-velocity curve,

$$K_{pr} = (109.2 \pm 3.2) \text{ km s}^{-1}$$

Now, removing the contribution of systemic velocity from the
relevant radial velocity data, we obtain:

Spectrum No.	Phase	$ V_{pr_o} $ (km/s)	$ V_{sec_o} $ (km/s)	$ V_{pr_o} / V_{sec_o} $ = q_{spec}
243/101	0.175	91	212	0.429
243/103	0.191	99	224	0.442
243/105	0.209	88	212	0.415
243/186	0.171	111	181	0.613
243/188	0.190	104	214	0.486
243/190	0.210	103	211	0.488
243/192	0.230	111	218	0.509
243/194	0.250	113	189	0.598
243/196	0.270	108	241	0.448
243/198	0.289	108	241	0.448

Thus,

$$q_{\text{spec}} = 0.49 \begin{matrix} + \\ - \end{matrix} 0.07 \quad (\text{s.d.})$$

Now, from equation 3.13,

$$K_{\text{sec}} = K_{\text{pr}}/q_{\text{spec}}$$

However, in addition to the spectroscopic mass ratio, we also have the photometric mass ratio,

$$q_{\text{phot}} = 0.52 \begin{matrix} + \\ - \end{matrix} 0.03$$

Thus, combining the spectroscopic and photometric mass ratios, in order to reduce errors, we have,

$$\begin{aligned} q_{\text{av}} &= [q_{\text{spec}} + q_{\text{phot}}]/2 \\ &= [(0.49 \begin{matrix} + \\ - \end{matrix} 0.07) + (0.52 \begin{matrix} + \\ - \end{matrix} 0.03)]/2 \\ &= 0.51 \begin{matrix} + \\ - \end{matrix} 0.04 \end{aligned}$$

The error on this being given by,

$$\begin{aligned} \sigma(q_{\text{spec}} + q_{\text{phot}}) &= [(\sigma q_{\text{spec}})^2 + (\sigma q_{\text{phot}})^2]^{1/2} \\ &= [(0.07)^2 + (0.03)^2]^{1/2} \\ &= 0.08 \end{aligned}$$

And so,

$$\begin{aligned} \sigma q_{\text{av}} &= \sigma(q_{\text{spec}} + q_{\text{phot}})/2 \\ &= 0.04 \end{aligned}$$

Thus,

$$K_{\text{sec}} = (214 \begin{matrix} + \\ - \end{matrix} 18) \text{ km s}^{-1}$$

The error being,

$$\begin{aligned} \Delta K_{\text{sec}} &= [(\Delta q)^2 + (\Delta K_{\text{pr}})^2]^{1/2} \\ &= [(0.078)^2 + (0.29)^2]^{1/2} \\ &= 0.083 \end{aligned}$$

Calculating the semi-major axes according to equations 3.2 and 3.4, we obtain,

$$\begin{aligned} a_{\text{pr}} \cdot \sin i &= (1.19 \begin{matrix} + \\ - \end{matrix} 0.04) \times 10^6 \text{ km} \\ &= (1.71 \begin{matrix} + \\ - \end{matrix} 0.05) R_{\odot} \end{aligned}$$

and,

$$\begin{aligned} a_{\text{sec}} \cdot \sin i &= (2.33 \pm 0.19) \times 10^6 \text{ km} \\ &= (3.34 \pm 0.28) R_{\odot} \end{aligned}$$

The binary component separation, a , calculated using equations 3.5, and 3.6, is,

$$a \cdot \sin i = (5.05 \pm 0.28) R_{\odot}$$

The component minimum masses, calculated according to equations 3.9 and 3.10, are,

$$M_{\text{pr}} \cdot \sin^3 i = (1.84 \pm 0.26) M_{\odot},$$

and,

$$M_{\text{sec}} \cdot \sin^3 i = (0.94 \pm 0.11) M_{\odot}$$

Appendix 5.2 Interstellar reddening.

Wolf and Kern (1983) uvby β indices are :

MJD	Phase	V	b-y	m_1	c_1	H β
44468.5131	0.768	10.49	0.182	0.170	0.824	2.777
44470.2937	0.147	10.58	0.184	0.152	0.865	2.767

(Phase values calculated according to the new ephemeris.)

From the standard relations for A-type stars from Table 1 of Crawford (1979), using the observed β index, since this is independent of reddening,

$$\beta = 2.777 \Rightarrow b-y = 0.169$$

$$m_1 = 0.195$$

$$c_1 = 0.734$$

$$M_V(\text{ZA}) = 2.83$$

$$\beta = 2.767 \Rightarrow b-y = 0.179$$

$$m_1 = 0.191$$

$$c_1 = 0.714$$

$$M_V(\text{ZA}) = 2.86$$

$$\Rightarrow \delta m_1 = 0.025, 0.039$$

$$\delta c_1 = 0.090, 0.151$$

Now, for $2.880 > \beta > 2.720$, Crawford gives, (if $\delta m_1 > 0$)

$$(b-y)_0 = 2.946 - 1.00\beta_1 - 0.1 \delta c_1 - 0 \delta m_1$$

$$\Rightarrow (b-y)_0 = 0.160, 0.164$$

Now, considering the observed (b-y) values,

$$\Rightarrow \text{Reddening, } E(b-y) = 0.022, 0.020$$

The Johnson colours observed during secondary eclipse are :

MJD	Phase	(B-V)
45668.89535	0.4823	0.256
45668.91462	0.5067	0.268

So, using the standard relation,

$$E(b-y) = 0.74 \times E(B-V),$$

the reddening of the Johnson indices are,

$$\begin{aligned} E(B-V) &= 0.030, 0.027 \\ &= 0.029 \pm 0.002 \text{ (sd)} \end{aligned}$$

Therefore, the dereddened Johnson colours observed during secondary eclipse are,

$$(B-V)_o = 0.226, 0.241$$

Now, removing the reddening from our observed (B-V) indices, which lie nearest in phase to the Wolf and Kern data, we have,

MJD	Phase	(B-V)	(B-V) _o
45265.98721	0.7686	0.279	0.250
45259.96701	0.1525	0.294	0.265

Table 1 of Popper (1980) suggests that for the above values of $(B-V)_o$, we should expect $(b-y)_o$ indices of 0.150 and 0.161, respectively. This shows excellent agreement with the values of 0.160 and 0.164, from the Wolf and Kern data.

Appendix 5.3 Primary component absolute visual magnitude from
uvby β indices.

From Appendix 5.2 :

$$E(b-y) = 0.022, 0.020$$

Also, the standard relations give,

$$E(m_1) = -0.32 \times E(b-y)$$

$$\Rightarrow E(m_1) = -0.007, -0.006$$

$$E(c_1) = 0.20 \times E(b-y)$$

$$\Rightarrow E(c_1) = 0.004, 0.004$$

$$\Rightarrow (m_1)_0 = 0.177, 0.158$$

$$\Rightarrow (c_1)_0 = 0.828, 0.869$$

$$\Rightarrow \delta m_1 = 0.018, 0.033$$

$$\Rightarrow \delta c_1 = 0.094, 0.155$$

Now, Crawford (1979) gives an expression for absolute visual magnitudes, allowing for evolutionary effects, (i.e. the fact that two stars with the same temperature may not have the same luminosity since one may be more evolved than the other),

$$M_V = M_V(\beta, \text{ZAMS}) - f \cdot \delta c_1 ,$$

where the factor 'f' is found from analysis of clusters where A-type stars are evolved away from the ZAMS. This suggests that the value of 'f' is around 9. Thus, substituting the appropriate values for M_V (Appendix 5.2) and δc_1 in the equation, we obtain values for the visual magnitude of the primary component of,

$$M_V = 2.83 - 9 \times 0.094 = 1.98 ,$$

$$M_V = 2.86 - 9 \times 0.155 = 1.47 ,$$

assuming that the secondary component's contribution to the colour indices is negligible.

Appendix 5.4 Component visual and bolometric magnitudes and luminosities.

The dereddened Johnson colours observed during secondary eclipse are,

$$(B-V)_0 = 0.226, 0.241$$

Now, Popper (1980) gives an expression for absolute visual magnitudes,

$$M_V = -5 \log R - 10 F'_V + C_1,$$

(equation 5.0)

where, R is the stellar radius in solar units,

F'_V is the absolute visual flux,

C_1 is a constant. Popper gives it as 42.255 .

Now taking values of,

$$R = 2.09 \begin{matrix} + \\ - \end{matrix} 0.12, \text{ from the analysis,}$$

$$C_1 = 42.255,$$

and,

$$F'_V = 3.874, 3.870, \text{ from Table 1 of Popper (using the values of } (B-V)_0 \text{ above),}$$

we obtain values of the absolute visual magnitude of the primary component of,

$$M_{V \text{ pr}} = 1.91 \begin{matrix} + \\ - \end{matrix} 0.12$$

$$M_{V \text{ pr}} = 1.95 \begin{matrix} + \\ - \end{matrix} 0.12$$

$$\text{ie. } M_{V \text{ pr}} = 1.93 \begin{matrix} + \\ - \end{matrix} 0.12$$

This value is in reasonable agreement with the independent estimates of 1.98 and 1.47, using the uvby β indices (Appendix 5.3).

Table 1 of Popper gives a bolometric correction of -0.01 for the

primary component. This gives a bolometric magnitude for the primary component of,

$$M_{\text{bol pr}} = 1.92 \begin{matrix} + \\ - \end{matrix} 0.12$$

Now, using the luminosity ratio from the LIGHT solution, we can estimate the visual magnitude of the secondary component,

$$\begin{aligned} M_{\text{v sec}} &= (1.93 \begin{matrix} + \\ - \end{matrix} 0.12) + 2.5 \log(7.477) \\ &= 4.12 \begin{matrix} + \\ - \end{matrix} 0.12 \end{aligned}$$

Table 1 of Popper gives a bolometric correction of -0.17 for a star of temperature 5300K. Thus the bolometric magnitude of the secondary component is,

$$M_{\text{bol sec}} = 3.95 \begin{matrix} + \\ - \end{matrix} 0.12$$

Using Popper's value of 4.69 as the bolometric magnitude of the Sun, we obtain the primary component luminosity,

$$\begin{aligned} L_{\text{pr}} &= 10^{0.4(4.69 - (1.92 \pm 0.12))} L_{\odot} \\ &= 12.7 \begin{matrix} + \\ - \end{matrix} 1.4 L_{\odot} \end{aligned}$$

Similarly, for the secondary component luminosity,

$$\begin{aligned} L_{\text{sec}} &= 10^{0.4(4.69 - (3.95 \pm 0.12))} L_{\odot} \\ &= 2.0 \begin{matrix} + \\ - \end{matrix} 0.2 L_{\odot} \end{aligned}$$

Appendix 5.5 Expected colours of YY Cet.

From the V-magnitude light curve solution we have,

$$T_{\text{eff pr}} = 7500 \text{ K ,}$$

$$T_{\text{eff sec}} = 5314 \pm 55 \text{ K .}$$

Using the tables of Johnson (1966),

$$T_{\text{eff pr}} = 7500 \text{ K } \Rightarrow (B-V)_o = 0.234$$

$$(V-R)_o = 0.230$$

$$(V-I)_o = 0.348$$

$$T_{\text{eff sec}} = 5314 \text{ K } \Rightarrow (B-V)_o = 0.790$$

$$(V-R)_o = 0.618$$

$$(V-I)_o = 1.023$$

Converting the colour indices from the Johnson standard system to the Cape-Kron standard system using the conversion formulae of Cousins (1980),

$$\text{i. e. } (B-V)_{\text{kc}} = (B-V)_j$$

$$(V-R)_{\text{kc}} = 0.715(V-R)_j - 0.02$$

$$(V-I)_{\text{kc}} = 0.77(V-I)_j + 0.01$$

we obtain,

$$T_{\text{eff pr}} = 7500 \text{ K } \Rightarrow (V-R)_{o \text{ kc}} = 0.144$$

$$(V-I)_{o \text{ kc}} = 0.278$$

$$T_{\text{eff sec}} = 5314 \text{ K } \Rightarrow (V-R)_{o \text{ kc}} = 0.422$$

$$(V-I)_{o \text{ kc}} = 0.798$$

In order to estimate the expected colour indices of YY Cet we apply the following equation, derived from elementary formulae by

Skillen (1985),

$$(X-Y)^{\text{tot}} = 2.5 \log [(\text{dex}\{0.4(X-Y)^{\text{pr}}\} + L_x \cdot \text{dex}\{0.4(X-Y)^{\text{sec}}\}) / (1+L_x)]$$

(equation 5.1)

where,

L_x is the component luminosity ratio at wavelength 'x' ,

$(X-Y)^{\text{pr}}$ is the colour index of the primary component
corresponding to wavelengths 'x' and 'y' ,

$(X-Y)^{\text{sec}}$ is the colour index of the secondary component
corresponding to wavelengths 'x' and 'y' ,

$(X-Y)^{\text{tot}}$ is the combined colour index of both components.

Inserting the component colours and the individual V-magnitude luminosity ratios at each phase point given by the LIGHT solution, we obtain the values shown in Figure 5.3.

(The error on the secondary temperature gives rise to errors of about 0.002, 0.001 and 0.004 on the $(B-V)$, $(V-R)_{\text{ke}}$ and $(V-I)_{\text{ke}}$, respectively.)

These values appear to be in reasonable agreement with the observed colour indices (Figure 5.3), except near primary minimum, where the various estimated colours appear to be too blue. The reason for this may be due to the fact that in the previous equation the primary component colours used were those of the component as a whole, whereas in reality only the outer (reddened) limb of the component is visible. This should result in expected colours which are too blue.

However, account has still to be taken for the effects of interstellar reddening.

In Appendix 5.2 the interstellar reddening in $(B-V)$ was estimated to

be,

$$E(B-V) = 0.029 \pm 0.002 ,$$

and, from Appendix 4.2, we have the relationships,

$$E(V-R)_{kc} = (0.86 \pm 0.03) \times E(B-V)$$

$$E(V-I)_{kc} = (1.54 \pm 0.05) \times E(B-V)$$

for the estimated interstellar reddening for $(V-R)_{kc}$ and $(V-I)_{kc}$ respectively.

Inserting the estimated value of $E(B-V)$ in the above equations yields,

$$\begin{aligned} E(V-R)_{kc} &= (0.86 \pm 0.03) \times (0.0285 \pm 0.002) \\ &= 0.025 \pm 0.002 \end{aligned}$$

$$\begin{aligned} E(V-I)_{kc} &= (1.54 \pm 0.05) \times (0.0285 \pm 0.002) \\ &= 0.044 \pm 0.004 \end{aligned}$$

After the corrections are applied, the estimated colour indices show better agreement with the observed data of all three colours around primary minimum, and with the $(B-V)$ data around secondary minimum. However, when the reddening is added the expected colours appear too red around quadrature, and around the secondary minimum of the $(V-R)_{kc}$ data.

Although these results imply that the interstellar reddening may not be as great as that calculated in Appendix 5.2, the excellent agreement between the observed (dereddened) $(B-V)_o$ indices and the $(b-y)_o$ indices of Wolf and Kern, suggest otherwise.

Appendix 5.6 Angular momentum of YY Cet.

An expression for the orbital angular momentum is given by Vilhu (1982) as,

$$J_{\text{orb}} = 1.242 \times 10^{45} \cdot q(1+q)^{-2} \cdot M_{\text{tot}}^{5/3} \cdot P^{1/3} \text{ kg m}^2 \text{ s}^{-1}$$

(equation 5.2)

where, M_{tot} is the total mass of the binary in solar units,

q is the mass ratio (< 1),

P is the period in days.

From the analysis of the spectroscopic and photometric data of YY Cet,

$$M_{\text{pr}} = 1.84 \begin{matrix} + \\ - \end{matrix} 0.26 M_{\odot}$$

$$M_{\text{sec}} = 0.94 \begin{matrix} + \\ - \end{matrix} 0.11 M_{\odot}$$

Thus,

$$M_{\text{tot}} = 2.78 \begin{matrix} + \\ - \end{matrix} 0.28 M_{\odot}$$

The error on this being given by,

$$\begin{aligned} \sigma M_{\text{tot}} &= [(\sigma M_{\text{pr}})^2 + (\sigma M_{\text{sec}})^2]^{1/2} \\ &= [(0.26)^2 + (0.11)^2]^{1/2} M_{\odot} \\ &= 0.28 M_{\odot} \end{aligned}$$

From Appendix 5.1,

$$q_{\text{av}} = 0.51 \begin{matrix} + \\ - \end{matrix} 0.04$$

$$P = 0.7904596 \text{ days}$$

Thus, using the above relation,

$$J_{\text{orb}} = (1.41 \begin{matrix} + \\ - \end{matrix} 0.27) \times 10^{45} \text{ kg m}^2 \text{ s}^{-1}$$

The error on this being,

$$\Delta J_{\text{orb}} = [1^2(\Delta q)^2 + (-2)^2(\Delta(1+q))^2 + (5/3)^2(\Delta M_{\text{tot}})^2 + (1/3)^2(\Delta P)^2]^{1/2}$$

(equation 5.3)

Now, the rotational angular momentum, J_{rot} , of a rigidly rotating

star, is given by,

$$J_{\text{rot}} = (2/5).m.r^2.2\pi.P^{-1} \text{ kg m}^2 \text{ s}^{-1}$$

(equation 5.4)

where, m is the stellar mass in kg. (assuming uniform density),

r is the stellar radii in m. (assuming spherical star),

P is the period in seconds

(Since the contribution of the rotational angular momentum is small in comparison to the orbital angular momentum, then the above assumptions should make little difference to the total angular momentum estimate for the binary.)

From the analysis of YY Cet we have,

$$m_{\text{pr}} = 1.84 \pm 0.26 M_{\odot} = (3.66 \pm 0.52) \times 10^{30} \text{ kg}$$

$$m_{\text{sec}} = 0.94 \pm 0.11 M_{\odot} = (1.87 \pm 0.22) \times 10^{30} \text{ kg}$$

$$r_{\text{pr}} = 2.09 \pm 0.12 R_{\odot} = (1.45 \pm 0.08) \times 10^9 \text{ m}$$

$$r_{\text{sec}} = 1.63 \pm 0.09 R_{\odot} = (1.13 \pm 0.06) \times 10^9 \text{ m}$$

$$P = 6.830 \times 10^4 \text{ s} \quad (\text{assuming synchronous rotation}).$$

Using the above values we obtain,

$$J_{\text{rot pr}} = (2.83 \pm 0.51) \times 10^{44} \text{ kg m}^2 \text{ s}^{-1}$$

$$J_{\text{rot sec}} = (0.88 \pm 0.15) \times 10^{44} \text{ kg m}^2 \text{ s}^{-1}$$

The error on J_{rot} is given by,

$$\Delta J_{\text{rot}} = [(\Delta m)^2 + (2)^2.(\Delta r)^2 + (-1)^2.(\Delta P)^2]^{1/2}$$

(equation 5.5)

The total rotational angular momentum,

$$J_{\text{rot tot}} = J_{\text{rot pr}} + J_{\text{rot sec}}$$

(equation 5.6)

$$= [(2.83 \pm 0.51) + (0.88 \pm 0.15)] \times 10^{44} \text{ kg m}^2 \text{ s}^{-1}$$

$$= (3.7 \pm 0.5) \times 10^{44} \text{ kg m}^2 \text{ s}^{-1}$$

The error on this estimate is given by,

$$\begin{aligned}
\sigma_{J_{\text{rot tot}}} &= [(\sigma_{J_{\text{rot pr}}})^2 + (\sigma_{J_{\text{rot sec}}})^2]^{1/2} \\
&\hspace{15em} \text{(equation 5.7)} \\
&= [(0.51)^2 + (0.15)^2]^{1/2} \times 10^{44} \text{ kg m}^2 \text{ s}^{-1} \\
&= 0.53 \times 10^{44} \text{ kg m}^2 \text{ s}^{-1}
\end{aligned}$$

Thus, the total angular momentum of the system is given by,

$$\begin{aligned}
J_{\text{tot}} &= J_{\text{orb}} + J_{\text{rot tot}} \\
&\hspace{15em} \text{(equation 5.8)} \\
&= [(1.41 \pm 0.27) + (0.37 \pm 0.05)] \times 10^{45} \text{ kg m}^2 \text{ s}^{-1} \\
&= (1.78 \pm 0.27) \times 10^{45} \text{ kg m}^2 \text{ s}^{-1}
\end{aligned}$$

The error on this being,

$$\begin{aligned}
\sigma_{J_{\text{tot}}} &= [(\sigma_{J_{\text{orb}}})^2 + (\sigma_{J_{\text{rot tot}}})^2]^{1/2} \\
&\hspace{15em} \text{(equation 5.9)} \\
&= [(0.27)^2 + (0.05)^2]^{1/2} \times 10^{45} \text{ kg m}^2 \text{ s}^{-1} \\
&= 0.27 \times 10^{45} \text{ kg m}^2 \text{ s}^{-1}
\end{aligned}$$

(n.b. See Appendix B.)

Appendix 5.7 Estimate of angular momentum loss required for contact, assuming constant mass ratio.

The orbital angular momentum of the binary is given by,

$$J_{\text{orb}} = [G \cdot a \cdot (m_{\text{pr}})^2 \cdot (m_{\text{sec}})^2 \cdot (m_{\text{pr}} + m_{\text{sec}})^{-1}]^{1/2} \text{ kg m}^2 \text{ s}^{-1}$$

(equation 5.10a)

where, G is the gravitational constant,

a is the separation in metres,

m_{pr} and m_{sec} are the stellar masses in kg.

The error on the above equation is given by,

$$\Delta J_{\text{orb}} = [0.25x(\Delta a)^2 + (\Delta m_{\text{pr}})^2 + (\Delta m_{\text{sec}})^2 + 0.25x(\Delta(m_{\text{pr}} + m_{\text{sec}}))^2]^{1/2}$$

(equation 5.10b)

The separation, 'a', was found in Appendix 5.1 by the addition of the semi-major axes of the radial velocity curve. So, with an inclination of 87 ± 1 degrees, we have,

$$\begin{aligned} a &= (5.05 \pm 0.28) \times R_{\odot} \\ &= (3.51 \pm 0.19) \times 10^9 \text{ m} \end{aligned}$$

(Estimating the orbital angular momentum of YY Cet using the equation above results in a value of $1.41 \times 10^{45} \text{ kg m}^2 \text{ s}^{-1}$. This cross-checks with the estimate in Appendix 5.6.)

Now, for a very rough estimate of the amount of angular momentum YY Cet would have to lose in order to come into contact, the orbital angular momentum of the system, if it were in contact, must be calculated. (An accurate estimation would have to incorporate mass transfer within the system, mass loss out of the system, changes in the sizes of the stellar radii, and changes in period, etc..)

Assuming the masses and radii of the primary and secondary components remain constant, but that the separation of their centres is small enough to bring them into contact, then,

$$r_{pr} + r_{sec} = a_c, \text{ the separation needed for contact.}$$

(equation 5.11)

So, using the values from the analysis,

$$\begin{aligned} a_c &= [(2.09 \pm 0.12) + (1.63 \pm 0.09)] R_\odot \\ &= [(1.45 \pm 0.08) + (1.13 \pm 0.06)] \times 10^9 \text{ m} \\ &= (2.58 \pm 0.10) \times 10^9 \text{ m} \end{aligned}$$

The error on this being given by,

$$\sigma_{a_c} = [(\sigma_{r_{pr}})^2 + (\sigma_{r_{sec}})^2]^{1/2}$$

(equation 5.12)

$$\begin{aligned} &= [(0.08)^2 + (0.06)^2]^{1/2} \times 10^9 \text{ m} \\ &= 0.10 \times 10^9 \text{ m} \end{aligned}$$

The angular momentum corresponding to this is given by,

$$J_{orb\ c} = [G \cdot a_c \cdot (m_{pr})^2 \cdot (m_{sec})^2 \cdot (m_{pr} + m_{sec})^{-1}]^{1/2}$$

(equation 5.13)

Thus the difference in angular momentum between contact and non-contact states is,

$$\begin{aligned} J_{orb} - J_{orb\ c} &= [G \cdot a \cdot (m_{pr})^2 \cdot (m_{sec})^2 \cdot (m_{pr} + m_{sec})^{-1}]^{1/2} \\ &\quad - [G \cdot a_c \cdot (m_{pr})^2 \cdot (m_{sec})^2 \cdot (m_{pr} + m_{sec})^{-1}]^{1/2} \\ &= [G \cdot (m_{pr})^2 \cdot (m_{sec})^2 \cdot (m_{pr} + m_{sec})^{-1}]^{1/2} \times [a^{1/2} - a_c^{1/2}] \\ &= [G^{1/2} \cdot m_{pr} \cdot m_{sec} \cdot (m_{pr} + m_{sec})^{-1/2}] \times [a^{1/2} - a_c^{1/2}] \end{aligned}$$

(equation 5.14)

It is important to execute the calculation in this manner rather than to calculate the individual angular momentum estimates separately, computing the difference by subtraction, as this would lead to an over-estimation of the error. If no allowance is made

for the assumption of constant mass ratio, i.e. constant m_{pr} and m_{sec} , we are unable to remove the variables pertaining to mass as a common factor, as above. Instead, we must introduce two additional variables corresponding to the masses of the primary and secondary components in their contact configuration. This of course increases the error on the calculation of $J_{orb} - J_{orb c}$.

Now, substituting the relevant values in the above equation, we obtain,

$$J_{orb} - J_{orb c} = (2.01 \pm 0.38) \times 10^{44} \text{ kg m}^2 \text{ s}^{-1}$$

The error estimate on this value was calculated as follows :

$$\begin{aligned} \Delta[G^{1/2} \cdot m_{pr} \cdot m_{sec} \cdot (m_{pr} + m_{sec})^{-1/2}] \\ = [(\Delta m_{pr})^2 + (\Delta m_{sec})^2 + (-1/2)^2 \cdot (\Delta(m_{pr} + m_{sec}))^2]^{1/2} \end{aligned}$$

(equation 5.15)

From Appendix 5.1,

$$\Delta m_{pr} = 0.14, \quad \Delta m_{sec} = 0.12$$

and, from Appendix 5.6,

$$\Delta(m_{pr} + m_{sec}) = 0.10$$

Now, inserting these values in the above expression, we have,

$$\Delta[G^{1/2} \cdot m_{pr} \cdot m_{sec} \cdot (m_{pr} + m_{sec})^{-1/2}] = 0.19$$

Now,

$$\Delta a = 0.054$$

So,

$$\Delta a^{1/2} = 2^{-1/2} \times 0.054 = 0.04$$

And,

$$\Delta a_c = 0.039$$

So,

$$\Delta a_c^{1/2} = 2^{-1/2} \times 0.039 = 0.03$$

Thus,

$$a^{1/2} = (5.93 \pm 0.24) \times 10^4 \text{ m}^{1/2}$$

$$a_c^{1/2} = (5.08 \pm 0.15) \times 10^4 \text{ m}^{1/2}$$

When estimating the error on the $(a^{1/2} - a_c^{1/2})$ term, account must be taken of the fact that 'a' and 'a_c' are not independent of one another. The factor 'a_c' is directly proportional to the sizes of the stellar radii, which in turn are directly proportional to the separation of the stellar centres, 'a'. Thus, if the standard deviation of the above term was taken as,

$$\sigma(a^{1/2} - a_c^{1/2}) = [(\sigma a^{1/2})^2 + (\sigma a_c^{1/2})^2]^{1/2},$$

then no allowance would have been made for this relationship, the error being overestimated. As a more realistic estimate, the error is taken as,

$$\begin{aligned} \Delta(a^{1/2} - a_c^{1/2}) &= \Delta a^{1/2} \\ &= 0.04 \end{aligned}$$

Thus,

$$a^{1/2} - a_c^{1/2} = (8.50 \pm 0.34) \times 10^3 \text{ m}^{1/2}$$

So,

$$\begin{aligned} \Delta(J_{\text{orb}} - J_{\text{orb } c}) &= \\ &= [(\Delta[G^{1/2} \cdot m_{\text{pr}} \cdot m_{\text{sec}} \cdot (m_{\text{pr}} + m_{\text{sec}})^{-1/2}]^2 + (\Delta[a^{1/2} - a_c^{1/2}])^2]^{1/2} \\ & \hspace{15em} \text{(equation 5.17)} \\ &= [(0.19)^2 + (0.04)^2]^{1/2} \\ &= 0.19 \end{aligned}$$

Thus,

$$J_{\text{orb}} - J_{\text{orb } c} = (2.01 \pm 0.38) \times 10^{44} \text{ kg m}^2 \text{ s}^{-1}$$

Appendix 5.8. Estimate of rate of angular momentum loss by magnetic braking.

Vilhu (1982) gives an expression for the angular momentum of a rigid, rotating star,

$$\begin{aligned} J_{\text{rot}} &= K^2 \cdot M \cdot R \cdot V_{\text{rot}} , \\ &= K^2 \cdot M \cdot R^2 \cdot 2 \cdot \pi \cdot P^{-1} \end{aligned}$$

(equation 5.18)

where, K^2 is the gyration constant, (Vilhu uses 0.07),

M is the stellar mass,

R is the stellar radius,

V_{rot} is the stellar rotational velocity,

P is the period.

Vilhu assumes that the rotational velocity follows the 'law' found by Skumanich (1972),

$$\text{i.e. } V_{\text{rot}} \propto t^{1/2} ,$$

where, $t^{1/2}$ is the stellar 'age'.

After calibrating the $t^{1/2}$ formula with Pleiades cluster data, then taking the time-derivative of the J_{rot} formula above, Vilhu derived the relation for the rate of angular momentum loss by magnetic braking of a single main-sequence star of one solar mass :

$$dJ_{\text{rot}}/dt = -2 \times 10^{34} \cdot (P/3)^{-\alpha} \text{ kg m}^2 \text{ s}^{-1} \text{ yr}^{-1}$$

(equation 5.19)

where the period P , is expressed in days.

(See Chapter 1, Section 1.2.2, for a more detailed discussion.)

Now, generalising this for any star, taking into account the mass and radius dependence in the equation for J_{rot} , we assume that,

$$dJ_{\text{rot}}/dt = -2 \times 10^{34} \cdot (P/3)^{-\alpha} \cdot (r/r_{\odot})^2 \cdot (m/m_{\odot}) \text{ kg m}^2 \text{ s}^{-1} \text{ yr}^{-1}$$

(equation 5.20)

Now, any angular momentum loss from the binary by magnetic braking must originate from the magnetic field of the secondary component since the primary component has a radiative atmosphere, and should thus possess no magnetic field of any significance.

From previous analysis, for the secondary component we have,

$$r_{\text{sec}}/r_{\odot} = 1.63 \begin{matrix} + \\ - \end{matrix} 0.09$$

and,

$$m_{\text{sec}}/m_{\odot} = 0.94 \begin{matrix} + \\ - \end{matrix} 0.11$$

The error on equation 5.20 is given by,

$$\begin{aligned} \Delta[dJ_{\text{rot}}/dt] &= [2^2 \cdot (\Delta(r/r_{\odot}))^2 + (\Delta(m/m_{\odot}))^2]^{1/2} \\ &= [4 \cdot (0.06)^2 + (0.12)^2]^{1/2} \\ &= 0.17 \end{aligned}$$

(equation 5.22)

The classical rotation-age dependence ($V_{\text{rot}} \propto t^{1/2}$) suggests a value of 3 for the exponent α , for single solar-type main-sequence stars with rotation periods greater than about 3 days. However, studies suggest that a similar rotation-age dependence exists for periods less than 3 days, but with a value of α of about 1.5, rather than 3. (See Chapter 1, Section 1.2.2.)

Now, substituting the appropriate values in the above equation, using various values of α ,

$$\alpha = 1,$$

$$dJ_{\text{rot}}/dt = -(1.90 \pm 0.32) \times 10^{35} \text{ kg m}^2 \text{ s}^{-1} \text{ yr}^{-1}$$

$$\alpha = 2,$$

$$dJ_{\text{rot}}/dt = -(7.19 \pm 1.22) \times 10^{35} \text{ kg m}^2 \text{ s}^{-1} \text{ yr}^{-1}$$

$$\alpha = 3,$$

$$dJ_{\text{rot}}/dt = -(2.73 \pm 0.46) \times 10^{36} \text{ kg m}^2 \text{ s}^{-1} \text{ yr}^{-1}$$

$$\alpha = 1.5,$$

$$dJ_{\text{rot}}/dt = -(3.69 \pm 0.63) \times 10^{35} \text{ kg m}^2 \text{ s}^{-1} \text{ yr}^{-1}$$

Obviously, the value of the angular-momentum loss rate is very sensitive to the choice of the parameter α .

Appendix 5.9. Estimate of timescale for YY Cet to evolve into contact via magnetic braking.

In order to obtain a rough estimate of the time required for YY Cet to evolve into contact, we assume that all angular momentum lost from the binary is due to magnetic braking alone. In addition to this, any expansion of the primary component due to nuclear evolution, is ignored.

From Appendix 5.7 we obtain the expression for the estimated angular momentum difference between contact and non-contact states (equation 5.14):

$$J_{\text{orb}} - J_{\text{orb c}} = [G^{1/2} \cdot m_{\text{pr}} \cdot m_{\text{sec}} \cdot (m_{\text{pr}} + m_{\text{sec}})^{-1/2}] \times [a^{1/2} - a_c^{1/2}]$$

Also, from Appendix 5.8 we have the expression for the rate of angular momentum loss by magnetic braking (equation 5.20):

$$dJ_{\text{rot}}/dt = -2 \times 10^{34} \cdot (P/3)^{-\alpha} \cdot (r_{\text{sec}}/r_{\odot})^2 \cdot (m_{\text{sec}}/m_{\odot}) \text{ kg m}^2 \text{ s}^{-1} \text{ yr}^{-1}$$

Although we will now use the results from these calculations, it would be inappropriate to apply their original accompanying errors, since common factors may be cancelled out, thereby eliminating some contributing errors. As a simple estimate of the time taken for contact to be achieved, ' T_c ', we divide equation 5.14 by equation 5.20. After common factors have been cancelled, we have:

$$T_c = 5 \times 10^{-35} \cdot G^{1/2} \cdot m_{\odot} \cdot r_{\odot}^2 \cdot (P/3)^{\alpha} \times [m_{\text{pr}} \cdot (m_{\text{pr}} + m_{\text{sec}})^{-1/2} \cdot r_{\text{sec}}^{-2} \cdot (a^{1/2} - a_c^{1/2})] \text{ yr}$$

(equation 5.23)

Note that all factors which lie outside the square brackets in the above equation may be considered error free, allowing them to be disregarded in the estimation of errors.

The error on T_c is given by,

$$\begin{aligned} \Delta T_c &= [(\Delta m_{pr})^2 + (-1/2)^2 \cdot (\Delta(m_{pr} + m_{sec}))^2 \\ &\quad + 2^2 \cdot (\Delta r_{sec})^2 + (\Delta(a^{1/2} - a_c^{1/2}))^2]^{1/2} \end{aligned} \quad (\text{equation 5.24})$$

$$= [(0.14)^2 + (-1/2)^2 \cdot (0.10)^2 + 2^2 \cdot (0.06)^2 + (0.04)^2]^{1/2}$$

$$= 0.20 ,$$

inserting the errors found in previous appendices.

From Appendix 5.7, we have,

$$J_{orb} - J_{orb c} = 2.01 \times 10^{44} \text{ kg m}^2 \text{ s}^{-1}$$

Now, using the results for dJ_{rot}/dt , from Appendix 5.8., we find,

$$\alpha = 1,$$

$$\begin{aligned} T_c &= (1.06 \pm 0.21) \times 10^9 \text{ years.} \\ &\simeq (1.1 \pm 0.2) \times 10^9 \text{ years.} \end{aligned}$$

$$\alpha = 2,$$

$$\begin{aligned} T_c &= (2.80 \pm 0.56) \times 10^8 \text{ years.} \\ &\simeq (2.8 \pm 0.6) \times 10^8 \text{ years.} \end{aligned}$$

$$\alpha = 3,$$

$$\begin{aligned} T_c &= (7.36 \pm 1.47) \times 10^7 \text{ years.} \\ &\simeq (7.4 \pm 1.5) \times 10^7 \text{ years.} \end{aligned}$$

$$\alpha = 1.5,$$

$$\begin{aligned} T_c &= (5.45 \pm 1.09) \times 10^8 \text{ years.} \\ &\simeq (5.5 \pm 1.1) \times 10^8 \text{ years.} \end{aligned}$$

CHAPTER 6

CX AQUARI

6.1. INTRODUCCION:

An ephemeris for CX Aqr was given by Jensch (1934), and times of minima have published by a number of authors, eg. Jensch (1934), Soloviev (1936), Filin (1971), Klimek (1973), Krobusek and Mallama (1975), and Mallama et al. (1977). No previous spectroscopic observations have been reported.

6.2. OBSERVATIONS:

The photometric observations of CX Aqr were obtained by the author, during the period 19-28 October 1984, using the 0.5m telescope at the South African Astronomical Observatory (SAAO). The instrument was equipped with a Peoples Photometer and a set of BVRI_c filters. In order to obtain a well-resolved light curve, the variable and comparison stars were monitored through the V filter only. Observations of the variable star through all four filters were acquired at intervals of approximately 25 minutes (~ 0.03 of the orbital period). The comparison star, HD214156 (V=10.0), and check star, HD214184 (V=9.0), were both found to be constant in brightness to better than 0.015 mag. .

E and F-region standard stars (Menzies et al., 1980) were observed at regular intervals throughout each night, while a local standard, HD212132 (E972, $V=5.622$) was observed hourly to note any zero-point drifts, and to serve as a second check star.

The SAAO photometry reduction package was used to reduce the data to instrumental magnitudes, and transform all four-colour observation groups to the Cape-Kron standard system (Cousins, 1980). The errors of observation were typically 0.007mag. and 0.01mag., for the differential V-magnitudes and the colour indices, respectively.

The spectroscopic observations were obtained by Mr.S.A.Bell and Dr.A.J.Adamson, during the period 25-28 August 1985, at the Observatorio del Roque de los Muchachos, La Palma, using the 2.5m Isaac Newton Telescope equipped with the Intermediate Dispersion Spectrograph (IDS) and Image Photon Counting System (IPCS). The Jobin-Yvon 1200 grating was used in conjunction with Camera 2 of the IDS, providing spectra at a dispersion of 16.7\AA mm^{-1} . The spectra, centred alternately at 4040\AA and 4400\AA , have a useful wavelength range of approximately 480\AA , and were obtained using integration times of typically 500s (~ 0.01 of the orbital period). All stellar integrations were alternated with comparison-source exposures provided by a Cu-Ar lamp. On each night observations of radial-velocity standard stars, covering a range in spectral type of F7 to G8, were obtained for both wavelength ranges.

The spectra were originally stored on disk at the telescope, and later written to magnetic tape. The SPICA package was used to flat-field the data, which were then rectified and linearised (in $\ln\lambda$), by means of the spectroscopic image-processing package REDUCE (Hill, Fisher and Poeckert, 1982b).

6.3. REVISED EPHEMERIS:

Times of two primary minima were obtained from the photometric observations of 20 and 21 October 1984, using the method of Kwee and van Woerden (1956). A revised value for the orbital period was determined by applying a linear least-squares solution to these minima and to the recent times of minima published by Filin (1971), Klimek (1973), Krobusek and Mallama (1975), and Mallama et al. (1977), shown in Table 6.3; the resultant ephemeris is:

$$\text{MJD } 45994.89244 \pm 0.00006 + 0.5559864 \pm 0.000003 \text{ E (s.e.)}$$

Although this new value for the orbital period is in agreement with the value of 0.55599 days obtained by Jensch, the earlier times of minima indicate that there may have been a slight increase in the period over the past 50 years (Table 6.3). All orbital phases quoted in our analysis were calculated using the above ephemeris.

6.4. SPECTROSCOPIC ANALYSIS:

As well as 8 spectrograms of CX Aqr, a total of 16 spectrograms of 5 radial-velocity standard stars, selected from the lists of Batten, Harris, McClure and Scarfe (1983), were acquired.

The radial velocities of the standard stars were measured using the cross-correlation program VCROSS (Hill, 1982b), with each spectrum being cross correlated against all others within its wavelength-range group. The best results were obtained using the G8 standard star, HD213014, as a comparison, the mean radial-velocity residuals, in the sense standard minus observed, being, -0.8 ± 4.2 (sd) km s^{-1} and -0.6 ± 3.9 (sd) km s^{-1} , for the short- and long-wavelength ranges, respectively.

Four spectrograms of CX Aqr were obtained near each quadrature of the orbit. For both wavelength ranges, the variable star data were cross correlated against spectra of the G2V standard star HD32963, since this produced the most clearly defined peaks in the resultant cross-correlation functions (CCFs). The component radial velocities, determined by fitting double Gaussian profiles to the CCFs by least squares, are presented in Table 6.1.

For the late-type contact or near-contact binaries, circular orbits may be safely assumed. Our photometric data tend to confirm that this is indeed the case for CX Aqr, since mid-eclipse of the light curve occurs exactly at phase 0.5. With this assumption, the method of Irwin (1973) was applied to the radial-velocity data to

derive values for the systemic velocity, V_0 , and the velocity semi-amplitudes, K_{pr} and K_{sec} ; weights of 0.5 were assigned to the data for the secondary-component. These values were then used to calculate the spectroscopic mass ratio, and the minimum masses and separations, which are given in Table 6.5. (Details of these calculations are given in Appendix 6.1.) The component radial velocities and the orbital solutions are presented in Figure 6.1.

6.5. PHOTOMETRIC ANALYSIS:

The observed differential V-magnitudes for CX Aqr are given in Table 6.2, and the corresponding light curve is shown in Figure 6.2. The $BVRI_c$ colour indices listed in Table 6.4, together with the radial-velocity data, indicate that the primary minimum of the light curve is due to the eclipse of the hotter, more massive primary component by the smaller and cooler secondary. Since the secondary component appears to undergo a total or near-total eclipse, the colour indices obtained near the secondary minimum of the light curve were used to estimate the temperature of the primary component. From the tables of Popper (1980), these colours suggest a temperature of about 6400K for the averted hemisphere of the primary, assuming that the effects of interstellar reddening are negligible.

The selection of a comparison star of similar colour to the variable and lying in close proximity to it in the sky, enabled the differential V-magnitude data to be analysed on the instrumental system. Solutions to the light curve were sought using Hill's program LIGHT (Hill, 1979), with the primary component temperature

fixed at a value 6400K. Since it was not immediately clear whether the primary component possessed a convective or a radiative atmosphere, both were assumed in the search for a solution to the data.

The best solutions to the light curve were obtained when the mass ratios were set at values of 0.58 and 0.59, for the radiative and convective primary-component cases, respectively. Both adopted solutions indicate that the binary system is semi-detached, with the secondary component completely filling its Roche lobe. Slightly closer fits to the data were obtained at higher values of mass ratio for the convective primary-component case, but these lie well outside the 1σ upper limit of 0.58, determined from the spectroscopy. (Details of the adopted fits are given in Tables 6.6, 6.7 and 6.8 and displayed graphically in Figures 6.2, and 6.3.) Although the depths of both minima are reproduced by the adopted solutions, the fits do not precisely match the data either side of the quadratures. The reason for this is unclear. However, other solutions to the light curve were produced with various values of fixed mass ratio, for both convective and radiative primary cases (Tables 6.6 and 6.7), and all indicated similar semi-detached configurations; we may therefore have some confidence in the nature of the adopted photometric solution. When the mass ratio was treated as a free parameter, the LIGHT code failed to converge to a satisfactory solution.

Values for component masses, radii, luminosities, and absolute visual and bolometric magnitudes, derived from the orbital and photometric solutions, are given in Table 6.9, with details of the calculations given in Appendix 6.2. The expected observed colours from these solutions are calculated in Appendix 6.3, and shown graphically in Figures 6.4 and 6.5.

6.6. DISCUSSION:

There appears to be some discrepancy between the value for the mass ratio derived from the spectroscopy, and that suggested by the photometric solutions. This disagreement probably arises from the paucity of radial-velocity data.

It is clear from Tables 6.6 and 6.7 that the mass ratio does not play a particularly crucial role in determining the quality of fit to the light curve. This may explain why no satisfactory photometric solution could be obtained when the parameter was permitted to vary. We encountered similar problems when analysing the marginal-contact binary RV Crv (McFarlane, Hilditch and King, 1986; Chap. 7). Clearly, if we are forced to treat the mass ratio as a fixed quantity in the search for a photometric solution, then it is important to restrict its range by obtaining good quality spectroscopic observations to complement the photometry.

The physical parameters for CX Aqr, shown in Table 6.9, indicate that while the primary component lies on or near the main-sequence, the secondary component is clearly oversized (by $\sim 70\%$) and overluminous (by ~ 1.7 and 1.6 bol.mag., for the convective and radiative primary component cases, respectively) for its main-sequence mass (cf. data for main-sequence detached binaries compiled by Popper (1980): Figures 6.6, 6.7, 6.8 and 6.9). This strongly suggests that a mass-ratio reversal has occurred in the previous history of the binary, and that the now evolved secondary component was once the more massive star. This Algol-type configuration is similar to that found for the late-type near-contact binary YY Cet (McFarlane, King and Hilditch, 1986; Chap. 5), which is approximately 65% more massive than CX Aqr, and possesses a radiative primary component. The apparent slight increase in the orbital period of CX Aqr may indicate that mass transfer is taking place, from the less massive to the more massive component.

The total angular momentum of CX Aqr, assuming synchronous rotation of the components, is estimated in Appendix 6.4 to be $(7.9 \pm 1.0) \times 10^{44} \text{ kg m}^2 \text{ s}^{-1}$. Very rough calculations of angular-momentum loss via magnetic braking, based on the equations of Vilhu (1982), assuming a value of 1.5 for the exponent α , suggests that the binary may achieve contact within about $(1.3 \pm 0.2) \times 10^8$ years, if the primary component is convective, or within $(4.9 \pm 0.7) \times 10^8$ years, if the primary possesses a radiative atmosphere (see Appendices 6.5, 6.6, and 6.7).

Table 6.1. Radial velocities of CX Aqr.

Spectrum No.	MJD	Phase	V _{pr} (km s ⁻¹)	V _{sec} (km s ⁻¹)	
	46000+				
D231/029	303.04879	0.2517	-89	+215	L
D231/030	303.05573	0.2641	-93	+230	S
D231/034	303.07517	0.2992	-104	+211	S
D231/035	303.08211	0.3116	-89	+182	L
D232/009	303.92450	0.8267	+106	-178	L
D232/010	303.93283	0.8417	+101	-161	S
D233/018	305.00923	0.7777	+121	-204	L
D233/019	305.01686	0.7915	+138	-164	S

Spectrum No. indicates IPCS tape/run number.

L and S indicate long or short wavelength ranges, respectively.

Table 6.2. Differential V-magnitudes of CX Aqr.

MJD	PHASE	Diff. Mag. (v-c)	MJD	PHASE	Diff. Mag. (v-c)
45000.0+			45000.0+		
992.78766	0.2143	0.462	992.85754	0.3400	0.495
992.78802	0.2150	0.439	992.85840	0.3416	0.504
992.78833	0.2155	0.454	992.86023	0.3449	0.501
992.78870	0.2162	0.445	992.86542	0.3542	0.505
992.78955	0.2177	0.447	992.86578	0.3549	0.516
992.79144	0.2211	0.456	992.86615	0.3555	0.512
992.79773	0.2325	0.461	992.86646	0.3561	0.525
992.79803	0.2330	0.461	992.86993	0.3623	0.510
992.79840	0.2337	0.469	992.87030	0.3630	0.512
992.79877	0.2343	0.456	992.87061	0.3635	0.523
992.80157	0.2394	0.470	992.87555	0.3724	0.514
992.80194	0.2400	0.475	992.87592	0.3731	0.521
992.80231	0.2407	0.478	992.87622	0.3736	0.518
992.80261	0.2412	0.478	992.87659	0.3743	0.517
992.80573	0.2468	0.486	992.89465	0.4068	0.564
992.80609	0.2475	0.481	992.89496	0.4073	0.561
992.80640	0.2480	0.480	992.89532	0.4080	0.567
992.80676	0.2487	0.483	992.89569	0.4086	0.566
992.80774	0.2505	0.479	992.89667	0.4104	0.563
992.80963	0.2539	0.475	992.89856	0.4138	0.578
992.81525	0.2640	0.475	992.90338	0.4225	0.610
992.81561	0.2646	0.477	992.90375	0.4231	0.613
992.81592	0.2652	0.476	992.90405	0.4237	0.616
992.81628	0.2658	0.483	992.90442	0.4243	0.617
992.81946	0.2715	0.476	992.90710	0.4292	0.632
992.81982	0.2722	0.480	992.90741	0.4297	0.631
992.82019	0.2729	0.483	992.90778	0.4304	0.628
992.82050	0.2734	0.479	992.90814	0.4310	0.629
992.82361	0.2790	0.477	992.91071	0.4357	0.645
992.82397	0.2797	0.482	992.91107	0.4363	0.643
992.82434	0.2803	0.481	992.91138	0.4369	0.639
992.82465	0.2809	0.480	992.91174	0.4375	0.651
992.83850	0.3058	0.477	992.91260	0.4391	0.646
992.83887	0.3064	0.479	992.91449	0.4425	0.662
992.83923	0.3071	0.476	992.91919	0.4509	0.699
992.83954	0.3077	0.481	992.91956	0.4516	0.700
992.84039	0.3092	0.484	992.91986	0.4521	0.706
992.84229	0.3126	0.480	992.92023	0.4528	0.700
992.84729	0.3216	0.482	992.92303	0.4578	0.732
992.84766	0.3223	0.487	992.92334	0.4584	0.728
992.84802	0.3229	0.482	992.92371	0.4590	0.733
992.84839	0.3236	0.486	992.92407	0.4597	0.735
992.85144	0.3291	0.484	992.92706	0.4651	0.746
992.85181	0.3297	0.485	992.92743	0.4657	0.749
992.85217	0.3304	0.482	992.92773	0.4663	0.763
992.85248	0.3309	0.491	992.92810	0.4669	0.753
992.85651	0.3382	0.489	992.92865	0.4679	0.761
992.85687	0.3388	0.495	992.92969	0.4698	0.771
992.85718	0.3394	0.497	992.93335	0.4764	0.768

(continued).

Table 6.2. Differential V-magnitudes of CX Aqr (continued).

MJD	PHASE	Diff. Mag. (v-c)	MJD	PHASE	Diff. Mag. (v-c)
45000.0+			45000.0+		
992.93365	0.4769	0.769	993.79211	0.0210	1.436
992.93402	0.4776	0.781	993.79242	0.0215	1.423
992.93439	0.4782	0.780	993.79303	0.0226	1.401
992.94049	0.4892	0.799	993.79401	0.0244	1.364
992.94080	0.4898	0.791	993.79919	0.0337	1.236
992.94116	0.4904	0.802	993.79956	0.0344	1.218
992.94153	0.4911	0.815	993.79993	0.0350	1.208
992.94482	0.4970	0.801	993.80023	0.0356	1.219
992.94513	0.4976	0.797	993.80316	0.0408	1.125
992.94550	0.4982	0.795	993.80353	0.0415	1.114
992.94586	0.4989	0.793	993.80383	0.0420	1.102
992.94885	0.5043	0.792	993.80420	0.0427	1.093
992.94922	0.5049	0.812	993.80676	0.0473	1.020
992.94958	0.5056	0.805	993.80713	0.0480	1.011
992.94989	0.5061	0.798	993.80750	0.0486	1.010
992.95282	0.5114	0.788	993.80780	0.0492	0.994
992.95319	0.5121	0.788	993.82098	0.0729	0.832
992.95355	0.5127	0.795	993.82135	0.0735	0.839
992.95392	0.5134	0.786	993.82172	0.0742	0.831
992.95447	0.5144	0.782	993.82202	0.0748	0.819
992.95544	0.5161	0.779	993.82263	0.0758	0.818
992.95947	0.5234	0.788	993.82361	0.0776	0.815
992.95984	0.5240	0.782	993.82776	0.0851	0.689
992.96014	0.5246	0.777	993.82813	0.0857	0.690
992.96051	0.5252	0.768	993.82843	0.0863	0.675
993.76862	0.9787	1.454	993.82880	0.0869	0.671
993.76898	0.9794	1.465	993.83173	0.0922	0.673
993.76929	0.9799	1.479	993.83209	0.0929	0.668
993.76965	0.9806	1.475	993.83240	0.0934	0.667
993.77020	0.9815	1.514	993.83276	0.0941	0.668
993.77124	0.9834	1.530	993.83630	0.1004	0.609
993.77576	0.9915	1.640	993.83667	0.1011	0.612
993.77612	0.9922	1.644	993.83704	0.1018	0.611
993.77649	0.9929	1.658	993.83734	0.1023	0.598
993.77679	0.9934	1.668	993.83832	0.1041	0.598
993.77930	0.9979	1.706	993.84021	0.1075	0.590
993.77960	0.9985	1.706	993.84528	0.1166	0.567
993.77997	0.9991	1.706	993.84558	0.1171	0.565
993.78033	0.9998	1.713	993.84601	0.1179	0.560
993.78314	0.0048	1.684	993.84637	0.1186	0.561
993.78351	0.0055	1.666	993.84991	0.1249	0.555
993.78381	0.0060	1.667	993.85028	0.1256	0.545
993.78418	0.0067	1.656	993.85059	0.1261	0.539
993.78735	0.0124	1.590	993.85095	0.1268	0.546
993.78772	0.0131	1.575	993.85382	0.1319	0.536
993.78802	0.0136	1.565	993.85419	0.1326	0.538
993.78839	0.0143	1.553	993.85449	0.1332	0.534
993.79138	0.0196	1.453	993.85486	0.1338	0.539
993.79175	0.0203	1.436	993.87683	0.1733	0.533

(continued).

Table 6.2. Differential V-magnitudes of CX Aqr (continued).

MJD	PHASE	Diff. Mag. (v-c)	MJD	PHASE	Diff. Mag. (v-c)
45000.0+			45000.0+		
993.87720	0.1740	0.526	994.78436	0.8056	0.485
993.87750	0.1745	0.535	994.79169	0.8188	0.503
993.87787	0.1752	0.523	994.79199	0.8193	0.502
993.87872	0.1767	0.529	994.79236	0.8200	0.500
993.88062	0.1801	0.526	994.79272	0.8207	0.503
993.88635	0.1905	0.500	994.79559	0.8258	0.519
993.88666	0.1910	0.506	994.79596	0.8265	0.507
993.88702	0.1917	0.506	994.79626	0.8270	0.516
993.88739	0.1923	0.498	994.79663	0.8277	0.514
993.89044	0.1978	0.489	994.79962	0.8331	0.519
993.89081	0.1985	0.490	994.79993	0.8336	0.523
993.89117	0.1991	0.484	994.80029	0.8343	0.519
993.89148	0.1997	0.497	994.80066	0.8349	0.523
993.89496	0.2059	0.489	994.80145	0.8364	0.524
993.89532	0.2066	0.485	994.80334	0.8398	0.524
993.89563	0.2071	0.481	994.80823	0.8485	0.541
993.89600	0.2078	0.488	994.80859	0.8492	0.527
993.89685	0.2093	0.489	994.80890	0.8498	0.539
993.89874	0.2127	0.484	994.80927	0.8504	0.531
993.90363	0.2215	0.492	994.81219	0.8557	0.533
993.90399	0.2222	0.494	994.81256	0.8563	0.542
993.90430	0.2227	0.492	994.81293	0.8570	0.539
993.90466	0.2234	0.491	994.81323	0.8575	0.545
993.90765	0.2288	0.482	994.81592	0.8624	0.543
993.90802	0.2294	0.482	994.81628	0.8630	0.552
993.90839	0.2301	0.474	994.81665	0.8637	0.550
993.90869	0.2306	0.481	994.81696	0.8642	0.545
993.91168	0.2360	0.486	994.82867	0.8853	0.574
993.91205	0.2367	0.488	994.82904	0.8860	0.580
993.91235	0.2372	0.491	994.82941	0.8866	0.583
993.91272	0.2379	0.488	994.82971	0.8872	0.577
993.92352	0.2573	0.501	994.83057	0.8887	0.589
993.92389	0.2580	0.498	994.83246	0.8921	0.595
993.92419	0.2585	0.488	994.83722	0.9007	0.649
993.92535	0.2606	0.500	994.83759	0.9013	0.649
993.92725	0.2640	0.492	994.83795	0.9020	0.635
993.93207	0.2727	0.465	994.83826	0.9026	0.645
993.93243	0.2733	0.451	994.84082	0.9072	0.665
993.93280	0.2740	0.481	994.84113	0.9077	0.661
993.93311	0.2745	0.456	994.84149	0.9084	0.658
993.93579	0.2794	0.461	994.84186	0.9090	0.667
993.93616	0.2800	0.471	994.84491	0.9145	0.698
993.93652	0.2807	0.467	994.84521	0.9151	0.706
993.93689	0.2814	0.464	994.84558	0.9157	0.703
994.78064	0.7989	0.491	994.84595	0.9164	0.709
994.78094	0.7995	0.488	994.84674	0.9178	0.732
994.78131	0.8001	0.488	994.84863	0.9212	0.742
994.78168	0.8008	0.488	994.85339	0.9298	0.818
994.78247	0.8022	0.497	994.85376	0.9304	0.822

(continued).

Table 6.2. Differential V-magnitudes of CX Aqr (continued).

MJD	PHASE	Diff. Mag. (v-c)	MJD	PHASE	Diff. Mag. (v-c)
45000.0+			45000.0+		
994.85413	0.9311	0.835	994.91119	0.0337	1.220
994.85443	0.9316	0.831	994.91418	0.0391	1.156
994.85742	0.9370	0.864	994.91455	0.0398	1.154
994.85779	0.9377	0.868	994.91492	0.0404	1.138
994.85809	0.9382	0.883	994.91522	0.0410	1.135
994.85846	0.9389	0.887	994.91638	0.0431	1.112
994.86121	0.9438	0.937	994.91827	0.0465	1.071
994.86157	0.9445	0.947	994.92322	0.0554	0.954
994.86188	0.9450	0.981	994.92358	0.0560	0.951
994.86224	0.9457	0.960	994.92389	0.0566	0.945
994.87262	0.9644	1.207	994.92426	0.0572	0.943
994.87299	0.9650	1.207	994.92719	0.0625	0.871
994.87335	0.9657	1.213	994.92755	0.0632	0.855
994.87372	0.9663	1.238	994.92786	0.0637	0.855
994.87451	0.9678	1.240	994.92822	0.0644	0.855
994.87640	0.9712	1.296	994.93103	0.0694	0.797
994.88110	0.9796	1.457	994.93134	0.0700	0.781
994.88147	0.9803	1.461	994.93170	0.0706	0.783
994.88177	0.9808	1.471	994.93207	0.0713	0.777
994.88214	0.9815	1.485	994.93475	0.0761	0.764
994.88477	0.9862	1.565	994.93512	0.0768	0.762
994.88513	0.9869	1.584	994.93549	0.0774	0.759
994.88550	0.9875	1.582	994.93579	0.0780	0.761
994.88580	0.9881	1.595	46000.0+		
994.88849	0.9929	1.666	000.77360	0.5779	0.625
994.88879	0.9935	1.673	000.77395	0.5785	0.630
994.88916	0.9941	1.693	000.77429	0.5791	0.637
994.88953	0.9948	1.677	000.77464	0.5798	0.624
994.89197	0.9992	1.699	000.77545	0.5812	0.621
994.89233	0.9998	1.706	000.77646	0.5830	0.632
994.89270	0.0005	1.698	000.78014	0.5897	0.576
994.89301	0.0010	1.712	000.78048	0.5903	0.564
994.89563	0.0057	1.670	000.78083	0.5909	0.566
994.89600	0.0064	1.671	000.78118	0.5915	0.568
994.89630	0.0070	1.662	000.78363	0.5959	0.578
994.89667	0.0076	1.655	000.78398	0.5966	0.574
994.89954	0.0128	1.575	000.78433	0.5972	0.578
994.89984	0.0133	1.568	000.78467	0.5978	0.577
994.90021	0.0140	1.560	000.78738	0.6027	0.552
994.90057	0.0146	1.558	000.78773	0.6033	0.556
994.90112	0.0156	1.544	000.78808	0.6039	0.555
994.90210	0.0174	1.505	000.78842	0.6046	0.555
994.90613	0.0246	1.381	000.78926	0.6061	0.565
994.90649	0.0253	1.350	000.79026	0.6079	0.555
994.90686	0.0259	1.352	000.79403	0.6146	0.539
994.90717	0.0265	1.354	000.79437	0.6153	0.538
994.91016	0.0319	1.246	000.79474	0.6159	0.544
994.91052	0.0325	1.243	000.79509	0.6165	0.549
994.91089	0.0332	1.231	000.79789	0.6216	0.539

(continued).

Table 6.2. Differential V-magnitudes of CX Aqr (continued).

MJD	PHASE	Diff. Mag. (v-c)	MJD	PHASE	Diff. Mag. (v-c)
46000.0+			46000.0+		
000.79824	0.6222	0.538	000.86507	0.7424	0.457
000.79859	0.6228	0.540	000.86542	0.7430	0.468
000.79893	0.6235	0.546	000.86576	0.7437	0.462
000.80214	0.6292	0.519	000.86611	0.7443	0.458
000.80249	0.6299	0.524	000.86873	0.7490	0.462
000.80283	0.6305	0.508	000.86907	0.7496	0.462
000.80318	0.6311	0.515	000.86942	0.7502	0.461
000.80596	0.6361	0.536	000.86977	0.7509	0.458
000.80631	0.6367	0.528	000.88582	0.7797	0.502
000.80665	0.6373	0.527	000.88617	0.7804	0.498
000.80700	0.6380	0.527	000.88651	0.7810	0.502
000.80883	0.6413	0.517	000.88686	0.7816	0.504
000.81070	0.6446	0.525	000.88786	0.7834	0.514
000.81509	0.6525	0.492	000.88973	0.7868	0.519
000.81544	0.6531	0.490	000.89514	0.7965	0.510
000.81579	0.6538	0.498	000.89548	0.7971	0.507
000.81613	0.6544	0.490	000.89583	0.7977	0.494
000.81952	0.6605	0.502	000.89618	0.7984	0.504
000.81987	0.6611	0.504	000.89908	0.8036	0.493
000.82022	0.6617	0.504	000.89943	0.8042	0.492
000.82057	0.6624	0.502	000.89978	0.8048	0.493
000.82352	0.6677	0.502	000.90013	0.8055	0.494
000.82386	0.6683	0.496	000.90302	0.8107	0.513
000.82421	0.6689	0.498	000.90337	0.8113	0.508
000.82456	0.6696	0.505	000.90371	0.8119	0.516
000.83412	0.6867	0.491	000.90406	0.8125	0.512
000.83447	0.6874	0.487	000.90526	0.8147	0.497
000.83481	0.6880	0.492	000.90714	0.8181	0.512
000.83516	0.6886	0.493	000.91221	0.8272	0.510
000.83639	0.6908	0.494	000.91256	0.8278	0.507
000.83826	0.6942	0.484	000.91290	0.8284	0.513
000.84354	0.7037	0.464	000.91325	0.8291	0.510
000.84389	0.7043	0.467	000.91618	0.8343	0.526
000.84423	0.7049	0.465	000.91653	0.8350	0.516
000.84458	0.7056	0.461	000.91687	0.8356	0.523
000.84750	0.7108	0.468	000.91722	0.8362	0.528
000.84785	0.7114	0.468			
000.84819	0.7121	0.465			
000.84854	0.7127	0.465			
000.85177	0.7185	0.460			
000.85212	0.7191	0.465			
000.85246	0.7197	0.457			
000.85281	0.7204	0.465			
000.85423	0.7229	0.465			
000.85611	0.7263	0.457			
000.86125	0.7355	0.461			
000.86160	0.7362	0.471			
000.86194	0.7368	0.464			
000.86229	0.7374	0.464			

Table 6.3. Times of minima of CX Aqr and their residuals.

Ephemeris: $\text{MJD} = 45994.89244_{-0.00006}^{+0.00006} + 0.5559864_{-0.0000003}^{+0.0000003} E$

Time of minimum (MJD)	ΔMJD	$\Delta\text{MJD}/\text{period}$	Cycle No.	Residual (cycles)	
19651.771	26343.121	47380.872	-47381	-0.128	
24734.012	21260.880	38239.928	-38240	-0.072	
26265.779	19729.113	35484.884	-35485	-0.116	
26330.778	19664.114	35367.976	-35368	-0.024	
26330.804	19664.088	35367.929	-35368	-0.071	
26512.003	19482.879	35042.006	-35042	+0.006	
26545.918	19448.974	34981.024	-34981	+0.024	
26894.015	19100.877	34354.935	-34355	-0.065	
26928.981	19065.911	34292.045	-34292	+0.045	
26957.900	19036.992	34240.031	-34240	+0.031	
27059.703	18935.189	34056.928	-34057	-0.072	
27280.980	18713.912	33658.938	-33659	-0.062	
27305.989	18688.903	33613.957	-33614	-0.043	
27310.988	18683.904	33604.965	-33605	-0.035	
27324.891	18670.001	33579.959	-33580	-0.041	
27324.920	18669.972	33579.907	-33580	-0.093	
27338.777	18656.115	33554.984	-33555	-0.016	
27339.900	18654.992	33552.964	-33553	-0.036	
27358.803	18636.089	33518.965	-33519	-0.035	
27359.920	18634.972	33516.956	-33517	-0.044	
27366.029	18628.863	33505.968	-33506	-0.030	
27368.808	18626.084	33500.970	-33501	-0.030	
27383.820	18611.072	33473.969	-33474	-0.031	
27393.833	18601.059	33455.960	-33456	-0.040	
27397.724	18597.168	33448.962	-33449	-0.038	
27447.761	18547.131	33358.965	-33359	-0.035	
41160.032	4834.860	8696.004	-8696	+0.004	*
41541.999	4452.893	8008.996	-8009	-0.004	*
42309.264	3685.628	6628.989	-6629	-0.011	*
42343.173	3651.719	6568.001	-6568	+0.001	*
42665.089	3329.803	5989.001	-5989	+0.001	*
45993.78036	1.11208	2.000	-2	0.000	*
45994.89244	0.00000	0.000	0	0.000	*

* Data used in calculation of period.

Table 6.4. Standard Cape-Kron colour indices of CX Aqr.

MJD	PHASE	V	(B-V)	(V-R) _c	(V-I) _c
45000.0+					
992.78975	0.2181	10.541	0.484	0.312	0.629
992.80785	0.2506	10.535	0.491	0.294	0.604
992.84057	0.3095	10.537	0.487	0.306	0.650
992.85857	0.3419	10.562	0.498	0.302	0.616
992.89678	0.4106	10.653	0.485	0.290	0.600
992.91278	0.4394	10.724	0.480	0.276	0.565
992.92842	0.4675	10.822	0.455	0.254	0.552
992.95422	0.5139	10.852	0.436	0.257	0.499
993.76997	0.9811	11.519	0.616	0.337	0.659
993.79277	0.0221	11.489	0.540	0.377	0.723
993.82237	0.0754	10.831	0.488	0.314	0.655
993.83846	0.1043	10.671	0.484	0.315	0.633
993.87890	0.1770	10.573	0.487	0.305	0.611
993.89703	0.2097	10.549	0.484	0.294	0.608
993.92557	0.2610	10.534	0.485	0.300	0.607
994.78267	0.8026	10.539	0.486	0.300	0.605
994.80166	0.8367	10.579	0.487	0.300	0.622
994.83076	0.8891	10.640	0.496	0.293	0.594
994.84693	0.9181	10.770	0.515	0.284	0.598
994.87472	0.9681	11.294	0.575	0.309	0.654
994.90088	0.0152	11.615	0.544	0.382	0.789
994.91641	0.0431	11.171	0.485	0.362	0.694
46000.0+					
000.77508	0.5805	10.668	0.474	0.304	0.594
000.78888	0.6054	10.616	0.492	0.302	0.606
000.80852	0.6407	10.594	0.481	0.309	0.632
000.83638	0.6908	10.545	0.491	0.300	0.632
000.85413	0.7227	10.534	0.490	0.298	0.618
000.88796	0.7836	10.548	0.502	0.293	0.605
000.90526	0.8147	10.566	0.487	0.298	0.616

Table 6.5. Orbital solution for CX Aqr.

$$\begin{aligned}
 V_o &= 13 \begin{matrix} + \\ - \end{matrix} 4 \text{ km s}^{-1} \\
 K_{\text{pr}} &= 112 \begin{matrix} + \\ - \end{matrix} 9 \text{ km s}^{-1} \\
 K_{\text{sec}} &= 205 \begin{matrix} + \\ - \end{matrix} 9 \text{ km s}^{-1} \\
 q &= 0.55 \begin{matrix} + \\ - \end{matrix} 0.03 \\
 a_{\text{pr}} \sin i &= 1.22 \begin{matrix} + \\ - \end{matrix} 0.10 R_{\odot} \\
 a_{\text{sec}} \sin i &= 2.24 \begin{matrix} + \\ - \end{matrix} 0.10 R_{\odot} \\
 M_{\text{pr}} \sin^3 i &= 1.18 \begin{matrix} + \\ - \end{matrix} 0.13 M_{\odot} \\
 M_{\text{sec}} \sin^3 i &= 0.64 \begin{matrix} + \\ - \end{matrix} 0.06 M_{\odot}
 \end{aligned}$$

Table 6.6. Photometric solutions for CX Aqr assuming a convective primary-component atmosphere.

Fixed : $T_{\text{eff pri}} = 6400\text{K}$

$\beta_{\text{pri}} = 0.08, \beta_{\text{sec}} = 0.08$

q	T_{sec} (K)	$R_{\text{mean pri}}$	$R_{\text{mean sec}}$	Incl. (deg.)	χ^2 ($\times 10^{-4}$)	Mean Res. ($\times 10^{-2}$)	rms ($\times 10^{-2}$)
0.47	5192 ⁺²¹ ₋₂₁	0.373 ^{+0.002} _{-0.002}	0.314 ^{+0.002} _{-0.002}	86.6 ^{+0.4} _{-0.4}	11.94	-0.40	2.62
0.48	5143 ⁺²¹ ₋₂₁	0.373 ^{+0.002} _{-0.002}	0.316 ^{+0.002} _{-0.002}	85.9 ^{+0.4} _{-0.4}	11.51	-0.41	2.62
0.49	5255 ⁺¹⁷ ₋₁₇	0.375 ^{+0.002} _{-0.002}	0.318 ^{+0.002} _{-0.002}	86.8 ^{+0.3} _{-0.3}	9.418	-0.36	2.29
0.50	5252 ⁺¹⁶ ₋₁₆	0.375 ^{+0.002} _{-0.002}	0.319 ^{+0.002} _{-0.002}	86.6 ^{+0.3} _{-0.3}	8.260	-0.34	2.18
0.51	5297 ⁺¹⁹ ₋₁₉	0.382 ^{+0.002} _{-0.002}	0.321 ^{+0.002} _{-0.002}	87.2 ^{+0.4} _{-0.4}	11.72	-0.42	2.23
0.52	5304 ⁺²³ ₋₂₃	0.383 ^{+0.002} _{-0.002}	0.323 ^{+0.002} _{-0.002}	86.4 ^{+0.5} _{-0.5}	16.93	-0.46	2.51
0.53	5302 ⁺²⁰ ₋₂₀	0.383 ^{+0.002} _{-0.002}	0.324 ^{+0.002} _{-0.002}	86.5 ^{+0.4} _{-0.4}	13.22	-0.39	2.28
0.54	5299 ⁺¹⁷ ₋₁₇	0.383 ^{+0.002} _{-0.002}	0.326 ^{+0.002} _{-0.002}	86.4 ^{+0.4} _{-0.4}	9.836	-0.33	2.05
0.55	5293 ⁺¹¹ ₋₁₁	0.383 ^{+0.001} _{-0.001}	0.327 ^{+0.001} _{-0.001}	86.8 ^{+0.2} _{-0.2}	4.524	-0.19	1.64
0.56	5295 ⁺¹⁴ ₋₁₄	0.382 ^{+0.002} _{-0.002}	0.328 ^{+0.001} _{-0.001}	86.2 ^{+0.3} _{-0.3}	6.373	-0.27	1.79
0.57	5288 ⁺¹⁰ ₋₁₀	0.382 ^{+0.001} _{-0.001}	0.330 ^{+0.001} _{-0.001}	86.5 ^{+0.2} _{-0.2}	3.484	-0.11	1.53
0.58	5289 ⁺⁹ ₋₉	0.381 ^{+0.002} _{-0.002}	0.332 ^{+0.001} _{-0.001}	86.3 ^{+0.3} _{-0.3}	3.332	-0.08	1.51
0.59	5289 ⁺⁹ ₋₉	0.382 ^{+0.002} _{-0.002}	0.333 ^{+0.001} _{-0.001}	86.2 ^{+0.3} _{-0.3}	3.209	-0.07	1.49
0.60	5287 ⁺¹⁰ ₋₁₀	0.383 ^{+0.003} _{-0.003}	0.333 ^{+0.002} _{-0.002}	86.3 ^{+0.4} _{-0.4}	3.279	0.14	1.49
0.61	5284 ⁺¹⁰ ₋₁₀	0.381 ^{+0.003} _{-0.003}	0.333 ^{+0.002} _{-0.002}	86.2 ^{+0.3} _{-0.3}	3.234	0.11	1.49
0.62	5277 ⁺⁹ ₋₉	0.381 ^{+0.003} _{-0.003}	0.333 ^{+0.002} _{-0.002}	86.2 ^{+0.4} _{-0.4}	3.203	0.06	1.49
0.63	5272 ⁺⁹ ₋₉	0.380 ^{+0.002} _{-0.002}	0.334 ^{+0.002} _{-0.002}	86.0 ^{+0.4} _{-0.4}	3.220	-0.07	1.49
0.64	5265 ⁺⁹ ₋₉	0.381 ^{+0.002} _{-0.002}	0.333 ^{+0.002} _{-0.002}	86.1 ^{+0.4} _{-0.4}	3.208	-0.03	1.50
0.65	5263 ⁺¹⁰ ₋₁₀	0.380 ^{+0.003} _{-0.003}	0.332 ^{+0.002} _{-0.002}	86.1 ^{+0.4} _{-0.4}	3.221	0.03	1.50

Radii measured in units of semi-major axis of the relative orbit.

χ^2 measured in units of magnitude squared.

Mean residual and rms measured in units of magnitude.

Table 6.7. Photometric solutions for CX Aqr assuming a radiative primary-component atmosphere.

Fixed : $T_{\text{eff pri}} = 6400\text{K}$

$\beta_{\text{pri}} = 0.25, \beta_{\text{sec}} = 0.08$

q	T_{sec} (K)	$R_{\text{mean pri}}$	$R_{\text{mean sec}}$	Incl. (deg.)	χ^2 ($\times 10^{-4}$)	Mean Res. ($\times 10^{-2}$)	rms ($\times 10^{-2}$)
0.47	4929 ⁺¹⁷ ₋₁₇	0.375 ^{+0.001} _{-0.001}	0.314 ^{+0.001} _{-0.001}	87.3 ^{+0.3} _{-0.3}	7.245	-0.49	2.15
0.48	4936 ⁺¹⁶ ₋₁₆	0.376 ^{+0.001} _{-0.001}	0.316 ^{+0.001} _{-0.001}	87.1 ^{+0.3} _{-0.3}	6.388	-0.44	2.04
0.49	4990 ⁺³² ₋₃₂	0.377 ^{+0.005} _{-0.005}	0.318 ^{+0.005} _{-0.005}	85.7 ^{+0.9} _{-0.9}	23.13	-0.40	2.92
0.50	4984 ⁺¹⁵ ₋₁₅	0.378 ^{+0.001} _{-0.001}	0.319 ^{+0.001} _{-0.001}	86.9 ^{+0.3} _{-0.3}	6.258	-0.18	1.92
0.51	5001 ⁺²⁶ ₋₂₆	0.377 ^{+0.004} _{-0.004}	0.321 ^{+0.004} _{-0.004}	85.7 ^{+0.8} _{-0.8}	15.85	-0.26	2.50
0.52	5000 ⁺²⁹ ₋₂₉	0.375 ^{+0.005} _{-0.005}	0.323 ^{+0.005} _{-0.005}	85.4 ^{+0.9} _{-0.9}	13.87	-0.27	2.39
0.53	4987 ⁺¹⁶ ₋₁₆	0.374 ^{+0.003} _{-0.003}	0.324 ^{+0.002} _{-0.002}	85.9 ^{+0.5} _{-0.5}	5.169	-0.16	1.82
0.54	4982 ⁺¹⁷ ₋₁₇	0.374 ^{+0.003} _{-0.003}	0.326 ^{+0.002} _{-0.002}	85.7 ^{+0.5} _{-0.5}	4.657	-0.14	1.76
0.55	4976 ⁺¹⁶ ₋₁₆	0.374 ^{+0.003} _{-0.003}	0.327 ^{+0.002} _{-0.002}	85.6 ^{+0.4} _{-0.4}	4.277	-0.11	1.71
0.56	4976 ⁺¹⁶ ₋₁₆	0.373 ^{+0.002} _{-0.002}	0.328 ^{+0.002} _{-0.002}	85.5 ^{+0.3} _{-0.3}	4.113	-0.10	1.69
0.57	4975 ⁺¹⁶ ₋₁₆	0.372 ^{+0.002} _{-0.002}	0.330 ^{+0.002} _{-0.002}	85.3 ^{+0.2} _{-0.2}	3.914	-0.08	1.66
0.58	4968 ⁺¹⁵ ₋₁₅	0.372 ^{+0.002} _{-0.002}	0.332 ^{+0.002} _{-0.002}	85.2 ^{+0.2} _{-0.2}	3.746	-0.03	1.65
0.59	4964 ⁺¹⁵ ₋₁₅	0.371 ^{+0.002} _{-0.002}	0.333 ^{+0.002} _{-0.002}	85.1 ^{+0.2} _{-0.2}	3.762	-0.07	1.65
0.60	4958 ⁺¹⁵ ₋₁₅	0.371 ^{+0.002} _{-0.002}	0.332 ^{+0.002} _{-0.002}	85.1 ^{+0.2} _{-0.2}	3.774	-0.07	1.65
0.61	4958 ⁺¹⁵ ₋₁₅	0.370 ^{+0.002} _{-0.002}	0.333 ^{+0.002} _{-0.002}	85.0 ^{+0.2} _{-0.2}	3.840	-0.13	1.65

Radii measured in units of semi-major axis of the relative orbit.

χ^2 measured in units of magnitude squared.

Mean residual and rms measured in units of magnitude.

Table 6.8. Adopted photometric solutions for CX Aqr.

	Radiative primary component:		Convective primary component:	
	Primary component	Secondary component	Primary component	Secondary component
Inclination (deg)		85.2 ⁺ ₋ 0.2		86.2 ⁺ ₋ 0.3
Mass Ratio *1		0.58		0.59
Luminosity Ratio *2		4.884		4.075
Temperature (K)	6400	4969 ⁺ ₋ 15	6400	5289 ⁺ ₋ 9
Radius (mean) *3	0.372 ⁺ ₋ 0.002	0.332 ⁺ ₋ 0.002	0.382 ⁺ ₋ 0.002	0.333 ⁺ ₋ 0.001
Radius (polar) *3	0.357 ⁺ ₋ 0.002	0.312 ⁺ ₋ 0.002	0.365 ⁺ ₋ 0.002	0.313 ⁺ ₋ 0.001
β *4	0.25	0.08	0.08	0.08
Roche lobe radii *3	0.427	0.333	0.425	0.334

*1 Fixed.

*2 V filter luminosity ratio at first quadrature from the LIGHT solution.

*3 Unit is semi-major axis of the relative orbit.

*4 Prescribed gravity-darkening exponents.

Table 6.9. Astrophysical data for CX Aqr.

	Radiative primary component:		Convective primary component:	
	Primary component	Secondary component	Primary component	Secondary component
Mass (M_{\odot})	1.19 ⁺ ₋ 0.13	0.64 ⁺ ₋ 0.06	1.19 ⁺ ₋ 0.13	0.64 ⁺ ₋ 0.06
Radius (R_{\odot})	1.29 ⁺ ₋ 0.05	1.15 ⁺ ₋ 0.05	1.33 ⁺ ₋ 0.05	1.16 ⁺ ₋ 0.05
Absolute vis.mag.	3.64 ⁺ ₋ 0.09 *	5.36 ⁺ ₋ 0.09 **	3.57 ⁺ ₋ 0.08 *	5.10 ⁺ ₋ 0.08 **
Absolute bol.mag.	3.61 ⁺ ₋ 0.09	5.04 ⁺ ₋ 0.09 ***	3.54 ⁺ ₋ 0.08	4.88 ⁺ ₋ 0.08 ***
Luminosity (L_{\odot})	2.70 ⁺ ₋ 0.22	0.72 ⁺ ₋ 0.06	2.88 ⁺ ₋ 0.21	0.84 ⁺ ₋ 0.06

* Calculated from equation 2 of Popper (1980) using the primary radius from the LIGHT solution, and the separation from the orbital solution.

** Calculated using the luminosity ratio from the LIGHT solution.

*** Bolometric corrections from Popper (1980).

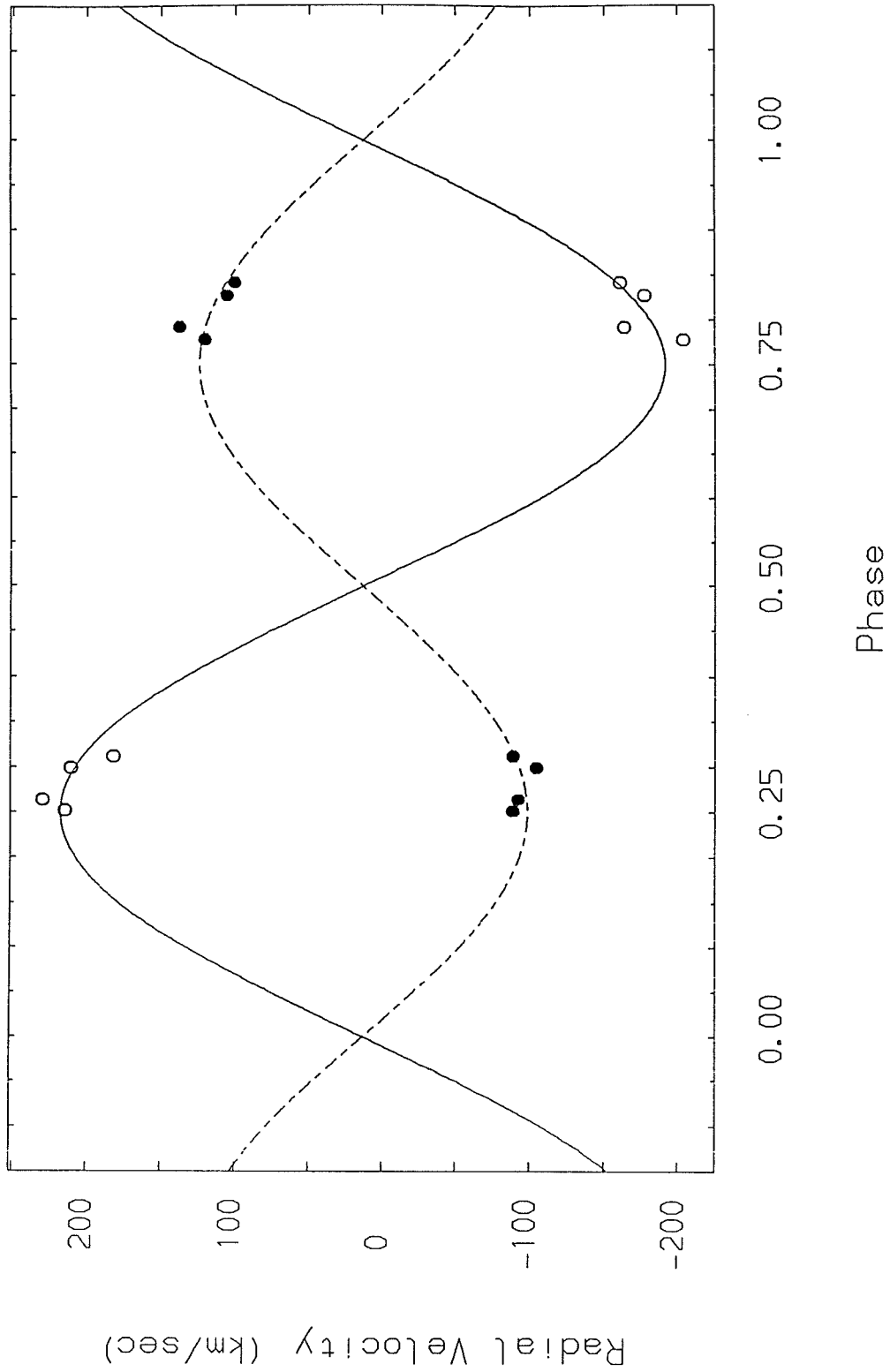


Figure 6.1.
 Radial velocities of the primary and secondary components of CX Aqr (closed and open circles, respectively) plotted against photometric phase, together with their orbital solutions.

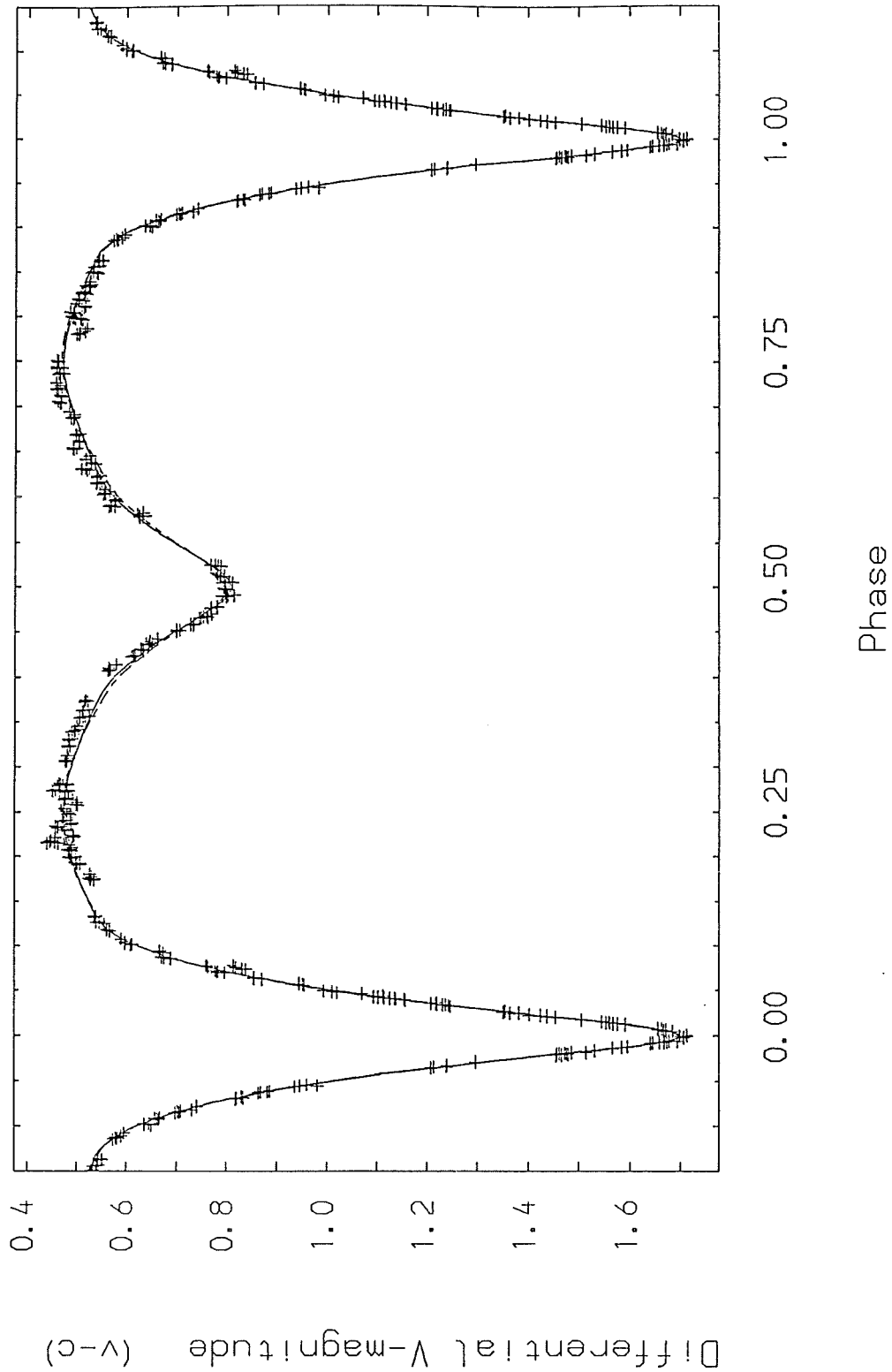


Figure 6.2.

V-light curve of CX Aqr showing the individual observations from Table 6.2. and the adopted theoretical light curves from the final models given in Table 6.8 . The solutions employing the radiative and convective primary components are given by the broken and solid lines, respectively.

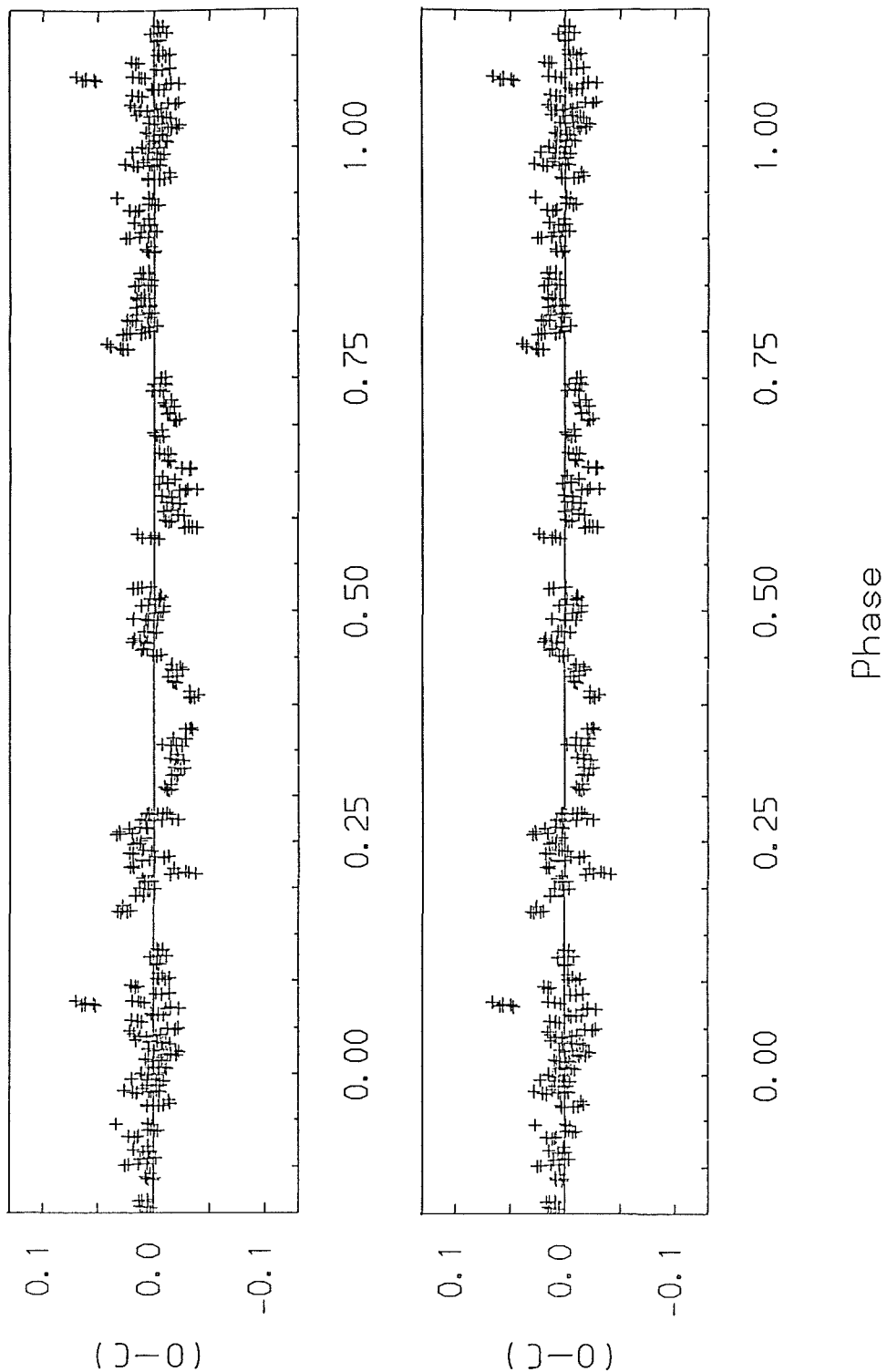


Figure 6.3.

V-magnitude residuals (in the sense observed minus calculated) for the adopted photometric solutions shown in Figure 6.2. The upper box refers to the solution employing the radiative primary component, and the lower box to that with the convective primary.

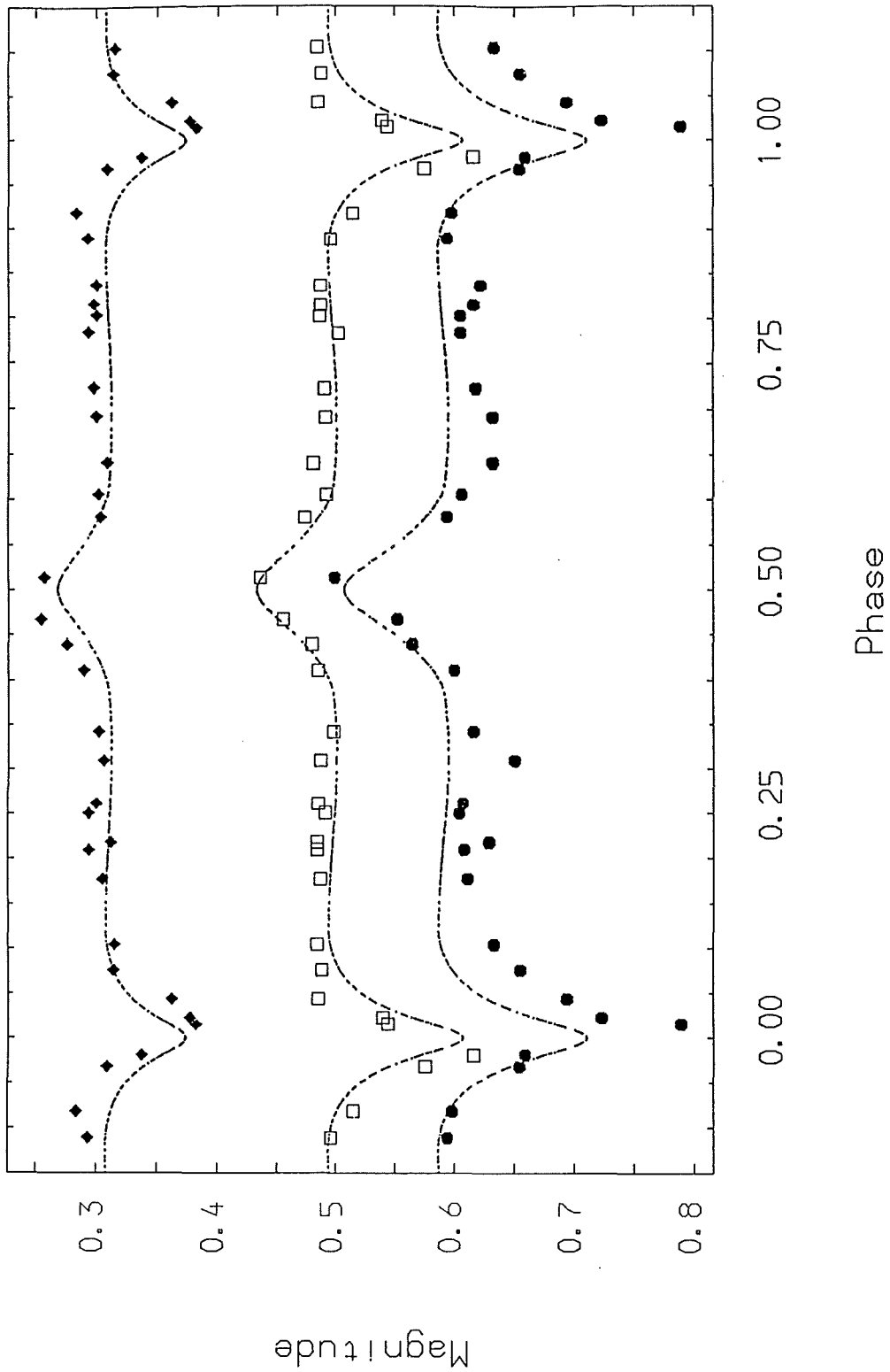


Figure 6.4.

Cape-Kron colour indices of CX Aqr plotted against phase. The $(B-V)_{kc}$, $(V-R)_{kc}$ and $(V-I)_{kc}$ are the open squares, diamonds and circles, respectively. The expected colour indices, calculated from the LIGHT solution employing the radiative primary component, are shown by dots (Appendix 6.3).

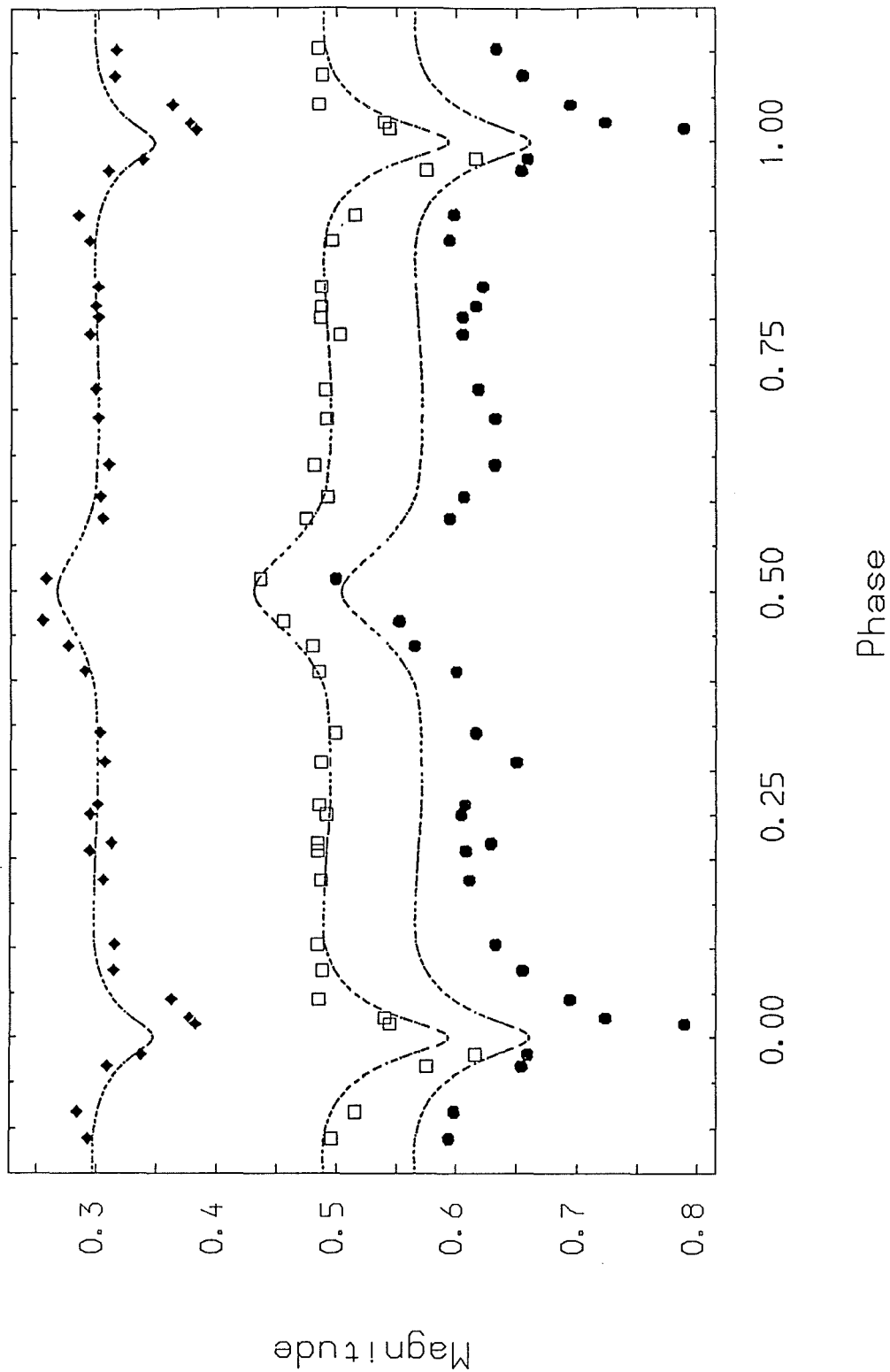


Figure 6.5.
 Cape-Kron colour indices of CX Aqr plotted against phase. The $(B-V)$, $(V-R)_{kc}$ and $(V-I)_{kc}$ are the open squares, diamonds and circles, respectively. The expected colour indices, calculated from the LIGHT solution employing the convective primary component, are shown by dots (Appendix 6.3).

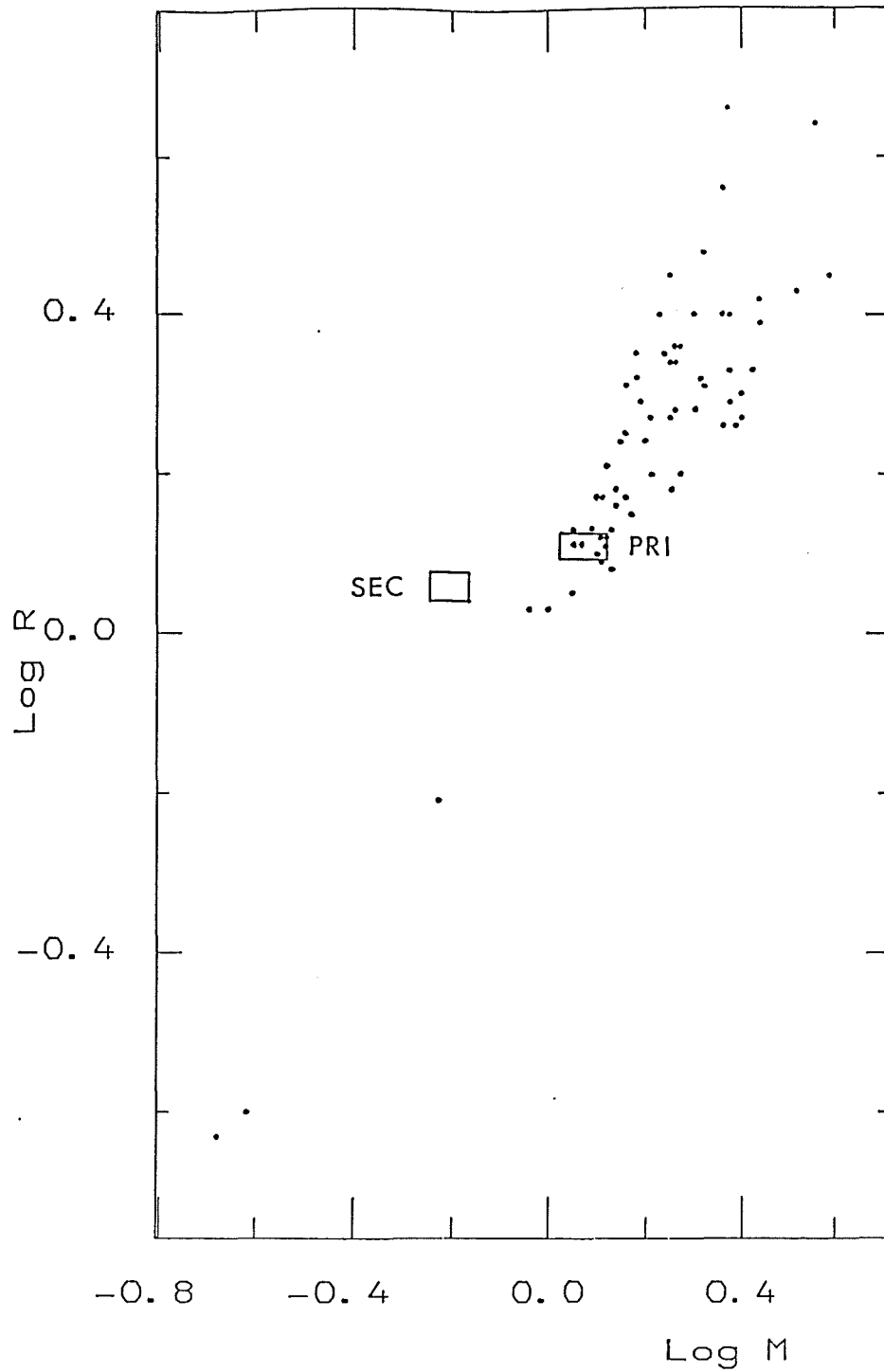


Figure 6.6.

Mass-radii data for the primary and secondary components of CX Aqr, from the LIGHT solution employing the radiative primary component, plotted together with the mass-radii data for main-sequence detached binaries from Popper(1980). While the primary component lies within or very near the main-sequence band, the secondary component lies above it, suggesting that the star is evolved. (See also Figure 6.7.)

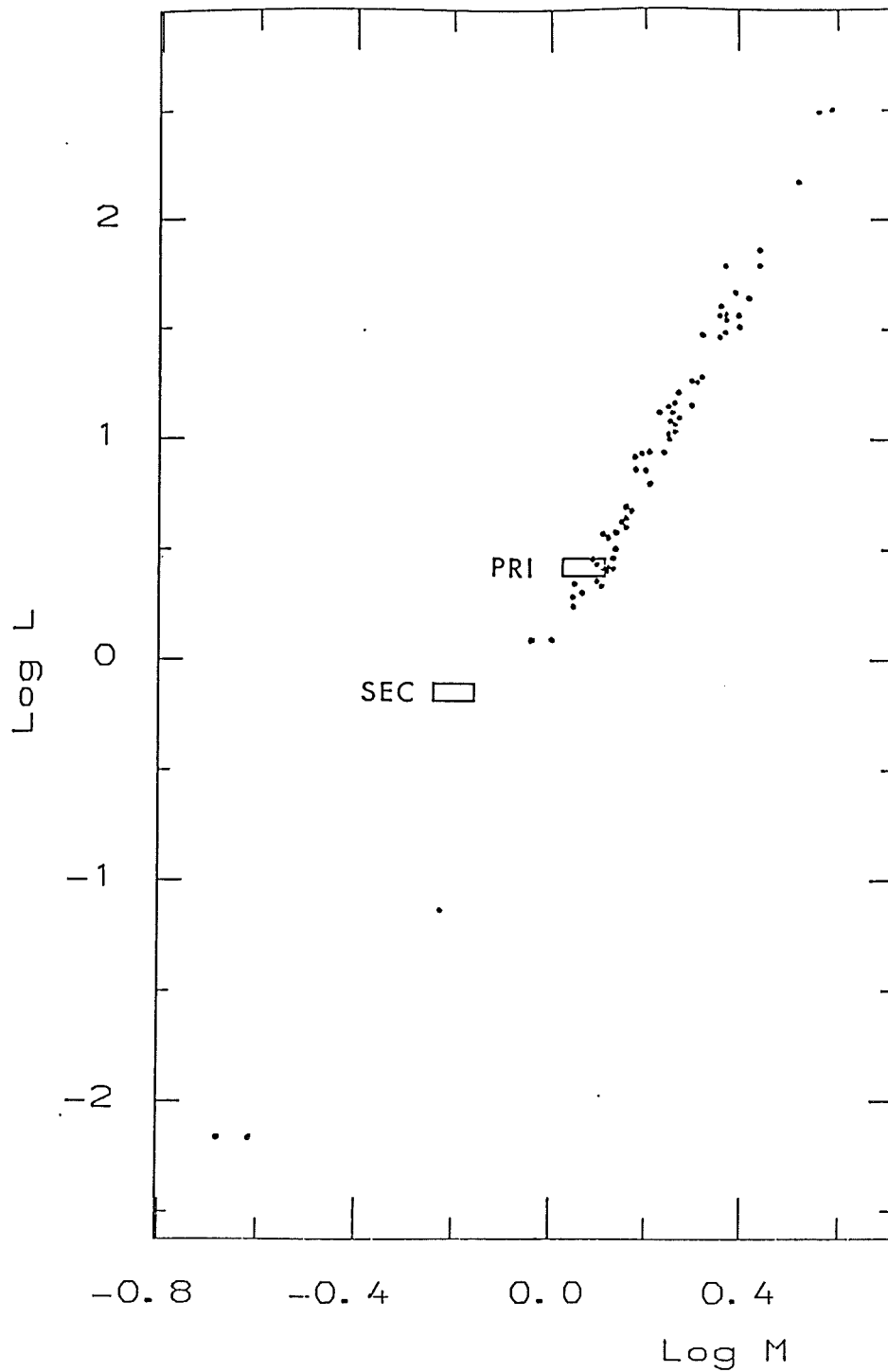


Figure 6.7.

Mass-luminosity data for the primary and secondary components of CX Aqr, from the LIGHT solution employing the radiative primary component, plotted together with the mass-luminosity data for main-sequence detached binaries from Popper(1980). While the primary component lies within or very near the main-sequence band, the secondary component lies above it, suggesting that the star is evolved. (See also Figure 6.6.)

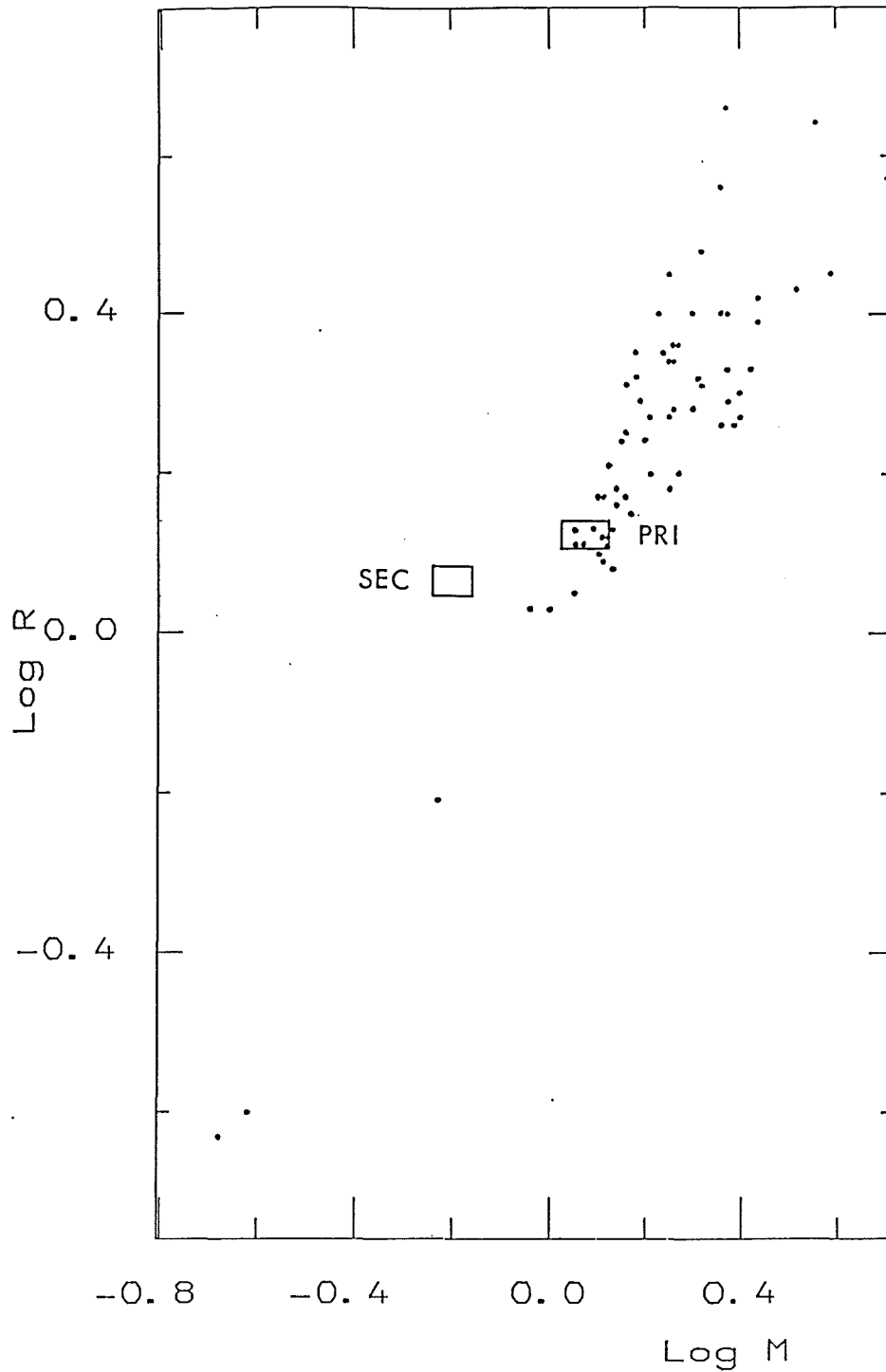


Figure 6.8.

Mass-radii data for the primary and secondary components of CX Aqr, from the LIGHT solution employing the convective primary component, plotted together with the mass-radii data for main-sequence detached binaries from Popper(1980). While the primary component lies within or very near the main-sequence band, the secondary component lies above it, suggesting that the star is evolved. (See also Figure 6.9.)

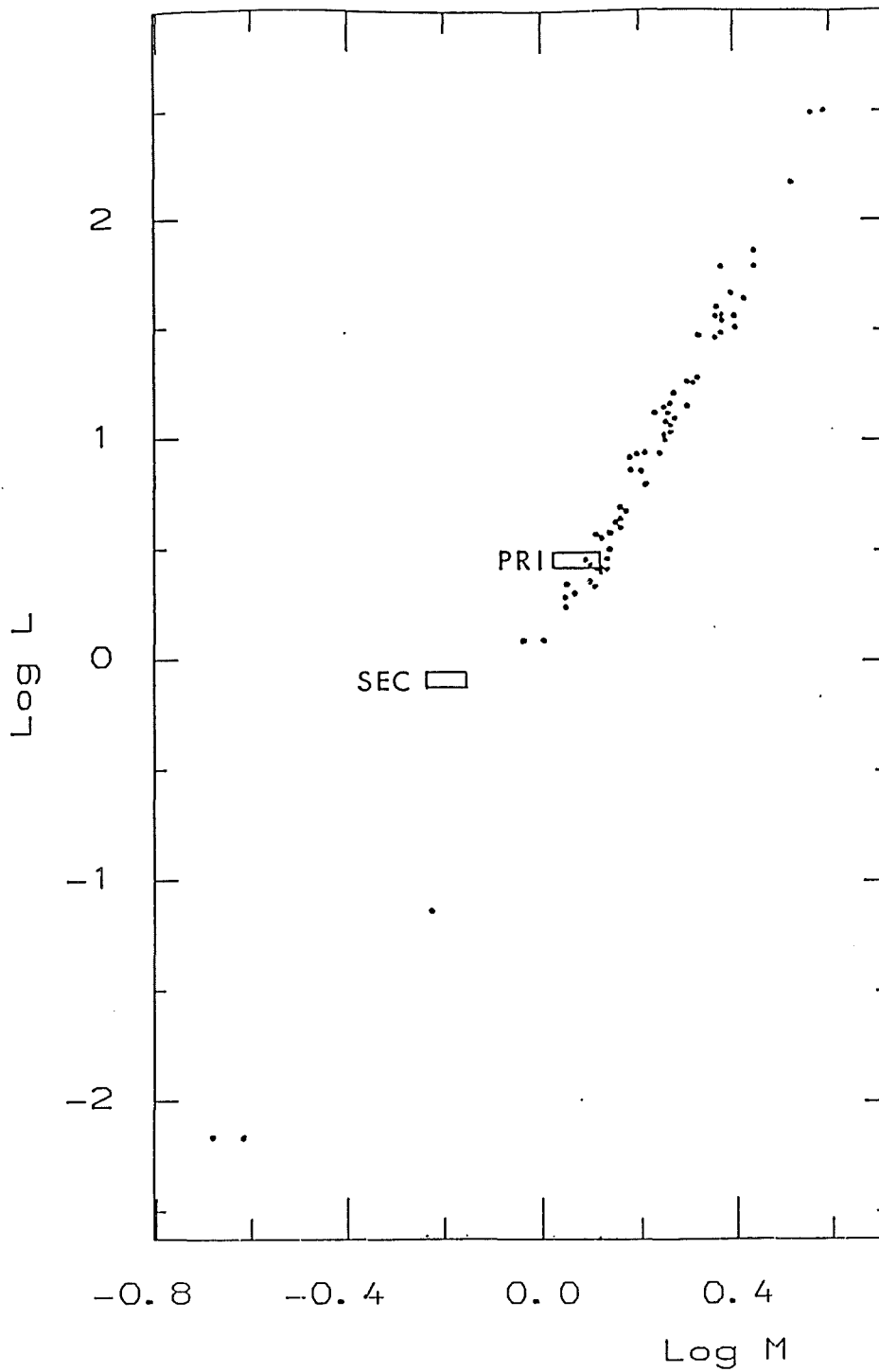


Figure 6.9.

Mass-luminosity data for the primary and secondary components of CX Aqr, from the LIGHT solution employing the convective primary component, plotted together with the mass-luminosity data for main-sequence detached binaries from Popper(1980). While the primary component lies within or very near the main-sequence band, the secondary component lies above it, suggesting that the star is evolved. (See also Figure 6.8.)

Appendix 6.1 Component mass-ratio, minimum masses and separations
calculated from the radial-velocity data.

The analysis of the radial-velocity data using Irwin's technique,
gave:

Spectroscopic mass ratio,

$$q_{\text{spec}} = 0.55 \begin{matrix} + \\ - \end{matrix} 0.03$$

Systemic velocity,

$$V_0 = (13.0 \begin{matrix} + \\ - \end{matrix} 4.3) \text{ km s}^{-1}$$

Component radial-velocity semi-amplitudes,

$$K_{\text{pr}} = (111.5 \begin{matrix} + \\ - \end{matrix} 8.7) \text{ km s}^{-1}$$

$$K_{\text{sec}} = (204.6 \begin{matrix} + \\ - \end{matrix} 9.3) \text{ km s}^{-1}$$

Now, calculating the semi-major axes using equations 3.2 and 3.4,

$$\begin{aligned} a_{\text{pr}} \cdot \sin i &= (8.52 \begin{matrix} + \\ - \end{matrix} 0.66) \times 10^5 \text{ km} \\ &= (1.22 \begin{matrix} + \\ - \end{matrix} 0.10) R_{\odot} \end{aligned}$$

$$\begin{aligned} a_{\text{sec}} \cdot \sin i &= (1.56 \begin{matrix} + \\ - \end{matrix} 0.07) \times 10^6 \text{ km} \\ &= (2.24 \begin{matrix} + \\ - \end{matrix} 0.10) R_{\odot} \end{aligned}$$

The binary component separation, a , calculated according to
equations 3.5 and 3.6, is,

$$a \cdot \sin i = (3.46 \begin{matrix} + \\ - \end{matrix} 0.14) R_{\odot}$$

Finally, calculating the minimum masses using equations 3.9
and 3.10,

$$M_{\text{pr}} \cdot \sin^3 i = (1.18 \begin{matrix} + \\ - \end{matrix} 0.13) M_{\odot}$$

$$M_{\text{sec}} \cdot \sin^3 i = (0.64 \begin{matrix} + \\ - \end{matrix} 0.06) M_{\odot}$$

Appendix 6.2 Component visual and bolometric magnitudes and luminosities.

The Johnson colours observed during secondary eclipse are,

$$(B-V) = 0.455, 0.436$$

Using the data from the LIGHT solution which employed the radiative primary component atmosphere:

Applying equation 5.0 with values of F' of 3.804 and 3.809, (assuming interstellar reddening is negligible), we obtain,

$$M_{V \text{ pr}} = 3.64 \begin{matrix} + \\ - \end{matrix} 0.09$$

Applying a bolometric correction of -0.03 mag. (Table 1 of Popper, 1980),

$$M_{\text{bol pr}} = 3.61 \begin{matrix} + \\ - \end{matrix} 0.09$$

Now, using the V-magnitude luminosity ratio at quadrature, from the LIGHT solution,

$$\begin{aligned} M_{V \text{ sec}} &= (3.64 \begin{matrix} + \\ - \end{matrix} 0.09) + 2.5 \log(4.884) \\ &= 5.36 \begin{matrix} + \\ - \end{matrix} 0.09 \end{aligned}$$

Applying a bolometric correction of -0.32 mag. (Table 1 of Popper)

$$M_{\text{bol sec}} = 5.04 \begin{matrix} + \\ - \end{matrix} 0.09$$

Finally, using a value of 4.69 for the bolometric magnitude of the Sun, the component luminosities are given by,

$$\begin{aligned} L_{\text{pr}} &= 10^{0.4(4.69 - (3.61 \pm 0.09))} L_{\odot} \\ &= 2.70 \begin{matrix} + \\ - \end{matrix} 0.22 L_{\odot} \end{aligned}$$

$$L_{\text{sec}} = 10^{0.4(4.69 - (5.04 \pm 0.09))} L_{\odot}$$

$$= 0.72 \pm 0.06 L_{\odot}$$

Now, using the data from the LIGHT solution which employed the convective primary component atmosphere:

Applying equation 5.0 with the new component radii,

$$M_{\text{V pr}} = 3.57 \pm 0.08$$

and,

$$M_{\text{bol pr}} = 3.54 \pm 0.08$$

Using the V-magnitude luminosity ratio at quadrature from the LIGHT solution,

$$M_{\text{V sec}} = (3.57 \pm 0.08) + 2.5 \log(4.075)$$

$$= 5.10 \pm 0.08$$

Applying a bolometric correction of -0.22 mag. (Table 1 of Popper),

$$M_{\text{bol sec}} = 4.88 \pm 0.08$$

Finally, again assuming a value of 4.69 for the bolometric magnitude of the Sun, the component luminosities are given by,

$$L_{\text{pr}} = 10^{0.4(4.69 - (3.54 \pm 0.08))} L_{\odot}$$

$$= (2.88 \pm 0.21) L_{\odot}$$

$$L_{\text{sec}} = 10^{0.4(4.69 - (4.88 \pm 0.08))} L_{\odot}$$

$$= (0.84 \pm 0.06) L_{\odot}$$

Appendix 6.3 Expected colours of CX Aqr.

From the LIGHT solution employing the radiative primary component:

$$T_{\text{eff pr}} = 6400\text{K}$$

$$T_{\text{eff sec}} = (4969 \pm 15) \text{ K}$$

The tables of Johnson (1966) give,

$$T_{\text{eff pr}} = 6400\text{K} \Rightarrow (B-V)_o = 0.430$$

$$(V-R)_o = 0.400$$

$$(V-I)_o = 0.640$$

$$T_{\text{eff sec}} = 4969\text{K} \Rightarrow (B-V)_o = 0.920$$

$$(V-R)_o = 0.740$$

$$(V-I)_o = 1.220$$

Applying the conversion formulae of Cousins (1980) (Appendix 5.5),

$$T_{\text{eff pr}} = 6400\text{K} \Rightarrow (V-R)_{o \text{ kc}} = 0.266$$

$$(V-I)_{o \text{ kc}} = 0.503$$

$$T_{\text{eff sec}} = 4969\text{K} \Rightarrow (V-R)_{o \text{ kc}} = 0.509$$

$$(V-I)_{o \text{ kc}} = 0.949$$

Now, from the LIGHT solution employing the convective primary component:

$$T_{\text{eff sec}} = (5289 \pm 9) \text{ K}$$

The tables of Johnson (1966) give,

$$T_{\text{eff sec}} = 5289\text{K} \Rightarrow (B-V)_o = 0.800$$

$$(V-R)_o = 0.625$$

$$(V-I)_o = 1.035$$

Again, applying the conversion formulae of Cousins (1980),

$$T_{\text{eff sec}} = 5289\text{K} \Rightarrow (V-R)_{\text{O kc}} = 0.427$$

$$(V-I)_{\text{O kc}} = 0.807$$

The expected colours of CX Aqr, calculated using equation 5.1 (assuming negligible interstellar reddening), for the LIGHT solutions employing the radiative and convective primary components, are shown in Figures 6.4 and 6.5, respectively.

The expected colour indices for $(B-V)$ and $(V-R)_{\text{kc}}$ seem to be in reasonable agreement with the observed colour indices, for both LIGHT solutions, except around primary minimum, where the solution which employed the radiative primary component provides a closer fit to the observed data. (A similar situation to this was encountered in the analysis of YY Cet (see Figure 5.3), where a possible explanation for the effect was proposed (see Appendix 5.5).) However, the expected $(V-I)_{\text{kc}}$ indices appear to be too blue, for both photometric solutions; the LIGHT solution with the convective primary being the worse of the two. The reason for this is unclear.

Appendix 6.4 Angular momentum of Cx Aqr.

From the orbital solution and the LIGHT solution which employed the radiative primary component (Solution 1):

$$m_{pr} = (2.38 \pm 0.26) \times 10^{30} \text{ kg}$$

$$m_{sec} = (1.28 \pm 0.12) \times 10^{30} \text{ kg}$$

$$a = (2.42 \pm 0.10) \times 10^9 \text{ m}$$

$$r_{pr} = (8.98 \pm 0.35) \times 10^8 \text{ m}$$

$$r_{sec} = (8.00 \pm 0.35) \times 10^8 \text{ m}$$

Calculating the orbital angular momentum of the system according to equations 5.10a and 5.10b,

$$J_{orb} = (6.40 \pm 0.96) \times 10^{44} \text{ kg m}^2 \text{ s}^{-1}$$

The total rotational angular momentum of the components, given by equations 5.4, 5.5, 5.6 and 5.7, is,

$$J_{rot tot} = (1.43 \pm 0.14) \times 10^{44} \text{ kg m}^2 \text{ s}^{-1}$$

Finally, the total angular momentum of the system, calculated using equations 5.8 and 5.9, is,

$$J_{tot} = (7.83 \pm 0.97) \times 10^{44} \text{ kg m}^2 \text{ s}^{-1}$$

Now, using the data derived from the orbital solution and the LIGHT solution employing the convective primary component (Solution 2):

$$r_{pr} = (9.26 \pm 0.35) \times 10^8 \text{ m}$$

$$r_{sec} = (8.07 \pm 0.35) \times 10^8 \text{ m}$$

Again, using the same equations as above,

$$J_{orb} = (6.40 \pm 0.96) \times 10^{44} \text{ kg m}^2 \text{ s}^{-1}$$

$$J_{rot tot} = (1.51 \pm 0.15) \times 10^{44} \text{ kg m}^2 \text{ s}^{-1}$$

$$J_{tot} = (7.91 \pm 0.97) \times 10^{44} \text{ kg m}^2 \text{ s}^{-1}$$

(n.b. See Appendix B.)

Appendix 6.5 Estimate of angular momentum losses required for contact, assuming constant mass ratio.

For Solution 1:

The separation of the component centres required for contact to be achieved, calculated according equations 5.11 and 5.12, is,

$$a_c = (1.70 \pm 0.05) \times 10^9 \text{ m}$$

Estimating the difference in angular momentum between contact and non-contact states using equations 5.14 and 5.15, yields,

$$J_{\text{orb}} - J_{\text{orb } c} = (1.03 \pm 0.16) \times 10^{44} \text{ kg m}^2 \text{ s}^{-1}$$

For Solution 2:

$$a_c = (1.73 \pm 0.05) \times 10^9 \text{ m}$$

and,

$$J_{\text{orb}} - J_{\text{orb } c} = (9.88 \pm 1.50) \times 10^{43} \text{ kg m}^2 \text{ s}^{-1}$$

Appendix 6.6 Estimate of rate of angular momentum loss by
magnetic braking.

The estimates of angular momentum loss by magnetic braking will be substantially different for Solutions 1 and 2: in Solution 1, where the primary component possesses a radiative atmosphere, any angular momentum loss must arise only the secondary component; on the other hand, for Solution 2, where both components possess convective atmospheres, angular momentum may be lost from both components.

For Solution 1:

Using equations 5.20 and 5.21 to estimate the rate of angular momentum loss via magnetic braking,

$$\begin{aligned} dJ_{\text{rot}}/dt &= dJ_{\text{rot sec}}/dt \\ &= -(1.69 \pm 0.21) \times 10^{34} \times 0.18533^{-\alpha} \text{ kg m}^2 \text{ s}^{-1} \text{ yr}^{-1} \end{aligned}$$

Adopting various values for the exponent α ,

$$\alpha = 1,$$

$$dJ_{\text{rot}}/dt = -(9.12 \pm 1.13) \times 10^{34} \text{ kg m}^2 \text{ s}^{-1} \text{ yr}^{-1}$$

$$\alpha = 2,$$

$$dJ_{\text{rot}}/dt = -(4.92 \pm 0.61) \times 10^{35} \text{ kg m}^2 \text{ s}^{-1} \text{ yr}^{-1}$$

$$\alpha = 3,$$

$$dJ_{\text{rot}}/dt = -(2.65 \pm 0.33) \times 10^{36} \text{ kg m}^2 \text{ s}^{-1} \text{ yr}^{-1/N}$$

$$\alpha = 1.5,$$

$$dJ_{\text{rot}}/dt = -(2.12 \pm 0.26) \times 10^{35} \text{ kg m}^2 \text{ s}^{-1} \text{ yr}^{-1}$$

Similarly, for Solution 2:

$$dJ_{\text{rot pri}}/dt = -(4.21 \pm 0.57) \times 10^{34} \times 0.18533^{-\alpha} \text{ kg m}^2 \text{ s}^{-1} \text{ yr}^{-1}$$

and,

$$dJ_{\text{rot sec}}/dt = -(1.72 \pm 0.21) \times 10^{34} \times 0.18533^{-\alpha} \text{ kg m}^2 \text{ s}^{-1} \text{ yr}^{-1}$$

Thus,

$$\begin{aligned} dJ_{\text{rot}}/dt &= dJ_{\text{rot pri}}/dt + dJ_{\text{rot sec}}/dt \\ &= -(5.93 \pm 0.61) \times 10^{34} \times 0.18533^{-\alpha} \text{ kg m}^2 \text{ s}^{-1} \text{ yr}^{-1} \end{aligned}$$

Again, adopting various values of α ,

$$\alpha = 1,$$

$$dJ_{\text{rot}}/dt = -(3.20 \pm 0.33) \times 10^{35} \text{ kg m}^2 \text{ s}^{-1} \text{ yr}^{-1}$$

$$\alpha = 2,$$

$$dJ_{\text{rot}}/dt = -(1.73 \pm 0.18) \times 10^{36} \text{ kg m}^2 \text{ s}^{-1} \text{ yr}^{-1}$$

$$\alpha = 3,$$

$$dJ_{\text{rot}}/dt = -(9.32 \pm 0.96) \times 10^{36} \text{ kg m}^2 \text{ s}^{-1} \text{ yr}^{-1}$$

$$\alpha = 1.5,$$

$$dJ_{\text{rot}}/dt = -(7.43 \pm 0.76) \times 10^{35} \text{ kg m}^2 \text{ s}^{-1} \text{ yr}^{-1}$$

Appendix 6.7 Estimate of timescale for CX Aqr to evolve into contact via magnetic braking.

For Solution 1:

Applying equations 5.23 and 5.24 to obtain an estimate of the timescale required for CX Aqr to achieve contact via angular momentum loss via magnetic braking, yields,

$$T_c = (6.12 \pm 0.88) \times 10^9 \times 0.18533^\alpha \text{ yr}$$

So, for various values of α ,

$$\alpha = 1,$$

$$\begin{aligned} T_c &= (1.13 \pm 0.16) \times 10^9 \text{ yr} \\ &\approx (1.1 \pm 0.2) \times 10^9 \text{ yr} \end{aligned}$$

$$\alpha = 2,$$

$$\begin{aligned} T_c &= (2.10 \pm 0.30) \times 10^8 \text{ yr} \\ &\approx (2.1 \pm 0.3) \times 10^9 \text{ yr} \end{aligned}$$

$$\alpha = 3,$$

$$\begin{aligned} T_c &= (3.90 \pm 0.56) \times 10^7 \text{ yr} \\ &\approx (3.9 \pm 0.6) \times 10^7 \text{ yr} \end{aligned}$$

$$\alpha = 1.5,$$

$$\begin{aligned} T_c &= (4.88 \pm 0.70) \times 10^8 \text{ yr} \\ &\approx (4.9 \pm 0.7) \times 10^8 \text{ yr} \end{aligned}$$

For Solution 2:

It would be inappropriate to apply equations 5.23 and 5.24 to estimate T_c , since angular momentum loss by magnetic braking is taking place from both components. So to obtain an estimate of T_c

we simply apply the formula,

$$T_c = (J_{orb} - J_{orb c}) \times (dJ_{rot}/dt)^{-1} \text{ yr}$$

with the error on this given by,

$$\Delta T_c = [(\Delta(J_{orb} - J_{orb c}))^2 + (\Delta(dJ_{rot}/dt))^2]^{1/2}$$

Thus, applying the relevant equations from Appendices 6.5 and 6.6,

we obtain

$$T_c = (1.67 \pm 0.31) \times 10^9 \times 0.18533^\alpha \text{ yr}$$

Inserting various values for the exponent α ,

$\alpha=1$,

$$\begin{aligned} T_c &= (3.10 \pm 0.57) \times 10^8 \text{ yr} \\ &\approx (3.1 \pm 0.6) \times 10^8 \text{ yr} \end{aligned}$$

$\alpha=2$,

$$\begin{aligned} T_c &= (5.74 \pm 1.05) \times 10^8 \text{ yr} \\ &\approx (5.7 \pm 1.1) \times 10^8 \text{ yr} \end{aligned}$$

$\alpha=3$,

$$\begin{aligned} T_c &= (1.06 \pm 0.19) \times 10^7 \text{ yr} \\ &\approx (1.1 \pm 0.2) \times 10^7 \text{ yr} \end{aligned}$$

$\alpha=1.5$,

$$\begin{aligned} T_c &= (1.33 \pm 0.24) \times 10^8 \text{ yr} \\ &\approx (1.3 \pm 0.2) \times 10^8 \text{ yr} \end{aligned}$$

CHAPTER 7

RV CORVI

7.1. INTRODUCTION:

The star RV Crv (HD109796) was first noted to be variable by Swope and the light elements given by Buttery (1942) showed that the star is an eclipsing binary system which displays an EB-type light curve with an orbital period of 0.75 day. Accordingly the system was placed on the observing list of our programme of reticon spectroscopy and $BVRI_c$ photometry of contact and near-contact binaries (Hilditch et al. 1984; Chap. 2).

Struve and Gratton (1948) published a single-spectrum radial-velocity curve for the system and found a pronounced shift in phase of 0.13 day from the ephemeris published by Buttery. They assigned a spectral-type of F0 which did not seem to vary appreciably with phase, and derived a mass function of $0.033 M_{\odot}$. Koch et al. (1963) list primary and secondary component spectral types of F0 and G0 respectively. Lucy and Sweeney (1971) re-examined the radial-velocity data and found the value of the mass function to be $0.026 \pm 0.005 M_{\odot}$. An improved ephemeris and UBV light curve were published by Abhyankar et al. (1973). Using the second method of Kopal (1959), they produced a tentative photometric solution which, when combined with the spectroscopic elements of Struve and Gratton, suggested that the system may be in

contact. Their analysis suggested spectral types of F0III and K for the two components. Giuricin et al. (1982) re-analysed the light curve of Abhyankar et al. using the light curve synthesis code of Wood, and found the system to be an evolved contact binary of mass ratio ~ 0.3 . Wolf and Kern (1983) published $uvby\beta$ indices of RV Crv in their survey of Southern Hemisphere eclipsing binaries.

7.2. OBSERVATIONS:

The photoelectric observations were obtained at the South African Astronomical Observatory (SAAO), by the author, during the period March 9-April 3 1984, using the 0.5m telescope equipped with a Peoples Photometer, and a set of BVRI_c filters. The variable and comparison stars were monitored through the V-filter, with regular observations of the variable through all four filters at intervals of approximately 25 minutes (~ 0.02 period), to note any colour changes. The comparison star, SA0157438 ($V = 9.1$), and check star, SA0157442 ($V = 8.6$) were found to be constant in brightness to better than ~ 0.01 mag. .

Regular observations of E and F region standards (Menzies, Banfield, and Laing, 1980) were taken throughout each night, and a local standard, HD104731 (E540, $V = 5.149$), was observed hourly as a check for zero-point drifts, and to serve as an additional check star.

The initial reduction of the observations was carried out at Cape Town, by means of the SAAO photometry reduction package, and finalised at St. Andrews. The errors of observation were typically 0.005 mag. for the differential V-magnitudes, and 0.01 mag. for the colour indices.

The spectroscopic observations were obtained by Dr. D. J. King, using the RPCS/ITS spectrograph and reticon detector system at the f/18 Cassegrain focus of the 1.9m telescope at SAAO, during the period April 3-9 1985. Grating 3 was used, providing 30\AA mm^{-1} in the blue region of the second-order spectrum. Spectra centred at about 4200\AA and with a useful range of approximately 500\AA were obtained, with a slit width of $200\mu\text{m}$ and typical integration times of 1000s (~ 1.5 per cent of the orbital period). On most nights four radial-velocity standard stars were observed covering a spectral range A5 to K2. All stellar integrations were alternated with comparison-source exposures (a Cu-Ar lamp).

The spectra were written to magnetic tape at Cape Town, and later processed on a VAX 11/750 at the University of Durham, flat fielding the data by means of the SPICA package. The spectroscopic image-processing package REDUCE (Hill, Fisher and Poeckert, 1982b), which was run on a VAX 11/780 at the University of St. Andrews, was then used to measure the comparison spectra, and rectify, linearize (in $\ln\lambda$), and filter the stellar spectra.

7.3. REVISED EPHEMERIS:

The method of Kwee and van Woerden (1956) was used to calculate the epoch of primary eclipse from the photoelectric observations obtained on April 1 1984. From the epoch determined by Abhyankar et al., a new value for the orbital period was calculated, yielding a revised ephemeris of:

$$\text{MJD } 45791.8578_{-0.0003}^{+0.0003} + 0.7472503_{-0.0000001}^{+0.0000001} E \text{ (s.e.)}$$

This new estimate of the orbital period is slightly shorter than the value of 0.7472521 days given by Abhyankar et al. . Although the epoch published by Buttery suggests that the period of RV Crv may have decreased slightly over the past 40 years, we are unable to say whether this is indeed the case since there are no other reliable published times of minima. All orbital phases used in our analysis were calculated by means of the above ephemeris.

It should be noted that the primary minimum is very distorted, and that minimum light occurs before mid-eclipse. It would perhaps have been more appropriate to calculate the epoch using the data at secondary minimum, since this appears to be fairly symmetric. However, the error in the calculated time of secondary minimum was found to be about six times greater than that quoted for the deeper eclipse.

7.4. SPECTROSCOPIC ANALYSIS:

A total of 40 spectrograms of RV Crv were obtained, as well as 14 spectrograms of 10 radial-velocity standard stars, selected from the lists of Evans et al. (1957, 1959, 1964).

The cross-correlation program VCROSS (Hill, 1982) was used to measure the standard star spectra, all spectra being cross-correlated against several comparison stars of various spectral types. The best results were obtained using an F2V standard, HD142529, as the comparison, and fitting a single Gaussian profile to the cross-correlation functions (CCFs). The mean residual, in the sense of standard minus observed, was -0.3 ± 5.3 (sd) km s^{-1} . The results indicated no hour angle dependence or other peculiarities.

The spectra of RV Crv were cross-correlated against the F2V standard star HD142529, since this produced well-defined peaks in the CCFs. Gaussian profiles were fitted to the functions by least squares, a double Gaussian fit being adopted for the double-lined phases. The resultant velocities for the primary and secondary components, together with times of observations, are presented in Table 7.1 and Figure 7.1.

The absence of any radial velocity measurements of the secondary component around first quadrature results from the fact that the CCFs at these phases were found to exhibit only single peaks. The reason for this is unclear, although a similar situation

has been noted by McFarlane et al. (1985) for YY Cet (Chap. 5), and Hilditch and King (1985) for the binary RT Scl. Another interesting feature of the radial-velocity curves concerns the data around second quadrature. While the secondary component radial velocities appear to fall into two distinct groups, depending on which night the observations were obtained, the corresponding primary component data show no signs of such an effect. Again, the reason for this is unclear. The effects of rotational distortion can be seen to either side of primary eclipse.

Since there are no indications of orbital eccentricity from either the photometric or spectroscopic data, it is reasonable to assume a circular orbit. With this assumption, the Lehman-Filhes method was applied to the radial-velocity curve of the primary component in order to derive values for the systemic velocity, V_o , and the semi-amplitude, K_{pr} . Using these values, together with the radial velocity data for both components around second quadrature (ie. between phase 0.65 and 0.80), the spectroscopic mass ratio was obtained. This was then used to calculate the velocity semi-amplitude of the secondary component, K_{sec} , and the values of the minimum masses and separations. The results are given in Table 7.4. Since there is very good agreement between the spectroscopic mass ratio and that obtained from the photometry, we would have preferred to calculate the above parameters using an average of the two values in order to reduce errors. However, since the photometric mass ratio was treated as a fixed quantity in the light curve solutions, we were unable to do this. Thus the errors quoted for the various parameters derived using the spectroscopic mass ratio are somewhat pessimistic.

7.5. PHOTOMETRIC ANALYSIS:

The differential V-magnitude light curve of RV Crv is shown in Figure 7.2 and the observations are listed in Table 7.2. Unfortunately, there was insufficient time remaining in our observing run to obtain photometric data between phases 0.67 to 0.88. An examination of the radial-velocity curves and the observed colour indices (Table 7.3) reveals that the primary minimum of the light curve is due to the transit of the cooler, less massive secondary component across the face of the hotter primary.

The colour indices observed during the total eclipse of the secondary component were used to estimate the temperature of the primary, using the tables of Popper (1980). Although we were unable to obtain an accurate estimate of the effects of interstellar reddening from the $uvby\beta$ data published by Wolf and Kern (1983), since their observations were taken only at primary eclipse, calculations using the $uvby\beta$ indices together with the empirical calibrations of Crawford (1975), suggested that the interstellar reddening was less than 0.02 mag. in (B-V). Since such small reddening should have no noticeable effect on the final photometric solution, the temperature of the primary component was calculated directly from the colour indices observed during secondary eclipse. These data suggested a temperature of about 6600K for the averted hemisphere of the primary component.

The light curve was analysed on the instrumental system since the careful selection of the comparison star allowed extinction and second-order colour effects to be ignored. The light-curve analysis code LIGHT (Hill, 1979), was used to analyse the differential V-magnitude data.

In all cases, solutions were sought with the primary-component temperature fixed at a value of 6600K. Since at this temperature it is not possible to say with certainty whether the primary component possesses a convective or a radiative atmosphere, both were assumed in the search for a fit to the data. Initial attempts, with the inclination, secondary temperature, and both radii as free parameters, proved fruitless. Over a very wide range of mass ratio it was impossible to obtain a solution which matched the entire light curve: the gradients of the theoretical fits were found to be too steep around primary minimum, and too shallow around secondary, even when the depths of both eclipses were predicted correctly. It appeared that the LIGHT code was unable to synthesize the observations, probably because of some anomaly on the surface of one, or both, of the components.

A possible way around this problem was proposed by Kaluzny (1986a), who encountered similar difficulties. Kaluzny suggested that the light curves may be reproduced if the albedo of the secondary component is allowed to have a value greater than unity. This permits the computer code to 'simulate' either an abnormally hot region on the facing side of the secondary component, or alternatively, an abnormally cool region on the averted

hemisphere.

When the albedo of the secondary component was treated as a free parameter, and the mass ratio fixed at various values, several close fits to the light curve were finally obtained, with both convective and radiative atmospheres for the primary component. The parameters corresponding to these are given in Tables 7.5 and 7.6. However, when the mass ratio was allowed to vary, the LIGHT code failed to converge to a solution. Although the solutions appear to be fairly insensitive to the choice of mass ratio, the best results were obtained with the values set at 0.27 and 0.28, for the convective and radiative primary component cases, respectively, with the latter case providing a slightly closer fit to the data. These mass ratios appear to be in very good agreement with the value of 0.27 ± 0.04 determined from the radial velocity data.

The two solutions are very similar, with the only main differences being in the values for the secondary-component temperature, which appears to be about 700K hotter for the convective case, and for the secondary albedo, which is lower for the radiative solution. Kaluzny (1986a) found similar results in his analysis of the binary WZ Cep. Since it is impossible to say which solution bears the greater resemblance to reality, parameters were derived using both fits.

The details of the solutions are given in Table 7.7, and suggest that the secondary component lies close to the Roche surface. Because of the limited accuracy with which the light-curve synthesis code can fit the observed data with its inherent scatter,

we are unable to ascertain whether the binary is in a semi-detached configuration with the primary component completely filling its Roche lobe, or whether it is in a state of marginal contact. Both solutions to the differential V-magnitude data are shown in Figure 7.2 . Unfortunately, the theoretical fits to the light curve do not exactly match the depth of the observed secondary minimum, which appears to be about 0.007 mag. deeper than the solutions predict, and, for the convective case, the observed data at quadrature, which appears to be about 0.01 mag. brighter than predicted. Another disturbing aspect of the solutions concern the V-magnitude residuals of the fits, shown in Figure 7.3, which deviate by no more than about 0.02 mag. from the observed data, but are clearly dependent on phase. Kaluzny (1986d) has noted a similar effect in his analysis of the binary BE Cep. . These effects may be a result of our attempt to simulate by a rather crude parameterisation, what is probably a very complex physical phenomenon in the atmospheres of the binary components.

The parameters from the light curve solutions were combined with the results of the spectroscopic analysis, to derive the astrophysical data for the binary which are given in Table 7.8 . A comparison of these data with the mass-radius and mass-luminosity data for main-sequence detached binaries (Popper, 1980), indicates that while the primary component lies near or within the main-sequence bands, the secondary component is clearly oversized and overluminous for its mass, its radius being about two and a half times greater than expected (Figures 7.6, 7.7, 7.8 and 7.9).

7.6. DISCUSSION:

Although the photometric solutions do not provide exact fits to the differential V-magnitude data, they are close enough for us to have reasonable confidence in the accuracy of the derived parameters. The radiative and convective solutions, given in Table 7.7, suggest values of 2.59 ± 0.12 and 3.20 ± 0.23 , respectively, for the albedo of the secondary component. For this single wavelength data, this result may be interpreted either as a region of 'excess' luminosity on the facing hemispheres of one or both of the components, presumably related to some form of mass-transfer process, or as an area of extensive starspot activity located on the averted hemisphere, or perhaps a combination of both effects. Only full light curves obtained over a wide wavelength range will be able to discriminate between these alternative interpretations of an anomalous 'albedo'.

The hot-spot hypothesis was first proposed by Naqvi and Gronbech (1976), who suggested that a hot region on the surface of the larger component of the contact binary TY Men may have been responsible for asymmetries in the observed light curves. Naqvi and Gronbech also observed a blue excess in their colour indices of about 0.02 mag. in (B-V), around the brighter, first quadrature. Such an effect has also been noted by Kaluzny, who analysed five contact binaries, CN And, WZ Cep, AU Ser, FT Lup and AG Vir, which appear to be similar to RV Crv, (Kaluzny 1983,1986a,1986b,1986c). Indeed, our data for RV Crv, taken around first quadrature, appears to be bluer than expected, by about 0.02 mag. in (B-V), (see

Appendix 7.3, and Figures 7.4 and 7.5).

For all the binaries discussed above, the first quadrature always appears to be the brighter, sometimes by over 0.05 mag. . Kaluzny has argued that such a difference in light level cannot be accounted for by starspot activity on the secondary component, but must be a result of a relatively small area of enhanced luminosity on the surface of the binaries, around the region of the connecting neck. For the systems where both quadratures have been observed, Kaluzny fits to the lower value, weighting to zero those phases where an excess luminosity is suspected. He also found it impossible to reproduce the observed curvature of the first maximum light. Since there is some evidence in the light curve of RV Crv to suggest that second quadrature may be less bright than first quadrature, namely the observations obtained between phases 0.88 and 0.91, closer fits to the data may have been obtained if we had been able to fit the solutions to the second maximum light.

Further evidence for an abnormally bright region visible during first quadrature comes from our spectroscopic data. The observations obtained around phase 0.25 show no indication of an additional peak in the cross-correlation functions due to the presence of the secondary-component spectrum, unlike the data acquired around phase 0.75 . This may be the result of the light from a hot-spot shrouding the contribution of the secondary component in the CCFs.

Another feature that appears to be a characteristic of these systems, which is present in the light curve of RV Crv, is the asymmetric shape of the base of the primary minimum, which exhibits a pronounced shoulder on the ascending branch. Naqvi and Gronbech associate this with the presence of a region of excess luminosity.

The anomalous distribution of surface brightness over the two stars may be due to a hot-spot caused by the transfer of mass from the primary to the secondary component. Since the photometric solution shows that the primary component fills its Roche lobe and that the secondary component is very close to contact (indeed, in contact to within the errors of the solution), and grossly oversized for its mass, it seems most likely that some form of mass and energy transfer must be taking place between the components. Thus RV Crv shares many of the characteristics established for FT Lup (Hilditch et al., 1984) and RT Scl (Hilditch and King, 1985).

The detailed UBVR photometric studies of VW Cep and W UMa carried out by Linnell (1982,1985) demonstrate that there is substantial ambiguity in interpreting the asymmetries of the observed light curves. Whether Mullan's (1975) starspot model or Rucinski's (1974) hot secondary model is to be preferred depends upon successfully interpreting detailed changes in colour indices over a wide wavelength range as a function of orbital phase. Similarly, observations over a wide wavelength range will be required if we are to determine whether or not the anomalous distribution of light on the surfaces of the marginal contact systems are due to regions of enhanced luminosity. Such

observations, together with spectroscopically defined mass ratios providing limitations on the range of possible solutions, would prove to be most beneficial to our understanding of the mass and energy transfer processes taking place between the components.

Table 7.1. Radial velocities of RV Crv.

Spectrum No.	MJD	Phase	V_{pr} (km s^{-1})	V_{sec} (km s^{-1})
	46000+			
439/009	158.87502	0.157	-40	
439/011	158.88754	0.174	-39	
439/013	158.90003	0.191	-44	
439/015	158.91460	0.210	-50	
439/017	158.93198	0.233	-45	
439/019	158.94100	0.245	-46	
439/021	158.96182	0.273	-23	
439/023	158.97642	0.293	-36	
439/025	158.99030	0.311	-35	
439/027	159.00349	0.329	-33	
439/029	159.01670	0.347 *
439/062	159.94309	0.586	37	
439/064	159.95558	0.603	56	
439/066	159.96879	0.621	64	
439/068	159.98198	0.638	62	-222
439/070	159.99655	0.658	72	-224
439/072	160.00976	0.676	77	-216
439/074	160.02226	0.692	71	-214
439/076	160.03614	0.711	80	-226
439/078	160.04935	0.729	78	-234
439/080	160.06184	0.745	80	-223
439/082	160.07503	0.763	89	-231
439/084	160.08821	0.781	85	-219
439/086	160.10143	0.798	72	-225
439/111	162.79655	0.405	-24	
439/113	162.80976	0.423	-3	
439/115	162.82295	0.440	2	
439/117	162.83613	0.458	3	
439/119	162.85073	0.478	10	
439/121	162.86461	0.496	30	
439/125	162.88963	0.530	33	
440/004	163.76809	0.705	79	-204
440/006	163.78267	0.725	82	-205
440/008	163.79655	0.743	85	-199
440/010	163.80976	0.761	89	-187
440/012	163.82295	0.779	87	-193
440/014	163.83544	0.795	93	-187
440/036	163.98198	0.991	30	
440/038	163.99516	0.009	8	
440/040	164.00768	0.026	-12	

Spectrum No. indicates RPCS tape/run number.

* Very poor cross-correlation peak. Not used for radial velocity determination.

Table 7.2. Differential V-magnitudes of RV Crv.

MJD	PHASE	Diff. Mag. (v-c)	MJD	PHASE	Diff. Mag. (v-c)
45000.0+			45000.0+		
768.05475	0.1459	-0.874	792.04053	0.2447	-0.975
768.06482	0.1594	-0.897	792.05823	0.2683	-0.973
768.07104	0.1677	-0.912	792.06409	0.2762	-0.972
768.07916	0.1786	-0.923	792.06781	0.2812	-0.972
768.08905	0.1918	-0.938	792.07275	0.2878	-0.967
768.09485	0.1996	-0.949	792.07886	0.2959	-0.963
768.10254	0.2099	-0.952	792.08289	0.3013	-0.960
768.13000	0.2466	-0.970	792.08673	0.3065	-0.958
768.13727	0.2564	-0.977	792.09766	0.3211	-0.940
791.76709	0.8787	-0.792	792.10559	0.3317	-0.931
791.77625	0.8910	-0.764	792.11719	0.3472	-0.917
791.78101	0.8974	-0.753	792.12244	0.3543	-0.905
791.78760	0.9062	-0.723	792.12836	0.3622	-0.892
791.79578	0.9171	-0.687	792.77087	0.2220	-0.954
791.79993	0.9227	-0.659	792.77869	0.2325	-0.962
791.80396	0.9281	-0.638	792.78259	0.2377	-0.964
791.82001	0.9495	-0.543	792.78766	0.2445	-0.972
791.82776	0.9599	-0.491	792.79431	0.2534	-0.970
791.83508	0.9697	-0.445	792.79895	0.2596	-0.967
791.84174	0.9786	-0.423	792.80341	0.2656	-0.969
791.84967	0.9892	-0.418	792.81812	0.2853	-0.965
791.85345	0.9943	-0.414	792.82416	0.2933	-0.959
791.85767	0.9999	-0.420	792.83130	0.3029	-0.955
791.86163	0.0053	-0.420	792.83661	0.3100	-0.946
791.86664	0.0119	-0.424	792.84314	0.3187	-0.940
791.87238	0.0196	-0.431	792.84705	0.3240	-0.936
791.87665	0.0253	-0.437	792.85095	0.3292	-0.932
791.88159	0.0320	-0.449	792.87189	0.3572	-0.901
791.88757	0.0400	-0.481	792.87799	0.3654	-0.893
791.89111	0.0447	-0.506	792.88202	0.3708	-0.883
791.91052	0.0707	-0.630	792.88776	0.3784	-0.878
791.91809	0.0808	-0.682	792.89569	0.3891	-0.858
791.92450	0.0894	-0.718	792.89948	0.3941	-0.845
791.93005	0.0968	-0.741	792.90369	0.3998	-0.836
791.93774	0.1071	-0.776	792.91693	0.4175	-0.795
791.94165	0.1123	-0.794	792.92303	0.4257	-0.775
791.94568	0.1177	-0.808	792.92816	0.4325	-0.759
791.96350	0.1416	-0.858	792.93207	0.4377	-0.746
791.97107	0.1517	-0.879	792.93732	0.4448	-0.726
791.97473	0.1566	-0.889	792.97150	0.4905	-0.676
791.97968	0.1632	-0.897	792.97693	0.4978	-0.676
791.98547	0.1710	-0.910	792.98016	0.5021	-0.674
791.98901	0.1757	-0.919	792.98352	0.5066	-0.681
792.00909	0.2026	-0.949	792.98712	0.5114	-0.677
792.01508	0.2106	-0.956	792.99054	0.5160	-0.676
792.01941	0.2164	-0.961	792.99487	0.5218	-0.676
792.02448	0.2232	-0.964	792.99988	0.5285	-0.679
792.03247	0.2339	-0.968	793.00342	0.5332	-0.681
792.03662	0.2394	-0.973	793.00696	0.5380	-0.689

(continued).

Table 7.2. Differential V-magnitudes of RV Crv (continued).

MJD	PHASE	Diff. Mag. (v-c)
45000.0+		
793.01050	0.5427	-0.695
793.01520	0.5490	-0.708
793.02002	0.5554	-0.722
793.02338	0.5599	-0.736
793.02704	0.5648	-0.748
793.03235	0.5719	-0.768
793.03668	0.5777	-0.784
793.05029	0.5960	-0.829
793.05603	0.6036	-0.849
793.06012	0.6091	-0.861
793.06494	0.6156	-0.875
793.07086	0.6235	-0.887
793.07483	0.6288	-0.896
793.07880	0.6341	-0.901
793.08887	0.6476	-0.918
793.09460	0.6553	-0.923
793.09802	0.6598	-0.926
793.10156	0.6646	-0.932

Table 7.3. Standard Cape-Kron colour indices of RV Crv.

MJD	PHASE	V	(B-V)	(V-R) _{kc}	(V-I) _{kc}
45000+					
768.05476	0.1459	8.711	0.384	0.237	0.463
768.07918	0.1786	8.656	0.383	0.236	0.453
768.13001	0.2467	8.616	0.397	0.231	0.468
791.76712	0.8788	8.796	0.397	0.226	0.474
791.78757	0.9061	8.869	0.401	0.226	0.461
791.82002	0.9496	9.049	0.414	0.234	0.468
791.84175	0.9786	9.169	0.414	0.274	0.493
791.86663	0.0119	9.166	0.417	0.249	0.494
791.88158	0.0318	9.140	0.399	0.260	0.499
791.91055	0.0706	8.959	0.383	0.249	0.481
791.93004	0.0967	8.848	0.381	0.240	0.475
791.96351	0.1415	8.729	0.384	0.236	0.463
791.97965	0.1631	8.690	0.388	0.235	0.463
792.00908	0.2024	8.637	0.383	0.230	0.457
792.02447	0.2230	8.623	0.388	0.230	0.461
792.05820	0.2682	8.617	0.391	0.232	0.458
792.07278	0.2877	8.623	0.391	0.229	0.458
792.09767	0.3210	8.649	0.407	0.222	0.457
792.77086	0.2219	8.646	0.357	0.236	0.472
792.78767	0.2444	8.627	0.369	0.229	0.462
792.81810	0.2851	8.632	0.393	0.230	0.459
792.83659	0.3099	8.650	0.389	0.239	0.467
792.87190	0.3571	8.695	0.394	0.241	0.473
792.88777	0.3783	8.718	0.401	0.239	0.471
792.91696	0.4174	8.801	0.395	0.237	0.463
792.93734	0.4447	8.868	0.399	0.235	0.466
792.97149	0.4904	8.915	0.384	0.232	0.452
792.99487	0.5217	8.910	0.381	0.233	0.465
793.01522	0.5489	8.876	0.379	0.236	0.466
793.05030	0.5959	8.756	0.382	0.239	0.467
793.06497	0.6155	8.711	0.383	0.234	0.460
793.08889	0.6475	8.667	0.383	0.222	0.451

Table 7.4. Orbital solution for RV Crv.

V_o	$= 19.0 \begin{smallmatrix} + \\ - \end{smallmatrix} 1.2 \text{ km s}^{-1}$
q	$= 0.27 \begin{smallmatrix} + \\ - \end{smallmatrix} 0.04$
K_{pr}	$= 64.0 \begin{smallmatrix} + \\ - \end{smallmatrix} 1.3 \text{ km s}^{-1}$
K_{sec}	$= 235 \begin{smallmatrix} + \\ - \end{smallmatrix} 37 \text{ km s}^{-1}$
$a_{pr} \sin i$	$= 0.95 \begin{smallmatrix} + \\ - \end{smallmatrix} 0.02 R_\odot$
$a_{sec} \sin i$	$= 3.45 \begin{smallmatrix} + \\ - \end{smallmatrix} 0.51 R_\odot$
$M_{pr} \sin^3 i$	$= 1.63 \begin{smallmatrix} + \\ - \end{smallmatrix} 0.48 M_\odot$
$M_{sec} \sin^3 i$	$= 0.44 \begin{smallmatrix} + \\ - \end{smallmatrix} 0.11 M_\odot$
$rms(pr)$	$= 6 \text{ km s}^{-1}$

Table 7.5. Photometric solutions for RV Crv assuming a radiative primary-component atmosphere.

Fixed : $T_{\text{eff pri}} = 6600\text{K}$, $A_{\text{pri}} = 1.0$
 $\beta_{\text{pri}} = 0.25$, $\beta_{\text{sec}} = 0.08$

q	$T_{\text{eff sec}}$ (K)	$R_{\text{mean sec}}$	$R_{\text{mean pri}}$	incl. (deg.)	A_{sec}	χ^2 ($\times 10^{-4}$)	Mean Res. ($\times 10^{-2}$)	rms ($\times 10^{-2}$)
0.21	5238 ⁺ ₁₀₂	0.253 ⁺ _{0.005}	0.502 ⁺ _{0.007}	86.0 ⁺ _{3.5}	2.45 ⁺ _{0.53}	14.82	-1.49	2.86
0.23	5188 ⁺ ₇₂	0.259 ⁺ _{0.003}	0.499 ⁺ _{0.004}	85.9 ⁺ _{1.8}	2.51 ⁺ _{0.36}	7.379	-1.01	2.04
0.24	5166 ⁺ ₅₈	0.262 ⁺ _{0.003}	0.498 ⁺ _{0.003}	86.1 ⁺ _{1.4}	2.53 ⁺ _{0.28}	4.822	-0.77	1.67
0.25	5140 ⁺ ₄₄	0.265 ⁺ _{0.002}	0.496 ⁺ _{0.002}	86.1 ⁺ _{1.0}	2.55 ⁺ _{0.21}	2.933	-0.54	1.33
0.26	5118 ⁺ ₃₄	0.268 ⁺ _{0.002}	0.495 ⁺ _{0.002}	86.3 ⁺ _{0.8}	2.56 ⁺ _{0.16}	1.730	-0.33	1.05
0.27	5092 ⁺ ₂₇	0.271 ⁺ _{0.001}	0.493 ⁺ _{0.001}	86.4 ⁺ _{0.6}	2.57 ⁺ _{0.12}	1.078	-0.12	0.86
0.28	5070 ⁺ ₂₆	0.272 ⁺ _{0.001}	0.492 ⁺ _{0.001}	86.5 ⁺ _{0.5}	2.59 ⁺ _{0.12}	0.9795	0.00	0.82
0.29	5051 ⁺ ₂₆	0.270 ⁺ _{0.001}	0.489 ⁺ _{0.001}	86.4 ⁺ _{0.5}	2.63 ⁺ _{0.12}	0.9949	-0.06	0.83
0.30	5040 ⁺ ₂₇	0.268 ⁺ _{0.001}	0.486 ⁺ _{0.001}	86.7 ⁺ _{0.6}	2.62 ⁺ _{0.12}	1.064	-0.18	0.84
0.31	5007 ⁺ ₃₄	0.267 ⁺ _{0.002}	0.483 ⁺ _{0.002}	86.5 ⁺ _{0.7}	2.65 ⁺ _{0.15}	1.704	-0.63	0.87
0.33	5008 ⁺ ₂₉	0.262 ⁺ _{0.001}	0.478 ⁺ _{0.001}	87.0 ⁺ _{0.8}	2.69 ⁺ _{0.13}	1.245	-0.34	0.87

Radii measured in units of semi-major axis of the relative orbit.

χ^2 measured in units of magnitude squared.

Mean residual and rms measured in units of magnitude.

Table 7.6. Photometric solutions for RV Crv assuming a convective primary-component atmosphere.

Fixed : $T_{\text{eff pri}} = 6600\text{K}$, $A_{\text{pri}} = 0.5$
 $\beta_{\text{pri}} = 0.08$, $\beta_{\text{sec}} = 0.08$

q	$T_{\text{eff sec}}$ (K)	$R_{\text{mean sec}}$	$R_{\text{mean pri}}$	incl. (deg.)	A_{sec}	χ^2 ($\times 10^{-4}$)	Mean Res. ($\times 10^{-2}$)	rms ($\times 10^{-2}$)
0.21	5766 ⁺⁹⁸ ₋₉₈	0.253 ^{+0.005} _{-0.005}	0.517 ^{+0.008} _{-0.008}	82.6 ^{+2.8} _{-2.8}	3.13 ^{+0.86} _{-0.86}	19.56	-2.41	3.11
0.23	5858 ⁺⁴⁷ ₋₄₇	0.259 ^{+0.003} _{-0.003}	0.484 ^{+0.004} _{-0.004}	90.0 ^{+2.9} _{-2.9}	3.74 ^{+0.46} _{-0.46}	7.275	-0.59	2.35
0.24	5835 ⁺⁴⁰ ₋₄₀	0.262 ^{+0.002} _{-0.002}	0.485 ^{+0.004} _{-0.004}	90.0 ^{+2.5} _{-2.5}	3.35 ^{+0.39} _{-0.39}	5.507	-0.45	2.07
0.25	5789 ⁺³² ₋₃₂	0.265 ^{+0.002} _{-0.002}	0.502 ^{+0.003} _{-0.003}	86.2 ^{+1.6} _{-1.6}	3.61 ^{+0.30} _{-0.30}	2.761	-0.46	1.40
0.26	5809 ⁺²⁷ ₋₂₇	0.268 ^{+0.002} _{-0.002}	0.498 ^{+0.002} _{-0.002}	87.9 ^{+2.9} _{-2.9}	3.39 ^{+0.25} _{-0.25}	2.040	-0.16	1.25
0.27	5792 ⁺²⁵ ₋₂₅	0.271 ^{+0.002} _{-0.002}	0.495 ^{+0.002} _{-0.002}	86.3 ^{+1.3} _{-1.3}	3.20 ^{+0.23} _{-0.23}	1.887	-0.06	1.19
0.28	5791 ⁺²⁷ ₋₂₇	0.270 ^{+0.002} _{-0.002}	0.492 ^{+0.002} _{-0.002}	87.0 ^{+1.9} _{-1.9}	3.18 ^{+0.25} _{-0.25}	2.190	-0.08	1.28
0.29	5781 ⁺²⁹ ₋₂₉	0.267 ^{+0.002} _{-0.002}	0.489 ^{+0.003} _{-0.003}	88.1 ^{+3.4} _{-3.4}	3.16 ^{+0.26} _{-0.26}	2.503	-0.01	1.38
0.30	5737 ⁺³⁴ ₋₃₄	0.264 ^{+0.002} _{-0.002}	0.481 ^{+0.003} _{-0.003}	90.0 ^{+1.9} _{-1.9}	2.93 ^{+0.32} _{-0.32}	3.978	-0.08	1.73
0.31	5745 ⁺³³ ₋₃₃	0.263 ^{+0.003} _{-0.003}	0.483 ^{+0.003} _{-0.003}	88.8 ^{+1.8} _{-1.8}	3.21 ^{+0.29} _{-0.29}	3.089	-0.07	1.54
0.33	5740 ⁺³⁵ ₋₃₅	0.257 ^{+0.002} _{-0.002}	0.475 ^{+0.003} _{-0.003}	90.0 ^{+1.8} _{-1.8}	3.22 ^{+0.34} _{-0.34}	4.180	-0.13	1.79

Radii measured in units of semi-major axis of the relative orbit.

χ^2 measured in units of magnitude squared.

Mean residual and rms measured in units of magnitude.

Table 7.7. Adopted photometric solutions for RV Crv.

	Radiative primary component:		Convective primary component:	
	Primary component	Secondary component	Primary component	Secondary component
Inclination (deg)		$86.5_{-0.5}^{+0.5}$		$86.3_{-1.3}^{+1.3}$
Mass Ratio *1		0.28		0.27
Luminosity Ratio *2		9.084		6.164
Temperature (K)	6600	5070_{-26}^{+26}	6600	5792_{-25}^{+25}
A *3	1.00	$2.59_{-0.12}^{+0.12}$	0.50	$3.20_{-0.23}^{+0.23}$
Radius (mean) *4	$0.492_{-0.001}^{+0.001}$	$0.272_{-0.001}^{+0.001}$	$0.495_{-0.002}^{+0.002}$	$0.271_{-0.002}^{+0.002}$
Radius (polar) *4	$0.461_{-0.001}^{+0.001}$	$0.255_{-0.001}^{+0.001}$	$0.464_{-0.002}^{+0.002}$	$0.254_{-0.002}^{+0.002}$
β *5	0.25	0.08	0.08	0.08
Roche lobe radii	0.492	0.276	0.495	0.273

*1 Fixed.

*2 V filter luminosity ratio at first quadrature from the LIGHT solution.

*3 Albedo (fixed for primary component).

*4 Unit is semi-major axis of the relative orbit.

*5 Prescribed gravity-darkening exponents.

(Although the solution was not very sensitive to the choice of the secondary component gravity-darkening exponent in the range 0.03-0.08, slightly better results were obtained when the value was set at the upper limit.)

Table 7.8. Astrophysical data for RV Crv.

	Radiative primary component:		Convective primary component:	
	Primary component	Secondary component	Primary component	Secondary component
Mass (M_{\odot})	$1.64_{-0.48}^{+0.48}$	$0.44_{-0.11}^{+0.11}$	$1.64_{-0.48}^{+0.48}$	$0.44_{-0.11}^{+0.11}$
Radius (R_{\odot})	$2.16_{-0.25}^{+0.25}$	$1.20_{-0.14}^{+0.14}$	$2.18_{-0.25}^{+0.25}$	$1.19_{-0.14}^{+0.14}$
Absolute vis.mag.	$2.40_{-0.26}^{+0.26}$ *	$4.80_{-0.26}^{+0.26}$ **	$2.39_{-0.25}^{+0.25}$ *	$4.36_{-0.25}^{+0.25}$ **
Absolute bol.mag.	$2.38_{-0.26}^{+0.26}$	$4.52_{-0.26}^{+0.26}$ ***	$2.37_{-0.25}^{+0.25}$	$4.22_{-0.25}^{+0.25}$ ***
Luminosity (L_{\odot})	$8.4_{-2.0}^{+2.0}$	$1.2_{-0.3}^{+0.3}$	$8.5_{-2.0}^{+2.0}$	$1.5_{-0.4}^{+0.4}$

* Calculated from equation 2 of Popper (1980) using the primary radius from the LIGHT solution, and the separation from the orbital solution.

** Calculated using the luminosity ratio from the LIGHT solution.

*** Bolometric corrections from Popper (1980).

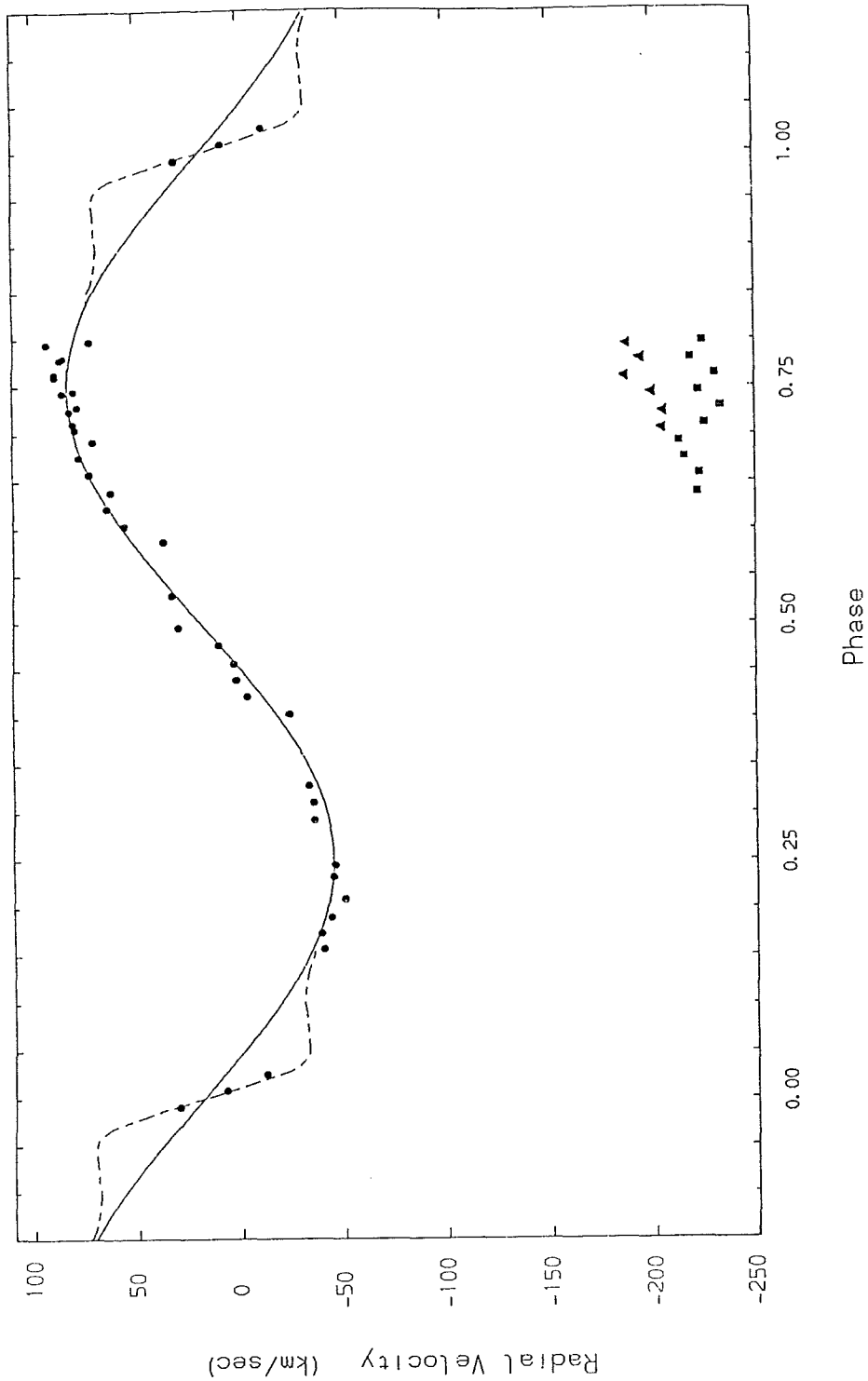


Figure 7.1.

Radial velocities of the primary and secondary components of RV Crv plotted against photometric phase, together with the orbital solution for the primary component, assuming a circular orbit. The secondary component data is shown by either squares or triangles, depending on which night the observations were obtained. The broken line is the expected rotational distortion through primary eclipse of the velocity curve of the primary component, calculated from the final parameters of the system, assuming a synchronously rotating primary.

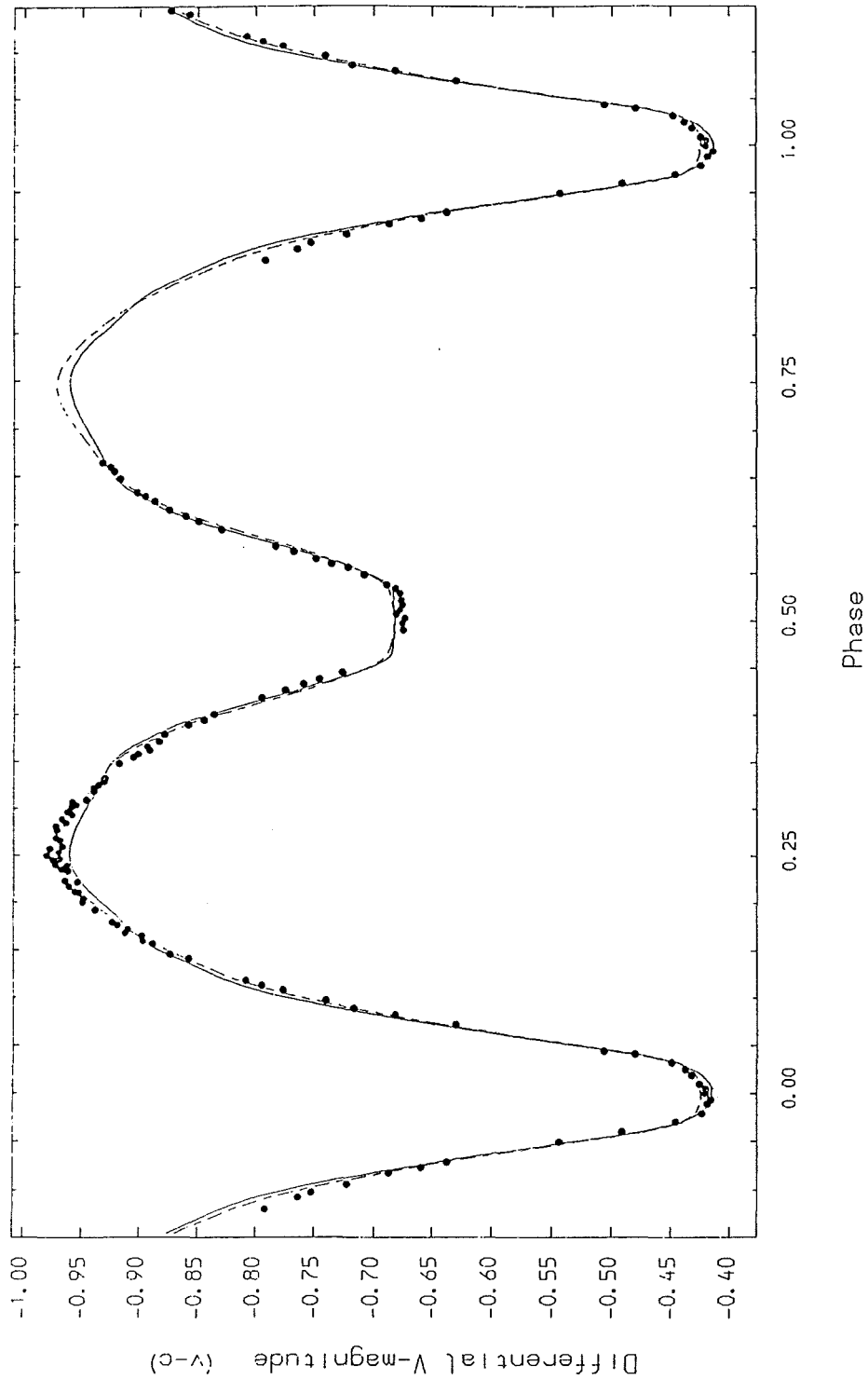


Figure 7.2.

V-light curve of RV Crv showing the individual observations from Table 7.2. and the adopted theoretical light curves from the final models given in Table 7.7 . The solutions employing the radiative and convective primary components are given by the broken and solid lines, respectively.

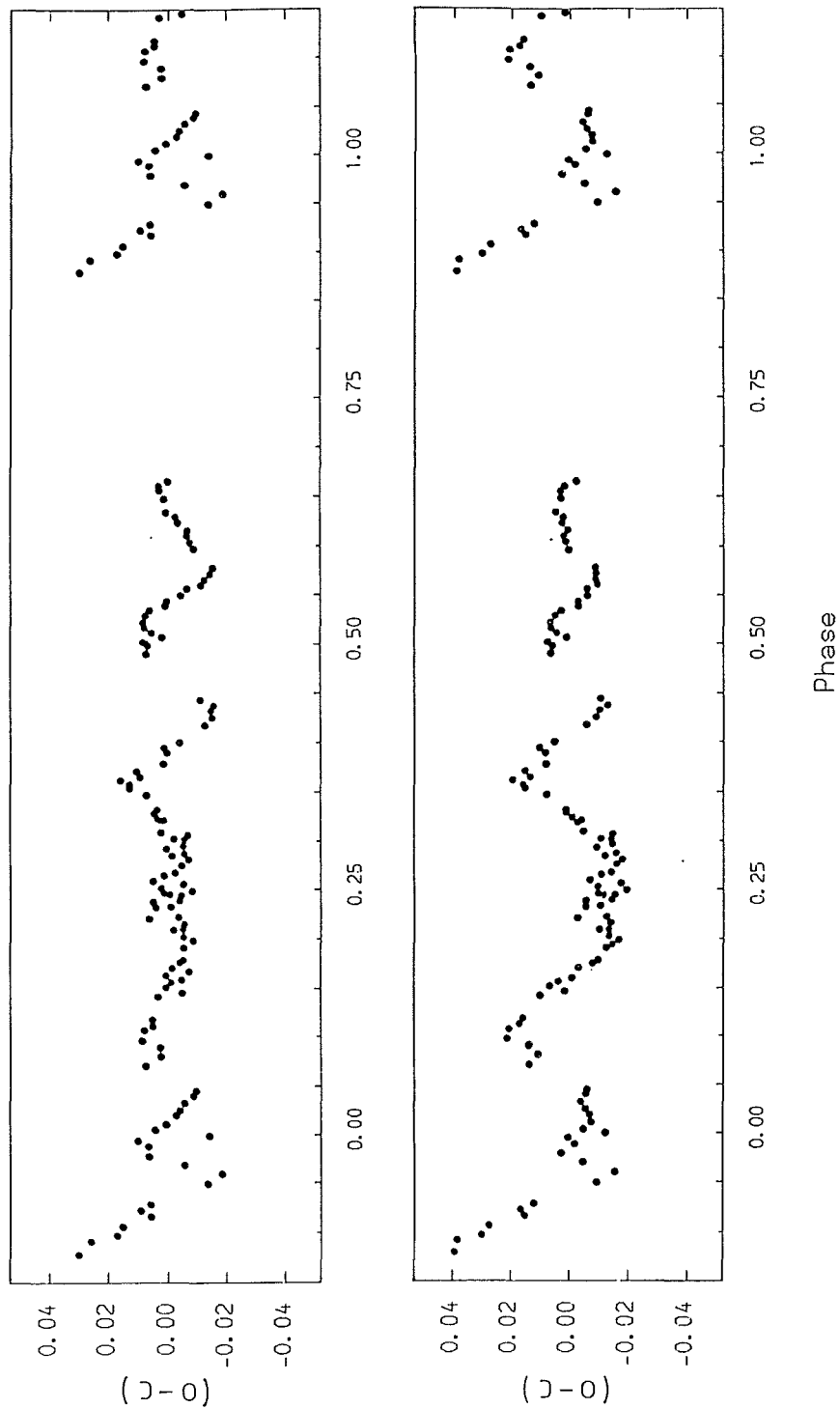


Figure 7.3.

V-magnitude residuals (in the sense observed minus calculated) for the adopted photometric solutions shown in Figure 7.2. The upper box refers to the solution employing the radiative primary component, and the lower box to that with the convective primary.

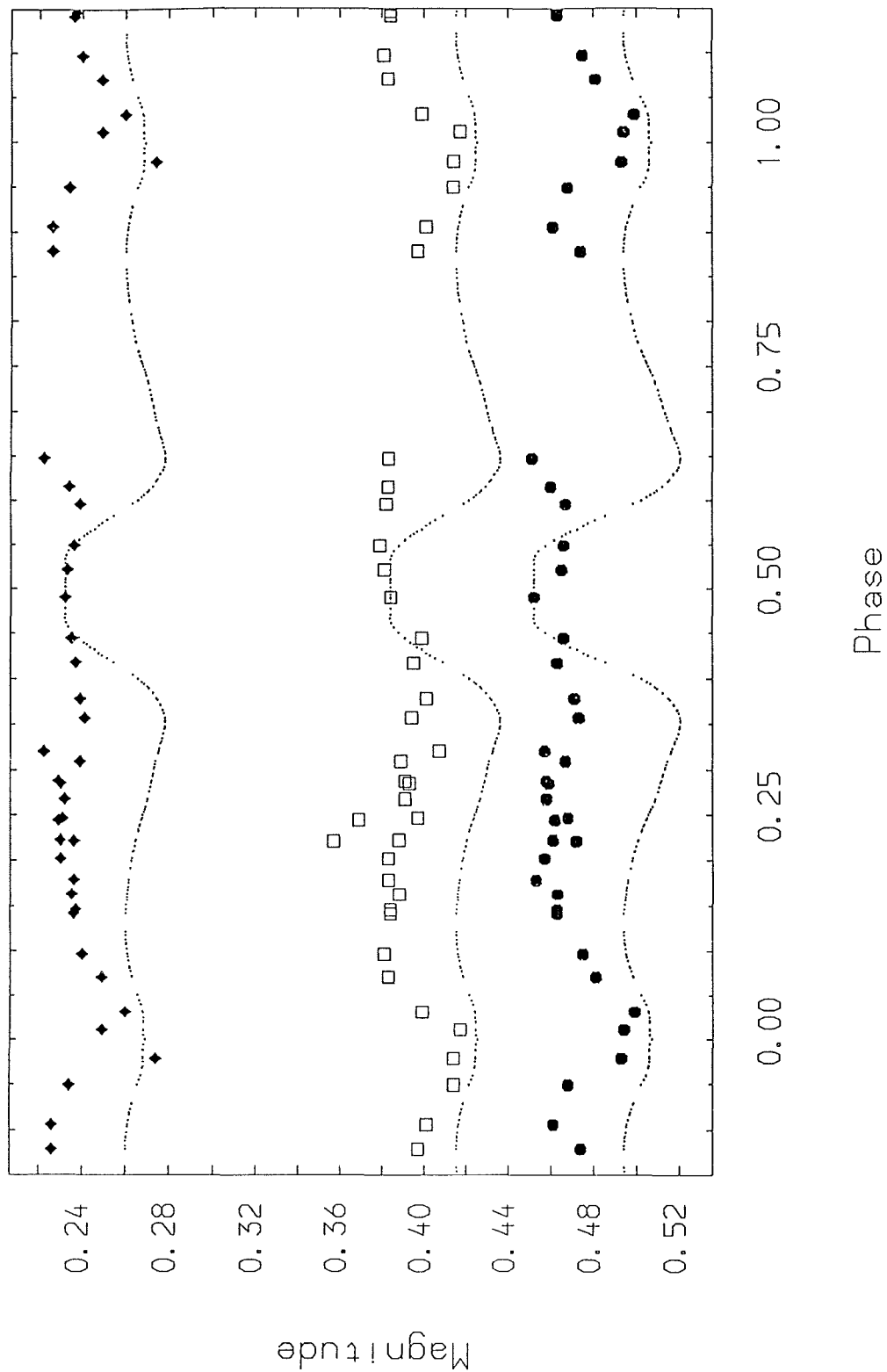


Figure 7.4.
 Cape-Kron colour indices of RV Crv plotted against phase. The $(B-V)$, $(V-R)_{kc}$ and $(V-I)_{kc}$ are the open squares, diamonds and circles, respectively. The expected colour indices, calculated from the LIGHT solution employing the radiative primary component, are shown by dots (Appendix 7.3).

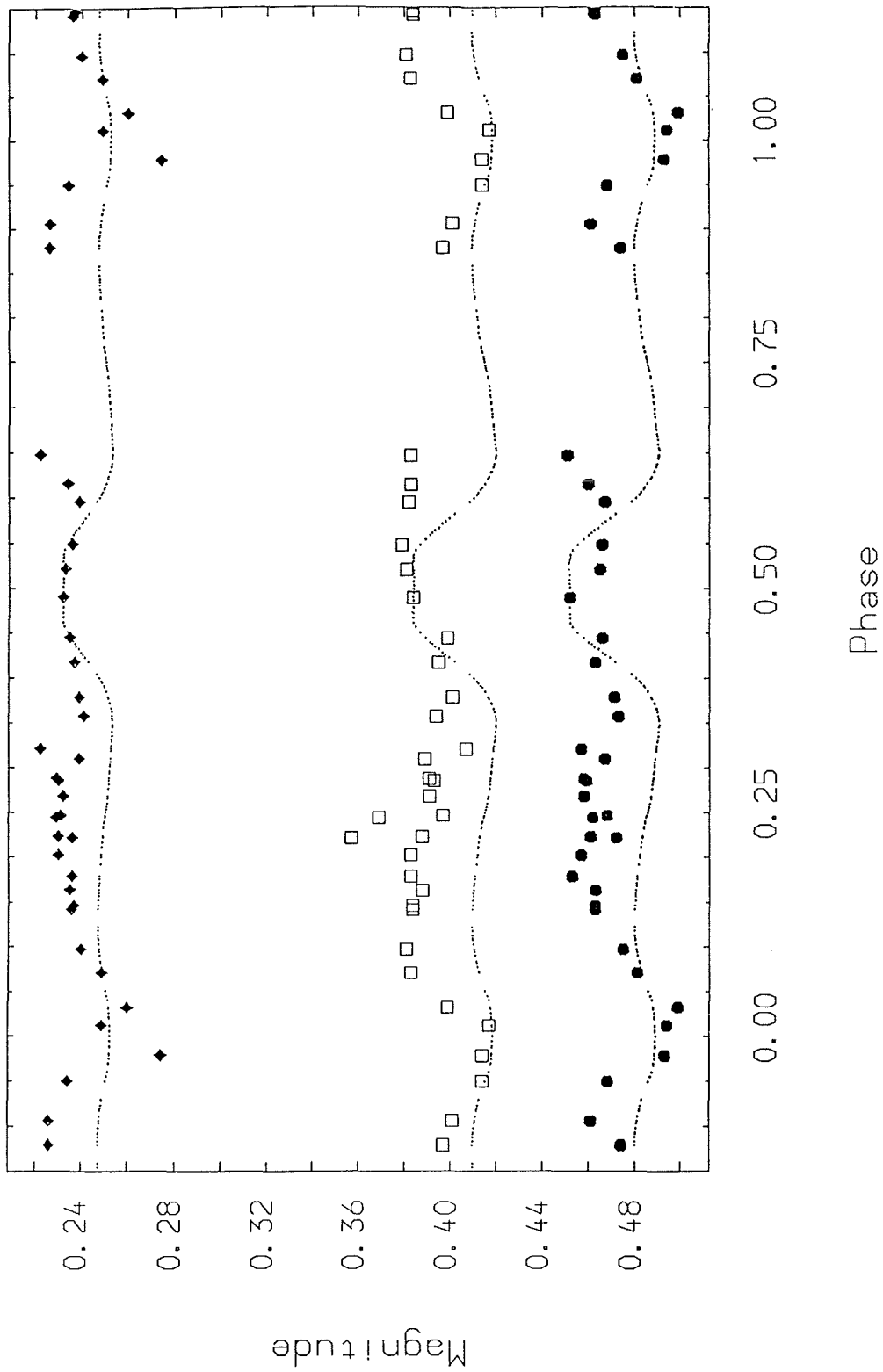


Figure 7.5.
 Cape-Kron colour indices of RV Crv plotted against phase. The $(B-V)$, $(V-R)_{kc}$ and $(V-I)$ are the open squares, diamonds and circles, respectively. The expected colour indices, calculated from the LIGHT solution employing the convective primary component, are shown by dots (Appendix 7.3).

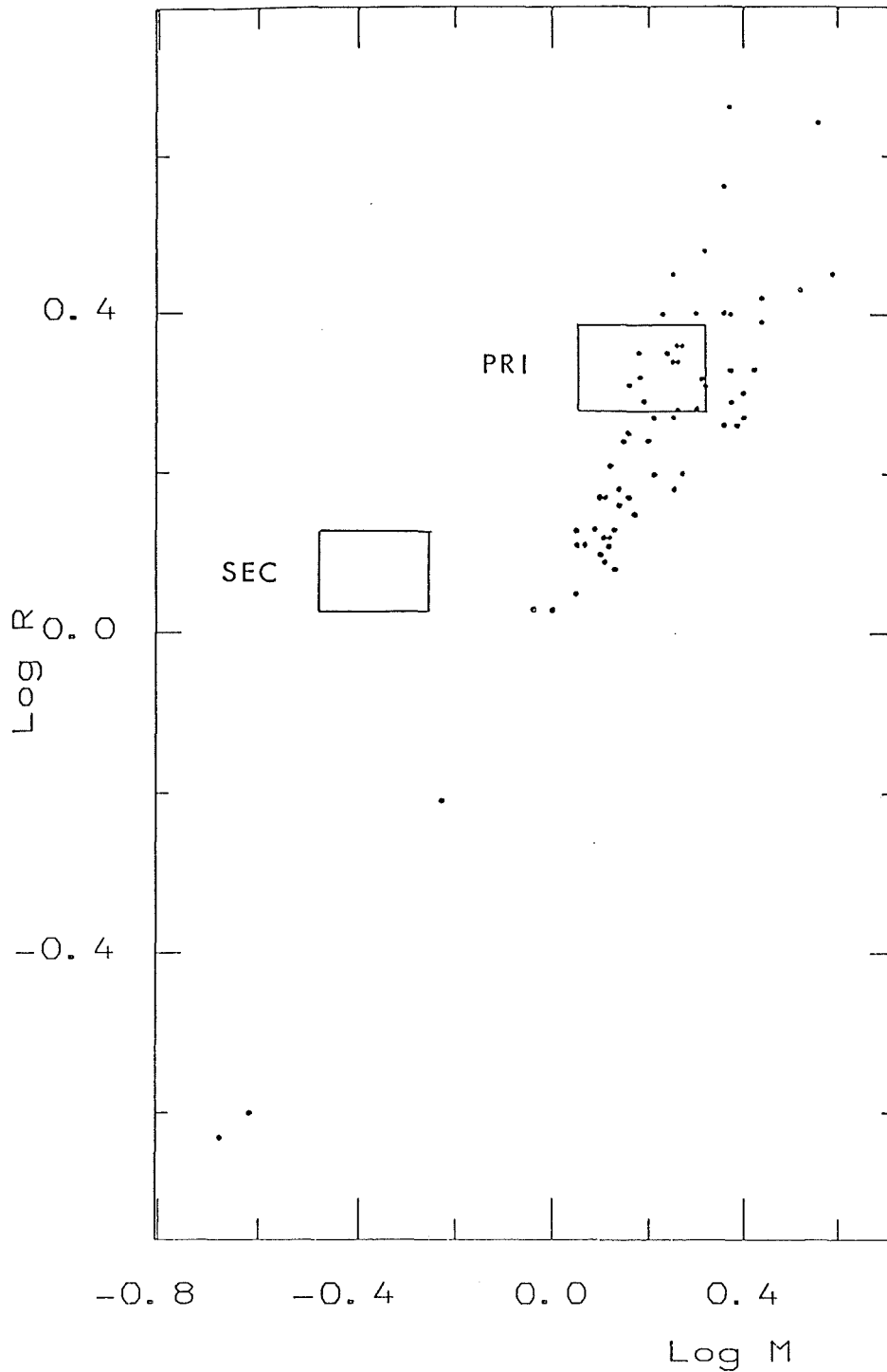


Figure 7.6.
 Mass-radii data for the primary and secondary components of RV Crv, from the LIGHT solution employing the radiative primary component, plotted together with the mass-radii data for main-sequence detached binaries from Popper(1980). While the primary component lies within the main-sequence band, the secondary component is clearly oversized for its mass. (See also Figure 7.7.)

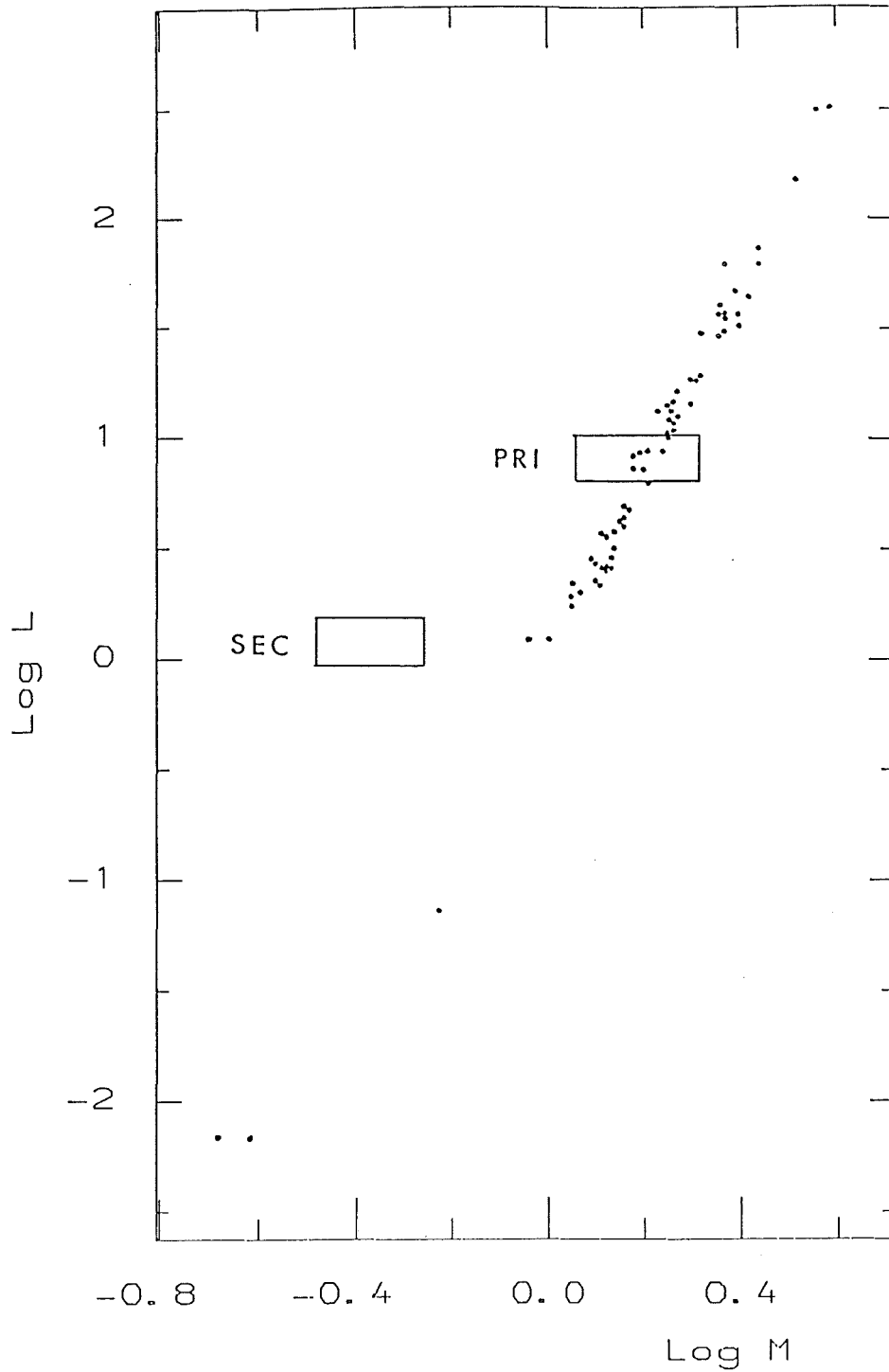


Figure 7.7.

Mass-luminosity data for the primary and secondary components of RV Crv, from the LIGHT solution employing the radiative primary component, plotted together with the mass-luminosity data for main-sequence detached binaries from Popper(1980). While the primary component lies within the main-sequence band, the secondary component is clearly overluminous for its mass. (See also Figure 7.6.)

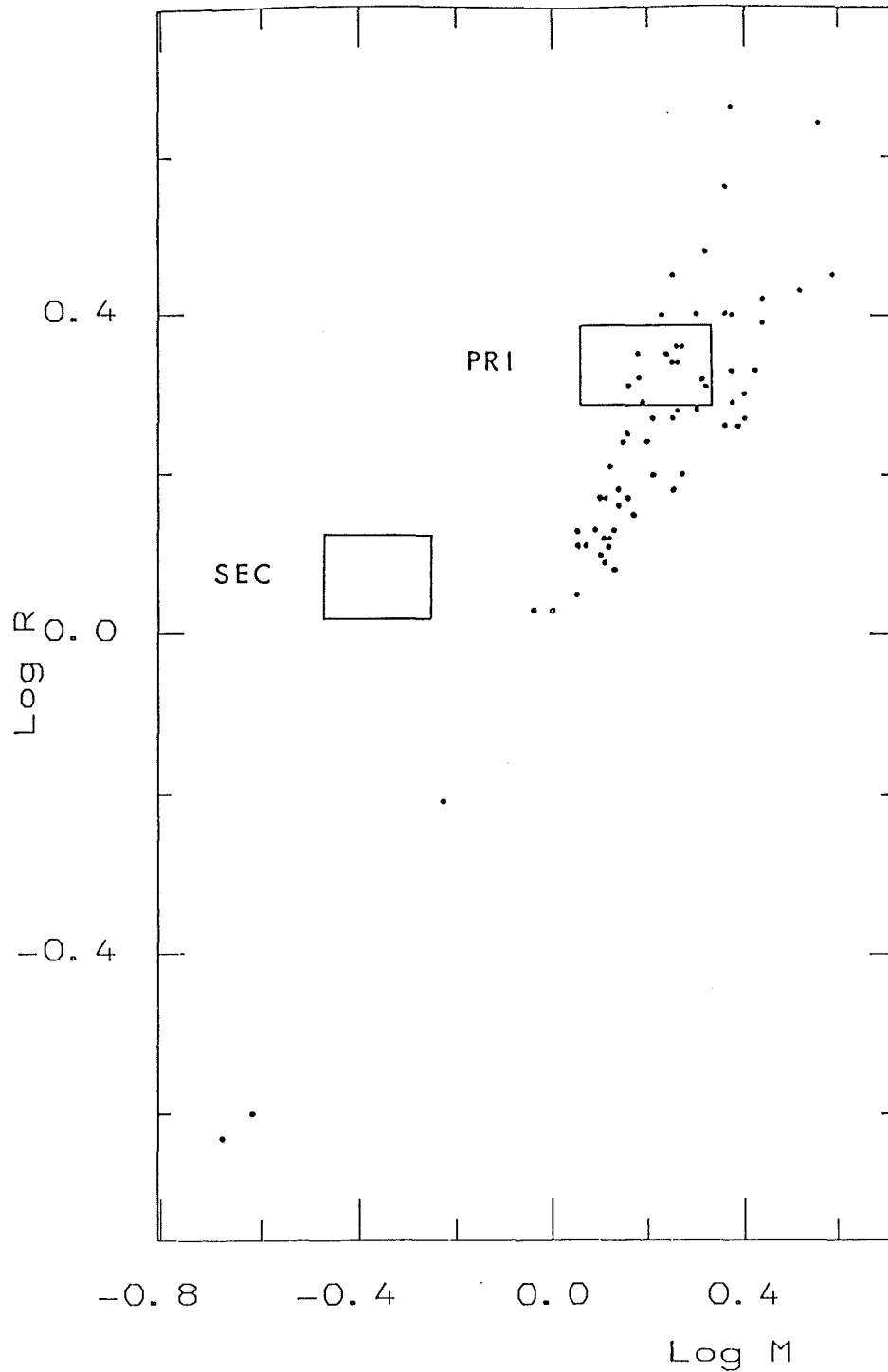


Figure 7.8.

Mass-radii data for the primary and secondary components of RV Crv, from the LIGHT solution employing the convective primary component, plotted together with the mass-radii data for main-sequence detached binaries from Popper(1980). While the primary component lies within or the main-sequence band, the secondary component is clearly oversized for its mass. (See also Figure 7.9.)

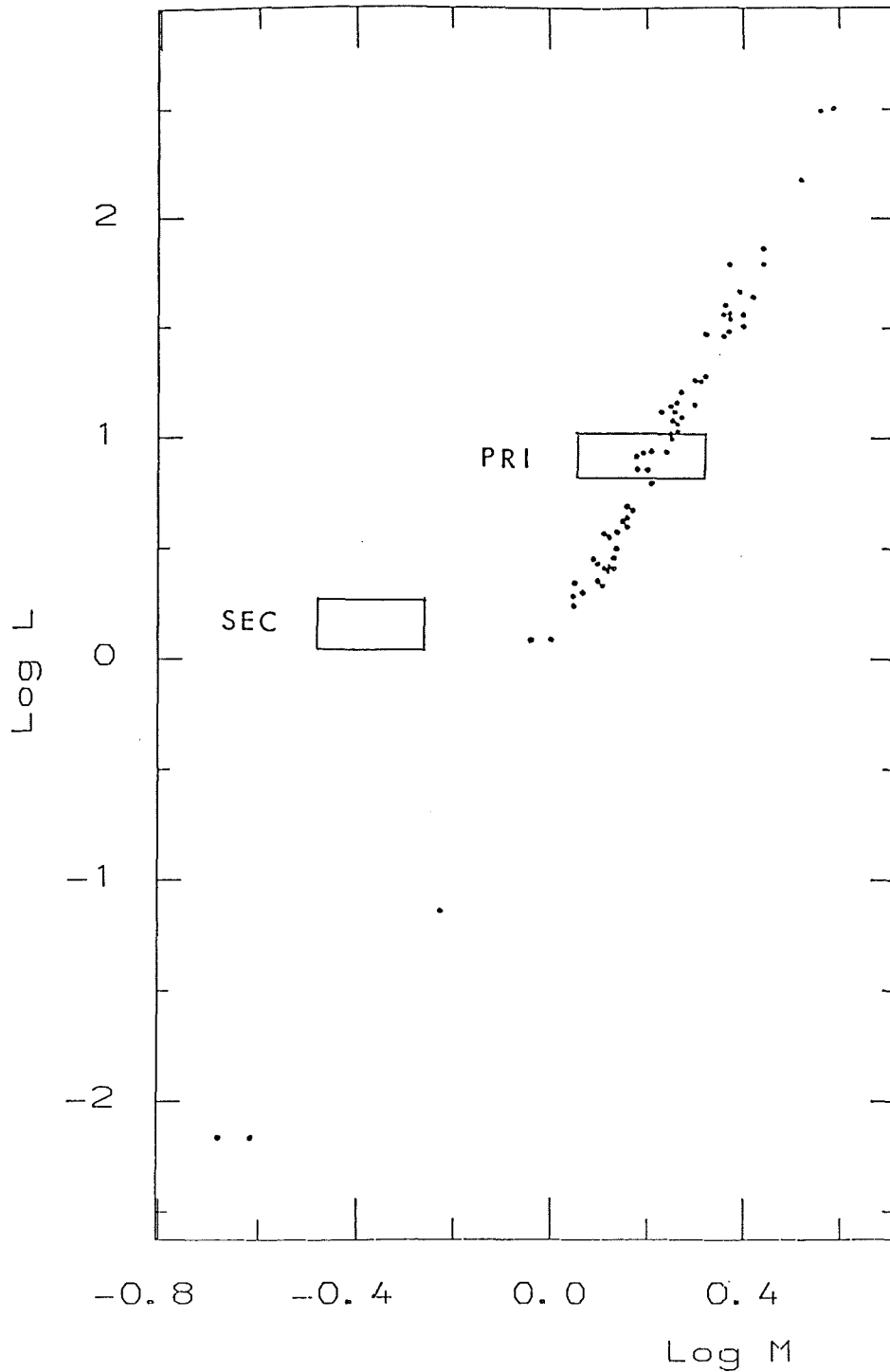


Figure 7.9.

Mass-luminosity data for the primary and secondary components of RV Crv, from the LIGHT solution employing the convective primary component, plotted together with the mass-luminosity data for main-sequence detached binaries from Popper(1980). While the primary component lies within the main-sequence band, the secondary component is clearly overluminous. (See also Figure 7.8.)

Appendix 7.1 Component mass-ratio, minimum masses and separations
calculated from the Lehman-Filhes orbit solution.

The analysis of the primary-component radial-velocity data using the
method of Lehman-Filhes, adopting a circular orbit, yields:

Systemic velocity,

$$V_o = (19.0 \pm 1.2) \text{ km s}^{-1}$$

Primary component radial-velocity semi-amplitude,

$$K_{pr} = (64.0 \pm 1.3) \text{ km s}^{-1}$$

Removing the systemic velocity from the measured radial velocities
for the double-lined phases, gives:

Spectrum Number	Phase	$ V_{pr_o} $ (km/s)	$ V_{sec_o} $ (km/s)	$ V_{pr_o} / V_{sec_o} $ = q_{spec}
439/068	0.638	43	241	0.180
439/070	0.658	53	243	0.220
439/072	0.676	58	235	0.249
439/074	0.692	52	232	0.224
439/076	0.711	61	245	0.250
439/078	0.729	59	253	0.234
439/080	0.745	61	242	0.252
439/082	0.763	70	250	0.279
439/084	0.781	66	238	0.278
439/086	0.798	53	244	0.218
440/004	0.705	60	223	0.270
440/006	0.725	63	224	0.281
440/008	0.743	66	218	0.305
440/010	0.761	70	206	0.340
440/012	0.779	68	212	0.320
440/014	0.795	74	206	0.362

Thus,

$$q_{\text{spec}} = 0.27 \pm 0.04$$

and, from equation 3.13,

$$K_{\text{sec}} = (235 \pm 37) \text{ km s}^{-1}$$

Now, calculating the semi-major axes using equations 3.2 and 3.4, gives,

$$\begin{aligned} a_{\text{pr}} \cdot \sin i &= (6.58 \pm 0.13) \times 10^5 \text{ km} \\ &= (0.95 \pm 0.02) R_{\odot} \end{aligned}$$

$$\begin{aligned} a_{\text{sec}} \cdot \sin i &= (2.40 \pm 0.38) \times 10^6 \text{ km} \\ &= (3.45 \pm 0.51) R_{\odot} \end{aligned}$$

The binary component separation, calculated using equations 3.5 and 3.6, is,

$$a \cdot \sin i = (4.40 \pm 0.51) R_{\odot}$$

Finally, the component minimum masses calculated according to equations 3.9 and 3.10, are,

$$\begin{aligned} M_{\text{pr}} \cdot \sin^3 i &= (1.63 \pm 0.48) M_{\odot} \\ M_{\text{sec}} \cdot \sin^3 i &= (0.44 \pm 0.11) M_{\odot} \end{aligned}$$

Appendix 7.2 Component visual and bolometric magnitudes and luminosities.

The Johnson colours observed during secondary eclipse are,

$$(B-V) = 0.384, 0.381$$

Using the data from the LIGHT solution which employed the radiative primary component atmosphere:

Applying equation 5.0 with values of F' of 3.818 and 3.819, (assuming interstellar reddening is negligible), we obtain,

$$M_{V \text{ pr}} = 2.40 \begin{matrix} + \\ - \end{matrix} 0.26$$

Applying a bolometric correction of -0.02 mag. (Table 1 of Popper, 1980),

$$M_{\text{bol pr}} = 2.38 \begin{matrix} + \\ - \end{matrix} 0.26$$

Now, using the V-magnitude luminosity ratio at quadrature, from the LIGHT solution,

$$\begin{aligned} M_{V \text{ sec}} &= (2.40 \begin{matrix} + \\ - \end{matrix} 0.26) + 2.5 \log(9.084) \\ &= 4.80 \begin{matrix} + \\ - \end{matrix} 0.26 \end{aligned}$$

Applying a bolometric correction of -0.28 mag. (Table 1 of Popper)

$$M_{\text{bol sec}} = 4.52 \begin{matrix} + \\ - \end{matrix} 0.26$$

Finally, using a value of 4.69 for the bolometric magnitude of the Sun, the component luminosities are given by,

$$\begin{aligned} L_{\text{pr}} &= 10^{0.4(4.69 - (2.38 \pm 0.26))} L_{\odot} \\ &= 8.39 \begin{matrix} + \\ - \end{matrix} 2.03 L_{\odot} \end{aligned}$$

$$L_{\text{sec}} = 10^{0.4(4.69 - (4.52 \pm 0.26))} L_{\odot}$$

$$= 1.17 \pm 0.29 L_{\odot}$$

Now, using the data from the LIGHT solution which employed the convective primary component atmosphere:

Applying equation 5.0 with the new component radii,

$$M_{\text{V pr}} = 2.39 \pm 0.25$$

and,

$$M_{\text{bol pr}} = 2.37 \pm 0.25$$

Using the V-magnitude luminosity ratio at quadrature from the LIGHT solution,

$$M_{\text{V sec}} = (2.39 \pm 0.25) + 2.5 \log(6.164)$$

$$= 4.36 \pm 0.25$$

Applying a bolometric correction of -0.14 mag. (Table 1 of Popper),

$$M_{\text{bol sec}} = 4.22 \pm 0.25$$

Finally, again assuming a value of 4.69 for the bolometric magnitude of the Sun, the component luminosities are given by,

$$L_{\text{pr}} = 10^{0.4(4.69 - (2.37 \pm 0.25))} L_{\odot}$$

$$= (8.47 \pm 1.97) L_{\odot}$$

$$L_{\text{sec}} = 10^{0.4(4.69 - (4.22 \pm 0.25))} L_{\odot}$$

$$= (1.54 \pm 0.36) L_{\odot}$$

Appendix 7.3 Expected colours of RV Crv.

From the LIGHT solution employing the radiative primary component:

$$T_{\text{eff pr}} = 6600\text{K}$$

$$T_{\text{eff sec}} = (5070 \pm 26) \text{ K}$$

The tables of Johnson (1966) give,

$$T_{\text{eff pr}} = 6600\text{K} \Rightarrow (B-V)_o = 0.383$$

$$(V-R)_o = 0.367$$

$$(V-I)_o = 0.580$$

$$T_{\text{eff sec}} = 5070\text{K} \Rightarrow (B-V)_o = 0.881$$

$$(V-R)_o = 0.701$$

$$(V-I)_o = 1.157$$

Applying the conversion formulae of Cousins (1980) (Appendix 5.5),

$$T_{\text{eff pr}} = 6600\text{K} \Rightarrow (V-R)_{o \text{ kc}} = 0.242$$

$$(V-I)_{o \text{ kc}} = 0.457$$

$$T_{\text{eff sec}} = 5070\text{K} \Rightarrow (V-R)_{o \text{ kc}} = 0.610$$

$$(V-I)_{o \text{ kc}} = 0.901$$

Now, from the LIGHT solution employing the convective primary component:

$$T_{\text{eff sec}} = (5792 \pm 25) \text{ K}$$

The tables of Johnson (1966) give,

$$T_{\text{eff sec}} = 5792\text{K} \Rightarrow (B-V)_o = 0.623$$

$$(V-R)_o = 0.525$$

$$(V-I)_o = 0.852$$

Again, applying the conversion formulae of Cousins (1980),

$$T_{\text{eff sec}} = 5792\text{K} \Rightarrow (V-R)_{\text{O kc}} = 0.355$$

$$(V-I)_{\text{O kc}} = 0.666$$

The expected colours of RV Crv, calculated using equation 5.1 (assuming negligible interstellar reddening), for the LIGHT solutions employing the radiative and convective primary components, are shown in Figures 7.4 and 7.5, respectively.

The expected colour indices of RV Crv appear to be in reasonable agreement with the observed data at both primary and secondary minima, for both photometric solutions. However, there exists a large discrepancy between the observed and calculated colours at those phases lying outside eclipse; the observed colours appearing to be about 0.04 mag. and 0.02 mag. bluer than expected, for the LIGHT solutions employing the radiative and convective primary components, respectively. This effect may be caused by a hotspot situated near the connecting neck of the binary.

Appendix 7.4 Angular momentum of RV Crv.

From the orbital solution and the LIGHT solution which employed the radiative primary component:

$$m_{pr} = (3.28 \pm 0.96) \times 10^{30} \text{ kg}$$

$$m_{sec} = (0.88 \pm 0.22) \times 10^{30} \text{ kg}$$

$$a = (3.06 \pm 0.35) \times 10^9 \text{ m}$$

$$r_{pr} = (1.50 \pm 0.17) \times 10^9 \text{ m}$$

$$r_{sec} = (0.84 \pm 0.10) \times 10^9 \text{ m}$$

Calculating the orbital angular momentum of the system according to equations 5.10a and 5.10b,

$$J_{orb} = (7.45 \pm 6.06) \times 10^{44} \text{ kg m}^2 \text{ s}^{-1}$$

The total rotational angular momentum of the components, given by equations 5.4, 5.5, 5.6 and 5.7, is,

$$J_{rot\ tot} = (3.11 \pm 1.06) \times 10^{44} \text{ kg m}^2 \text{ s}^{-1}$$

Finally, the total angular momentum of the system, calculated using equations 5.8 and 5.9, is,

$$J_{tot} = (1.06 \pm 0.62) \times 10^{45} \text{ kg m}^2 \text{ s}^{-1}$$

Now, using the data derived from the orbital solution and the LIGHT solution employing the convective primary component:

$$r_{pr} = (1.52 \pm 0.17) \times 10^9 \text{ m}$$

$$r_{sec} = (0.83 \pm 0.10) \times 10^9 \text{ m}$$

Again, using the same equations as above,

$$J_{orb} = (7.45 \pm 6.06) \times 10^{44} \text{ kg m}^2 \text{ s}^{-1}$$

$$J_{rot\ tot} = (3.19 \pm 1.09) \times 10^{44} \text{ kg m}^2 \text{ s}^{-1}$$

$$J_{tot} = (1.06 \pm 0.62) \times 10^{45} \text{ kg m}^2 \text{ s}^{-1}$$

(n. b. See Appendix B.)

CHAPTER 8

EZ HYDRAE, AD PHOENICIS & RS COLUMBAE

8.1. INTRODUCTION:

EZ Hydrae:

The variability of EZ Hya was first discovered by Hoffmeister (1931). Zessewitsch (1949) classified the system as a W UMa-type binary of orbital period 0.449768 days, with a displaced secondary minimum in the light curve. Times of minima have been published by Pohl and Kizilirmak (1972), Bookmyer (1974), and Bookmyer and Faulkner (1978), who also reported a revised estimate of the period of 0.44975201 days. Koch (1974) determined a CN index for EZ Hya, and Eggen (1978) has published colour indices. The spectral type of EZ Hya was classified as G5 by MacDonald (1964), and as F9 by Gotz and Wenzel (1966). King and Hilditch (1984) have published radial-velocity data for the binary, determining a value for the mass ratio of 0.25 ± 0.01 . Finally, Russo, Vittone and Milano (1984) report spectroscopic and photometric observations of the system.

AD Phoenicis:

Times of minimum light for AD Phe have been published by Strohmeier and Bauernfeind (1969). Strohmeier and Bauernfeind also determined a value for the orbital period of AD Phe of 0.6132295 days.

RS Columbae:

The variability of RS Col was first noted by Hoffmeister (1935, 1942), who also reported light variations of approximately 0.4 mag., of period 14.66 days (Hoffmeister, 1943a, 1943b). Times of minima for the system have been given by Bond and Landolt (1969), who identified RS Col as a W UMA-type binary, with an orbital period of either 0.4017 days or 0.6740 days.

8.2. PHOTOMETRIC OBSERVATIONS:

The photoelectric observations of the three contact systems were obtained using the 0.5m telescope at the South African Astronomical Observatory (SAAO), which was equipped with a Peoples Photometer and a set of BVRI_c filters.

A comparison star and a check star were selected for each variable star. The stars chosen were of similar colour to the variables, and lay in close proximity to them in the sky, thus virtually eliminating any extinction or second-order colour effects in the calculation of the differential magnitudes. A local standard

star was also selected for each variable, to serve as an additional check star, and to monitor any drifts in the zero points.

The observations of EZ Hya were obtained by the author during the period 7-30 March 1984. The comparison star, SA0155167 (V=9.0, F8), and check star, SA0155189 (V=8.9, F5), were both found to be constant in brightness to better than ~ 0.01 mag. . The local E-region standard was E445 (HD82224, V=6.601).

The author obtained the observations of AD Phe during the period 19-30 October 1984. Both the comparison star, SA0215431 (V=8.7, F2), and check star SA0215421 (V=8.8, F8), were found to be constant in light to better than ~ 0.01 mag. . E106 (HD9404, V=7.863) was selected as the local standard star.

Dr.D.J.King obtained colour indices of RS Col over the period 19-25 October 1982, and the author obtained observations of the star between 23 November and 3 December 1983. The comparison star, SA0170274 (V=9.2, F5), and check star, SA0170206 (V=9.1, F8) were found to be constant in brightness to better than ~ 0.01 mag. . The local standard star was E253 (HD27471, V=7.535).

As discussed in Chapter 4, the variable and comparison stars were monitored using only the V filter, with observations of the variables through all four filters at intervals of approximately 25 minutes. The stellar integrations were carried out in units of 30 seconds, two consecutive units for the comparison star observations, alternating with four consecutive units for the variable. For EZ Hya and RS Col, these observations were averaged

to single values when calculating the instrumental magnitudes.

Sets of E- and F-region standard stars were observed at the beginning and end of each night (if weather permitted). The local standard stars were observed hourly, and red and blue standards were observed at intervals of approximately two hours.

All data were first reduced to instrumental magnitudes, using the SAAO photometry reduction program, with all four-colour observation sets being further reduced to standard magnitudes and colours. The differential magnitudes were calculated using the technique described in Chapter 4.

8.3. REVISED EPHEMERIDES:

In common with the previous analyses, all times of minima were calculated using the method of Kwee and van Woerden (1956).

Two times of minima (primary and secondary), were obtained for EZ Hya. The primary eclipse, although very distorted (see Figure 8.3a), appears to be complete. The secondary minimum is displaced by approximately +0.004 days (i.e. occurring later than expected). This is smaller than the displacement of +0.018 days, reported by Zessewitsch (1949). A revised estimate for the orbital period of EZ Hya was obtained by applying a linear least-squares solution to all published times of minima for the system. This revised period, together with the time of primary minimum obtained by the author, yields an updated ephemeris:

$$\text{MJD } 45767.9188_{-0.0008}^{+0.0008} + 0.4497489_{-0.0000006}^{+0.0000006} \text{ E (s.e.)}$$

The revised ephemeris for EZ Hya indicates that there has been a significant decrease in the orbital period of the system since 1975, in agreement with the findings of King and Hilditch (1984). Residuals for the published times of minima, calculated using the above ephemeris, are given in Table 8.1a and in Figure 8.1a. These results indicate that there may have been abrupt changes in the period of EZ Hya, as suggested by Russo et al. (1984).

Because the light curve of EZ Hya is fairly symmetric around secondary minimum, but very distorted near primary, the orbital phases used in the photometric analysis were not calculated using the above time of primary minimum, but instead, calculated so as to place secondary minimum at phase 0.5 .

Five times of minima (four primary and one secondary), were obtained for AD Phe. The primary and secondary minima of the light curve appear to be of nearly equal depth, and neither appears to be total or annular. A linear least-squares analysis of the author's times of minima (two of which were obtained on a single night), and those of Strohmeier and Bauernfeind (1969), demonstrate that the orbital period of AD Phe is about 0.3799344 days. This is substantially shorter than the period of 0.6132295 days, reported by Strohmeier and Bauernfeind. The new period, together with one of the author's times of primary minimum, yields a revised ephemeris:

$$\text{MJD } 46002.8683_{-0.0001}^{+0.0001} + 0.3799344_{-0.0000004}^{+0.0000004} \text{ E (s.e.)}$$

Residuals for the times of minima, calculated using the new ephemeris, are shown in Figure 8.1b and Table 8.1b. The residuals indicate that there may be very rapid changes in the orbital period of AD Phe, or that there may be a third component present. (The latter hypothesis seems unlikely, since there is no evidence for a third component in the observed colour indices of the binary.)

Two times of minima (primary and secondary) were obtained for RS Col. From the author's photometry it is clear that the orbital period of RS Col is nearer to Bond and Landolt's (1969) upper estimate of 0.6740 days. The new times of minima, combined with the time of primary minimum published by Bond and Landolt, gives a revised ephemeris:

$$\text{MJD } 45670.9118_{-0.0004}^{+0.0004} + 0.67235579_{-0.00000001}^{+0.00000001} \text{ E (s.e.)}$$

The residuals for the times of minima, calculated using this ephemeris, are given in Table 8.1c. (Since only three observations were employed in the calculation of the orbital period, the corresponding error on the value is unrealistically small.)

8.4. PHOTOMETRIC ANALYSES:

The observed differential V-magnitudes for EZ Hya, AD Phe and RS Col are given in Tables 8.3a, 8.3b and 8.3c, and presented graphically in Figures 8.3a.i, 8.3b.i and 8.3c.i. The light curves of AD Phe and RS Col display minima which are of nearly equal depth, while for EZ Hya the depths of primary and secondary minima differ

by about 0.1 mag. . . As discussed earlier, the primary eclipse of the light curve of EZ Hya appears to be total/annular; the spectroscopic data of King and Hilditch (1984) show that the system is a W-type W UMa binary, with the smaller secondary component appearing hotter than its companion.

For EZ Hya, the level of maximum light observed at first quadrature appears to be about 0.1 mag. brighter than that observed at second quadrature. Furthermore, the differential V-magnitude data around phase 0.75, which is composed of observations obtained over a period of 22 days, shows a distinct change in the maximum light level of about 0.02 mag. . The heavily distorted primary minimum strongly suggests that starspots are present on the surface of the binary. For the light curve of AD Phe, first quadrature appears to be about 0.05 mag. brighter than second quadrature, although the curve appears to be fairly stable over the period of 10 days when the observations were obtained. Neither eclipse appears to be complete. Finally, the levels of maximum light at the quadratures of RS Col are nearly equal, although the position of maximum light near first quadrature appears to be slightly displaced from phase 0.25, towards secondary minimum. As in the case of AD Phe, both eclipses appear to be partial.

The observed colour indices for the three binaries are listed in Tables 8.2a, 8.2b and 8.2c, and displayed graphically in Figures 8.2a, 8.2b and 8.2c, indicate that there is very little change in the colours of the systems with phase. The temperatures of the primary components of AD Phe and RS Col were estimated from

the colours observed near secondary eclipse, while for EZ Hya, the primary-component temperature was estimated from the colours near primary eclipse. The tables of Popper (1980) yielded temperatures of 5690K, 5850K and 5950K, for the primary components of EZ Hya, AD Phe and RS Col, respectively.

Solutions to the light curves were sought using the WUMA3 code of Rucinski (1973), employing the atmospheres from Table 5b of Kurucz (1979). (A detailed description of the WUMA3 code is given in Section 4.4.3.) In the search for the photometric solutions, primary-component temperatures were fixed, as were the gravity-darkening exponents and the albedos, which were set to values appropriate for convective common envelopes.

Before WUMA3 could be run, spline points had to be calculated from the observed data, at phase intervals of 0.01. For each light curve, the data from phase 0.0 to 0.5 was analysed separately from the data from phase 0.5 to 1.0. Since WUMA3 expects the larger component to be eclipsed at primary minimum, the data for EZ Hya had to be shifted in phase so as to place the shallower minimum at phase 0.0, before analysis could proceed.

Unfortunately, no satisfactory photometric solutions could be obtained for EZ Hya, either with the mass ratio set at the spectroscopic value of 0.25, or with the ratio treated as a free parameter. Perhaps this is not surprising when one considers the 'distortions' evident in the light curve. Details of the analysis are given in Table 8.4a and in Figures 8.3a.i-iv.

When the mass ratio of AD Phe was treated as a free parameter, a photometric solution could only be obtained for the first half of the light curve. This yielded a value for q of 0.94 ± 0.03 , which if correct, places AD Phe as the W UMa-type binary with the highest mass ratio (higher than SW Lac with its mass ratio of 0.87). For the data from the second half of the light curve, q drifted towards unity, and was eventually fixed at the physically unrealistic value of 1.0. Details of both these solutions are given in Table 8.4b and Figures 8.3b.i-vi. In order to obtain some estimate of the sensitivity of these solutions to mass ratio, new solutions were sought with q fixed at a lower value of 0.5. The resultant fits, details of which are given in Table 8.4b and Figures 8.3b.vii-xii, do not match the spline-fit data quite as well as the original solutions. The quality-of-fit parameters ('W' in Table 8.4b) are slightly higher for the second solutions, indicating a slightly poorer fit. These results imply that the mass ratio is not a particularly important factor in determining the best fit to the data. Thus, the value of 0.94 derived for the mass ratio in the first solution, must be treated with considerable caution.

The search for a photometric solution for RS Col involved using the data from the second half of the light curve only, since the position of maximum light near first quadrature is displaced from phase 0.25. Like AD Phe, when the mass ratio was treated as a free parameter, q drifted towards unity, and was finally fixed at value of 1.0. Details of this solution are given in Table 8.4c and in Figures 8.3c.i-iii. Again, to gauge some idea of the importance of the mass ratio to the fit, q was fixed at a value of 0.5, and a new

solution sought. The results of this second run, given in Table 8.4c and in Figures 8.3c.iv-vi, show that the former solution provides a slightly closer match to the data. So again, the mass ratio does not appear to be a particularly important factor in establishing the best fit to the light curve.

8.5. CONCLUSIONS:

Although the failure to obtain a photometric solution for EZ Hya is somewhat disappointing, the marked changes in the light curve, over what is a relatively short period of time, makes the system an attractive target for any future observations intended to gather information on starspot activity.

The results for AD Phe and RS Col demonstrate the importance of determining values for the mass ratios of contact binaries from spectroscopic observations. This is especially important for those contact systems with light curves which display partial eclipses.

Table 8.1a. Times of minima of EZ Hya and their residuals.

Ephemeris: $MJD = 45767.9188_{-0.0008}^{+0.0008} + 0.4497489_{-0.0000006}^{+0.0000006} E$

Time of minimum (MJD)	ΔMJD	$\Delta MJD/\text{period}$	Cycle No.	Residual (cycles)
40253.3256	5514.5932	12261.493	-12261.5	-0.007
40255.3477	5512.5711	12256.997	-12257.0	-0.003
40269.2921	5498.6267	12225.992	-12226.0	-0.008
40634.2745	5133.6443	11414.467	-11414.5	-0.033
40981.0293	4786.8895	10643.471	-10643.5	-0.029
42449.2404	3318.6784	7378.958	-7379.0	-0.042
42451.2660	3316.6528	7374.455	-7374.5	-0.045
42452.1672	3315.7516	7372.451	-7372.5	-0.049
42453.2887	3314.6301	7369.957	-7370.0	-0.043
42454.1878	3313.7310	7367.958	-7368.0	-0.042
42455.0883	3312.8305	7365.956	-7366.0	-0.044
42456.2139	3311.7049	7363.453	-7363.5	-0.047
42457.1128	3310.8060	7361.454	-7361.5	-0.046
42458.2351	3309.6837	7358.959	-7359.0	-0.041
42459.1351	3308.7837	7356.958	-7357.0	-0.042
42461.1617	3306.7571	7352.452	-7352.5	-0.048
45767.9188	0.0000	0.000	0.0	0.000
45788.8363	-20.9175	-46.509	+46.5	+0.009

Table 8.1b. Times of minima of AD Phe and their residuals.

Ephemeris: $MJD = 46002.8683_{-0.0001}^{+0.0001} + 0.3799344_{-0.0000004}^{+0.0000004} E$

Time of minimum (MJD)	ΔMJD	$\Delta MJD/\text{period}$	Cycle No.	Residual (cycles)
28672.156	17330.712	45615.011	-45615.0	+0.011
28699.112	17303.756	45544.062	-45544.0	+0.062
28722.123	17280.745	45483.496	-45483.5	-0.004
28829.822	17173.046	45200.029	-45200.0	+0.029
28841.800	17161.068	45168.502	-45168.5	+0.002
28860.795	17142.073	45118.507	-45118.5	+0.007
36780.940	9221.928	24272.421	-24272.5	-0.079
36783.992	9218.876	24264.388	-24264.5	-0.112
36787.976	9214.892	24253.902	-24254.0	-0.098
36788.942	9213.926	24251.360	-24251.5	-0.140
36810.959	9191.909	24193.410	-24193.5	-0.090
36841.964	9160.904	24111.804	-24112.0	-0.196
36846.875	9155.993	24098.878	-24099.0	-0.122
38282.969	7719.899	20319.031	-20319.0	+0.031
38294.951	7707.917	20287.494	-20287.5	-0.006
38314.914	7687.954	20234.951	-20235.0	-0.049
38318.873	7683.995	20224.530	-20224.5	+0.030
38338.837	7664.031	20171.984	-20172.0	-0.016
38354.804	7648.064	20129.959	-20130.0	-0.041
38641.993	7360.875	19374.068	-19374.0	+0.068
38693.895	7308.973	19237.460	-19237.5	-0.040
38710.807	7292.061	19192.947	-19193.0	+0.053
38725.772	7277.097	19153.561	-19153.5	+0.061
39006.004	6996.864	18415.976	-18416.0	-0.024
39361.035	6641.833	17481.525	-17481.5	+0.025
39388.958	6613.910	17408.031	-17408.0	+0.031
39413.823	6589.045	17342.585	-17342.5	+0.085
39443.816	6559.053	17263.646	-17263.5	+0.146
39444.814	6558.054	17261.016	-17261.0	+0.016
39767.937	6234.931	16410.546	-16410.5	+0.046
45997.9291	4.9391	13.000	-13.0	0.000
45999.0676	3.8006	10.003	-10.0	+0.003
45999.8289	3.0393	8.000	-8.0	0.000
46000.0199	2.8483	7.497	-7.5	-0.003
46002.8683	0.0000	0.000	0.0	0.000

Table 8.1c. Times of minima of RS Col and their residuals.

Ephemeris: $MJD = 45670.9118_{-0.0004}^{+0.0004} + 0.67235579_{-0.00000001}^{+0.00000001} E$

Time of minimum (MJD)	ΔMJD	$\Delta MJD/\text{period}$	Cycle No.	Residual (cycles)
39535.6652	6135.2466	9124.997	-9125.0	-0.003
45669.9032	1.0086	1.500	-1.5	0.000
45670.9118	0.0000	0.000	0.0	0.000

Table 8.2a. Standard Cape-Kron colour indices of EZ Hya.

MJD	PHASE	V	(B-V)	(V-R) _{kc}	(V-I) _{kc}
45000+					
766.82684	0.5721	10.861	0.644	0.390	0.745
766.86958	0.6671	10.608	0.633	0.383	0.727
766.89456	0.7227	10.555	0.639	0.377	0.728
767.79128	0.7165	10.551	0.635	0.363	0.715
767.84136	0.8279	10.618	0.649	0.370	0.725
767.85909	0.8673	10.671	0.649	0.380	0.730
767.89667	0.9508	10.996	0.674	0.377	0.759
767.93982	0.0468	11.040	0.647	0.402	0.772
767.95733	0.0857	10.813	0.635	0.397	0.757
767.97540	0.1259	10.652	0.628	0.380	0.733
768.00636	0.1947	10.524	0.627	0.363	0.697
786.87904	0.1574	10.572	0.627	0.373	0.714
786.89813	0.1999	10.528	0.625	0.374	0.704
786.92057	0.2498	10.483	0.625	0.365	0.703
786.95519	0.3268	10.554	0.630	0.362	0.707
786.97244	0.3651	10.616	0.635	0.358	0.711
787.91784	0.4672	10.992	0.664	0.357	0.705
787.95723	0.5548	10.966	0.634	0.398	0.758
788.77655	0.3767	10.632	0.643	0.358	0.711
788.79408	0.4155	10.742	0.650	0.355	0.726
788.82318	0.4802	11.017	0.663	0.387	0.753
788.85511	0.5512	10.972	0.647	0.384	0.748
788.88559	0.6189	10.720	0.635	0.391	0.765
788.93089	0.7196	10.575	0.640	0.373	0.720
788.94730	0.7561	10.559	0.641	0.374	0.723

Table 8.2b. Standard Cape-Kron colour indices of AD Phe.

MJD	PHASE	V	(B-V)	(V-R) _{kc}	(V-I) _{kc}
45000+					
993.01481	0.0655	10.590	0.579	0.370	0.691
993.03277	0.1127	10.432	0.583	0.356	0.682
993.06208	0.1899	10.306	0.580	0.351	0.685
993.08094	0.2395	10.268	0.585	0.339	0.663
993.97212	0.5851	10.535	0.596	0.366	0.710
993.99010	0.5199	10.417	0.590	0.354	0.689
994.01977	0.7106	10.307	0.581	0.350	0.682
994.03688	0.7556	10.311	0.589	0.348	0.676
994.07450	0.8546	10.383	0.598	0.334	0.654
994.97559	0.2263	10.253	0.574	0.353	0.673
994.99323	0.2727	10.240	0.592	0.328	0.653
995.02240	0.3495	10.321	0.585	0.337	0.662
995.04103	0.3985	10.424	0.601	0.339	0.657
995.07025	0.4755	10.738	0.624	0.338	0.684
997.91825	0.9715	10.719	0.634	0.337	0.667
997.93588	0.0179	10.760	0.607	0.367	0.699
997.96395	0.0918	10.469	0.578	0.370	0.698
997.98300	0.1419	10.348	0.571	0.355	0.674
998.01870	0.2359	10.246	0.592	0.334	0.659
998.03651	0.2827	10.264	0.591	0.336	0.673
998.06649	0.3617	10.355	0.604	0.317	0.631
998.90100	0.5581	10.639	0.596	0.357	0.689
998.91946	0.6067	10.467	0.580	0.368	0.704
998.94625	0.6772	10.332	0.582	0.343	0.687
998.96497	0.7265	10.290	0.593	0.340	0.659
998.99986	0.8183	10.322	0.596	0.337	0.651
999.01839	0.8671	10.377	0.607	0.320	0.644
999.04814	0.9454	10.617	0.627	0.328	0.659
999.81076	0.9526	10.645	0.622	0.336	0.675
999.82846	0.9992	10.777	0.605	0.356	0.692
999.84792	0.0504	10.646	0.576	0.375	0.702
999.87596	0.1242	10.375	0.570	0.352	0.674
999.89364	0.1708	10.300	0.575	0.349	0.662
999.98554	0.4127	10.486	0.609	0.334	0.658
46000+					
000.01516	0.4906	10.767	0.621	0.352	0.677
000.03718	0.5486	10.693	0.601	0.368	0.712
000.05856	0.6048	10.491	0.588	0.365	0.700
000.97387	0.0140	10.774	0.609	0.360	0.705
000.99126	0.0597	10.614	0.565	0.384	0.712
001.01497	0.1222	10.389	0.586	0.341	0.657
001.03249	0.1683	10.326	0.596	0.330	0.669
001.04996	0.2142	10.275	0.573	0.344	0.681
001.06524	0.2545	10.249	0.577	0.346	0.684
002.85264	0.9590	10.670	0.628	0.329	0.650
002.89185	0.0622	10.589	0.582	0.360	0.707
002.92223	0.1421	10.352	0.583	0.345	0.667
002.93890	0.1860	10.296	0.582	0.348	0.670
002.96426	0.2527	10.254	0.584	0.346	0.677
002.98175	0.2988	10.266	0.595	0.331	0.667
003.01533	0.3872	10.420	0.598	0.336	0.676
003.02971	0.4250	10.537	0.603	0.337	0.682

Table 8.2c. Standard Cape-Kron colour indices of RS Col.

MJD	PHASE	V	(B-V)	(V-R) _{kc}	(V-I) _{kc}
45000+					
262.01697	0.8475	9.581	0.556	0.335	0.655
262.05154	0.8990	9.678	0.560	0.337	0.673
262.09902	0.9696	9.896	0.570	0.351	0.688
263.10137	0.4604	9.826	0.563	0.325	0.643
266.08787	0.9022	9.679	0.559	0.334	0.649
266.99943	0.2580	9.552	0.541	0.342	0.633
267.09244	0.3963	9.653	0.549	0.335	0.661
661.84159	0.5098	9.906	0.558	0.321	0.637
661.88115	0.5686	9.754	0.548	0.325	0.639
661.89845	0.5944	9.680	0.543	0.327	0.645
661.91817	0.6237	9.626	0.548	0.322	0.636
662.00063	0.7463	9.508	0.541	0.321	0.623
662.02895	0.7885	9.541	0.546	0.326	0.633
665.85289	0.4758	9.909	0.568	0.325	0.629
665.87254	0.5051	9.959	0.556	0.330	0.655
665.90409	0.5520	9.868	0.551	0.324	0.646
666.98610	0.1613	9.593	0.550	0.326	0.643
667.00553	0.1902	9.542	0.547	0.323	0.642
667.03696	0.2369	9.509	0.546	0.323	0.625
667.80220	0.3751	9.658	0.552	0.317	0.643
667.82099	0.4030	9.695	0.556	0.315	0.631
667.84115	0.4330	9.768	0.560	0.320	0.643
668.03267	0.7178	9.500	0.543	0.321	0.634
668.04900	0.7421	9.504	0.545	0.321	0.636
668.06639	0.7680	9.500	0.547	0.322	0.635
668.08336	0.7932	9.524	0.550	0.325	0.633
669.04663	0.2259	9.283	0.551	0.332	0.642
669.06520	0.2535	9.273	0.549	0.324	0.641
669.79823	0.3438	9.597	0.544	0.316	0.638
669.81604	0.3703	9.623	0.549	0.314	0.631
669.84481	0.4131	9.703	0.550	0.319	0.645
669.86207	0.4387	9.774	0.562	0.321	0.634
669.88908	0.4789	9.888	0.556	0.329	0.647
669.90304	0.4997	9.907	0.566	0.328	0.653
669.91887	0.5232	9.881	0.554	0.336	0.660
669.94767	0.5660	9.753	0.562	0.326	0.628
669.96637	0.5939	9.686	0.548	0.328	0.632
669.99851	0.6417	9.589	0.545	0.319	0.625
670.01583	0.6674	9.561	0.548	0.320	0.624
670.04466	0.7103	9.518	0.547	0.321	0.632
670.06173	0.7357	9.513	0.550	0.317	0.629
670.80492	0.8410	9.607	0.548	0.317	0.636
670.82369	0.8690	9.646	0.560	0.326	0.641
670.85255	0.9119	9.726	0.561	0.328	0.651
670.86956	0.9372	9.801	0.574	0.322	0.642
670.90047	0.9832	9.913	0.572	0.330	0.658

*
*

(continued.)

Table 8.2c. Standard Cape-Kron colour indices of RS Col (continued).

MJD	PHASE	V	(B-V)	(V-R) _{kc}	(V-I) _{kc}
45000+					
670.91586	0.0060	9.925	0.571	0.329	0.665
670.93009	0.0272	9.898	0.570	0.338	0.645
670.95716	0.0675	9.774	0.559	0.329	0.624
670.97185	0.0893	9.719	0.555	0.334	0.653
670.99742	0.1273	9.635	0.558	0.330	0.643
671.01325	0.1509	9.592	0.551	0.332	0.641
671.04582	0.1993	9.548	0.554	0.317	0.620
671.06262	0.2243	9.522	0.547	0.326	0.638
673.80380	0.3013	9.551	0.547	0.304	0.630
673.81903	0.3239	9.568	0.546	0.314	0.631
673.83723	0.3510	9.593	0.549	0.327	0.634

* Substantial drift in photometer sensitivity due to moisture on detector. This only affects the standard V-magnitudes, not the colour indices (see Chapter 5).

Table 8.3a. Differential V-magnitudes of EZ Hya.

MJD	PHASE	Diff.Mag. (v-c)	MJD	PHASE	Diff.Mag. (v-c)
45000.0+			45000.0+		
766.80524	0.5147	1.685	786.90985	0.2166	1.152
766.81195	0.5296	1.676	786.91455	0.2270	1.139
766.81842	0.5440	1.612	786.92059	0.2404	1.143
766.82684	0.5627	1.512	786.92816	0.2573	1.140
766.83673	0.5847	1.428	786.93201	0.2658	1.139
766.84271	0.5980	1.382	786.95520	0.3174	1.208
766.84930	0.6127	1.345	786.96155	0.3315	1.224
766.86957	0.6577	1.259	786.96619	0.3418	1.241
766.87970	0.6803	1.227	786.97241	0.3557	1.268
766.88641	0.6952	1.213	787.91785	0.4578	1.638
766.89453	0.7132	1.207	787.92847	0.4814	1.681
766.90417	0.7347	1.199	787.93286	0.4912	1.683
766.91199	0.7520	1.210	787.93677	0.4999	1.686
766.91791	0.7652	1.210	787.94159	0.5106	1.677
767.79126	0.7071	1.207	787.94629	0.5210	1.671
767.79962	0.7257	1.200	787.95062	0.5307	1.648
767.80585	0.7395	1.214	787.95721	0.5453	1.623
767.81189	0.7529	1.201	787.96613	0.5651	1.509
767.81946	0.7698	1.218	787.97003	0.5738	1.473
767.82379	0.7794	1.228	787.97382	0.5822	1.444
767.82794	0.7886	1.235	788.77667	0.3674	1.271
767.84137	0.8185	1.276	788.78436	0.3845	1.333
767.84875	0.8349	1.312	788.78845	0.3936	1.362
767.85327	0.8450	1.328	788.79407	0.4060	1.397
767.85907	0.8578	1.332	788.80188	0.4234	1.478
767.86719	0.8759	1.373	788.80774	0.4364	1.543
767.87109	0.8846	1.398	788.81140	0.4446	1.580
767.87518	0.8937	1.432	788.82318	0.4708	1.671
767.89667	0.9414	1.661	788.83026	0.4865	1.686
767.90448	0.9588	1.743	788.83386	0.4945	1.687
767.90906	0.9690	1.752	788.83734	0.5023	1.691
767.91339	0.9786	1.747	788.84113	0.5107	1.690
767.91760	0.9880	1.742	788.84528	0.5199	1.682
767.92133	0.9963	1.739	788.84943	0.5291	1.670
767.92529	0.0051	1.737	788.85510	0.5417	1.632
767.92963	0.0147	1.729	788.86267	0.5586	1.552
767.93402	0.0245	1.731	788.86670	0.5675	1.505
767.93982	0.0374	1.707	788.88562	0.6096	1.381
767.95734	0.0763	1.479	788.89270	0.6253	1.336
767.96497	0.0933	1.389	788.89648	0.6338	1.319
767.96967	0.1038	1.351	788.90942	0.6625	1.270
767.97540	0.1165	1.318	788.91364	0.6719	1.251
767.98303	0.1335	1.273	788.91925	0.6844	1.235
767.98755	0.1435	1.253	788.93091	0.7103	1.233
767.99164	0.1526	1.237	788.93823	0.7266	1.223
768.00635	0.1853	1.187	788.94202	0.7350	1.221
768.01385	0.2020	1.169	788.94733	0.7468	1.216
786.87903	0.1480	1.228	788.95441	0.7625	1.220
786.88635	0.1643	1.204	788.95819	0.7710	1.222
786.89063	0.1738	1.192	788.96216	0.7798	1.226
786.89813	0.1905	1.189	788.96576	0.7878	1.234

Table 8.3b. Differential V-magnitudes of AD Phe.

MJD	PHASE	Diff.Mag. (v-c)	MJD	PHASE	Diff.Mag. (v-c)
45000.0+			45000.0+		
993.01276	0.0601	2.344	993.07990	0.2368	1.972
993.01306	0.0609	2.338	993.08075	0.2390	1.967
993.01343	0.0618	2.327	993.08264	0.2440	1.974
993.01379	0.0628	2.328	993.08820	0.2586	2.010
993.01465	0.0650	2.325	993.08856	0.2596	1.993
993.01648	0.0699	2.299	993.08893	0.2605	1.996
993.02209	0.0846	2.247	993.08929	0.2615	1.994
993.02240	0.0854	2.244	993.09235	0.2695	1.995
993.02277	0.0864	2.249	993.09265	0.2703	1.993
993.02313	0.0874	2.241	993.09302	0.2713	1.987
993.02649	0.0962	2.192	993.09338	0.2723	1.988
993.02679	0.0970	2.184	993.97003	0.5796	2.284
993.02716	0.0980	2.192	993.97040	0.5806	2.279
993.02753	0.0989	2.182	993.97076	0.5816	2.277
993.03070	0.1073	2.179	993.97107	0.5824	2.273
993.03107	0.1083	2.165	993.97192	0.5846	2.268
993.03137	0.1091	2.180	993.97382	0.5896	2.244
993.03174	0.1100	2.164	993.97937	0.6042	2.217
993.03259	0.1123	2.161	993.97968	0.6050	2.213
993.03448	0.1172	2.145	993.98004	0.6060	2.208
993.03979	0.1312	2.122	993.98041	0.6070	2.206
993.04016	0.1322	2.113	993.98340	0.6148	2.187
993.04053	0.1332	2.120	993.98370	0.6156	2.184
993.04083	0.1340	2.118	993.98407	0.6166	2.180
993.04431	0.1431	2.094	993.98444	0.6176	2.178
993.04468	0.1441	2.087	993.98804	0.6270	2.158
993.04498	0.1449	2.088	993.98834	0.6278	2.158
993.04535	0.1458	2.083	993.98871	0.6288	2.150
993.04852	0.1542	2.073	993.98907	0.6298	2.153
993.04883	0.1550	2.069	993.98993	0.6320	2.155
993.04919	0.1560	2.065	993.99182	0.6370	2.147
993.04956	0.1569	2.061	993.99731	0.6514	2.118
993.06000	0.1844	2.043	993.99768	0.6524	2.128
993.06036	0.1854	2.040	993.99799	0.6532	2.115
993.06073	0.1863	2.032	993.99835	0.6542	2.117
993.06104	0.1871	2.031	994.00140	0.6622	2.104
993.06189	0.1894	2.040	994.00177	0.6632	2.101
993.06378	0.1944	2.020	994.00214	0.6641	2.092
993.06927	0.2088	2.008	994.00244	0.6649	2.098
993.06958	0.2096	1.997	994.00562	0.6733	2.085
993.06995	0.2106	2.010	994.00598	0.6743	2.088
993.07031	0.2115	2.005	994.00635	0.6752	2.085
993.07416	0.2217	1.982	994.00665	0.6760	2.077
993.07446	0.2225	1.991	994.01770	0.7051	2.048
993.07483	0.2234	1.980	994.01807	0.7061	2.047
993.07520	0.2244	1.986	994.01837	0.7069	2.041
993.07886	0.2340	1.983	994.01874	0.7078	2.049
993.07922	0.2350	1.974	994.01959	0.7101	2.035
993.07959	0.2360	1.978	994.02148	0.7151	2.041

(continued).

Table 8.3b. Differential V-magnitudes of AD Phe (continued).

MJD	PHASE	Diff.Mag. (v-c)	MJD	PHASE	Diff.Mag. (v-c)
45000.0+			45000.0+		
994.02673	0.7289	2.029	994.98376	0.2478	1.984
994.02710	0.7298	2.022	994.98682	0.2559	1.990
994.02747	0.7308	2.023	994.98718	0.2568	1.990
994.02777	0.7316	2.021	994.98755	0.2578	1.988
994.03076	0.7395	2.021	994.98785	0.2586	1.991
994.03113	0.7404	2.023	994.99109	0.2671	1.989
994.03149	0.7414	2.024	994.99146	0.2681	1.988
994.03186	0.7424	2.014	994.99176	0.2689	1.989
994.03479	0.7501	2.041	994.99213	0.2698	1.987
994.03516	0.7511	2.037	994.99310	0.2724	2.003
994.03546	0.7519	2.034	994.99500	0.2774	2.005
994.03583	0.7528	2.037	995.00006	0.2907	2.000
994.03668	0.7551	2.039	995.00043	0.2917	2.003
994.03857	0.7600	2.042	995.00079	0.2926	2.001
994.04388	0.7740	2.035	995.00116	0.2936	2.000
994.04425	0.7750	2.026	995.00458	0.3026	2.000
994.04462	0.7760	2.036	995.00488	0.3034	2.008
994.04492	0.7768	2.038	995.00525	0.3044	2.009
994.04816	0.7853	2.029	995.00562	0.3053	2.006
994.04852	0.7862	2.036	995.00885	0.3138	2.038
994.04883	0.7870	2.033	995.00916	0.3146	2.036
994.04919	0.7880	2.038	995.00952	0.3156	2.038
994.05243	0.7965	2.039	995.00989	0.3166	2.040
994.05273	0.7973	2.042	995.02020	0.3437	2.065
994.05310	0.7983	2.041	995.02051	0.3445	2.074
994.05347	0.7992	2.049	995.02087	0.3455	2.067
994.07245	0.8492	2.110	995.02124	0.3465	2.065
994.07275	0.8500	2.109	995.02234	0.3493	2.066
994.07312	0.8510	2.118	995.02423	0.3543	2.070
994.07349	0.8519	2.115	995.03015	0.3699	2.112
994.07428	0.8540	2.113	995.03052	0.3709	2.117
994.07617	0.8590	2.123	995.03082	0.3717	2.111
994.08118	0.8722	2.117	995.03119	0.3726	2.114
994.08154	0.8731	2.132	995.03455	0.3815	2.128
994.08185	0.8739	2.132	995.03485	0.3823	2.135
994.08221	0.8740	2.137	995.03522	0.3832	2.134
994.08502	0.8823	2.150	995.03558	0.3842	2.137
994.08539	0.8833	2.145	995.03870	0.3924	2.171
994.08569	0.8841	2.152	995.03900	0.3932	2.165
994.08606	0.8850	2.157	995.03937	0.3942	2.165
994.97333	0.2203	2.004	995.03973	0.3951	2.171
994.97369	0.2213	1.998	995.04114	0.3988	2.171
994.97406	0.2223	2.002	995.04303	0.4038	2.192
994.97437	0.2231	1.992	995.04834	0.4178	2.247
994.97559	0.2263	1.990	995.04871	0.4187	2.248
994.97748	0.2313	1.990	995.04901	0.4196	2.257
994.98273	0.2451	1.984	995.04938	0.4205	2.256
994.98309	0.2461	1.981	995.05255	0.4289	2.275
994.98346	0.2470	1.977	995.05292	0.4298	2.270

(continued).

Table 8.3b. Differential V-magnitudes of AD Phe (continued).

MJD	PHASE	Diff.Mag. (v-c)	MJD	PHASE	Diff.Mag. (v-c)
45000.0+			45000.0+		
995.05322	0.4306	2.285	997.94641	0.0456	2.395
995.05359	0.4316	2.281	997.94672	0.0464	2.392
995.05737	0.4416	2.334	997.94708	0.0474	2.396
995.05774	0.4425	2.335	997.95081	0.0572	2.333
995.05804	0.4433	2.340	997.95117	0.0581	2.328
995.05841	0.4443	2.342	997.95154	0.0591	2.325
995.06799	0.4695	2.460	997.95184	0.0599	2.321
995.06836	0.4705	2.465	997.96167	0.0858	2.232
995.06873	0.4714	2.459	997.96198	0.0866	2.229
995.06903	0.4722	2.465	997.96234	0.0875	2.226
995.07019	0.4753	2.471	997.96271	0.0885	2.210
995.07208	0.4803	2.484	997.96399	0.0919	2.214
995.07764	0.4949	2.526	997.96588	0.0968	2.200
995.07794	0.4957	2.533	997.97144	0.1115	2.140
995.07831	0.4967	2.522	997.97174	0.1123	2.141
995.07867	0.4976	2.524	997.97211	0.1132	2.138
995.08191	0.5061	2.519	997.97247	0.1142	2.136
995.08228	0.5071	2.510	997.97583	0.1230	2.120
995.08264	0.5081	2.520	997.97614	0.1238	2.125
995.08301	0.5090	2.516	998.89880	0.5523	2.377
995.08655	0.5183	2.509	998.89917	0.5533	2.378
995.08691	0.5193	2.507	998.89948	0.5541	2.372
995.08728	0.5203	2.523	998.89984	0.5551	2.366
995.08759	0.5211	2.513	998.90094	0.5580	2.365
997.91602	0.9656	2.437	998.90283	0.5629	2.362
997.91638	0.9666	2.431	998.90875	0.5785	2.287
997.91675	0.9675	2.443	998.90906	0.5793	2.292
997.91705	0.9683	2.449	998.90942	0.5803	2.278
997.91821	0.9714	2.479	998.90979	0.5812	2.268
997.92010	0.9764	2.494	998.91309	0.5899	2.233
997.92560	0.9908	2.532	998.91345	0.5909	2.230
997.92596	0.9918	2.530	998.91376	0.5917	2.229
997.92633	0.9928	2.528	998.91412	0.5927	2.226
997.92664	0.9936	2.526	998.91699	0.6002	2.227
997.92993	0.0022	2.523	998.91736	0.6012	2.219
997.93030	0.0032	2.516	998.91766	0.6020	2.224
997.93060	0.0040	2.529	998.91803	0.6029	2.206
997.93097	0.0050	2.520	998.91968	0.6073	2.207
997.93414	0.0133	2.518	998.92157	0.6123	2.181
997.93451	0.0143	2.518	998.92676	0.6259	2.163
997.93488	0.0152	2.505	998.92712	0.6269	2.163
997.93518	0.0160	2.503	998.92749	0.6278	2.151
997.93646	0.0194	2.502	998.92780	0.6286	2.150
997.93750	0.0221	2.496	998.93060	0.6360	2.123
997.94202	0.0340	2.452	998.93097	0.6370	2.124
997.94232	0.0348	2.449	998.93134	0.6380	2.138
997.94269	0.0358	2.441	998.93164	0.6388	2.131
997.94305	0.0368	2.441	998.93463	0.6466	2.147
997.94604	0.0446	2.409	998.93500	0.6476	2.140

(continued).

Table 8.3b. Differential V-magnitudes of AD Phe (continued).

MJD	PHASE	Diff. Mag. (v-c)	MJD	PHASE	Diff. Mag. (v-c)
45000.0+			45000.0+		
998.93536	0.6486	2.117	999.01642	0.8619	2.108
998.93573	0.6495	2.117	999.01678	0.8629	2.096
998.94403	0.6714	2.087	999.01709	0.8637	2.111
998.94440	0.6723	2.073	999.01843	0.8672	2.132
998.94476	0.6733	2.075	999.02032	0.8722	2.145
998.94507	0.6741	2.076	999.02588	0.8868	2.152
998.94623	0.6772	2.076	999.02618	0.8876	2.151
998.94806	0.6820	2.066	999.02655	0.8886	2.157
998.95294	0.6948	2.074	999.02692	0.8895	2.165
998.95331	0.6958	2.068	999.03009	0.8979	2.183
998.95361	0.6966	2.062	999.03040	0.8987	2.182
998.95398	0.6976	2.068	999.03076	0.8997	2.187
998.95837	0.7091	2.053	999.03113	0.9006	2.196
998.95874	0.7101	2.054	999.03394	0.9080	2.213
998.95905	0.7109	2.047	999.03430	0.9090	2.229
998.95941	0.7119	2.054	999.03467	0.9099	2.226
998.96271	0.7205	2.037	999.03497	0.9107	2.231
998.96307	0.7215	2.033	999.04578	0.9392	2.327
998.96338	0.7223	2.029	999.04614	0.9401	2.327
998.96375	0.7233	2.028	999.04651	0.9411	2.334
998.96497	0.7265	2.041	999.04681	0.9419	2.341
998.96686	0.7315	2.041	999.04822	0.9456	2.361
998.97229	0.7458	2.018	999.05011	0.9506	2.382
998.97266	0.7467	2.019	999.05524	0.9641	2.511
998.97296	0.7475	2.018	999.05560	0.9650	2.512
998.97333	0.7485	2.019	999.05597	0.9660	2.480
998.97614	0.7559	2.013	999.05627	0.9668	2.481
998.97644	0.7567	2.023	999.07013	0.0033	2.512
998.97681	0.7576	2.028	999.07043	0.0041	2.508
998.97717	0.7586	2.021	999.07080	0.0050	2.513
998.98047	0.7673	2.022	999.07117	0.0060	2.517
998.98077	0.7681	2.030	999.07397	0.0134	2.498
998.98114	0.7690	2.033	999.07434	0.0144	2.495
998.98151	0.7700	2.028	999.07471	0.0153	2.492
998.99768	0.8126	2.077	999.07501	0.0161	2.496
998.99799	0.8134	2.078	999.08832	0.0511	2.364
998.99835	0.8143	2.082	999.08868	0.0521	2.358
998.99872	0.8153	2.075	999.08905	0.0531	2.358
998.99982	0.8182	2.094	999.08936	0.0539	2.354
999.00171	0.8232	2.105	999.09277	0.0629	2.303
999.00708	0.8373	2.082	999.09314	0.0638	2.305
999.00745	0.8383	2.086	999.09351	0.0648	2.296
999.00775	0.8391	2.088	999.09387	0.0658	2.297
999.00812	0.8401	2.087	999.09698	0.0740	2.278
999.01190	0.8500	2.088	999.09735	0.0749	2.259
999.01221	0.8508	2.091	999.09772	0.0759	2.258
999.01257	0.8518	2.097	999.09802	0.0767	2.255
999.01294	0.8527	2.097	999.10120	0.0850	2.208
999.01605	0.8609	2.100	999.10150	0.0858	2.199

(continued).

Table 8.3b. Differential V-magnitudes of AD Phe (continued).

MJD	PHASE	Diff Mag. (v-c)	MJD	PHASE	Diff. Mag. (v-c)
45000.0+			45000.0+		
999.10187	0.0868	2.208	999.86417	0.0932	2.197
999.10223	0.0878	2.198	999.86452	0.0941	2.196
999.80857	0.9469	2.374	999.86487	0.0951	2.193
999.80892	0.9478	2.373	999.87372	0.1183	2.128
999.80927	0.9487	2.387	999.87407	0.1193	2.120
999.80961	0.9496	2.377	999.87442	0.1202	2.128
999.81069	0.9524	2.396	999.87476	0.1211	2.124
999.81256	0.9574	2.417	999.87594	0.1242	2.118
999.81876	0.9737	2.495	999.87782	0.1291	2.109
999.81910	0.9746	2.489	999.88305	0.1429	2.084
999.81945	0.9755	2.491	999.88340	0.1438	2.086
999.81980	0.9764	2.495	999.88375	0.1447	2.085
999.82298	0.9848	2.514	999.88409	0.1456	2.080
999.82333	0.9857	2.513	999.88743	0.1544	2.077
999.82368	0.9866	2.519	999.88777	0.1553	2.069
999.82402	0.9875	2.515	999.88812	0.1562	2.068
999.82697	0.9953	2.529	999.88847	0.1572	2.065
999.82732	0.9962	2.528	999.89148	0.1651	2.054
999.82767	0.9971	2.532	999.89182	0.1660	2.051
999.82802	0.9981	2.527	999.89217	0.1669	2.057
999.82881	0.0001	2.537	999.89252	0.1678	2.052
999.82982	0.0028	2.538	999.89355	0.1705	2.053
999.83357	0.0127	2.522	999.89542	0.1755	2.038
999.83392	0.0136	2.509	999.90049	0.1888	2.063
999.83427	0.0145	2.505	999.90084	0.1897	2.072
999.83461	0.0154	2.507	999.90119	0.1906	2.067
999.83731	0.0225	2.481	999.90153	0.1915	2.045
999.83766	0.0234	2.484	999.92005	0.2403	2.091
999.83800	0.0243	2.480	999.92040	0.2412	2.106
999.83835	0.0252	2.481	999.92075	0.2421	2.106
999.84138	0.0332	2.459	999.92109	0.2430	2.101
999.84173	0.0341	2.457	999.98317	0.4064	2.205
999.84208	0.0351	2.451	999.98351	0.4073	2.212
999.84243	0.0360	2.441	999.98386	0.4082	2.222
999.84570	0.0446	2.407	999.98421	0.4092	2.229
999.84605	0.0455	2.409	999.98565	0.4129	2.228
999.84640	0.0464	2.398	999.98753	0.4179	2.243
999.84674	0.0473	2.393	999.99280	0.4318	2.308
999.84790	0.0504	2.385	999.99314	0.4327	2.302
999.84978	0.0553	2.361	999.99349	0.4336	2.313
999.85537	0.0700	2.296	999.99384	0.4345	2.320
999.85571	0.0709	2.294	999.99694	0.4427	2.339
999.85606	0.0719	2.290	999.99729	0.4436	2.343
999.85641	0.0728	2.281	999.99763	0.4445	2.354
999.85983	0.0818	2.243	999.99798	0.4454	2.357
999.86018	0.0827	2.242	46000.0+		
999.86053	0.0836	2.239	000.00935	0.4753	2.477
999.86087	0.0845	2.243	000.00969	0.4762	2.479
999.86383	0.0923	2.205	000.01004	0.4771	2.478

(continued).

Table 8.3b. Differential V-magnitudes of AD Phe (continued).

MJD	PHASE	Diff.Mag. (v-c)	MJD	PHASE	Diff.Mag. (v-c)
46000.0+			46000.0+		
000.01039	0.4781	2.479	000.07339	0.6439	2.119
000.01303	0.4850	2.494	000.07373	0.6448	2.123
000.01337	0.4859	2.491	000.07631	0.6516	2.121
000.01372	0.4868	2.494	000.07666	0.6525	2.115
000.01407	0.4878	2.502	000.07701	0.6534	2.122
000.01503	0.4903	2.510	000.07736	0.6543	2.115
000.01690	0.4952	2.508	000.97154	0.0078	2.520
000.02214	0.5090	2.510	000.97188	0.0087	2.507
000.02248	0.5099	2.512	000.97223	0.0097	2.509
000.02283	0.5108	2.514	000.97258	0.0106	2.518
000.02318	0.5117	2.510	000.97397	0.0142	2.511
000.02655	0.5206	2.502	000.97584	0.0192	2.499
000.02689	0.5215	2.507	000.98089	0.0325	2.460
000.02724	0.5224	2.504	000.98124	0.0334	2.456
000.02759	0.5233	2.489	000.98158	0.0343	2.453
000.03054	0.5311	2.459	000.98193	0.0352	2.443
000.03089	0.5320	2.463	000.98490	0.0430	2.425
000.03123	0.5329	2.458	000.98525	0.0439	2.412
000.03158	0.5338	2.455	000.98560	0.0448	2.413
000.03488	0.5425	2.413	000.98595	0.0458	2.412
000.03523	0.5434	2.421	000.98898	0.0537	2.367
000.03567	0.5446	2.415	000.98933	0.0547	2.366
000.03601	0.5455	2.408	000.98967	0.0556	2.374
000.03723	0.5487	2.408	000.99002	0.0565	2.364
000.03910	0.5536	2.385	000.99128	0.0598	2.334
000.04440	0.5676	2.316	000.99316	0.0647	2.308
000.04475	0.5685	2.317	000.99810	0.0778	2.253
000.04510	0.5694	2.313	000.99845	0.0787	2.242
000.04545	0.5703	2.310	000.99879	0.0796	2.243
000.04842	0.5782	2.302	000.99914	0.0805	2.231
000.04877	0.5791	2.288	001.00206	0.0882	2.209
000.04912	0.5800	2.294	001.00240	0.0891	2.198
000.04946	0.5809	2.280	001.00275	0.0900	2.198
000.05644	0.5993	2.236	001.00310	0.0909	2.199
000.05679	0.6002	2.234	001.00562	0.0975	2.173
000.05714	0.6011	2.227	001.00597	0.0985	2.168
000.05748	0.6020	2.223	001.00632	0.0994	2.164
000.05843	0.6045	2.203	001.00666	0.1003	2.166
000.06031	0.6095	2.188	001.01341	0.1180	2.111
000.06506	0.6220	2.163	001.01376	0.1190	2.122
000.06541	0.6229	2.156	001.01411	0.1199	2.114
000.06576	0.6238	2.143	001.01445	0.1208	2.111
000.06611	0.6247	2.152	001.01543	0.1234	2.118
000.06870	0.6315	2.139	001.01643	0.1260	2.109
000.06905	0.6325	2.142	001.02043	0.1365	2.099
000.06939	0.6334	2.144	001.02077	0.1374	2.090
000.06974	0.6343	2.136	001.02112	0.1383	2.088
000.07269	0.6420	2.117	001.02147	0.1393	2.088
000.07304	0.6430	2.121	001.02399	0.1459	2.087

(continued).

Table 8.3b. Differential V-magnitudes of AD Phe (continued).

MJD	PHASE	Diff.Mag. (v-c)	MJD	PHASE	Diff.Mag. (v-c)
46000.0+			46000.0+		
001.02434	0.1468	2.087	001.08207	0.2988	2.014
001.02468	0.1477	2.081	001.08242	0.2997	2.009
001.02503	0.1486	2.075	001.08276	0.3006	2.016
001.02756	0.1553	2.080	001.08311	0.3015	2.015
001.02790	0.1562	2.086	001.08695	0.3116	2.035
001.02825	0.1571	2.102	001.08730	0.3125	2.031
001.02860	0.1580	2.094	001.08765	0.3134	2.027
001.03105	0.1645	2.058	001.08799	0.3143	2.032
001.03140	0.1654	2.058	001.09092	0.3221	2.038
001.03174	0.1663	2.065	001.09127	0.3230	2.033
001.03209	0.1672	2.068	001.09162	0.3239	2.025
001.03281	0.1691	2.066	001.09196	0.3248	2.028
001.03382	0.1718	2.046	001.09590	0.3352	2.041
001.03740	0.1812	2.018	001.09625	0.3361	2.047
001.03775	0.1821	2.020	001.09659	0.3370	2.039
001.03810	0.1830	2.019	001.09694	0.3379	2.047
001.03845	0.1840	2.017	002.85030	0.9528	2.394
001.04104	0.1908	2.030	002.85065	0.9537	2.391
001.04139	0.1917	2.034	002.85099	0.9546	2.401
001.04173	0.1926	2.027	002.85134	0.9555	2.407
001.04208	0.1935	2.024	002.85272	0.9592	2.424
001.04482	0.2007	2.017	002.85459	0.9641	2.443
001.04517	0.2016	2.011	002.85947	0.9769	2.491
001.04552	0.2026	2.014	002.85981	0.9778	2.483
001.04587	0.2035	2.012	002.86016	0.9788	2.489
001.04843	0.2102	2.014	002.86051	0.9797	2.501
001.04878	0.2111	2.022	002.86105	0.9811	2.377
001.04913	0.2121	2.015	002.86140	0.9820	2.375
001.04948	0.2130	2.018	002.86175	0.9829	2.375
001.05038	0.2154	1.987	002.86209	0.9838	2.377
001.05139	0.2180	1.982	002.86671	0.9960	2.522
001.05532	0.2284	1.993	002.86706	0.9969	2.519
001.05567	0.2293	1.997	002.86741	0.9978	2.517
001.05602	0.2302	1.993	002.86775	0.9987	2.529
001.05636	0.2311	1.999	002.87044	0.0058	2.527
001.05914	0.2384	2.013	002.87079	0.0067	2.522
001.05949	0.2393	2.004	002.87113	0.0076	2.514
001.05984	0.2403	2.006	002.87148	0.0085	2.528
001.06018	0.2411	2.004	002.87433	0.0161	2.505
001.06370	0.2504	1.991	002.87468	0.0170	2.513
001.06405	0.2513	1.988	002.87502	0.0179	2.502
001.06440	0.2523	1.994	002.87537	0.0188	2.503
001.06474	0.2531	1.993	002.87854	0.0271	2.481
001.06566	0.2556	1.991	002.87889	0.0281	2.474
001.06666	0.2582	2.006	002.87924	0.0290	2.470
001.07107	0.2698	2.015	002.87958	0.0299	2.463
001.07142	0.2707	2.001	002.88236	0.0372	2.437
001.07177	0.2717	2.013	002.88271	0.0381	2.438
001.07212	0.2726	2.012	002.88305	0.0390	2.428

(continued).

Table 8.3b. Differential V-magnitudes of AD Phe (continued).

MJD	PHASE	Diff.Mag. (v-c)	MJD	PHASE	Diff.Mag. (v-c)
46000.0+			46000.0+		
002.88340	0.0399	2.425	002.95079	0.2173	2.008
002.88643	0.0479	2.392	002.95113	0.2182	2.007
002.88678	0.0488	2.384	002.95391	0.2255	2.026
002.88713	0.0497	2.384	002.95426	0.2264	2.026
002.88748	0.0507	2.373	002.95461	0.2274	2.024
002.89033	0.0582	2.351	002.95495	0.2282	2.019
002.89068	0.0591	2.342	002.96209	0.2470	1.998
002.89103	0.0600	2.334	002.96244	0.2480	1.992
002.89138	0.0609	2.332	002.96279	0.2489	1.992
002.89226	0.0632	2.334	002.96314	0.2498	1.994
002.89326	0.0659	2.306	002.96418	0.2525	1.998
002.89721	0.0763	2.267	002.96605	0.2575	1.998
002.89756	0.0772	2.259	002.97123	0.2711	1.995
002.89790	0.0781	2.254	002.97157	0.2720	2.000
002.89825	0.0790	2.253	002.97192	0.2729	1.995
002.90123	0.0869	2.233	002.97227	0.2738	1.997
002.90157	0.0877	2.220	002.97538	0.2820	2.009
002.90192	0.0887	2.220	002.97573	0.2829	2.003
002.90227	0.0896	2.218	002.97608	0.2839	2.008
002.90487	0.0964	2.196	002.97642	0.2848	2.007
002.90522	0.0974	2.190	002.97949	0.2928	2.002
002.90557	0.0983	2.189	002.97984	0.2938	2.002
002.90591	0.0992	2.191	002.98018	0.2947	2.008
002.92002	0.1363	2.099	002.98053	0.2956	2.001
002.92037	0.1372	2.104	002.98175	0.2988	2.009
002.92072	0.1382	2.100	002.98362	0.3037	2.009
002.92106	0.1390	2.096	002.98880	0.3173	2.031
002.92219	0.1420	2.087	002.98914	0.3182	2.030
002.92406	0.1469	2.085	002.98949	0.3192	2.032
002.92891	0.1597	2.065	002.98984	0.3201	2.029
002.92926	0.1606	2.070	002.99322	0.3290	2.051
002.92961	0.1615	2.070	002.99356	0.3299	2.056
002.92995	0.1624	2.060	002.99391	0.3308	2.057
002.93280	0.1699	2.057	002.99426	0.3317	2.055
002.93315	0.1709	2.056	002.99729	0.3397	2.057
002.93349	0.1718	2.061	002.99764	0.3406	2.055
002.93384	0.1727	2.053	002.99799	0.3415	2.059
002.93672	0.1803	2.049	002.99833	0.3424	2.070
002.93707	0.1812	2.045	003.01374	0.3830	2.149
002.93742	0.1821	2.047	003.01408	0.3839	2.157
002.93777	0.1830	2.041	003.01443	0.3848	2.156
002.93883	0.1858	2.044	003.01478	0.3857	2.162
002.94071	0.1908	2.035	003.01581	0.3884	2.155
002.94568	0.2038	2.017	003.01682	0.3911	2.166
002.94603	0.2048	2.013	003.02050	0.4008	2.186
002.94638	0.2057	2.021	003.02084	0.4017	2.182
002.94672	0.2066	2.017	003.02119	0.4026	2.189
002.95009	0.2155	2.017	003.02154	0.4035	2.183
002.95044	0.2164	2.011	003.02434	0.4109	2.211

(continued).

Table 8.3b. Differential V-magnitudes of AD Phe (continued).

MJD	PHASE	Diff.Mag. (v-c)
46000.0+		
003.02469	0.4118	2.211
003.02503	0.4127	2.221
003.02538	0.4136	2.223
003.02810	0.4208	2.260
003.02845	0.4217	2.269
003.02880	0.4226	2.262
003.02914	0.4235	2.262
003.03020	0.4263	2.267
003.03120	0.4289	2.285

Table 8.3c. Differential V-magnitudes of RS Col.

MJD	PHASE	Diff.Mag. (v-c)	MJD	PHASE	Diff.Mag. (v-c)
45000.0+			45000.0+		
661.84161	0.5098	-0.279	668.07355	0.7786	-0.648
661.85754	0.5335	-0.332	668.07782	0.7850	-0.645
661.86835	0.5496	-0.401	668.08337	0.7933	-0.637
661.87866	0.5649	-0.481	669.04663	0.2259	-0.657
662.00061	0.7463	-0.672	669.05383	0.2366	-0.667
662.01135	0.7623	-0.678	669.05908	0.2444	-0.668
662.01947	0.7744	-0.674	669.06519	0.2535	-0.665
662.02893	0.7884	-0.650	669.07318	0.2654	-0.658
662.04132	0.8069	-0.647	669.07727	0.2715	-0.660
662.04956	0.8191	-0.628	669.08215	0.2788	-0.661
662.05847	0.8324	-0.592	669.79822	0.3438	-0.603
665.85291	0.4759	-0.299	669.80524	0.3542	-0.597
665.86078	0.4876	-0.273	669.80975	0.3609	-0.580
665.86609	0.4955	-0.269	669.81604	0.3703	-0.576
665.87256	0.5051	-0.256	669.82404	0.3822	-0.554
665.88123	0.5180	-0.279	669.82843	0.3887	-0.544
665.88684	0.5263	-0.293	669.83313	0.3957	-0.531
665.89191	0.5339	-0.311	669.84479	0.4130	-0.489
665.90411	0.5520	-0.374	669.85181	0.4235	-0.460
665.91229	0.5642	-0.426	669.85626	0.4301	-0.442
665.91730	0.5716	-0.431	669.86206	0.4387	-0.415
665.92474	0.5827	-0.443	669.86963	0.4500	-0.377
665.94641	0.6149	-0.533	669.87396	0.4564	-0.358
665.95300	0.6247	-0.546	669.87823	0.4628	-0.329
665.95862	0.6331	-0.532	669.88910	0.4789	-0.299
666.98608	0.1613	-0.576	669.89404	0.4863	-0.286
666.99347	0.1722	-0.603	669.89819	0.4925	-0.283
666.99902	0.1805	-0.598	669.90302	0.4996	-0.280
667.00555	0.1902	-0.625	669.90887	0.5083	-0.281
667.01434	0.2033	-0.629	669.91394	0.5159	-0.291
667.01929	0.2106	-0.641	669.91888	0.5232	-0.307
667.02362	0.2171	-0.638	669.92499	0.5323	-0.321
667.03699	0.2370	-0.662	669.92926	0.5387	-0.339
667.80219	0.3750	-0.545	669.94769	0.5661	-0.436
667.80988	0.3865	-0.538	669.95593	0.5783	-0.453
667.81445	0.3933	-0.523	669.96045	0.5850	-0.470
667.82098	0.4030	-0.503	669.96637	0.5939	-0.503
667.82996	0.4164	-0.467	669.97449	0.6059	-0.538
667.83508	0.4240	-0.447	669.97882	0.6124	-0.551
667.84113	0.4330	-0.424	669.98303	0.6186	-0.566
667.84918	0.4449	-0.380	669.99854	0.6417	-0.596
667.85364	0.4516	-0.362	670.00537	0.6519	-0.605
667.85834	0.4586	-0.345	670.00970	0.6583	-0.614
668.03265	0.7178	-0.670	670.01581	0.6674	-0.622
668.03949	0.7280	-0.663	670.02368	0.6791	-0.637
668.04340	0.7338	-0.660	670.02795	0.6854	-0.640
668.04901	0.7422	-0.660	670.03320	0.6933	-0.649
668.05658	0.7534	-0.665	670.04468	0.7103	-0.661
668.06073	0.7596	-0.666	670.05139	0.7203	-0.664
668.06641	0.7680	-0.658	670.05554	0.7265	-0.672

(continued).

Table 8.3c. Differential V-magnitudes of RS Col (continued).

MJD	PHASE	Diff.Mag. (v-c)
45000.0+		
670.06171	0.7357	-0.664
670.06946	0.7472	-0.669
670.07446	0.7546	-0.672
670.07813	0.7601	-0.670
670.80493	0.8411	-0.593
670.81317	0.8533	-0.577
670.81763	0.8599	-0.560
670.82367	0.8689	-0.551
670.83136	0.8804	-0.536
670.83600	0.8873	-0.517
670.84039	0.8938	-0.500
670.85254	0.9119	-0.466
670.85944	0.9221	-0.431
670.86389	0.9287	-0.408
670.86957	0.9372	-0.386
670.87732	0.9487	-0.352
670.88165	0.9552	-0.333
670.88580	0.9613	-0.321
670.90045	0.9831	-0.269
670.90698	0.9928	-0.256
670.91113	0.9990	-0.255
670.91583	0.0060	-0.256
670.92133	0.0142	-0.265
670.92535	0.0202	-0.281
670.93011	0.0272	-0.282
670.93567	0.0355	-0.303
670.93994	0.0419	-0.323
670.94397	0.0478	-0.347
670.95715	0.0675	-0.405
670.96155	0.0740	-0.418
670.96539	0.0797	-0.435
670.97186	0.0893	-0.460
670.97900	0.1000	-0.488
670.98315	0.1061	-0.504
670.98700	0.1118	-0.516
670.99744	0.1274	-0.545
671.00397	0.1371	-0.561
671.00781	0.1428	-0.570
671.01324	0.1509	-0.591
671.02057	0.1618	-0.598
671.02478	0.1680	-0.610
671.02875	0.1739	-0.618
671.04584	0.1994	-0.637
671.05176	0.2082	-0.657
671.05719	0.2162	-0.668
671.06262	0.2243	-0.661
671.06964	0.2348	-0.667
671.07330	0.2402	-0.667
671.07709	0.2458	-0.666

Table 8.4a. EZ Hya: parameters for the theoretical light curves shown in Figures 8.3a.i, .ii, .iii and .iv .

Solution No.	I	II	III	IV
ϕ	0.0 to 0.5	0.5 to 1.0	0.0 to 0.5	0.5 to 1.0
q	* 0.25	* 0.25	0.31 ⁺ 0.02 ₋	0.23 ⁺ 0.01 ₋
i (deg.)	82.4 ⁺ 2.3 ₋	80.1 ⁺ 1.1 ₋	80.4 ⁺ 1.5 ₋	81.1 ⁺ 1.6 ₋
T _{pr} (K)	* 5690	* 5690	* 5690	* 5690
X	-0.052 ⁺ 0.007 ₋	-0.091 ⁺ 0.006 ₋	-0.035 ⁺ 0.007 ₋	-0.103 ⁺ 0.007 ₋
f	0.339 ⁺ 0.058 ₋	0.561 ⁺ 0.064 ₋	0.456 ⁺ 0.047 ₋	0.519 ⁺ 0.056 ₋
β_{pr} , β_{sec}	* 0.03	* 0.03	* 0.03	* 0.03
A _{pr} , A _{sec}	* 0.5	* 0.5	* 0.5	* 0.5
W	0.0146	0.0095	0.0104	0.0086

* Fixed

ϕ is the phase interval for the data used in the solution.

$$X = (T_{pr} - T_{sec}) / (T_{pr} + T_{sec})$$

f = $(S - S_o) / (S_i - S_o)$, is the Rucinski fill-out factor (see Section 4.4.3.1).

β is the gravity darkening exponent.

A is the albedo.

W = $\sum (w_i^{1/2} \cdot (o-c)_i)^2$, is a quality-of-fit parameter,

where, w_i is the weight assigned to a particular point. i.e. (relative int.)⁻¹,

and, (o-c) is the residual corresponding to the point.

N.B. It is clear from an examination of Figures 8.3a.i, .ii, .iii and .iv, that the above parameters in no way represent photometric solutions for the light curve of EZ Hya.

Table 8.4b. Photometric solutions for AD Phe.

Solution No.	V	VI	VII	VIII
ϕ	0.0 to 0.5	0.5 to 1.0	0.0 to 0.5	0.5 to 1.0
q	$0.94^{+0.03}$	* 1.00	* 0.50	* 0.50
i (deg.)	$73.6^{+0.1}$	$72.8^{+0.3}$	$75.0^{+0.2}$	$74.2^{+0.4}$
T_{pr} (K)	* 5850	* 5850	* 5850	* 5850
X	$0.006^{+0.002}$	$0.001^{+0.005}$	$0.007^{+0.003}$	$0.006^{+0.006}$
f	$0.849^{+0.008}$	$0.902^{+0.012}$	$0.796^{+0.013}$	$0.839^{+0.028}$
β_{pr}, β_{sec}	* 0.03	* 0.03	* 0.03	* 0.03
A_{pr}, A_{sec}	* 0.5	* 0.5	* 0.5	* 0.5
W	0.0010	0.0047	0.0021	0.0072

* Fixed

ϕ is the phase interval for the data used in the solution.

$$X = (T_{pr} - T_{sec}) / (T_{pr} + T_{sec})$$

f = $(S - S_0) / (S_i - S_0)$. is the Rucinski fill-out factor (see Section 4.4.3.1).

β is the gravity darkening exponent.

A is the albedo.

$W = \sum (w_i^{1/2} \cdot (o-c)_i)^2$, is a quality-of-fit parameter,

where, w_i is the weight assigned to a particular point, i.e. (relative int.)⁻¹,

and, (o-c) is the residual corresponding to the point.

Table 8.4c. Photometric solutions for RS Col.

Solution No.	IX	X
ϕ	0.5 to 1.0	0.5 to 1.0
q	* 1.00	* 0.50
i (deg.)	67.6 ⁺ _{0.3}	68.7 ⁺ _{0.4}
T _{pr} (K)	* 5950	* 5950
X	0.025 ⁺ _{0.007}	0.027 ⁺ _{0.008}
f	0.840 ⁺ _{0.016}	0.755 ⁺ _{0.021}
β_{pr} , β_{sec}	* 0.03	* 0.03
A _{pr} , A _{sec}	* 0.5	* 0.5
W	0.0035	0.0057

* Fixed

ϕ is the phase interval for the data used in the solutions.

$$X = (T_{pr} - T_{sec}) / (T_{pr} + T_{sec})$$

$f = (S - S_0) / (S_i - S_0)$, is the Rucinski fill-out factor (see Section 4.4.3.1).

β is the gravity darkening exponent.

A is the albedo.

$W = \sum (w_i^{1/2} \cdot (o-c)_i)^2$, is a quality-of-fit parameter,

where, w_i is the weight assigned to a particular point, i.e. (relative int.)⁻¹,

and, (o-c) is the residual corresponding to the point.

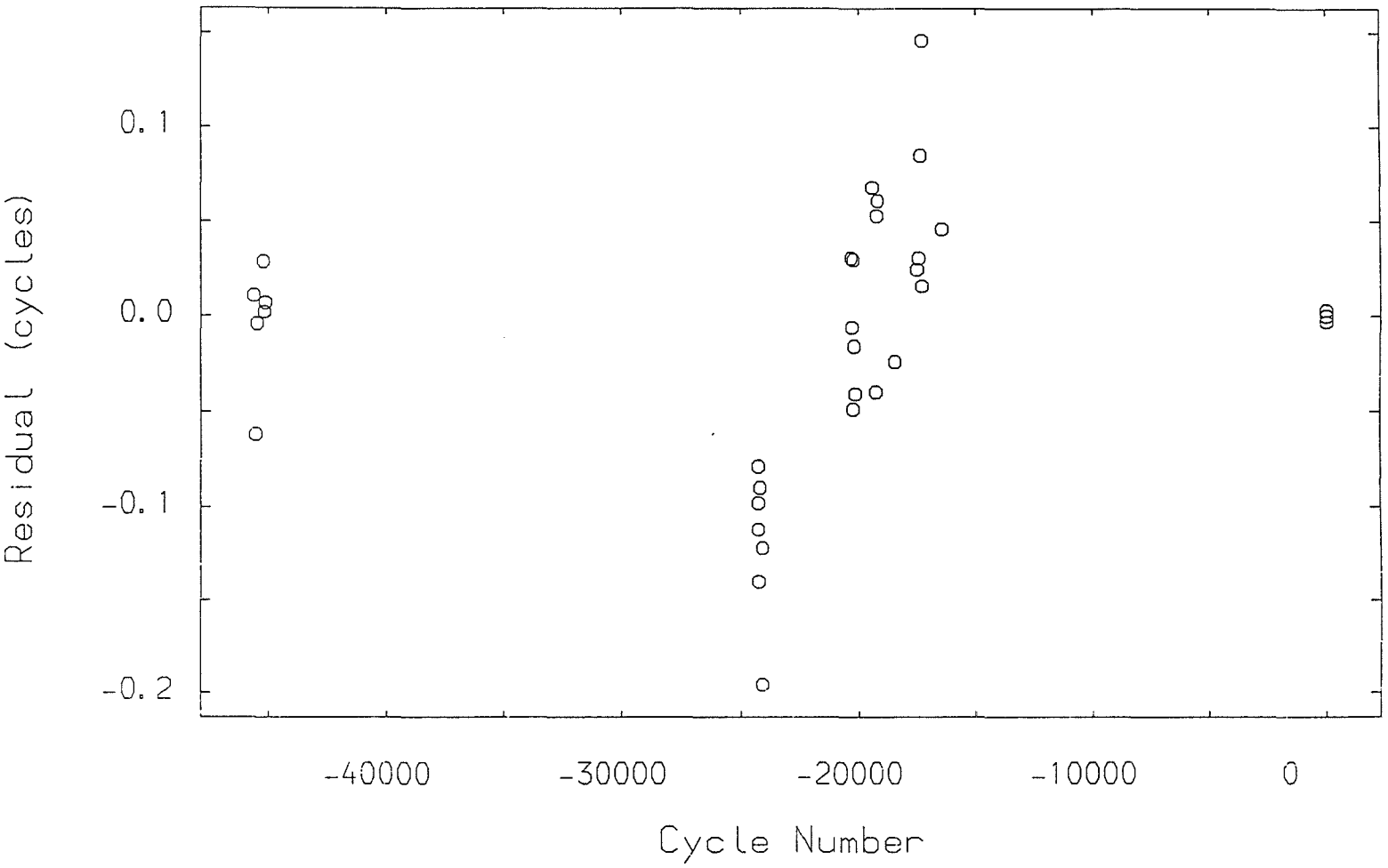


Figure 8.1b.
The residuals for the times of minima of AD Phe shown in Table 8.1b,
plotted against their relevant cycle number.

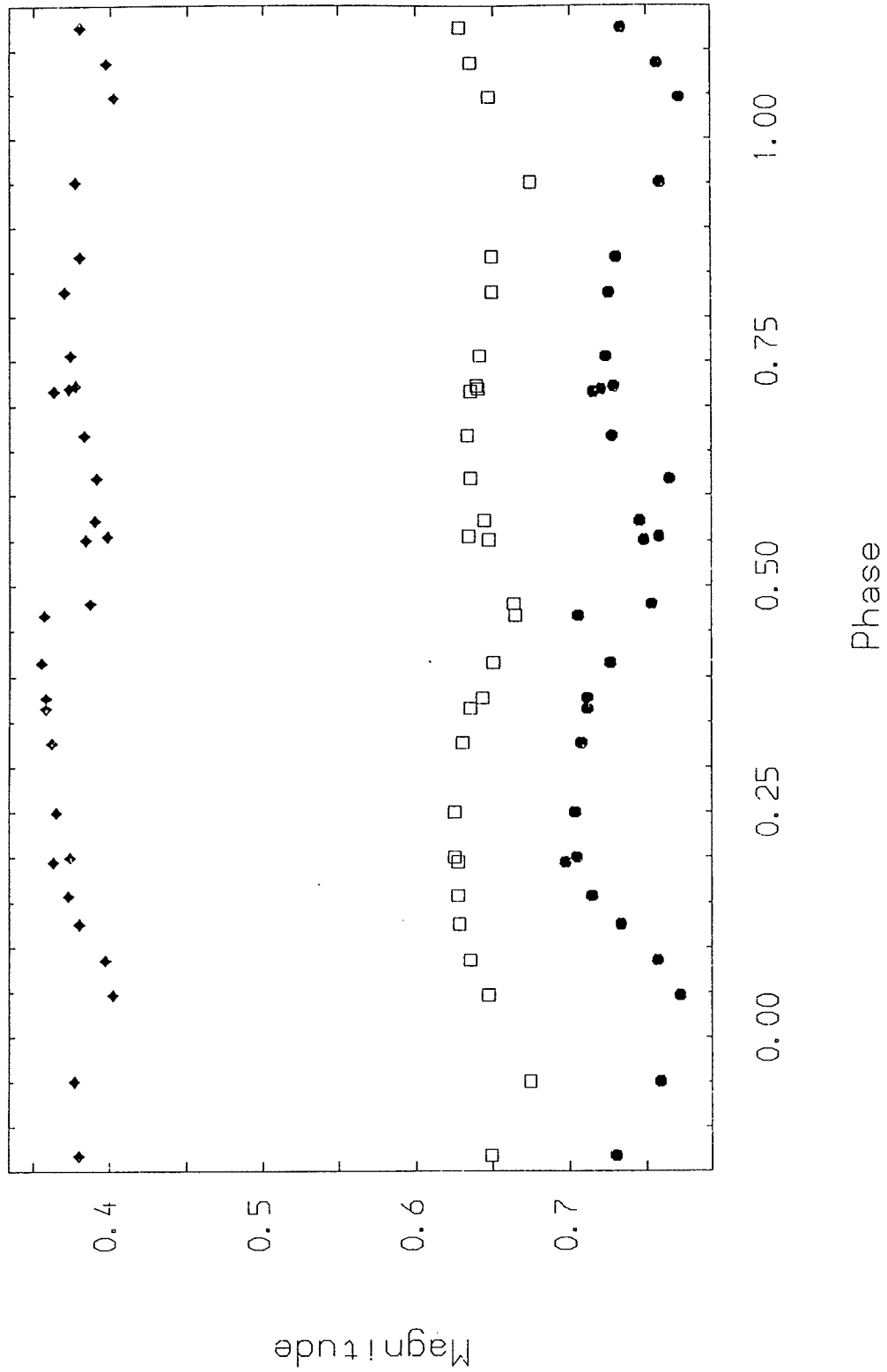


Figure 8.2a.
 Cape-Kron colour indices of EZ Hya plotted against phase. The $(B-V)$, $(V-R)_{ke}$ and $(V-I)_{ke}$ data are open-squares, diamonds and circles respectively.

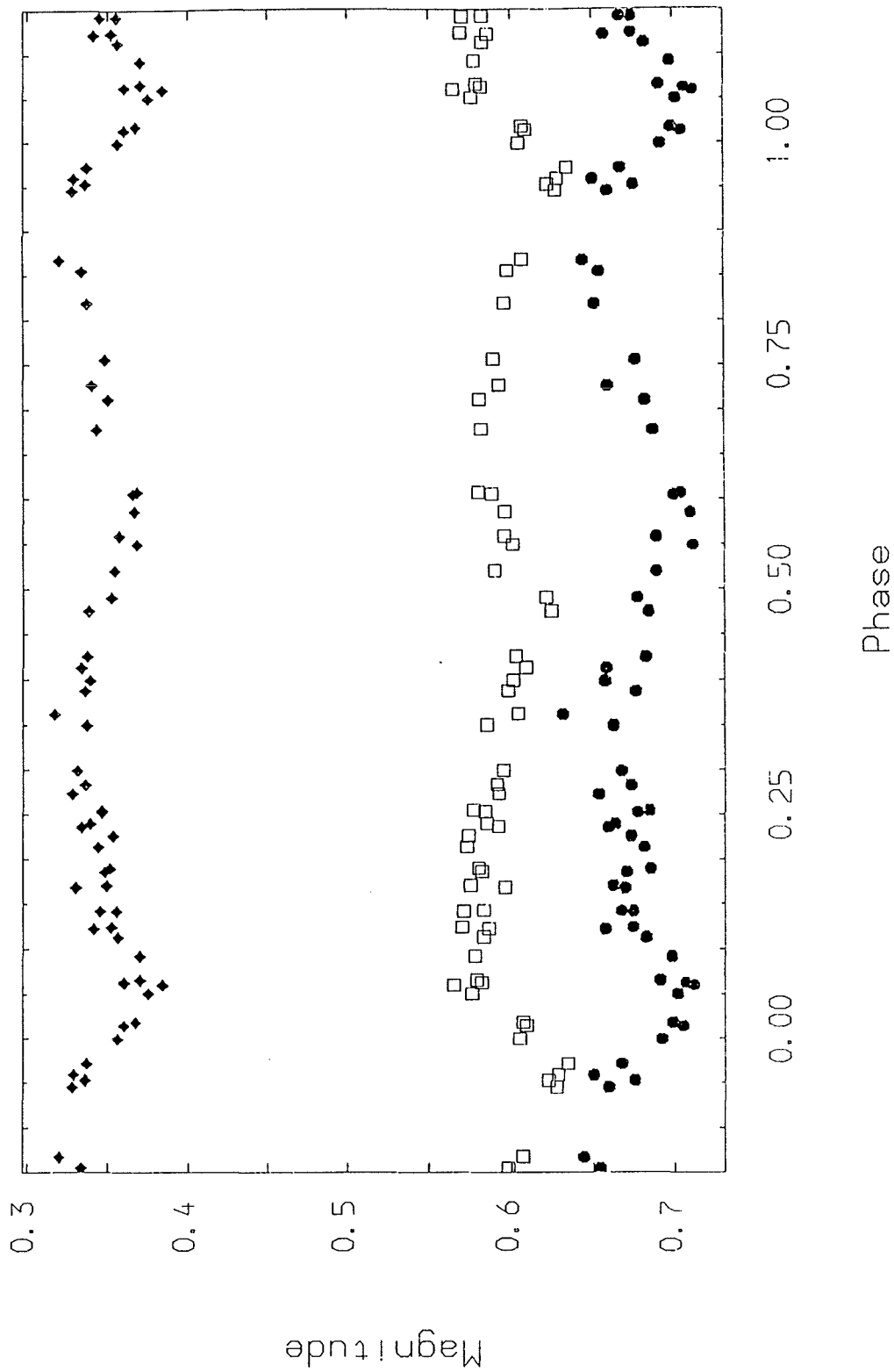


Figure 8.2b.
 Cape-Kron colour indices of AD Phe plotted against phase. The $(B-V)$, $(V-R)_{ke}$ and $(V-I)_{ke}$ data are open-squares, diamonds and circles, respectively.

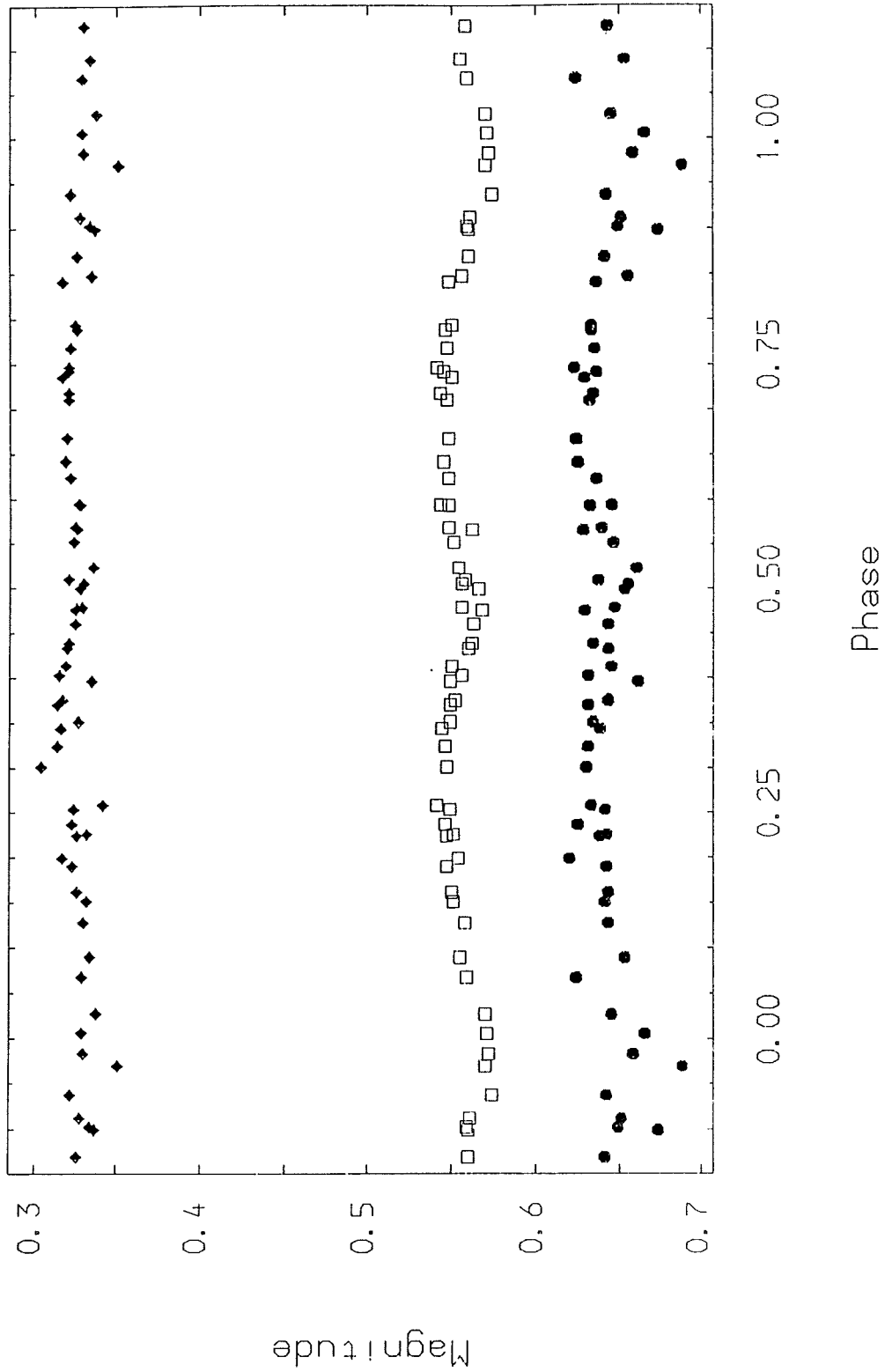


Figure 8.2c.
 Cape-Kron colour indices of RS Col plotted against phase. The $(B-V)$, $(V-R)_{kc}$ and $(V-I)_{kc}$ data are open-squares, diamonds and circles, respectively.

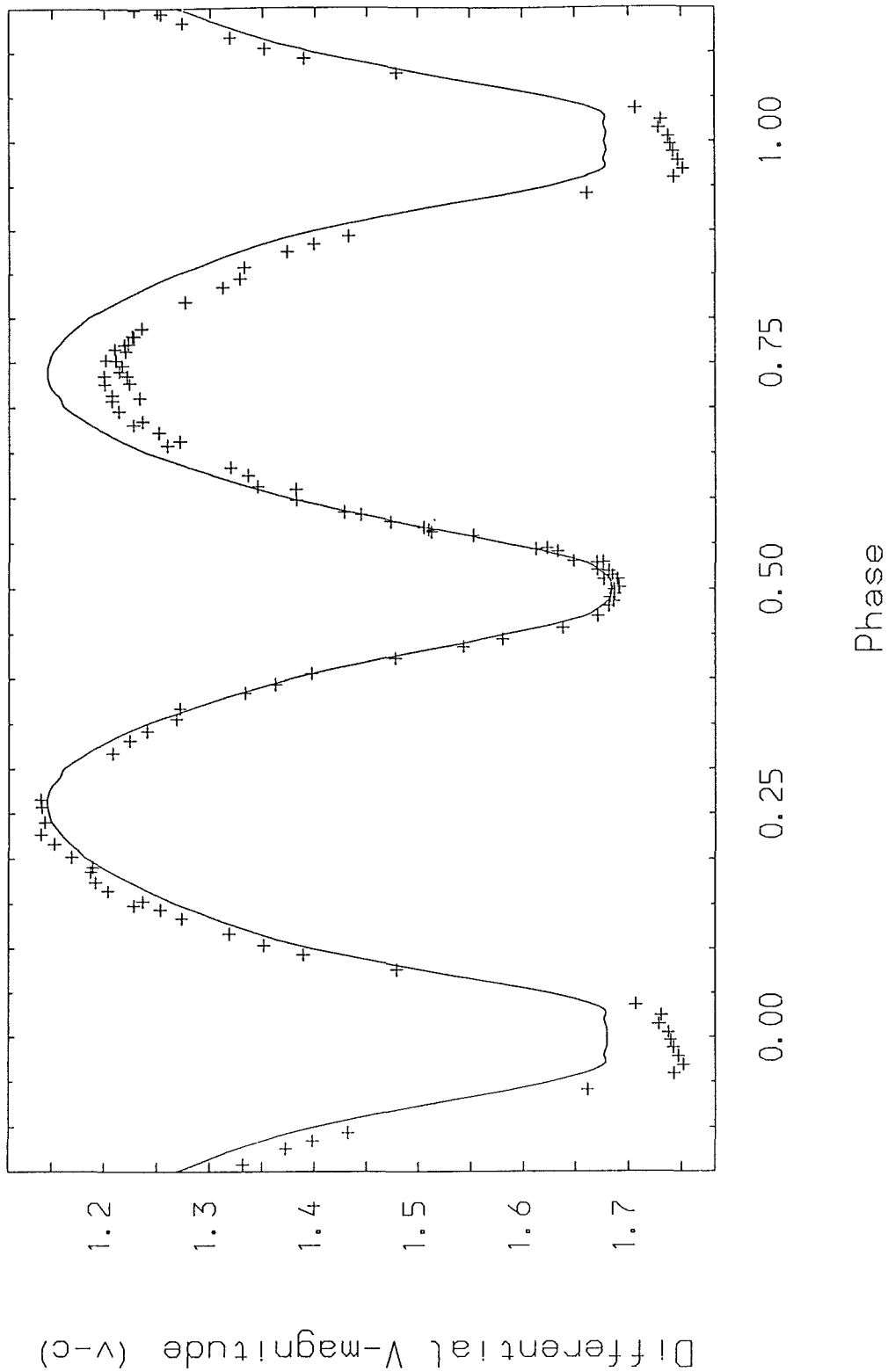


Figure 8.3a.i

V-light curve of EZ Hya showing the individual observations from Table 8.3a and the theoretical light curve from Table 8.4a - Solution I. (Clearly the theoretical curve does not represent a solution to the photometric data.)

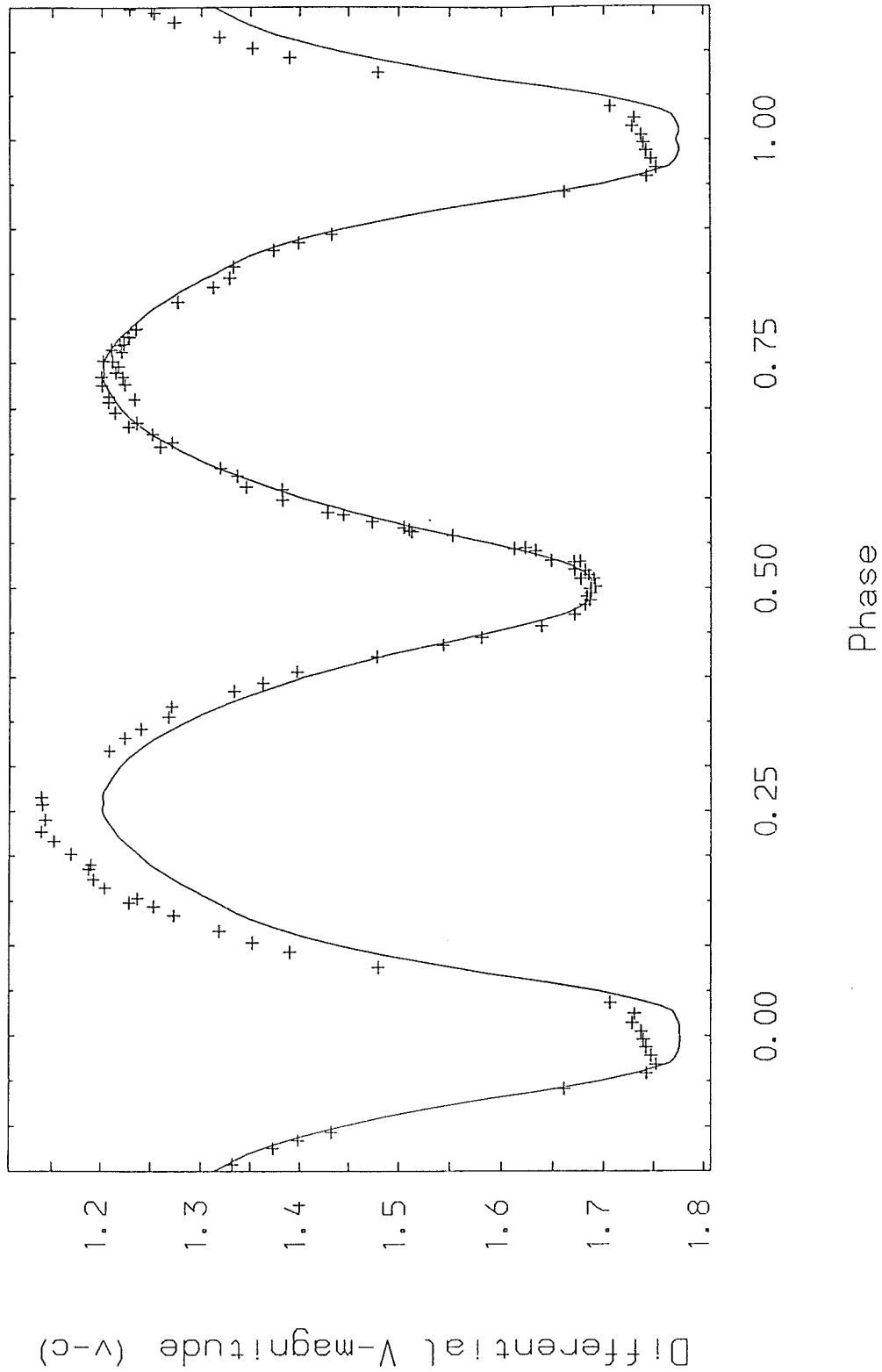


Figure 8.3a.ii
 V-light curve of EZ Hya showing the individual observations from Table 8.3a and the theoretical light curve from Table 8.4a - Solution II. (Clearly the theoretical curve does not represent a solution to the photometric data.)

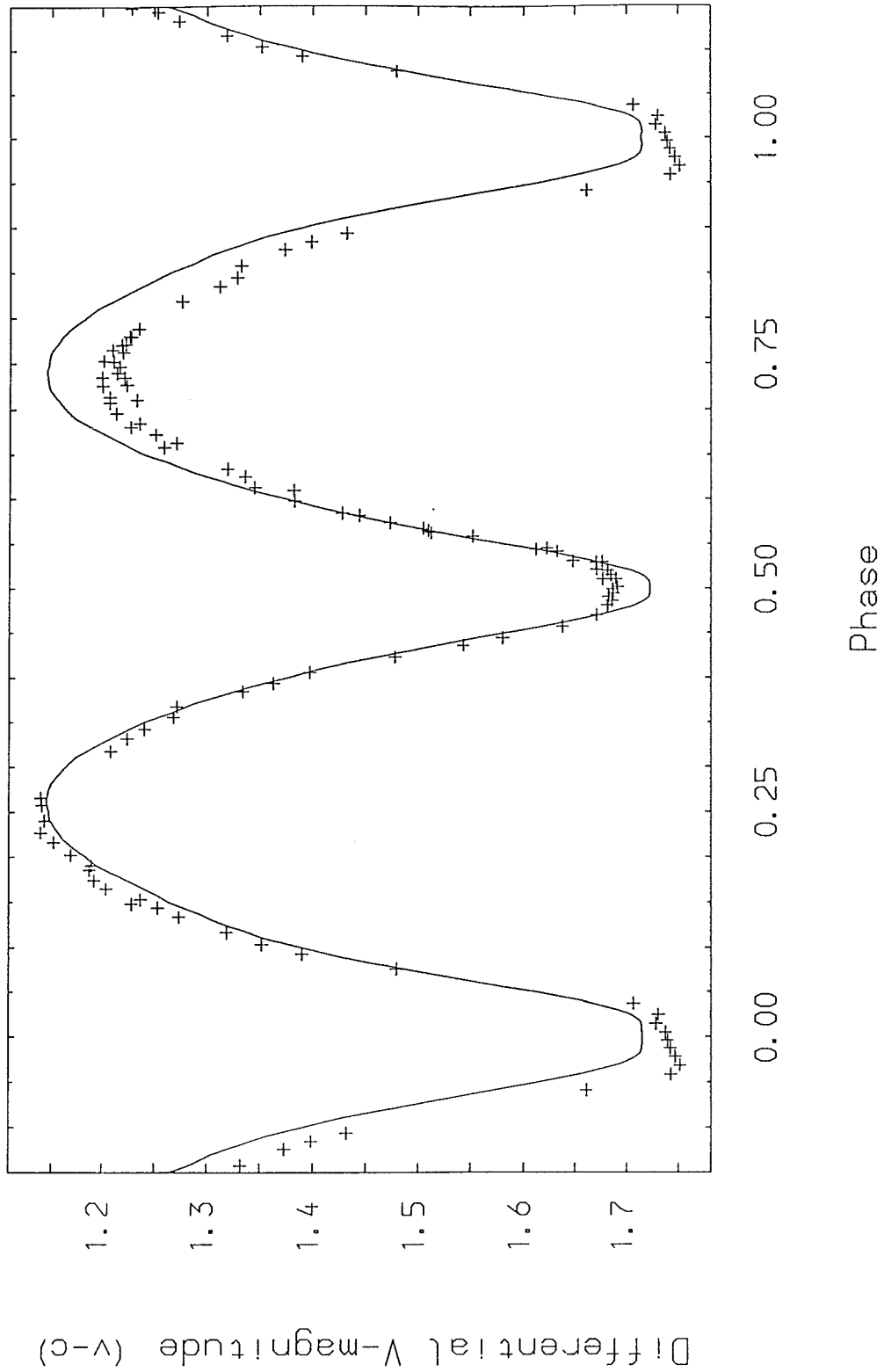


Figure 8.3a.iii
 V-light curve of EZ Hya showing the individual observations from Table 8.3a and the theoretical light curve from Table 8.4a - Solution III. (Clearly the theoretical curve does not represent a solution to the photometric data.)

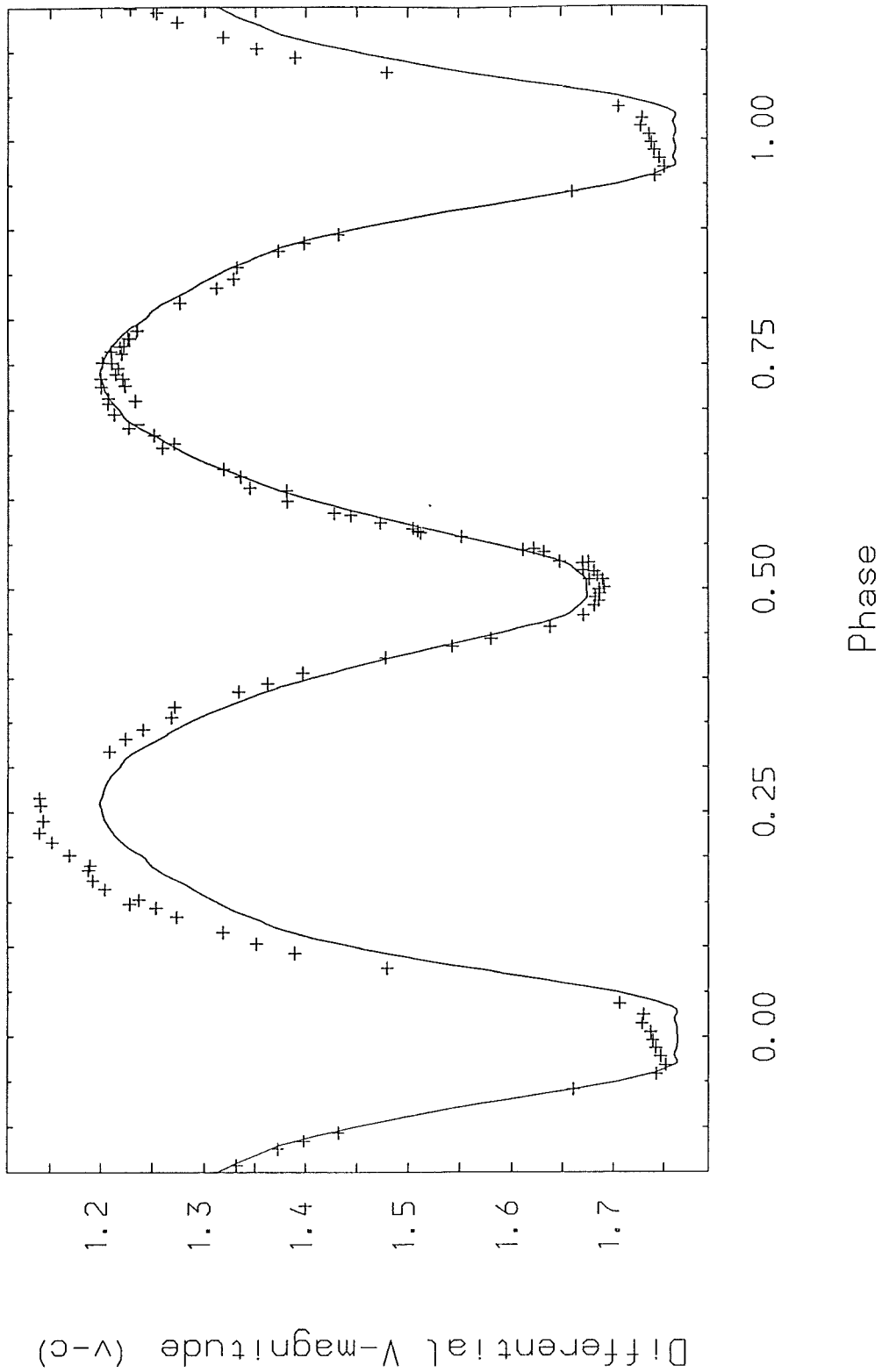


Figure 8.3a.iv
 V-light curve of EZ Hya showing the individual observations from Table 8.3a and the theoretical light curve from Table 8.4a - Solution IV. (Clearly the theoretical curve does not represent a solution to the photometric data.)

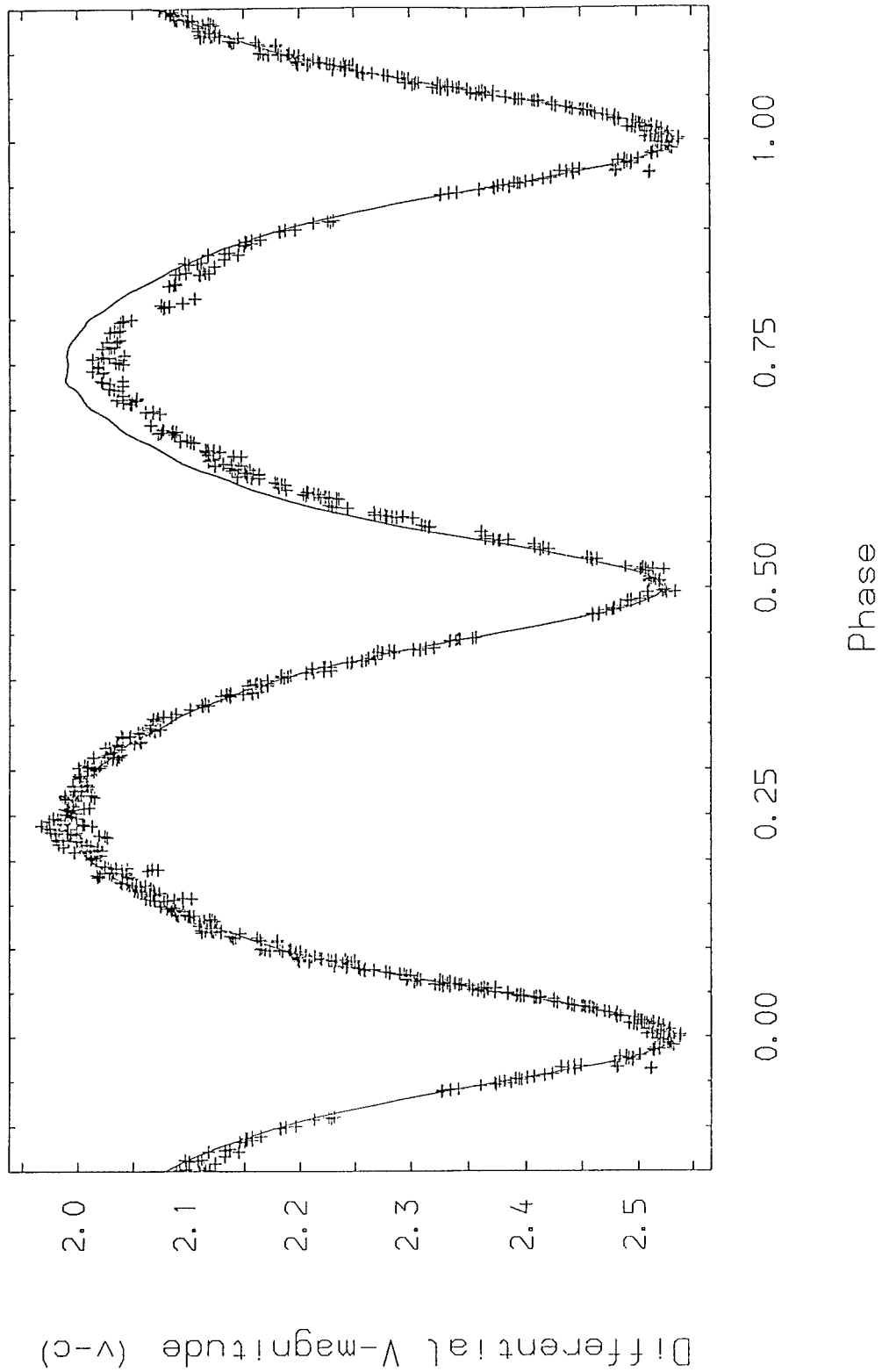


Figure 8.3b.i
 V-light curve of AD Phe showing the individual observations from Table 8.3b and the theoretical light curve from Table 8.4b - Solution V.

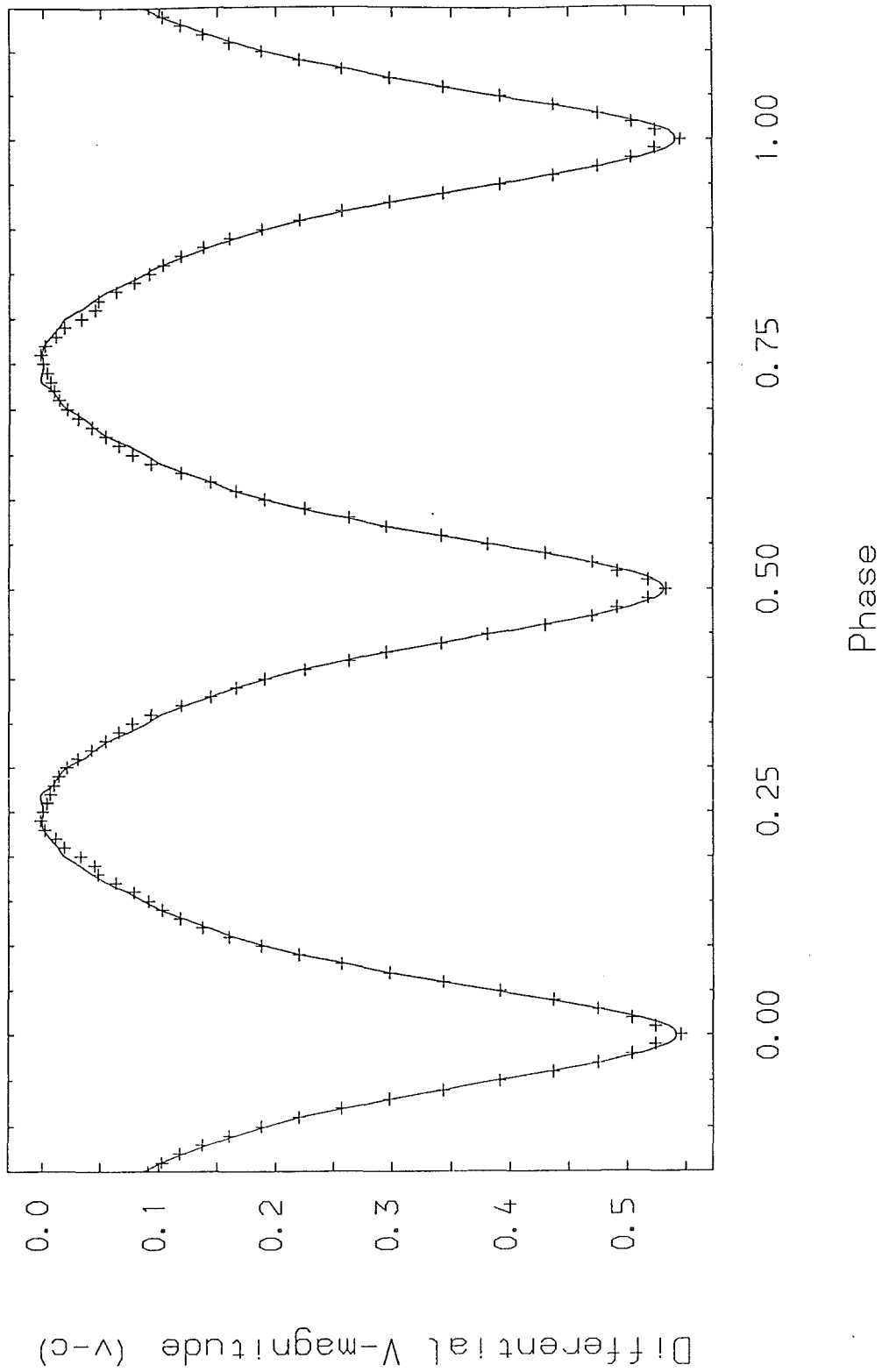


Figure 8.3b.ii
Theoretical light curve from Table 8.4b - Solution V, shown together with the spline points derived from the observed data for AD Phe between phase 0.0 and 0.5 .

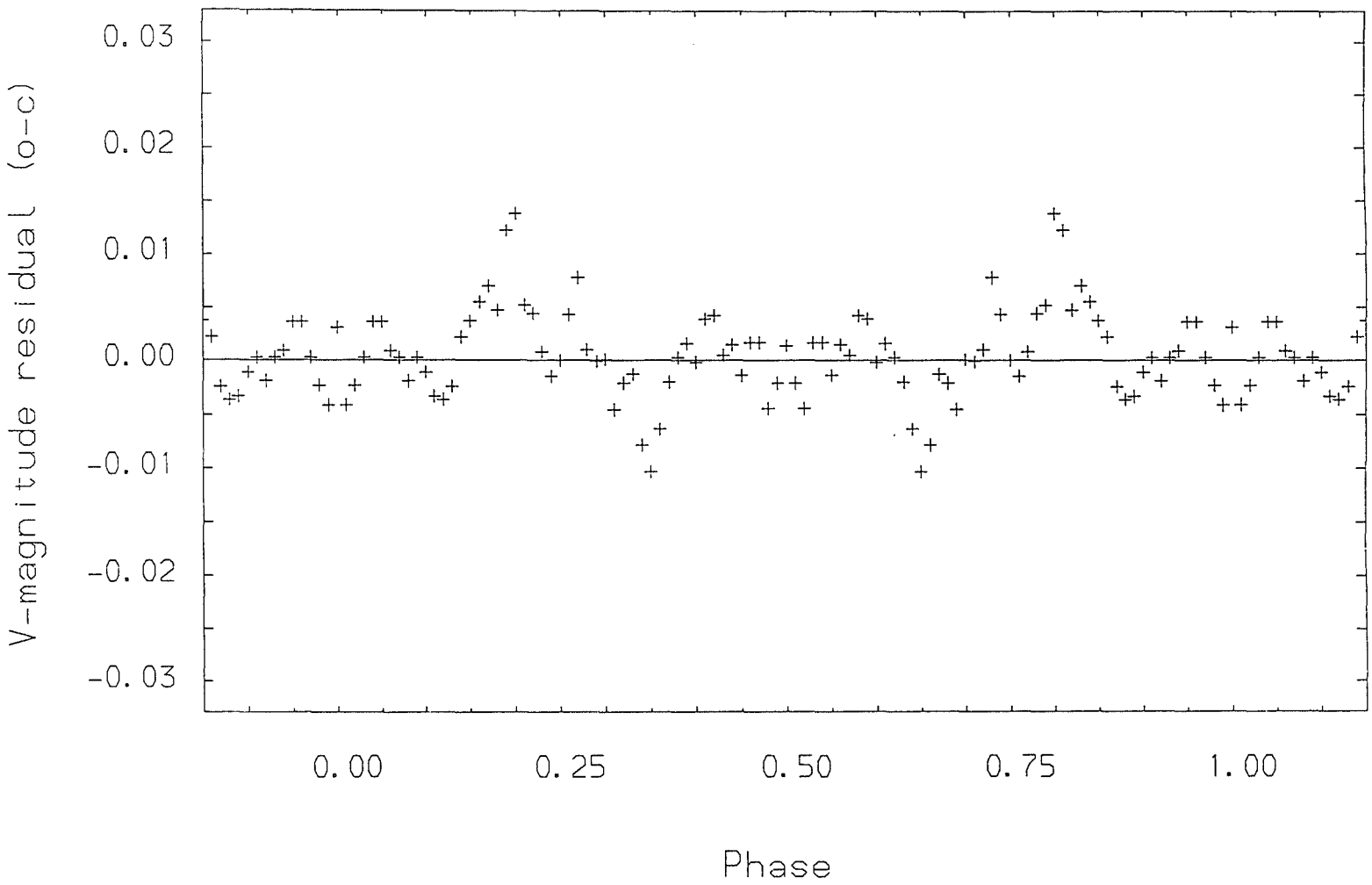


Figure 8.3b.iii
V-magnitude residuals (in the sense observed minus calculated), for
the fit shown in Figure 8.3b.ii .

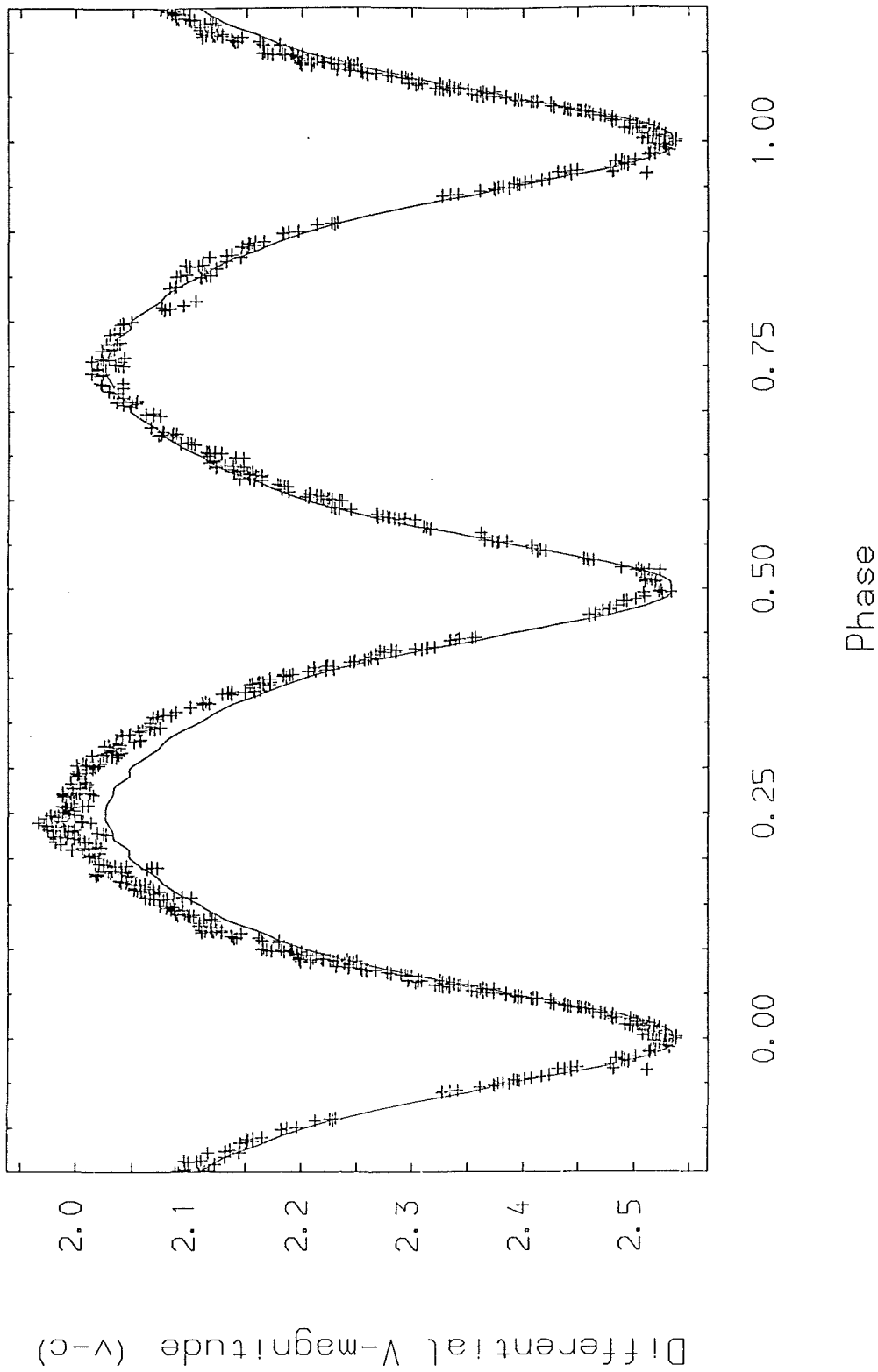


Figure 8.3b.iv
 V-light curve of AD Phe showing the individual observations from Table 8.3b and the theoretical light curve from Table 8.4b - Solution VI.

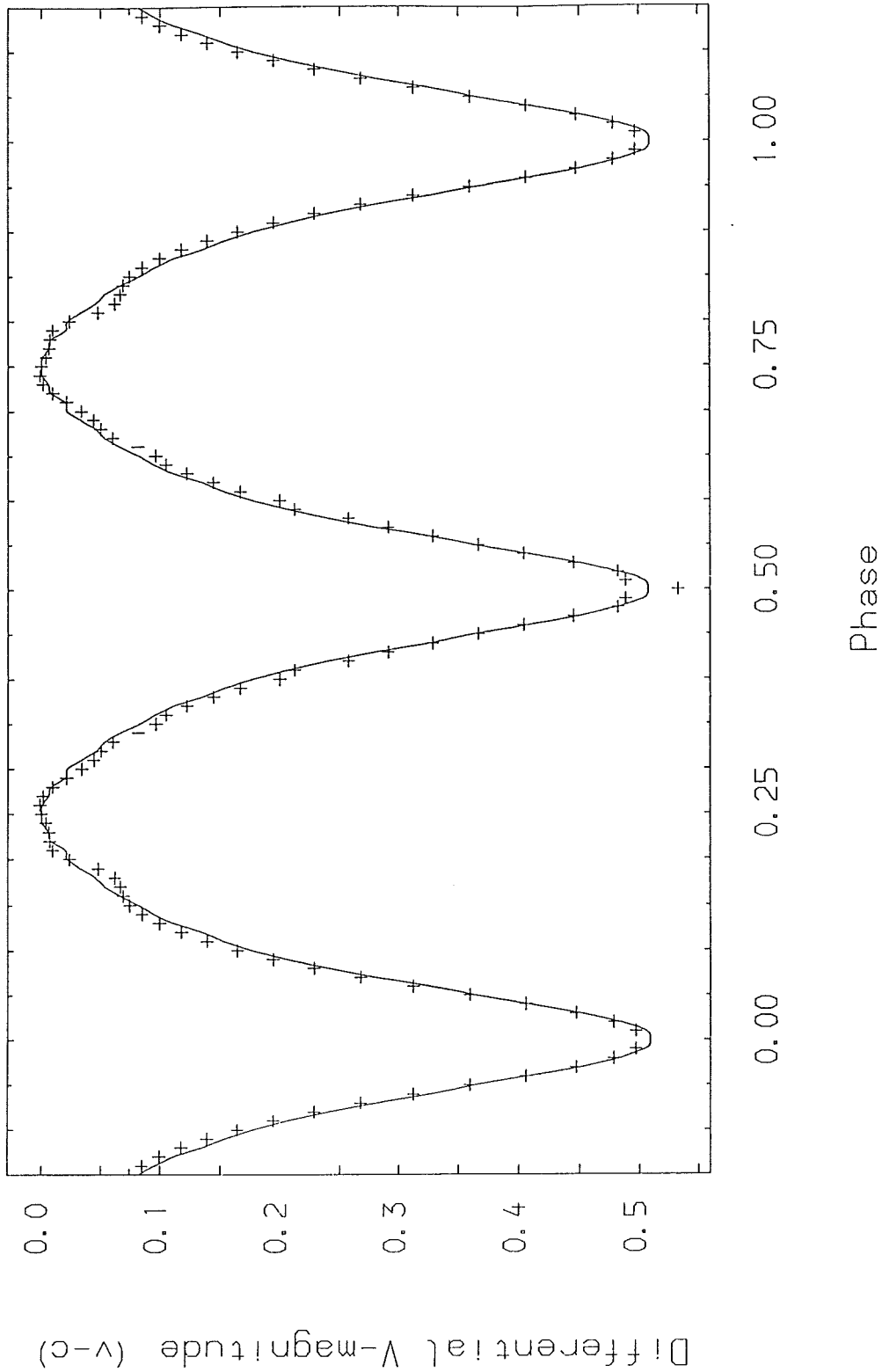


Figure 8.3b.v
Theoretical light curve from Table 8.4b - Solution VI, shown together with the spline points derived from the observed data for AD Phe between phase 0.5 and 1.0 .

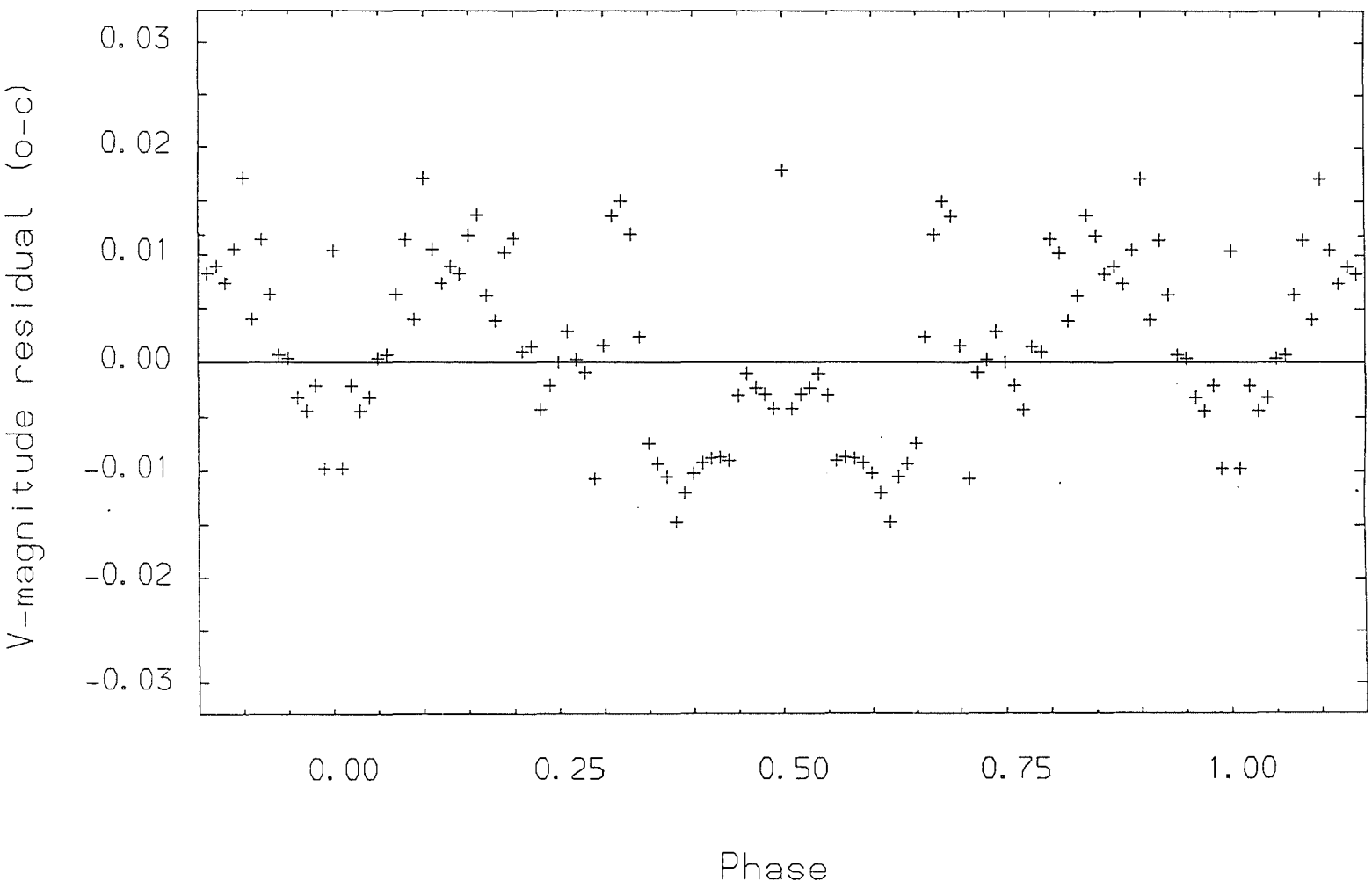


Figure 8.3b.v1
V-magnitude residuals (in the sense observed minus calculated), for
the fit shown in Figure 8.3b.v .

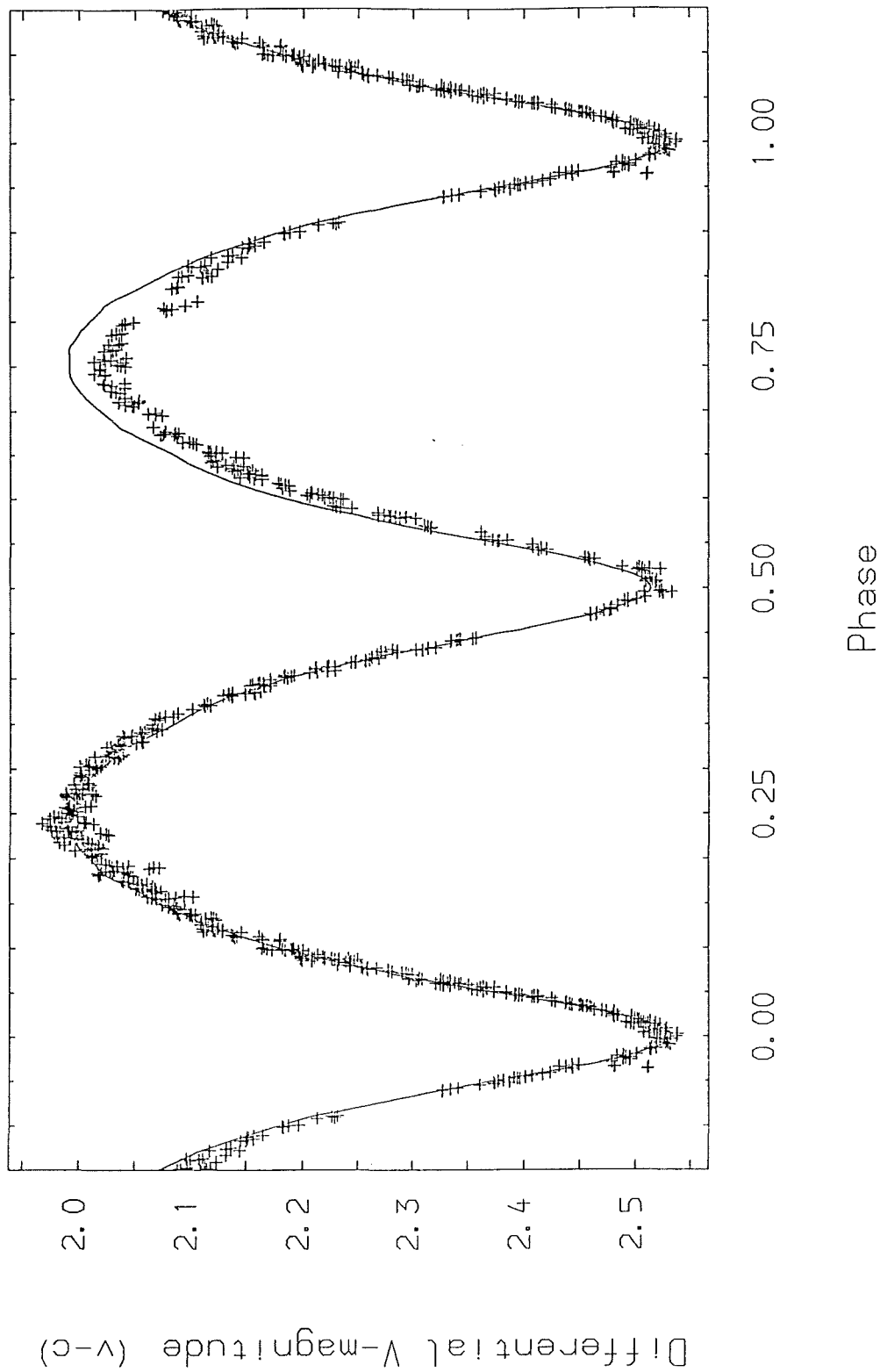


Figure 8.3b.vii
 V-light curve of AD Phe showing the individual observations from Table 8.3b and the theoretical light curve from Table 8.4b - Solution VII.

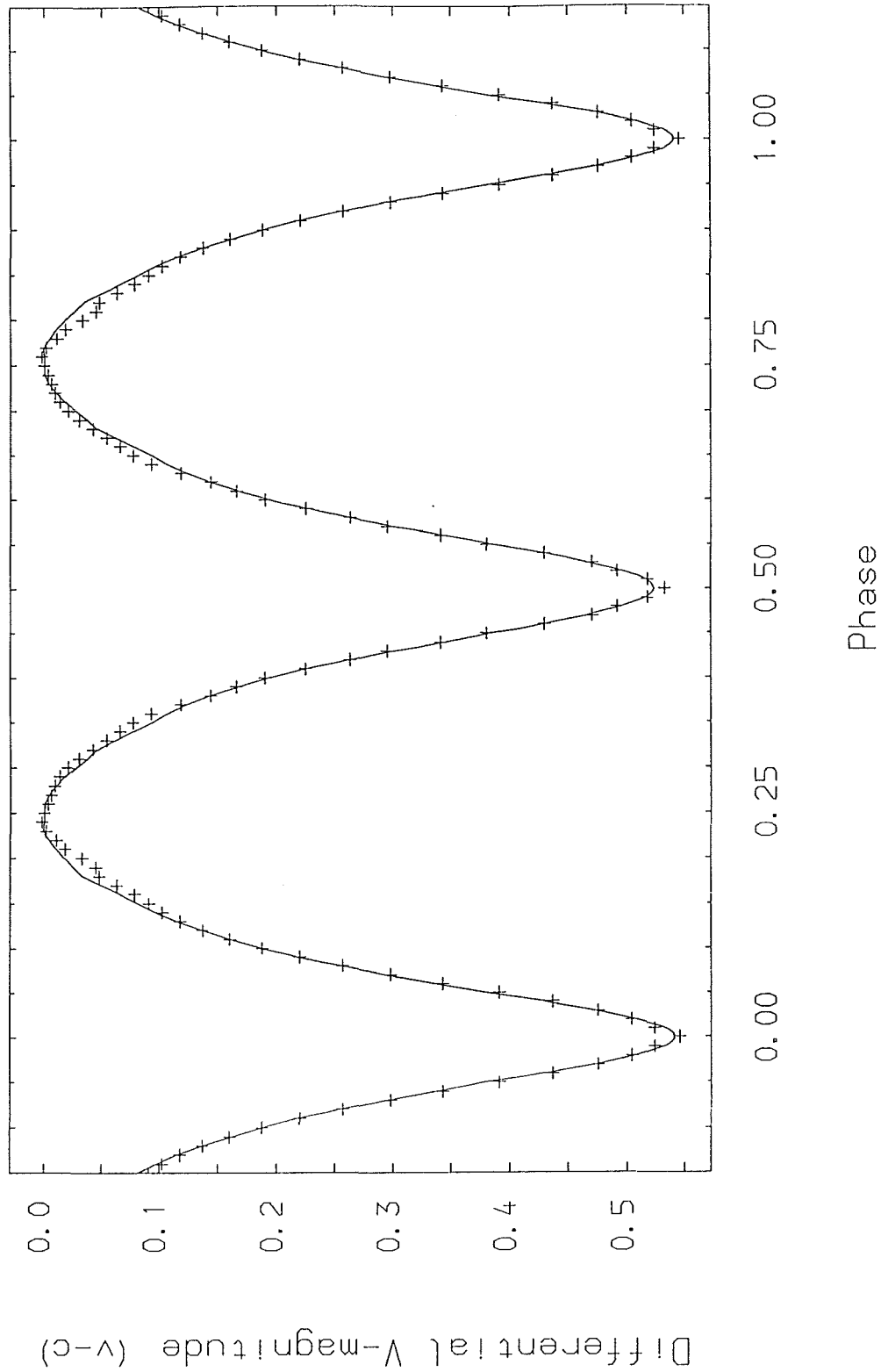


Figure 8.3b.viii
 Theoretical light curve from Table 8.4b - Solution VII, shown together with the spline points derived from the observed data for AD Phe between phase 0.0 and 0.5 .

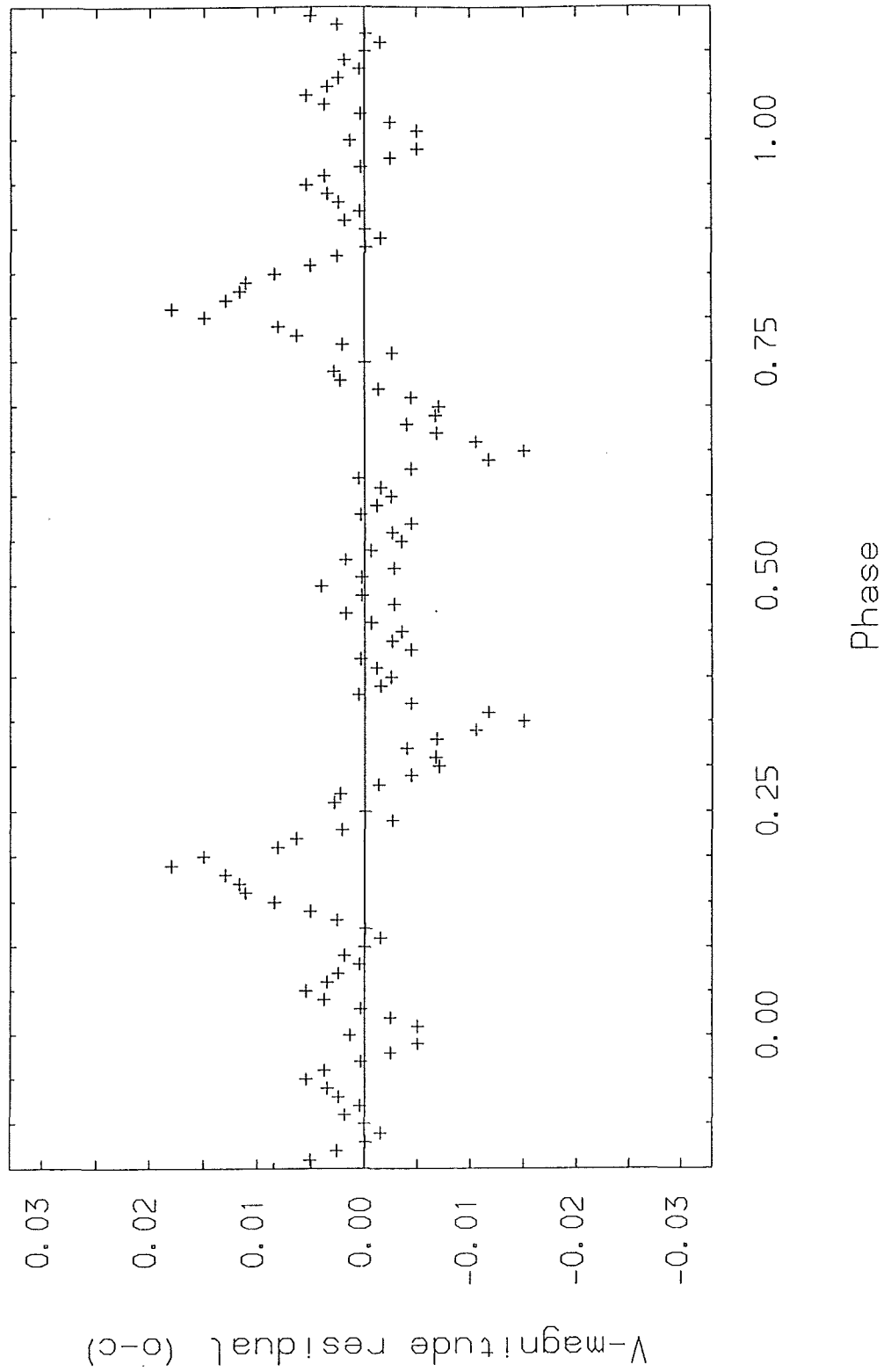


Figure 8.3b.ix
V-magnitude residuals (in the sense observed minus calculated), for
the fit shown in Figure 8.3b.viii .

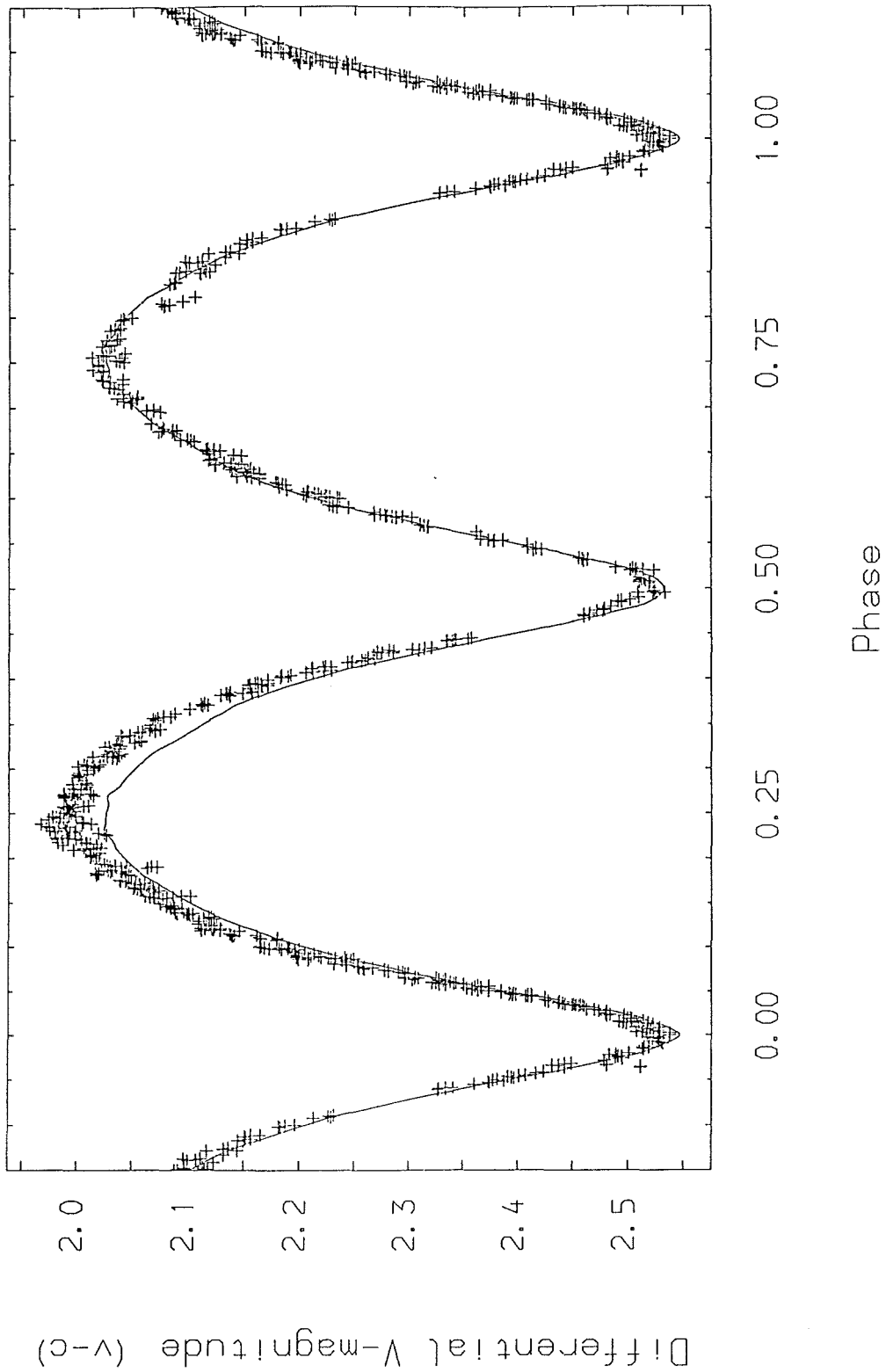


Figure 8.3b.x
 V-light curve of AD Phe showing the individual observations from Table 8.3b and the theoretical light curve from Table 8.4b - Solution VIII.

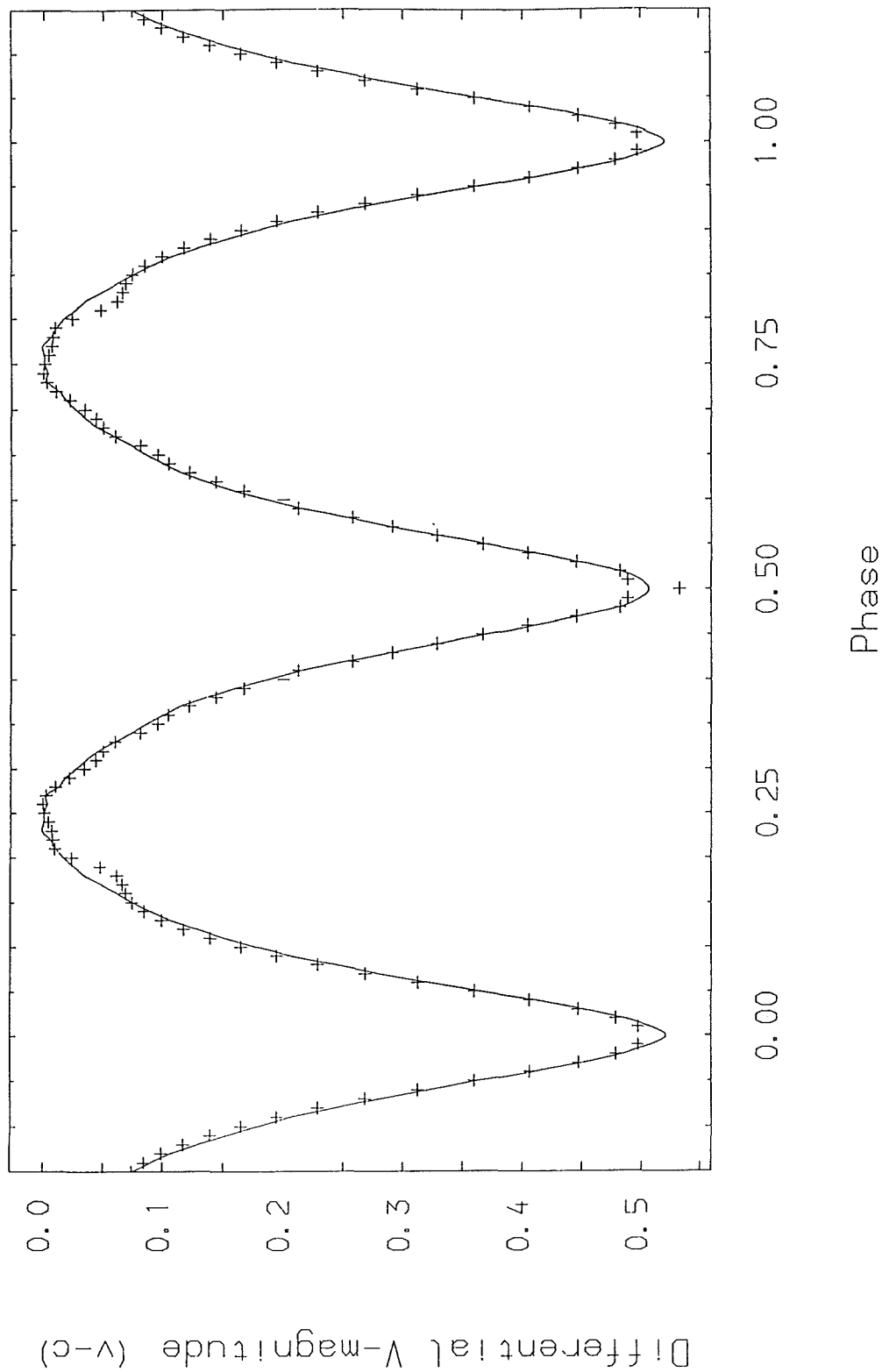


Figure 8.3b.xi
 Theoretical light curve from Table 8.4b - Solution VIII, shown together with the spline points derived from the observed data for AD Phe between phase 0.5 and 1.0 .

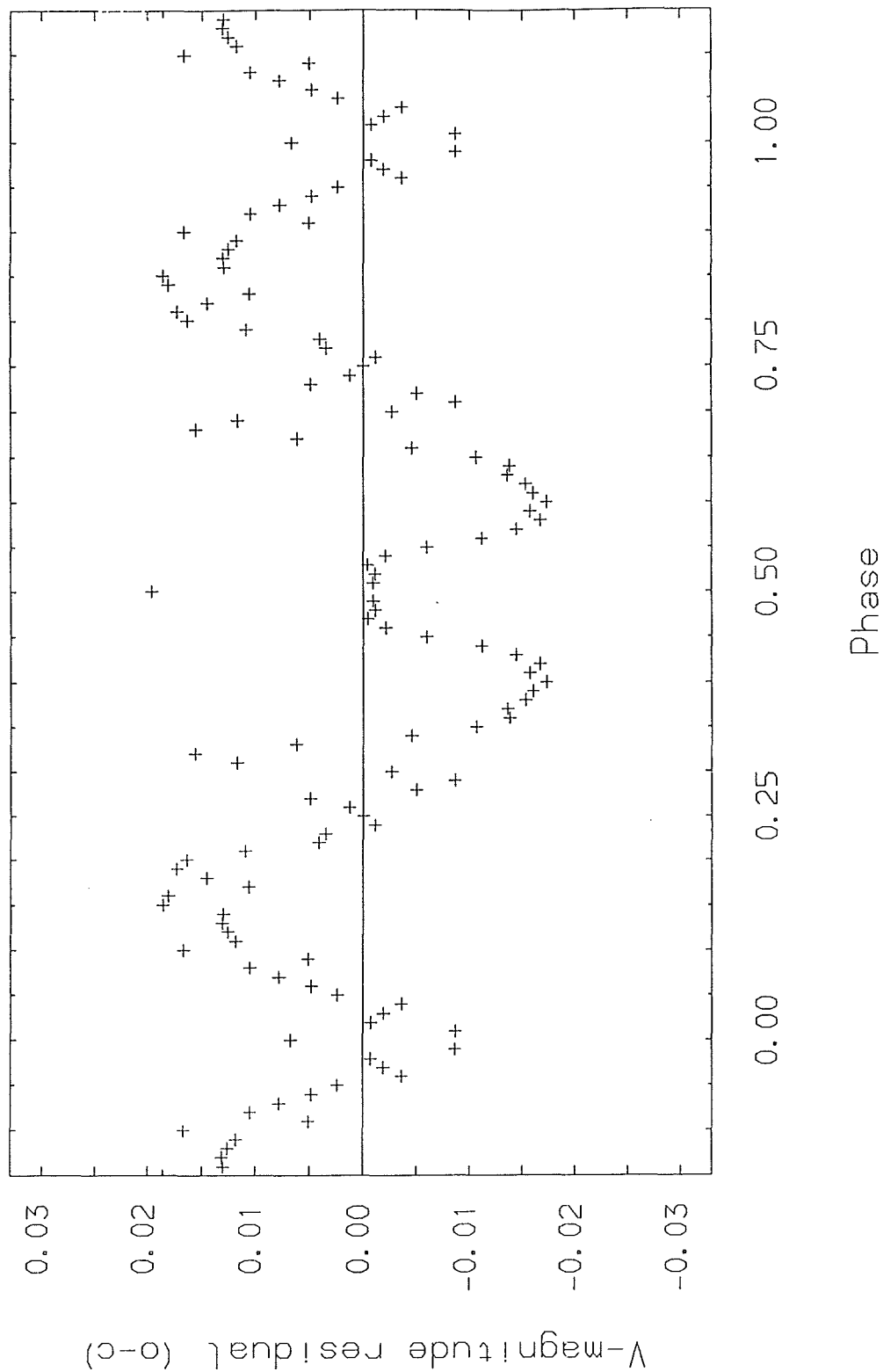


Figure 8.3b.xii
 V-magnitude residuals (in the sense observed minus calculated), for the fit shown in Figure 8.3b.xi .

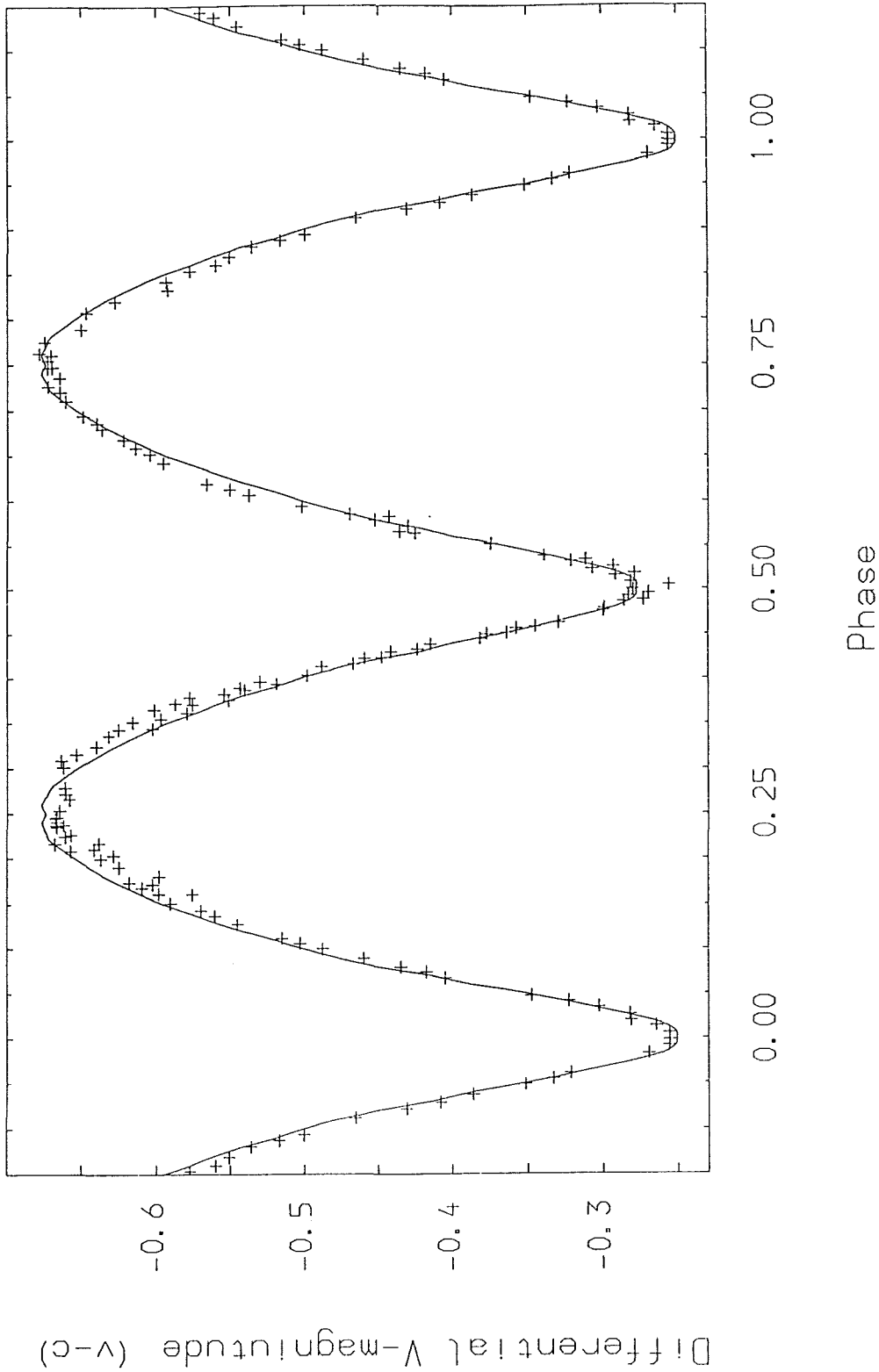


Figure 8.3c.i
 V-light curve of RS Col showing the individual observations from Table 8.3c and the theoretical light curve from Table 8.4c - Solution IX.

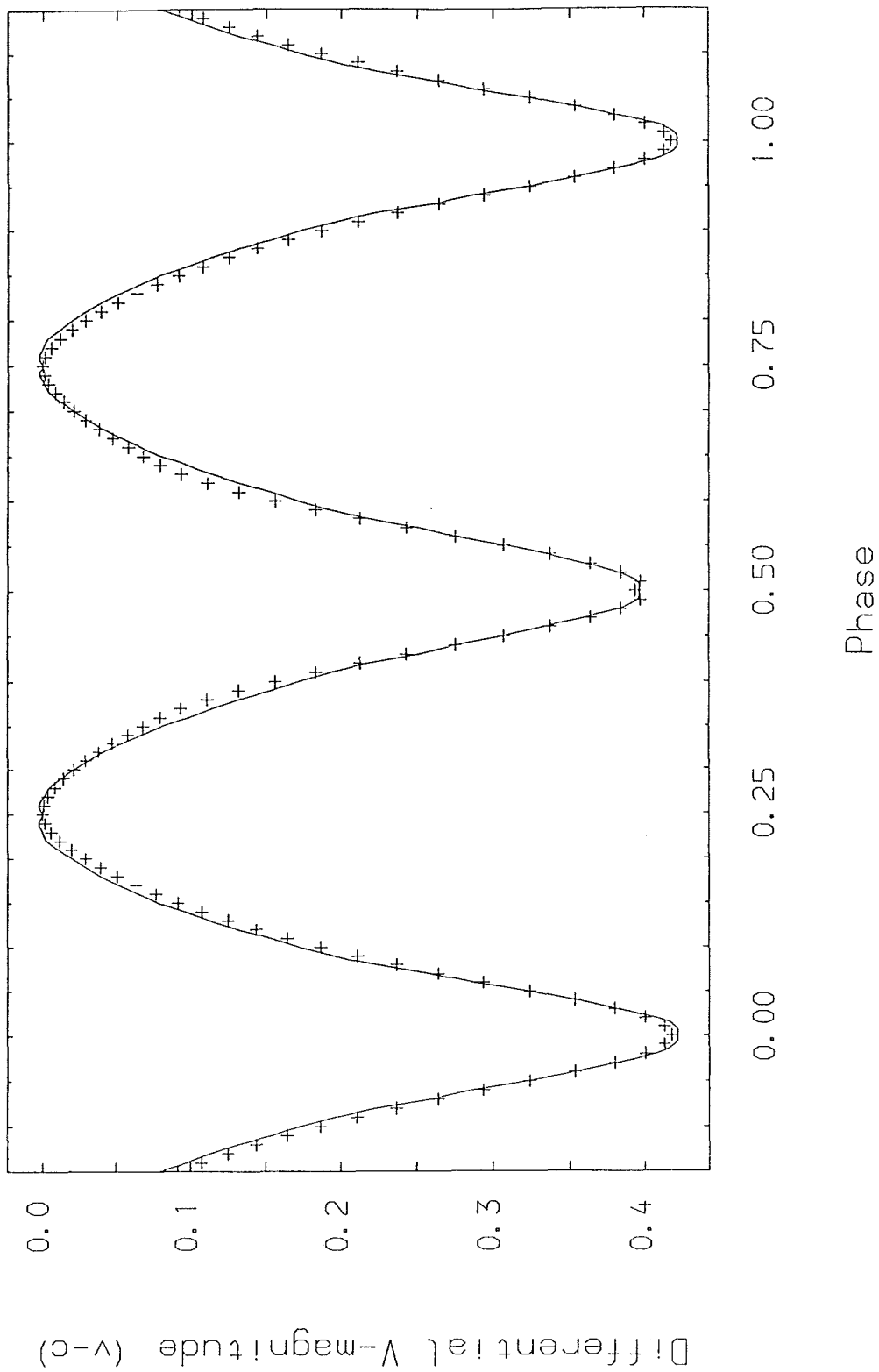


Figure 8.3c.ii
Theoretical light curve from Table 8.4c - Solution IX, shown together with the spline points derived from the observed data for RS Col between phase 0.0 and 0.5 .

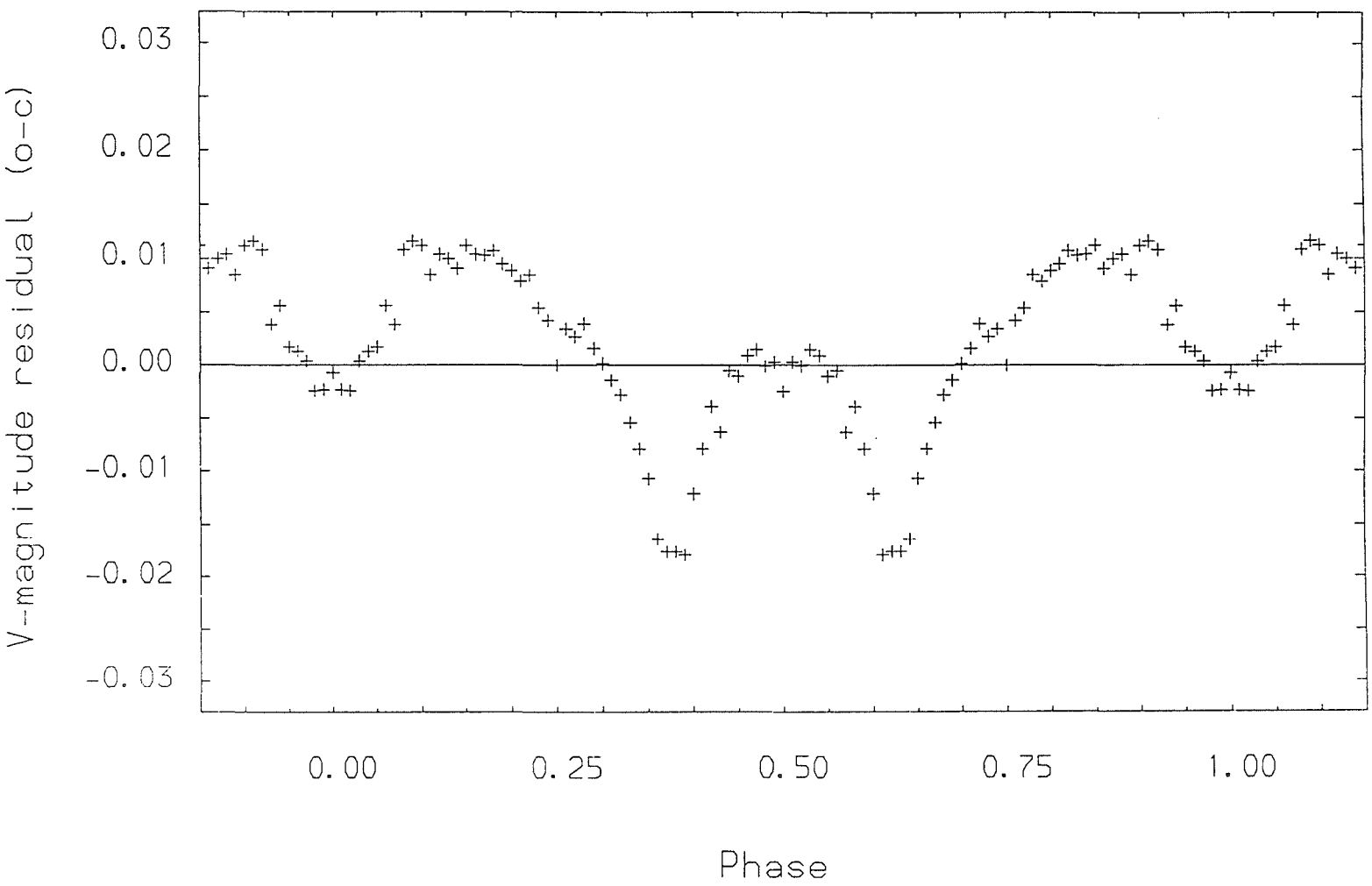


Figure 8.3c.iii
V-magnitude residuals (in the sense observed minus calculated), for
the fit shown in Figure 8.3c.ii .

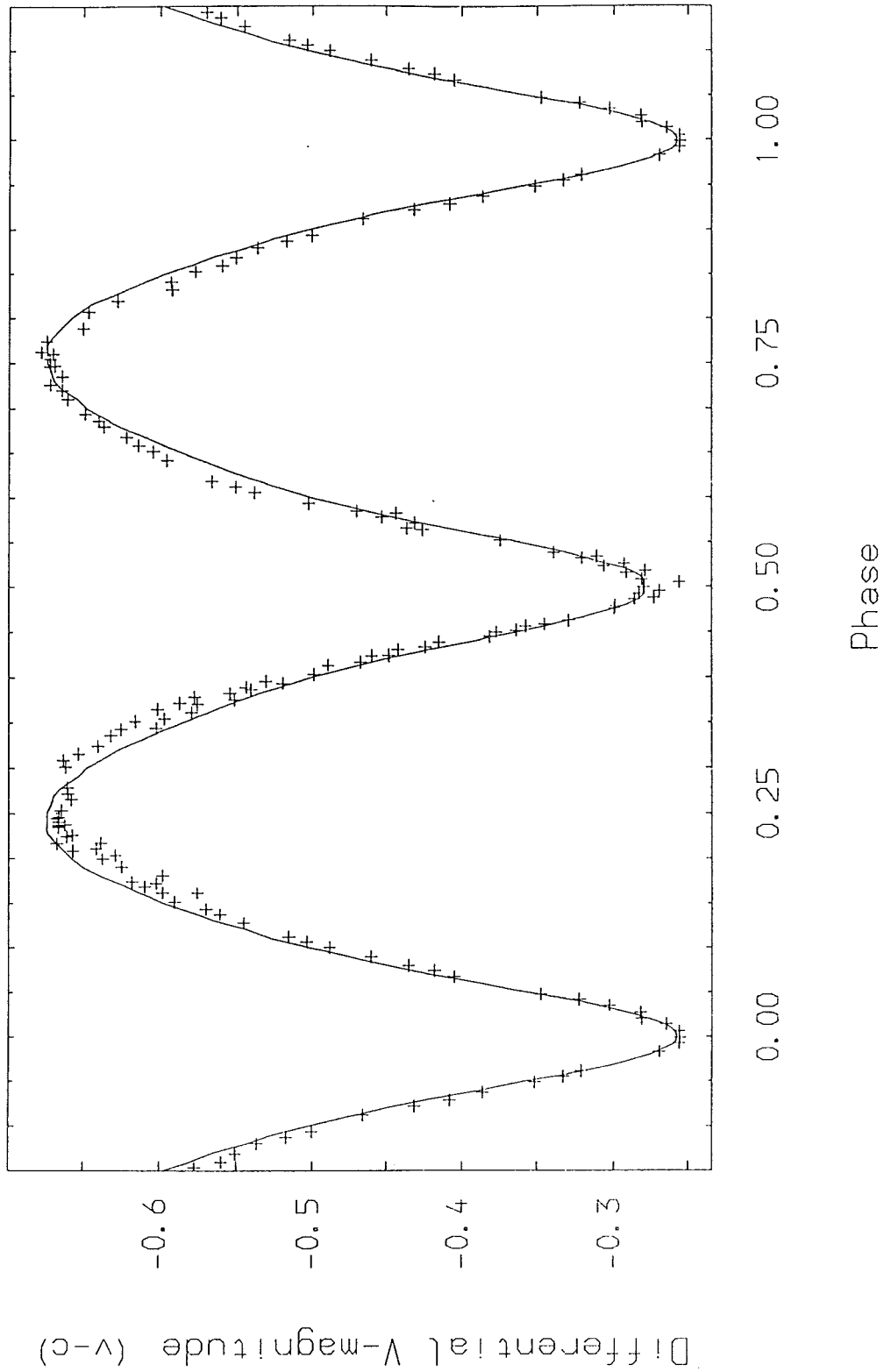


Figure 8.3c.iv
 V-light curve of RS Col showing the individual observations from Table 8.3c and the theoretical light curve from Table 8.4c - Solution X.

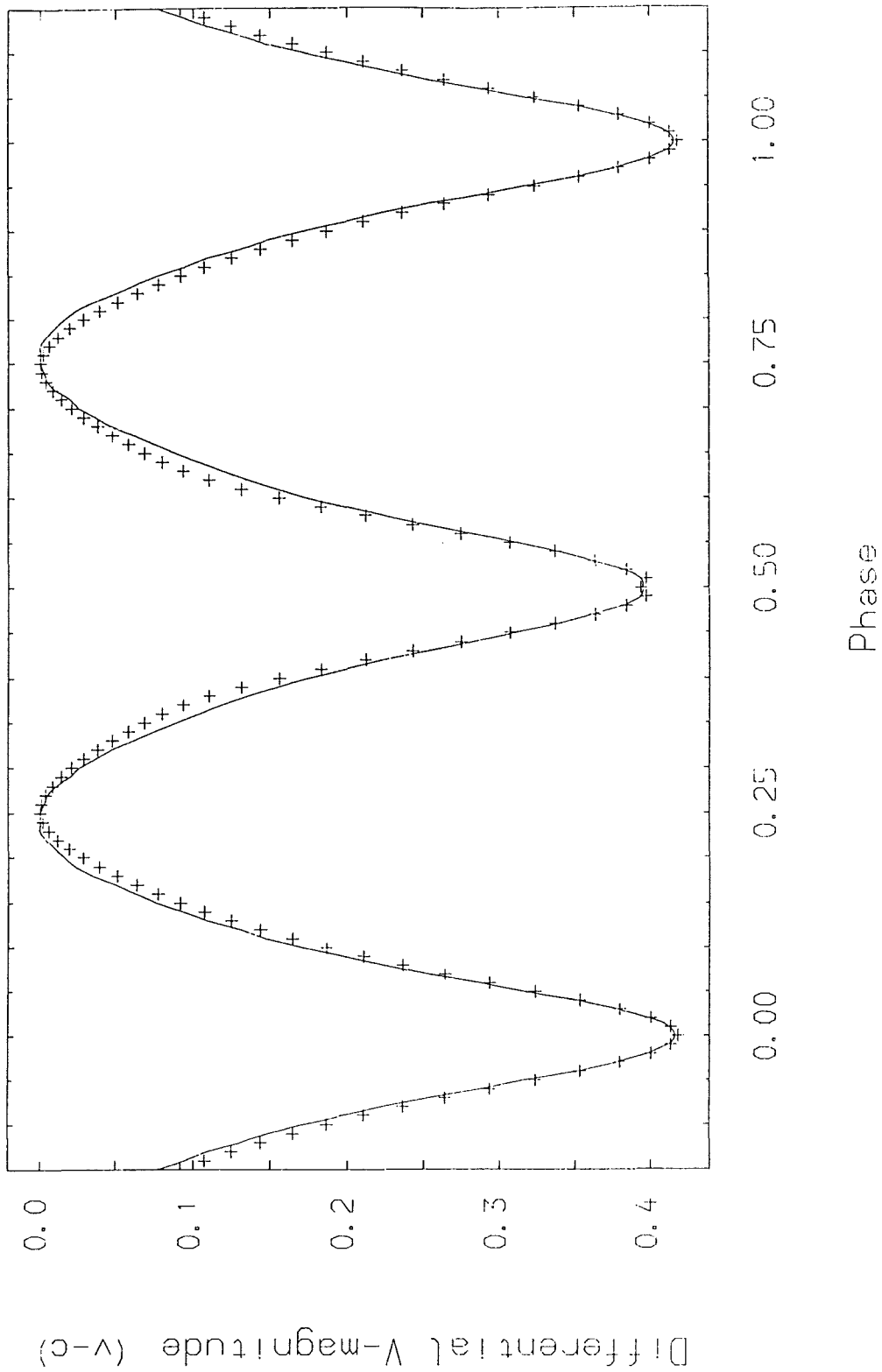


Figure 8.3c.v
 Theoretical light curve from Table 8.4c - Solution X, shown together
 with the spline points derived from the observed data for RS Col
 between phase 0.0 and 0.5 .

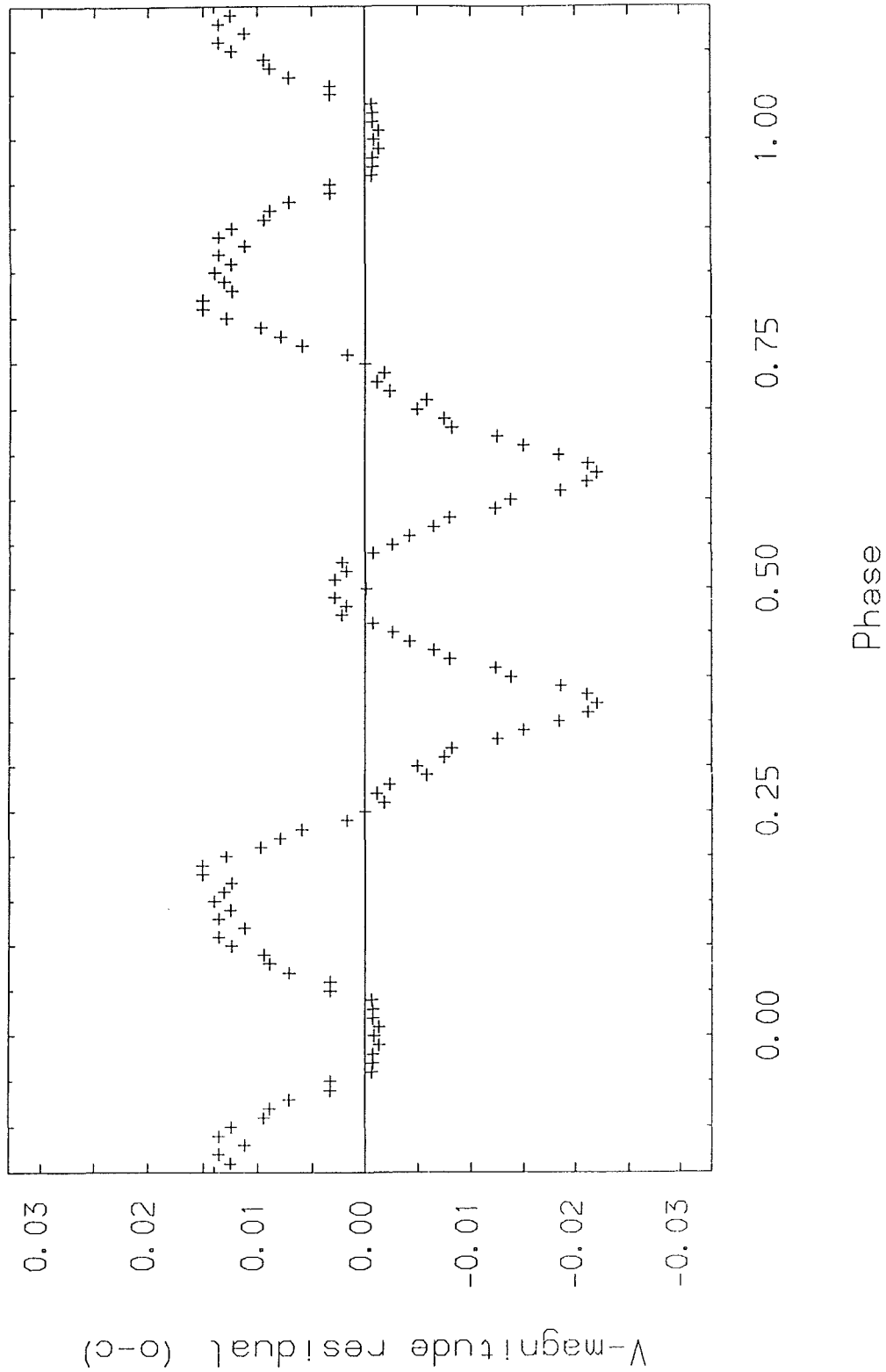


Figure 8.3c.vi
V-magnitude residuals (in the sense observed minus calculated), for
the fit shown in Figure 8.3c.v .

CHAPTER 9

CONCLUSIONS

9.1. EVOLUTION INTO CONTACT:

Mochnecki (1981) argued that some contact binaries possess too much angular momentum to have existed as contact systems at age zero. Although the evidence supporting this idea is very convincing, the theory has suffered from the lack of observed systems in near-contact detached or semi-detached configurations. The observations of the semi-detached systems YY Cet and CX Aqr have alleviated much of the uncertainty surrounding the theory that at least some W Uma-type binaries may have evolved into contact from non-contact states, by losing angular momentum via magnetic braking. A full discussion of the analyses of YY Cet and CX Aqr and the implications of the results are given in Chapters 5 and 6.

9.2. THE B-TYPE CONTACT BINARIES:

In Chapter 1 the two main objections to the TRO theory were discussed, namely the lack of observed systems in a state of broken contact (i.e. near-contact semi-detached systems whose primary components fill their Roche lobes), and the lack of observed systems in a state of marginal contact (i.e. contact systems whose components are of widely differing temperatures). Evidence in support of the existence of a broken-contact phase has been

presented by Hilditch and King (1986), who argue that the semi-detached binary RT Scl is in such a stage. The latter objection has been removed by the observation of several W UMa-type binaries with components which are of widely differing temperatures. Much of this work has been carried out by Dr.J.Kaluzny of the Warsaw University Observatory, who has argued that a hot-spot exists near the connecting neck of the binaries. Kaluzny also proposed that the light-curve synthesis codes could simulate this anomalous distribution of luminosity by allowing non-physical values for the secondary-component albedo. This suggests that all solutions of EB-type (in the sense Beta-Lyrae-type) light curves that have not employed the non-physical albedo in their analysis, and which indicate components in very-near-contact configurations, should be treated with caution. This includes Kaluzny and Semeniuk's (1984) analysis of the binary EG Cep. A fuller discussion of the B-type contact binaries is given in the analysis of RV Crv (Chapter 7).

9.3. CONTACT-BINARY DATA:

Data for late-type contact and near-contact binaries, compiled from various published sources, are presented in Table 9.1. The values for component masses, radii, luminosities and absolute visual magnitudes, have been calculated by Dr.R.W.Hilditch (except for YY Cet, CX Aqr and RV Crv), for those systems where good photometric and spectroscopic data exist.

The mass-radii and mass-luminosity data for the primary and secondary components of the systems are plotted together with Popper's (1980) data for main-sequence detached binaries, in Figures 9.1 and 9.2, respectively. The diagrams show that while the primary components of the contact binaries lie on or very close to the main-sequence band, all but one of the secondary components appear oversized and overluminous for their main-sequence mass, with the A-type secondaries apparently lying further off the main sequence than their W-type counterparts. Like the contact systems, the primary components of the semi-detached systems lie on the main sequence, while their secondaries are oversized and overluminous, although both components of the detached system ER Vul appear to lie on the main sequence. These results do not necessarily imply that the secondary components are all evolved, some may be oversized and overluminous as a result of energy transportation from their more massive companions.

Figure 9.3 shows a plot of effective-temperature against luminosity for the binary components, together with Popper's main-sequence data. The figure clearly shows that the primary components of the A-type and W-type contact systems all appear to lie within the main-sequence band, while almost all of the secondary components lie to the left of it, indicating temperatures higher than expected for their main-sequence luminosities. The secondary components of the A-type systems tend to lie further from the main sequence than the W-type secondary components, and also tend toward higher temperatures. The B-type contact systems on the other hand, show a different picture. For RV Crv, both the primary and

secondary components appear to lie on the main sequence. The position on the diagram of the two remaining B-type systems are uncertain, since no attempt was made to simulate anomalous distributions of luminosity when searching for their photometric solutions. Thus, the temperatures for the secondary components may be slightly greater than the published solutions suggest, although it is still very likely that the secondary components will remain to the right of the main sequence. For the semi-detached systems, the primary components appear to be main-sequence objects, while the secondaries are evolved, lying to the right of the main-sequence band. The components of the only detached system, ER Vul, both lie within the main sequence.

Finally, Figures 9.4 and 9.5 show a plot of:

$$q \text{ versus } \log[q.(1+q)^{-2}.P^{1/3}] ,$$

where 'q' is the mass ratio and 'P' is the orbital period in days.

Also,

$$q.(1+q)^{-2}.P^{1/3} \propto J_{\text{orb}}/M_{\text{tot}}^{5/3} ,$$

where J_{orb} is the orbital angular momentum and M_{tot} is the total mass of the binary.

The diagram, which depends only upon two parameters which are relatively easy to determine, namely the mass ratio and period, shows a clear division between the W-type systems, which tend to have higher mass ratios and shorter periods, and the A-type systems, which tend toward smaller mass ratios and longer periods. (The only W-type system lying outside the main group, is the unusual contact binary TZ Boo, whose light curve alternates between A-type and W-type.) The B-type contact binaries lie above the W-type group,

having a similar range of mass ratio to the W-types, but possessing longer orbital periods. The same is also true of the detached and semi-detached binaries, except that they possess longer periods still. These groupings may represent an evolutionary sequence, with the detached and semi-detached systems evolving into contact, and the W-type systems evolving towards smaller mass ratios and longer periods, finally ending up as A-type contact binaries.

9.4. CONCLUDING REMARKS:

The fact that the primary components of the contact binaries appear to lie on or near the main sequence may raise some interesting questions. Smith (1986) has suggested that luminosity transfer from the primary components of some A-type or W-type systems may not be sufficient to account for the excess luminosities observed for their secondaries, unless the primary components have evolved beyond the main-sequence. However, estimates of the expected component luminosities based upon the empirical mass-luminosity relationship of $L \propto M^{4.0}$, using the data shown in Figure 9.1, indicate that for most systems the primary components do have sufficient 'excess' luminosity from their evolution within the main sequence band to account for the observed secondary-component luminosities. Using the observed luminosities for the primary components themselves, as well as adding the excess luminosities of their secondaries, yields values for the average 'excess' primary-component bolometric magnitude over that expected for their masses of, $(0.5_{-0.9}^{+0.9})$ mag. and $(0.8_{-0.8}^{+0.8})$ mag., respectively (the errors being standard deviations). Unfortunately, because the errors involved in the estimates of the individual luminosities are

very large, no definitive conclusions can be drawn from these calculations. However, these mean 'excess' luminosities are based upon 20 systems, and the main-sequence band is of the order of 0.75 mag. wide in the relevant mass range. Thus it does not appear to be necessary to demand that the primary components have evolved beyond the main-sequence band in order to explain the excess luminosities of the secondary components.

In Chapter 7 the possible nature of the anomalous distribution of light on the surfaces of the B-type contact binaries was discussed. In order to determine whether the proposed hot-spot actually exists, simultaneous observations over a wide wavelength range (from ultraviolet to far infra-red) are required. Such observations will also be necessary to establish the nature of the W-type contact systems, that is, whether the secondary components are actually hotter than their more massive companions, or only appear so because the surfaces of the primary components are blemished by starspots (see Rucinski, 1985a). Although the latter hypothesis has become generally accepted as the correct explanation of the W-type phenomenon (winning by default), the debate is by no means over.

It has been argued that the presence of starspots is the only plausible explanation for the behaviour of the light curve of TZ Boo, which alternates between A-type and W-type. However, Bell (1986) has noted similar behaviour in the light curve of an early-type contact binary. If this is indeed the case, then some mechanism other than starspots may be responsible for the TZ Boo phenomenon, and perhaps the W-type phenomenon as well.

Table 9.1. Data on late-type contact and near-contact binaries.

Name	Type	Period (days)	Mass Ratio	M _{pr}	R _{pr}	L _{pr}	T _{pr}	Mv _{pr}
				M _{sec}	R _{sec}	L _{sec}	T _{sec}	Mv _{sec}
CC Com	W	0.221	0.52 s	0.69 0.32	0.71 0.52	0.21 0.11	4560	6.90 7.57
V523 Cas	W	0.237	0.42 p	--	--	--	--	--
BI Vul	W	0.252	0.69 p	--	--	--	--	--
FS CrA	W	0.264	0.76 p	--	--	--	--	--
FG Sct	W	0.271	0.79 p	--	--	--	--	--
VW Cep	W	0.278	0.41 s	0.82 0.34	0.87 0.58	0.63 0.28	5550	5.36 6.24
BX Peg	W	0.280	0.37 p	--	--	--	--	--
XY Leo	W	0.284	0.50 s	0.87 0.43	0.82 0.63	0.33 0.17	4800 5078	6.29 6.86
ER Cep	W	0.286	0.59 p	--	--	--	--	--
BW Dra	W	0.292	0.83 p	--	--	--	--	--
TZ Boo	W	0.297	0.13 s	0.65 0.09	0.92 0.35	1.05 0.15	6040	4.74 6.83
TW Cet	W	0.317	0.58 p	--	--	--	--	--
GW Cep	W	0.319	0.37 p	--	--	--	--	--
SW Lac	W	0.321	0.87 s	1.33 1.16	1.10 1.03	1.38 1.23	5830	4.43 4.57
YY Eri	W	0.321	0.59 s	0.94 0.55	0.98 0.77	1.74 1.07	6480	4.13 4.65
FG Hya	A	0.328	0.14 p	--	--	--	--	--
AB And	W	0.332	0.53 p	--	--	--	--	--
W UMa	W	0.334	0.45 s	1.14 0.55	1.13 0.80	1.35 0.63	5800 6200	4.51 5.26
RZ Com	W	0.338	0.43 s	1.11 0.48	1.10 0.75	2.40 1.12	6740	3.75 4.58
V575 Cen	W	0.343	0.68 s	0.85 0.60	0.97 0.83	1.32 0.98	6290	4.42 4.76
BV Dra	W	0.350	0.80 p	--	--	--	--	--
AC Boo	W	0.352	0.30 p	--	--	--	--	--
AH Cnc	W	0.360	0.50 p	--	--	--	--	--
RW PsA	W	0.360	0.81 p	--	--	--	--	--

(continued).

Table 9.1. Data on late-type contact and near-contact binaries (continued).

Name	Type	Period (days)	Mass Ratio	M _{pr}	R _{pr}	L _{pr}	T _{pr}	Mv _{pr}
				M _{sec}	R _{sec}	L _{sec}	T _{sec}	Mv _{sec}
AE Phe	W	0.362	0.40 p	--	--	--	--	--
AM Leo	W	0.366	0.42 p	--	--	--	--	--
HD101799	W	0.370	0.30 p	--	--	--	--	--
XY Boo	A	0.371	0.16 s	0.95	1.15	2.40	6650	3.75
				0.15	0.52	0.50		5.47
U Peg	W	0.375	0.41 s	1.10	1.18	2.51	6560	3.70
				0.46	0.79	1.15		4.57
TX Cnc	W	0.383	0.53 s	0.84	0.94	1.02	5850	4.77
				0.45	0.71	0.58	5955	5.38
AU Ser	W	0.386	0.67 p	--	--	--	--	--
W Crv	A	0.388	0.78 p	--	--	--	--	--
EM Lac	W	0.389	0.64 p	--	--	--	--	--
AH Vir	W	0.408	0.36 p	--	--	--	5450	--
				--	--	--	5630	--
V566 Oph	A	0.410	0.24 s	1.47	1.46	4.68	6890	3.03
				0.36	0.78	1.32		4.39
RZ Tau	A	0.416	0.37 p	--	--	--	--	--
WZ Cep	B	0.417	0.33 p	--	--	--	--	--
Y Sex	A	0.420	0.18 s	0.68	1.14	2.63	6770	3.67
				0.12	0.52	0.55		5.37
AK Her	A	0.422	0.26 p	--	--	--	--	--
ER Ori	W	0.423	0.76 p	--	--	--	--	--
AW UMa	A	0.439	0.07 s	1.7	--	--	7300	--
				0.12	--	--		--
EZ Hya	W	0.450	0.25 s	--	--	--	5690	--
V502 Oph	W	0.453	0.37 s	1.30	1.37	4.47	7000	3.07
				0.49	0.89	1.91		4.01
TY Men	A	0.462	0.22 p	--	--	--	--	--
FT Lup	B	0.470	0.43 s	1.43	1.45	3.98	6700	3.21
				0.61	0.99	0.58	4500?	5.78
DK Cyg	A	0.471	0.27 p	--	--	--	--	--
OO Aql	W	0.507	0.82 p	--	--	--	--	--
				--	--	--	--	--

(continued).

Table 9.1. Data on late-type contact and near-contact binaries (continued).

Name	Type	Period (days)	Mass Ratio	M_{pr} M_{sec}	R_{pr} R_{sec}	L_{pr} L_{sec}	T_{pr} T_{sec}	Mv_{pr} Mv_{sec}
RT Scl	Semi-det.	0.512	0.44 s	1.46 0.64	1.54 1.05	5.13 2.40	6900 4820	2.92 3.75
BU Vel	A	0.516	0.25 p	--	--	--	--	--
CX Aqr	Semi-det.	0.556	0.58 s	1.19 0.64	1.29 1.15	2.70 0.72	6400 4969	3.64 5.36
Eps CrA	A	0.591	0.11 p	--	--	--	--	--
AQ Tuc	A	0.595	0.35 s	2.13 0.75	2.01 1.26	8.71 3.47	6900	2.34 3.35
RR Cen	A	0.606	0.21 s	1.86 0.39	2.08 1.07	11.48 3.02	7250	2.06 3.51
UZ Leo	A	0.629	0.36 p	--	--	--	--	--
AG Vir	B	0.643	0.27 p	--	--	--	--	--
S Ant	A	0.648	0.59 p	--	--	--	--	--
V1010 Cyg	A	0.661	0.49 p	--	--	--	--	--
RS Sct	B	0.664	0.77 s	1.37 0.82	1.56 1.23	5.75 5.13	7000 4749?	2.79 3.31
ER Vul	Det.	0.698	0.93 s	0.93 0.92	1.14 1.07	1.38 1.20	5800?	4.49 4.63
RV Crv	B	0.747	0.27 s	1.64 0.44	2.18 1.19	8.5 1.5	6600 5792	2.39 4.36
V1073 Cyg	A	0.786	0.24 p	--	--	--	--	--
YY Cet	Semi-det.	0.790	0.52 s	1.84 0.94	2.09 1.63	12.7 2.0	7500 5314	1.93 4.12
MW Pav	A	0.795	0.18 p	--	--	--	--	--
TY Pup	A	0.819	0.33 p	--	--	--	--	--

s, p denote spectroscopic and photometric mass ratios, respectively,

M_{pr} , M_{sec} are the component masses in solar units,

R_{pr} , R_{sec} are the component radii in solar units,

L_{pr} , L_{sec} are the component luminosities in solar units,

Mv_{pr} , Mv_{sec} are the absolute visual magnitudes of the components.

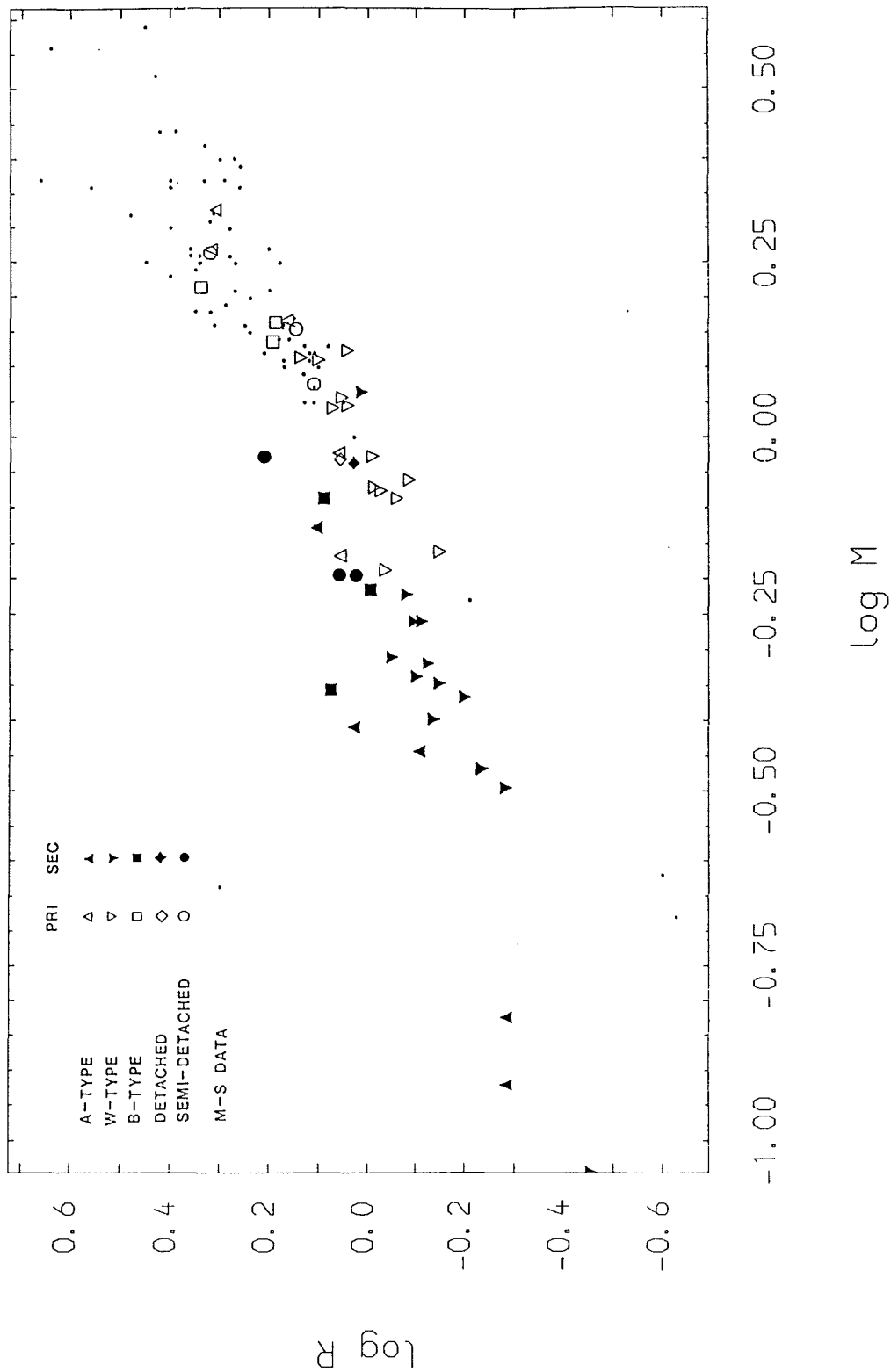


Figure 9.1.

Plot of mass against radius for the data on late-type contact and near-contact binaries shown in Table 9.1, together with Popper's (1980) data for main sequence detached binaries. The data are measured in solar units.

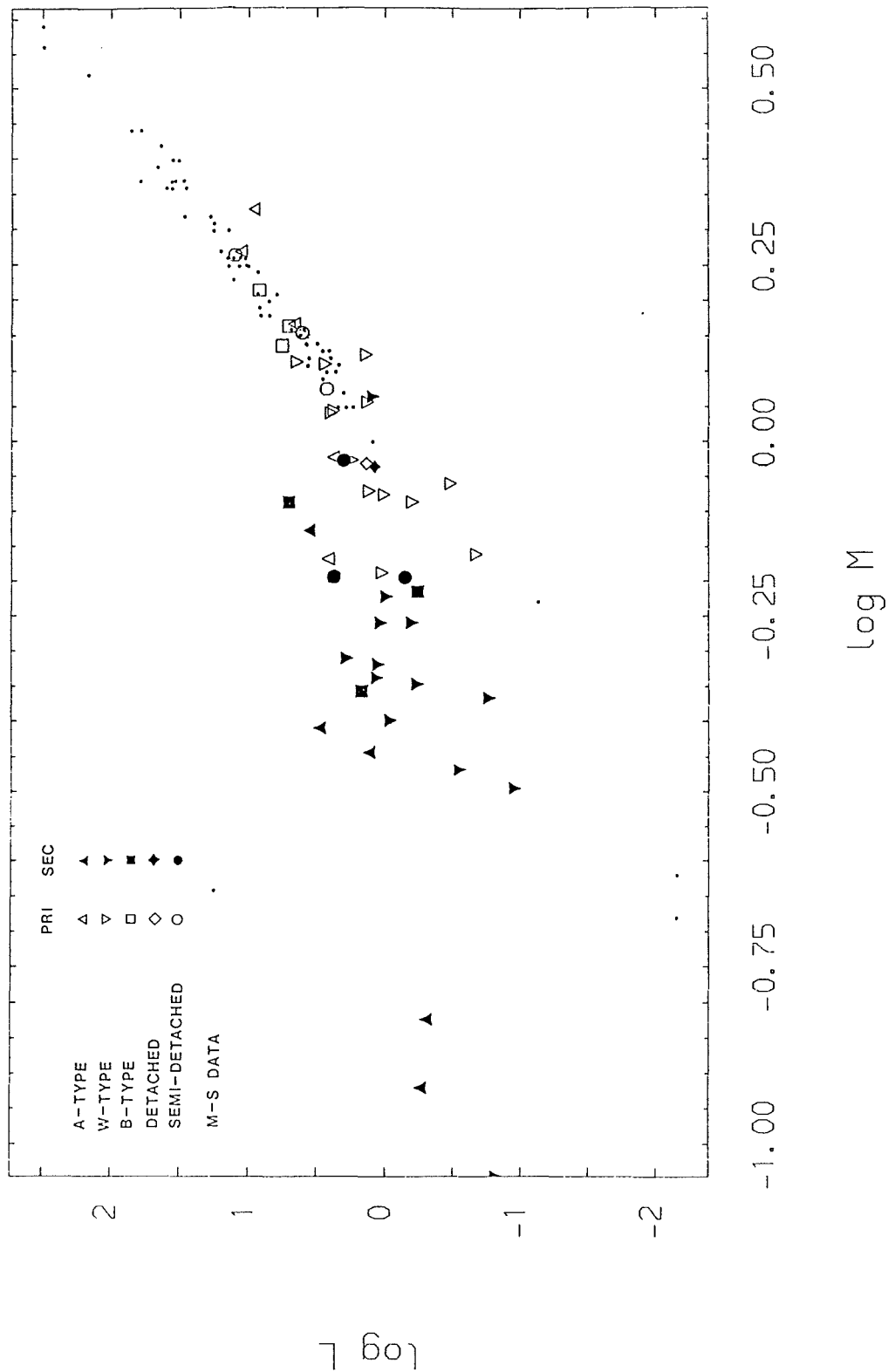


Figure 9.2.
 Plot of mass against luminosity for the data on late-type contact and near-contact binaries shown in Table 9.1, together with Popper's (1980) data for main sequence detached binaries. The data are measured in solar units.

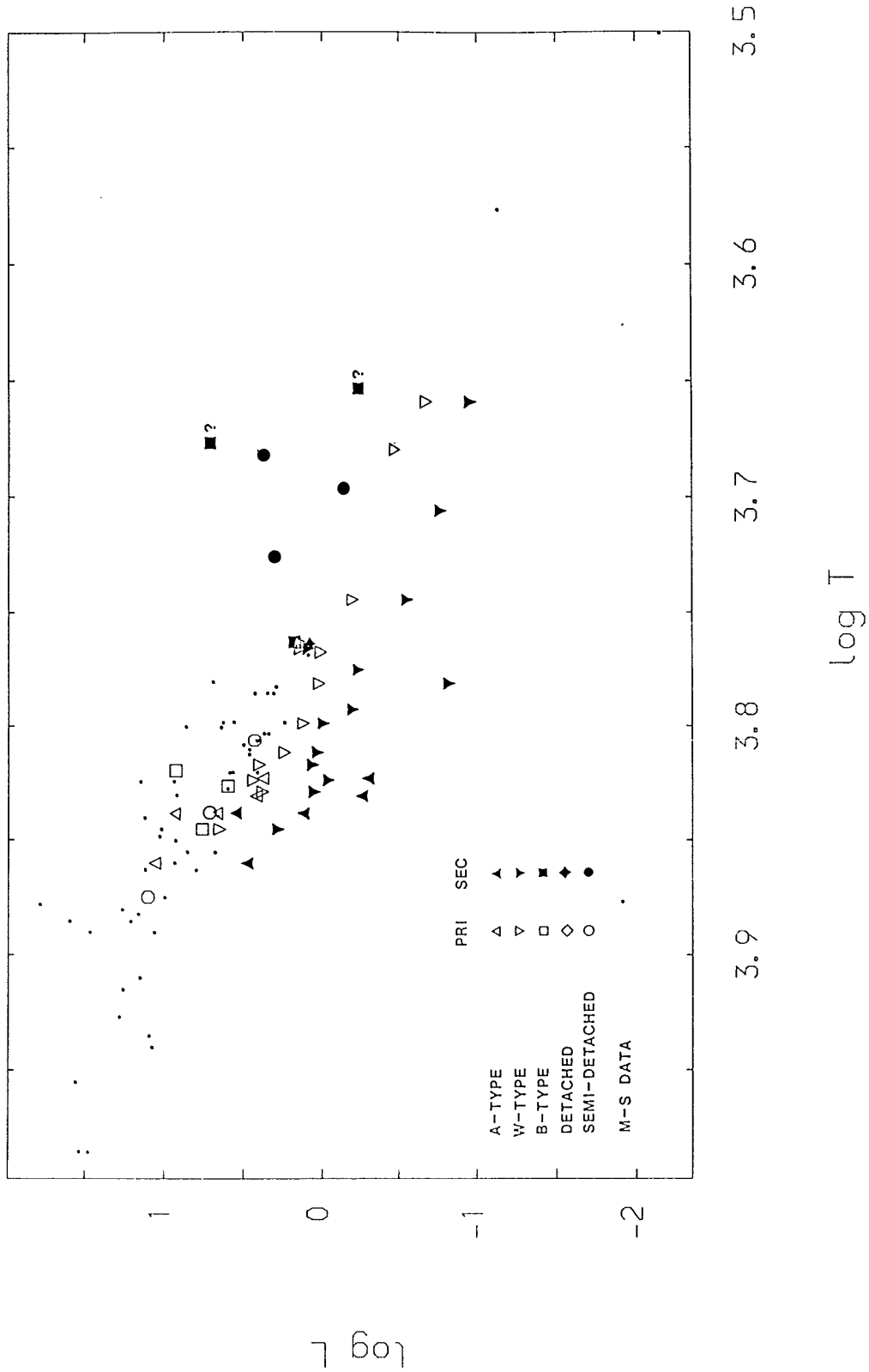


Figure 9.3.
 Plot of effective-temperature against luminosity for the data on late-type contact and near-contact binaries shown in Table 9.1, together with Popper's (1980) data for main sequence detached binaries. The temperatures are measured in Kelvin, while the luminosities are in solar units.

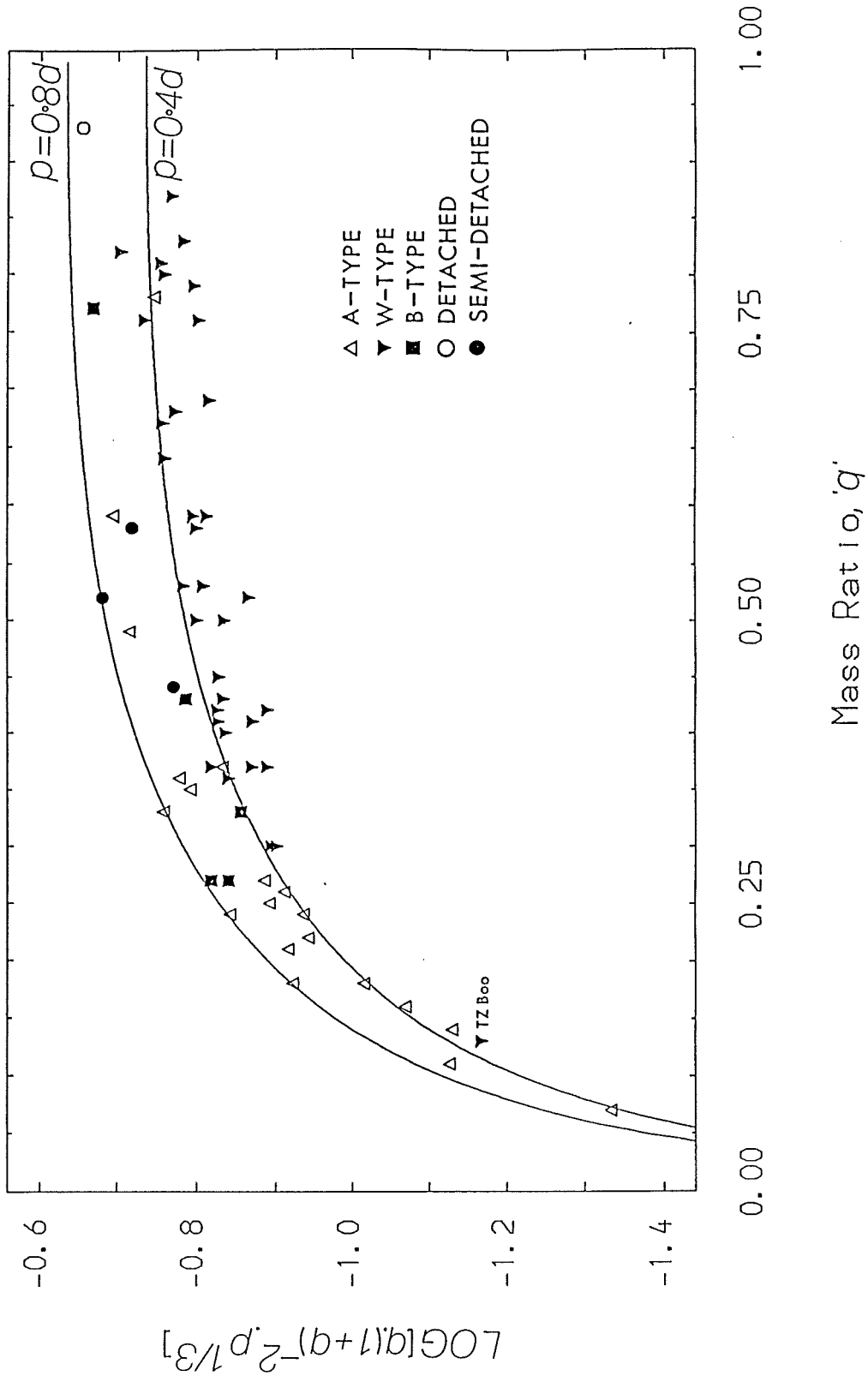
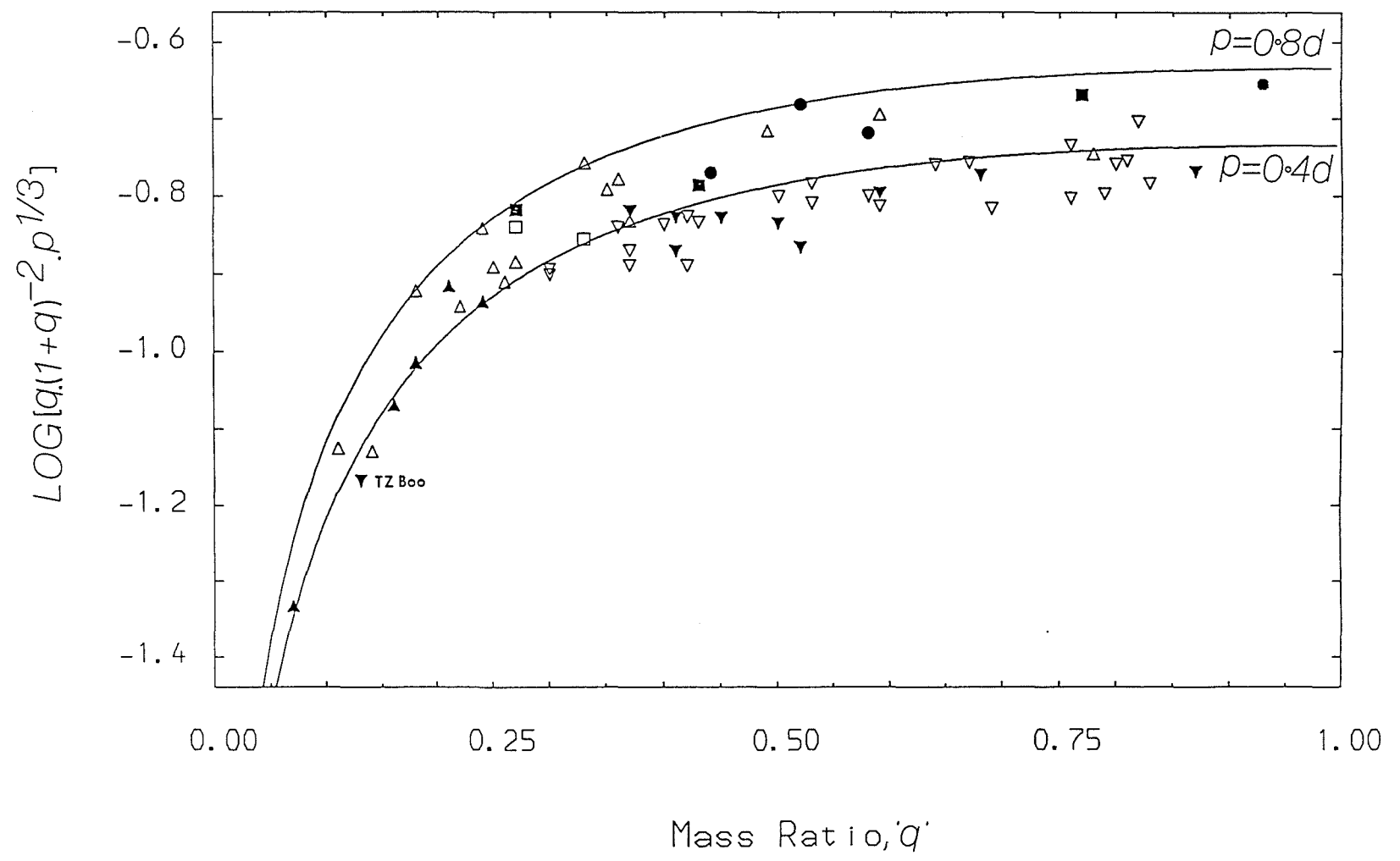


Figure 9.4.
 Plot of 'q against $\log[q.(1+q)^{-2}.p^{1/3}]$, for the data on late-type contact and near-contact binaries shown in Table 9.1, where 'q' is the mass ratio and 'P' is the orbital period expressed in days. The solid lines indicate points of constant period.

Figure 9.5.
Replot of Figure 9.4, but with the shaded symbols indicating spectroscopically defined mass ratios.



APPENDIX A

CALCULATION OF ERRORS

The methods of error calculation, used throughout this thesis, are as follows (see Barford (1967)):

For a linear combination of quantities,

$$z = a + b.x + c.y + \dots ,$$

the error is given by,

$$\sigma_z = [b^2.(\sigma_x)^2 + c^2.(\sigma_y)^2 + \dots]^{1/2} ,$$

where, z, x, y, \dots denote the quantities,

a, b, c, \dots are error free constants,

$\sigma_z, \sigma_x, \sigma_y, \dots$ are the actual errors on the quantities

(e.g. standard deviations).

For a general product,

$$z = a.x^b.y^c \dots ,$$

the error is given by,

$$\Delta z = [b^2.(\Delta x)^2 + c^2.(\Delta y)^2 + \dots]^{1/2} ,$$

where, $\Delta z, \Delta x, \Delta y, \dots$ are the proportional errors on the quantities,

$$\Delta z = (\sigma_z)/z, \Delta x = (\sigma_x)/x, \Delta y = (\sigma_y)/y, \dots$$

The errors on logarithms and exponentials were calculated by taking averages of upper and lower limits, rather than by the usual differential methods.

APPENDIX B

COMMENTS AND CORRECTIONS

Times of observations:

All times of observations quoted throughout this thesis are in Modified Heliocentric Julian Dates.

Rotational angular momentum:

In Chapters 5, 6 and 7 the rotational angular momenta of the components of YY Cet, CX Aqr and RV Crv were estimated using equation 5.4, namely,

$$J_{\text{rot}} = (2/5).m.r^2.2\pi.P^{-1} \text{ kg m}^2 \text{ s}^{-1}$$

However, this equation assumes uniform stellar density, which is far from the case in reality. A much more realistic estimate is given by equation 5.18, that is,

$$J_{\text{rot}} = (0.07).m.r^2.2\pi.P^{-1} \text{ kg m}^2 \text{ s}^{-1}$$

Thus, recalculating the rotational and total angular momenta from Chapters 5, 6 and 7, using equation 5.18, yields:

For YY Cet (Appendix 5.6):

$$J_{\text{rot tot}} = (6.5 \pm 0.9) \times 10^{43} \text{ kg m}^2 \text{ s}^{-1}$$

$$J_{\text{tot}} = (1.48 \pm 0.27) \times 10^{45} \text{ kg m}^2 \text{ s}^{-1}$$

For CX Aqr (Appendix 6.4):

Solution 1:

$$J_{\text{rot tot}} = (2.5 \pm 0.2) \times 10^{43} \text{ kg m}^2 \text{ s}^{-1}$$

$$J_{\text{tot}} = (6.65 \pm 0.96) \times 10^{44} \text{ kg m}^2 \text{ s}^{-1}$$

Solution 2:

$$J_{\text{rot tot}} = (2.6 \pm 0.3) \times 10^{43} \text{ kg m}^2 \text{ s}^{-1}$$

$$J_{\text{tot}} = (6.66 \pm 0.96) \times 10^{44} \text{ kg m}^2 \text{ s}^{-1}$$

For RV Crv (Appendix 7.4):

For the solution employing the radiative primary component:

$$J_{\text{rot tot}} = (5.4 \pm 1.9) \times 10^{43} \text{ kg m}^2 \text{ s}^{-1}$$

$$J_{\text{tot}} = (7.9 \pm 6.1) \times 10^{44} \text{ kg m}^2 \text{ s}^{-1}$$

For the solution employing the convective primary component:

$$J_{\text{rot tot}} = (5.6 \pm 1.9) \times 10^{43} \text{ kg m}^2 \text{ s}^{-1}$$

$$J_{\text{tot}} = (8.0 \pm 6.1) \times 10^{44} \text{ kg m}^2 \text{ s}^{-1}$$

REFERENCES:

Abhyankar, K.D., Parthasarathy, M., Sanwal, N.B. & Sarma, M.B.K.,
1973, *Astron. Astrophys. Suppl. Ser.*, 13, 101.

Aitken, R.G.,

1935, *The Binary Stars*,
McGraw-Hill, New York.

Anderson, L. & Shu, F.H.,

1977, *Astrophys. J.*, 214, 798.

Barford, N.C.,

1967, *Experimental Measurement: Precision, Error and Truth*.
Addison-Wesley Pub. Co., Inc., London.

Batten, A.H., Harris, H.C., McClure, R.D. & Scarfe, C.D.,

1983, *Publ. Dom. astrophys. Obs.*, 16, 143.

Bell, S.A.,

1986, *Priv. Comm.*

Bergeat, J., Lunel, M. & Sibille, F.,

1972, *Astron. Astrophys.*, 17, 215.

Bevington, P.R.,

1969, *Data Reduction and Error Analysis in the Physical
Sciences*,
McGraw-Hill, New York.

Biermann, P. & Thomas, H., -C.,

1972, *Astron. Astrophys.*, 16, 60.

Biermann, P. & Thomas, H., -C.,

1973, *Astron. Astrophys.*, 23, 55.

Binnendijk, L.,

1965, *Kleine Ver. Bam.*, 4, 40, 36.

Binnendijk, L.,

1970, *Vistas in Astron.*, 12, 217.

Binnendijk, L.,

1977, *Vistas in Astron.*, 21, 359.

Black, D.C. & Bodenheimer, P.,

1975, *Astrophys. J.*, 199, 619.

Black, D.C. & Bodenheimer, P.,

1976, *Astrophys. J.*, 206, 138.

Bodenheimer, P. & Ostriker, J.P.,

1973, *Astrophys. J.*, 180, 159.

Bodenheimer, P.,

1978, *Astrophys. J.*, 224, 488.

Bond, H.E. & Landolt, A.U.,

1969, *Publ. Astr. Soc. Pacific*, 81, 696.

Bookmyer, B.B.,

1974, *Inf. Bull. Var. Stars*, No. 919.

Bookmyer, B.B. & Faulkner, D.R.,

1978, *Publ. Astr. Soc. Pacific*, 90, 307.

Brenner, N.M.,

1970, 'FOURT', COSMIC/SHARE,

Univ. of Georgia.

Buttery, I.G.,

1942, *Ann. Harv. Coll. Obs.*, 109, 25.

Carbon, D.F. & Gingerich, O.J.,

1969, *Theory and Observations of Normal Stellar
Atmospheres*, 377.

MIT press, Cambridge, Mass.

ed. Gingerich, O.J.

- Chandrasekhar, S.,
1969, *Ellipsoidal Figures of Equilibrium*,
Yale Univ. Press.
- Cook, T.L. & Harlow, F.H.,
1978, *Astrophys. J.*, 225, 1005.
- Cooley, J.W. & Tukey, J.W.,
1965, *Math. Comput.*, 19, 297.
- Cousins, A.W.J.,
1980, *SAAO Circ.*, 1, 234.
- Crawford, D.L.,
1975, *Astr. J.*, 80, 955.
- Crawford, D.L.,
1979, *Astr. J.*, 84, 1858.
- Eaton, J.A., Wu, C., -C. & Rucinski, S.M.,
1980a, *I.A.U. Symp.*, 88, 501.
- Eaton, J.A., Wu, C., -C. & Rucinski, S.M.,
1980b, *Astrophys. J.*, 239, 919.
- Eaton, J.A. & Wu, C., -C.,
1981, *Astr. J.*, 86, 1387.
- Eaton, J.A.,
1983, *Astrophys. J.*, 268, 800.
- Eggen, O.J.,
1961, *Royal Obs. Bull.*, 31, E101.
- Eggen, O.J.,
1978, *Astron. J.*, 83, 288.
- Eggen, O.J.,
1967, *Mem. R. astr. Soc.*, 70, 111.

- Evans, D.S., Menzies, A. & Stoy, R.H.,
1957, Mon. Not. R. astr. Soc., 117, 534.
- Evans, D.S., Menzies, A. & Stoy, R.H.,
1959, Mon. Not. R. astr. Soc., 119, 638.
- Evans, D.S., Laing, J.D., Menzies, A. & Stoy, R.H.,
1964, R. Obs. Bull., No. 85.
- Faulkner, J.,
1976, I.A.U. Symp., 73, 193.
- Filin, P.,
1971, Inf. Bull. Var. Stars, No. 584.
- Flannery, B.P.,
1976, Astrophys. J., 205, 217.
- Geyer, E.H.,
1976, I.A.U. Symp., 73, 313.
- Gingold, R.A. & Monaghan, J.J.,
1977, Mon. Not. R. astr. Soc., 181, 375.
- Gingold, R.A. & Monaghan, J.J.,
1979, Mon. Not. R. astr. Soc., 184, 481.
- Gotz, W. von & Wenzel, W.,
1966, MVS Sonneberg, 3, 133.
- Guiricin, G., Mardirossian, F. & Mezzetti, M.,
1982, Astron. Astrophys. Suppl. Ser., 49, 89.
- Hayashi, C.,
1961, Pub. Astr. Soc. Japan, 13, 450.
- Hazlehurst, J.,
1970, Mon. Not. R. astr. Soc., 149, 129.
- Hazlehurst, J.,
1974, Astron. Astrophys., 36, 49.

Hazlehurst, J.,

1976. I.A.U. Symp., 73, 323.

Hazlehurst, J., Refsdal, S. & Stobbe, C.,

1977, Astron. Astrophys., 58, 47.

Hazlehurst, J. & Refsdal, S.,

1978, Astron. Astrophys., 62, L9.

Hazlehurst, J. & Refsdal, S.,

1980, Astron. Astrophys., 84, 200.

Hazlehurst, J., Hoppner, W. & Refsdal, S.,

1982, Astr. Astrophys., 109, 117.

Henden, A.A. & Kraitchuck, R.H.,

1982, Astronomical Photometry, 54.

Van Nostrand Reinhold Co. Inc., New York.

Hilditch, R.W.,

1973, Mon. Not. R. astr. Soc., 164, 101.

Hilditch, R.W.,

1981, Mon. Not. R. Astr. Soc., 196, 305.

Hilditch, R.W., King, D.J., Hill, G. & Poeckert, R.,

1984, Mon. Not. R. astr. Soc., 208, 135.

Hilditch, R.W. & King, D.J.,

1986, Submitted to Mon. Not. R. astr. Soc.

Hill, G.,

1979, Publ. Dom. astrophys. Obs., 15, 297.

Hill, G.,

1982a, Publ. Dom. astrophys. Obs., 16, 59.

Hill, G.,

1982b, Publ. Dom. astrophys. Obs., 16, 67.

- Hill, G., Fisher, W.A. & Poekert, R.
1982a, Publ.Dom.astrophys.Obs., 16, 27.
- Hill, G., Fisher, W.A. & Poekert, R.,
1982b, Publ.Dom.astrophys.Obs., 16, 43.
- Hill, G., Ramsden, D., Fisher, W.A. & Morris, S.C.,
1982, Publ.Dom.astrophys.Obs. 16, 11.
- Hoffmeister, C.,
1931, A.N., 242, 131.
- Hoffmeister, C.,
1935, A.N., 258, 39.
- Hoffmeister, C.,
1942, A.N., 273, 92.
- Hoffmeister, C.,
1943a, Kl.Veroff. Berlin-Babelsberg Obs., No.26.
- Hoffmeister, C.,
1943b, Kl.Veroff. Berlin-Babelsberg Obs., No.27.
- Huang, S., -S.,
1966, Ann. D'Astrophysique, 29, 331.
- Hutchings, J.B.,
1973. Astrophys.J., 180, 501.
- Iben, I.,
1967, Ann.Rev.Astr.Astrophys., 5, 571.
- Irwin, J.B.,
1973, Astrophys.J., 179, 241.
- Jeans, J.,
1929, Astronomy and Cosmology,
Cambridge Univ. Press.

Jensch, A.,

1934, Astr.Nach., 251, 327.

Johnson, H.L.,

1966, Ann.Rev.Astr.Astrophys., 4, 193.

Kaluzny, J.,

1983, Acta Astronomica, 33, 345.

Kaluzny, J. & Semenuik, I.,

1984, Acta Astronomica, 34, 433.

Kaluzny, J..

1986a, Acta Astronomica, 36, in press.

Kaluzny, J.,

1986b, Acta Astronomica, 36, in press.

Kaluzny, J.,

1986c, Acta Astronomica, 36, in press

Kaluzny, J.,

1986d, Submitted to Publ.Astr.Soc. Pacific.

King, D.J. & Hilditch, R.W.,

1984, Mon.Not.R.astr.Soc., 209, 645.

Klimek, Z.,

1973, Inf.Bull.Var. Stars, No.779.

Koch, R.H., Sobieski, S. & Wood, F.B.,

1963, A Finding List for Observers of Variable Stars,

Pennsylvania Univ. press.

Koch, R.H.,

1974, Astron.J., 79, 34.

Kopal, Z.,

1959, Close Binary Systems, Chap.6.,

J.Wiley & Sons, New York.

Kraicheva, Z.T., Popova, E.I., Tutokov, A.V. & Yungel'son, L.R.,

1979, *Sov. Astron.*, 23(3), 290.

Krobusek, B.A. & Mallama, A.D.,

1975, *Inf. Bull. Var. Stars*, No. 954.

Kuhi, L.V.,

1964, *Publ. Astr. Soc. Pacific*, 76, 430.

Kuiper, G.P.,

1941, *Astrophys. J.*, 93, 133.

Kurucz, R.L., Peytremann, E. & Avrett, E.H.,

1974, *Blanketed Model Atmospheres for Early-Type Stars*,
Smithsonian Inst. Press, Washington.

Kurucz, R.L.,

1979, *Astrophys. J. Suppl. Ser.*, 40, 1.

Kwee, K.K. & van Woerden, H.,

1956, *Bull. astr. Inst. Netherlands*, 12, 327.

Larson, R.B.,

1969, *Mon. Not. R. astr. Soc.*, 145, 271.

Larson, R.B.,

1972a, *Mon. Not. R. astr. Soc.*, 156, 437.

Larson, R.B.,

1972b, *Mon. Not. R. astr. Soc.*, 157, 121.

Leung, K.C.,

1980, *I. A. U. Symp.*, 88, 527.

Lin, D.N.C.,

1977, *Mon. Not. R. astr. Soc.*, 179, 265.

Linnell, A.P.,

1982, *Astrophys. J. Suppl. Ser.*, 50, 85.

Linnell, A.P.,

1985, *Astrophys.J.Suppl.Ser.*, 57, 611.

Lubow, S.H. & Shu, F.H.,

1977, *Astrophys.J.*, 216, 517.

Lucy, L.B.,

1968a, *Astrophys.J.*, 151, 1123.

Lucy, L.B.,

1968b. *Astrophys.J.*, 153, 877.

Lucy, L.B. & Sweeney, M.A.,

1971. *Astron.J.*, 76, 544.

Lucy, L.B.,

1973, *Astrophys.Sp.Sci.*, 22, 381.

Lucy, L.B.,

1974, *Astronom.J.*, 79, 745.

Lucy, L.B.,

1976, *Astrophys.J.*, 205, 208.

Lucy, L.B.,

1977, *Astronom.J.*, 82, 1013.

Lucy, L.B. & Ricco, E.,

1979, *Astronom.J.*, 84, 401.

Lucy, L.B. & Wilson, R.E.,

1979, *Astrophys.J.*, 231, 502.

Lyttleton, R.A.,

1953, *The Stability of Rotating Liquid Masses*,

Cambridge Univ. Press.

Mallama, A.D., Skillman, D.R., Pinto, P.A. & Krobusek, B.A.,

1977, *Inf.Bull.Var. Stars*, No.1249.

MacDonald, D.D.,

1964, Publ. of Leander McCormick Obs., 12.

McFarlane, T.M., King, D.J. & Hilditch, R.W.,

1986, Mon. Not. R. astr. Soc., 218, 159.

McFarlane, T.M., Hilditch, R.W. & King, D.J.,

1986, Submitted to Mon. Not. R. astr. Soc. .

McFarlane, T.M., Bell, S.A., Adamson, A.J. & Hilditch, R.W.,

1986, Submitted to Mon. Not. R. astr. Soc. .

McFarlane, T.M., King, D.J. & Hilditch, R.W.,

In preparation.

Menzies, J.W., Banfield, R.M. & Laing, J.D.,

1980, SAAO Circ., 1, 149.

Mestel, L.,

1968, Mon. Not. R. astr. Soc., 138, 359.

Mochmacki, S.W. & Doughty, N.A.,

1972a, Mon. Not. R. astr. Soc., 156, 51.

Mochmacki, S.W. & Doughty, N.A.,

1972b, Mon. Not. R. astr. Soc., 156, 243.

Mochmacki, S.W. & Whelan, J.A.J.,

1973, Astron. Astrophys., 25, 249.

Mochmacki, S.W.,

1981, Astrophys. J., 245, 650.

Moss, D.L. & Whelan, J.A.J.,

1970, Mon. Not. R. astr. Soc., 149, 147.

Moss, D.L.,

1971, Mon. Not. R. astr. Soc., 153, 41.

Moss, D.L. & Whelan, J.A.J.,

1973, Mon. Not. R. astr. Soc., 161, 239.

- Mullan, D.J.,
1975, *Astrophys. J.*, 198, 563.
- Napier, W.M.,
1981, *Mon. Not. R. astr. Soc.*, 194, 149.
- Naqvi, S.I.H. & Gronbech, B.,
1976, *Astron. Astrophys.*, 47, 315.
- Nariai, K.,
1980, *I.A.U. Symp.*, 88, 511.
- Norman, M.L. & Wilson, J.R.,
1978, *Astrophys. J.*, 224, 497.
- Okamoto, I. & Sato, K.,
1970, *Publ. Astr. Soc. Japan*, 22, 317.
- Ostriker, J.P. & Bodenheimer, P.,
1973, *Astrophys. J.*, 180, 171.
- Paczynski, B.,
1967, *Acta Astronomica*, 17, 287.
- Paczynski, B.,
1970a, *Acta Astronomica*, 20, 47.
- Paczynski, B.,
1970b, *Acta Astronomica*, 20, 195.
- Papaloizou, J. & Pringle, J.E.,
1979, *Mon. Not. R. astr. Soc.*, 189, 5p.
- Patterson, J.,
1984, *Astrophys. J. Suppl. Ser.*, 54, 443.
- Pohl, E. & Kizilirmak, A.,
1972, *Inf. Bull. Var. Stars*, No. 647.
- Popova, E.I., Tutukov, A.U. & Yungler'son, L.R.,
1982, *Soviet Astron. Lett.*, 8.

Popper, D.M.,

1980, *Ann.Rev.Astr.Astrophys.*, 18, 115.

Powell, M.J.D.,

1967, Report No. HL67/5309, AERE, Harwell.

Rahunen, T. & Vilhu, O.,

1977, *Astron.Astrophys.*, 56, 99.

Rahunen, T.,

1981, *Astron.Astrophys.*, 102, 81.

Rahunen, T. & Vilhu, O.,

1982, *I.A.U. Coll.*, 69, 289.

Rahunen, T.,

1982, *Astron.Astrophys.*, 109, 66.

Refsdal, S. & Stabell, R.,

1981, *Astron.Astrophys.*, 93, 297.

Robertson, J.A. & Eggleton, P.P.,

1977, *Mon.Not.R.astr.Soc.* 179, 359.

Roxburgh, I.W.,

1966, *Astrophys.J.*, 143, 111.

Rucinski, S.M.,

1973, *Acta Astronomica*, 23, 79.

Rucinski, S.M.,

1974, *Acta Astronomica*, 24, 119.

Rucinski, S.M.,

1978, *Non-stationary Evolution of Close Binaries*, 117.

Polish Scientific Publishers.

Rucinski, S.M.,

1985, *Interacting Binary Stars*,
Cambridge Univ. Press, Cambridge.

eds. Pringle, J.E. & Wade, R.A. .

Rucinski, S.M.,

1985a, *Interacting Binaries*,
D.Reidel Publ.Co., Holland.

eds. Eggleton, P.P. & Pringle, J.E. .

Russo, G., Vittone, A.A. & Milano, L.,

1984, *Astron.Astrophys.Suppl.Ser.*, 57, 69.

Schatzman, E.,

1962, *Annales D'Astrophysique*, 25, 18.

Scheffler, H.,

1982, *Landolt-Bornstein*,
*Numerical Data and Functional Relationships in
Science and Technology*, Vol.IV/2c, 46.
Springer-Verlag, Berlin.

eds. Schaifers, K. & Voigt, H.H.

Shu, F.H., Lubow, L.H. & Anderson, L.,

1976, *Astrophys.J.*, 209, 536.

Shu, F.H., Lubow, L.H. & Anderson, L.,

1979, *Astrophys.J.*, 229, 223.

Shu, F.H.,

1980, *I.A.U. Symp.*, 88, 477.

Skillen, W.J.,

1985, Ph.D. Thesis, University of St.Andrews.

Skumanich, A.,

1972, *Astrophys.J.*, 171, 565.

Smart, W.M.,

1977, A Textbook on Spherical Astronomy, Chap.14,
Cambridge Univ. Press, Cambridge.

Smith, D.H., Robertson, J.A. & Smith, R.C.,

1980, Mon.Not.R.astr.Soc., 190, 177.

Smith, M.A.,

1979, Publ.Astr.Soc. Pacific, 91, 737.

Smith, R.C.,

1984, Q.Jl.R.astr.Soc, 25, 405.

Smith, R.C.,

1986, Priv.Comm.

Soloviev, A.,

1936, Tadjik Obs.Circ., 18.

Strohmeier, W.,

1967, Inf.Bull.Var. Stars, No.225.

Strohmeier, W. & Bauernfeind, H.,

1969, Inf.Bull.Var. Stars, No.360.

Strohmeier, W. & Knigge, R.,

1969, Mon.Not.Astr.Soc. Southern Africa, 28, 75.

Struve, O. & Gratton, L.,

1948, Astrophys.J., 108, 497.

Tapia, S. & Whelan, J.,

1975, Astrophys.J., 200, 98.

Tassoul, J.,-L. & Ostriker, J.P.,

1970, Astron.Astrophys., 4, 423.

Thomas, H., -C.,

1977, Ann.Rev.Astron.Astrophys., 15, 127.

Van't Veer,F.,

1976, I.A.U. Symp.,73,343.

Van't Veer,F.,

1979, Astron.Astrophys.,80,287.

Vilhu,O.,

1973, Astron.Astrophys.,26,267.

Vilhu,O. & Rahunen,T.,

1980, I.A.U. Symp.,88,491.

Vilhu,O. & Rahunen,T.,

1981, I.A.U. Symp.,93,181.

Vilnu,O.,

1982, Astron.Astrophys.,109,17.

Vilhu,O.,

1983, Highlights of Astronomy,6,643.

Reidel Publ. Co., Holland.

ed. West,R.M. .

Webbink,R.F.,

1976, Astrophys.J.,209,829.

Wells,D.C., Greisen,E.W. & Harten,R.H.,

1981, Astrophys.J.Suppl.Ser.,44,363.

Whelan,J.A.J.,

1972, Mon.Not.R.astr.Soc.,156,115.

Williamon,R.M.,

1977, Bull.Am.Astr.Soc.,9,92.

Williamon,R.M.,

1978, Bull.Am.Astr.Soc.,10,102.

Wilson,O.C.,

1963, Astrophys.J.,138,832.

Wilson, O.C. & Skumanich, A.,

1964, *Astrophys. J.*, 140, 1401.

Wilson, R.E. & Devinney, E.J.,

1973, *Astrophys. J.*, 182, 539.

Wilson, R.E.,

1978, *Astrophys. J.*, 224, 885.

Wolf, G.W. & Kern, J.T.,

1983, *Astrophys. J. Suppl. Ser.*, 52, 429.

Zessewitsch, V.P.,

1949, I.A.U. Name List 45.